

## Analysis of Converter Small Signal Model Limitations and Oscillation Propagation in Medium Voltage and High Voltage DC Systems

PhD Thesis

Sophie Coffey

PEDEC

 $\label{eq:continuous} \mbox{Department of Electronic and Electrical Engineering} \\ \mbox{University of Strathclyde, Glasgow}$ 

September 27, 2025

This thesis is the result of the author's original research. It has been composed by the author and has not been previously submitted for examination which has led to the award of a degree.

The copyright of this thesis belongs to the author under the terms of the United Kingdom Copyright Acts as qualified by University of Strathclyde Regulation 3.50. Due acknowledgement must always be made of the use of any material contained in, or derived from, this thesis.

### Abstract

To combat climate change, the traditional electricity grids of the past with fossil fuel synchronous generation are being replaced with renewable based generation. The increasing penetration of inverter based resources (IBR) has resulted in the modern grid experiencing changes in dynamic characteristics caused by new devices, controls and time frames being introduced. This replacement of synchronous generation has resulted in several issues that need to be addressed to further progression in reaching Net Zero emissions.

Some of the new technologies in the modern grid to enable the integration of renewable generation are grid-tied converters, state-of-the-art control topologies and Medium Voltage Direct Current (MVDC) and High Voltage Direct Current (HVDC) transmission and distribution. The fundamental topologies, future prospects and applications of MVDC and HVDC need to be understood to achieve the full potential of these technologies. Therefore, this thesis presents a comprehensive analysis and overview of MVDC uses, demonstration projects, converter topologies, architecture structures, and unique issues and operations.

These new technologies are offering a wealth of solutions to technical challenges facing the integration of renewable generation, there are however, associated problems with each new evolution. Firstly, IBRs have been mainly controlled with grid following control, which requires the measurement of the grid voltage source to synchronise. This can contribute to grid issues and system instability. There have been several suggested amendments to classical GFL control to improve ancillary support to connected AC grids. For example, there has been discussion in the literature comparing the

inertial response provided by grid forming and following controllers, showing grid following converters can provide similar inertial responses to grid forming under certain conditions. However, the effect of providing an inertia response on stability of grid following connected systems needs to be assessed, with this thesis investigating the tuning limitations that restrict the capability of grid following converters to provide the required inertial response in an appropriate time.

With the differing control topologies being implemented, the rapidly changing grid composition is producing scenarios that are increasingly complex to model, as well as unwanted grid dynamics such as sub-synchronous oscillations (SSOs) that are not being predicted. The combination of new devices and controllers with faster time constants is resulting in an expansion of typically seen SSOs, from sub-synchronous resonances, device dependent SSOs, to sub-synchronous control interactions and subsynchronous torsional interactions. However, there are increasingly instances of SSOs persisting in the grid that were not accurately predicted. Capabilities and limitations of converter models need to be understood for recommendations to Transmission System Operators (TSOs), Original Equipment Manufacturers (OEMs), and project operators. Therefore this thesis assesses the impact of extreme parameter conditions on a series of common grid following and grid forming converter to grid small signal models of varying complexity, simplifications and assumptions. Additionally, comprehensive methods of assessment of dynamic transient and modal detail are presented to give an intuitive yet novel insight for showing capabilities of each model. This includes highlighting the effect of variations in low frequency modes on transient dynamic response, and a method of screening models for modal accuracy in identifying oscillatory SSOs, highlighting conditions where lower detail models do not represent low frequency oscillations when they are expected to.

The importance of dynamic detail is essential in larger more complex systems. The difficulties of not recognising unwanted SSOs and harmonics are compounded with increasing grid complexity. The development of interconnected HVDC systems has been enabled with voltage source converters (VSC) and furthermore with modular multilevel

converters (MMC), which provide large voltage step ups. HVDC-MMC systems have been stated to have an inherent "firewall" capability, which has been described as the prevention of unwanted oscillations between interconnected AC systems, because of the controllability on either side of the link. MMCs however have harmonics produced in internal circulating currents and sub-module voltages that need to be controlled, and require accurate modelling. Further to this, grid dynamics, accurate DC link representation, and converter control all need to be modelled to given a fully detailed representation of multiterminal MMC-HVDC systems and propagation between interconnected grids. Therefore, this thesis develops a highly detailed dynamic model of a point-to-point MMC-HVDC system for the effect of grid following and grid forming controls on the firewall capability of the system, assessing critical state dependencies that participate in oscillatory poorly damped modes. A firewall quantification metric is proposed to identify conditions that could cause oscillation propagation, and a comprehensive overview of the effect of changing system and control parameters on firewall capability.

Li	st of	Figure	es	ix
Li	st of	Table	S	$\mathbf{x}\mathbf{v}$
Li	st of	Acron	nyms	xvi
1	Intr	oducti	ion	1
	1.1	Motiv	ation	1
	1.2	Resear	rch Gaps	2
	1.3	Resear	rch Questions, Objectives and Methodologies	4
	1.4	Contri	ibutions	6
		1.4.1	Publications	7
	1.5	Thesis	S Outline	8
2	Rev	iew of	MVDC Applications, Technologies and Future Prospects	10
	2.1	Mediu	ım Voltage to High Voltage DC	11
	2.2	MVD	C applications	11
		2.2.1	Sea	14
		2.2.2	Rail Systems	18
		2.2.3	Network Distribution Grid Systems	21
	2.3	MVD	C For Grid Connected Applications	24
		2.3.1	Applications	24
		2.3.2	Grid Topologies	29
	2.4	Hardw	vare	30

		2.4.1	Converters	31
		2.4.2	Smart Transformer	39
		2.4.3	Insulated Gate Bipolar Transistor (IGBT) and MOSFETs	41
	2.5	Protec	etion	42
		2.5.1	Overview	42
		2.5.2	System Protections	42
		2.5.3	Converter Protection	44
		2.5.4	Control for Protection	45
	2.6	Conve	rter Control	45
		2.6.1	DC Control	47
		2.6.2	Network Level Control	48
	2.7	MVD0	C Conclusion	50
3	Pow	ver Co	nverter Modelling and Control	<b>52</b>
	3.1	Vector	Control and Representation of Converters and Grid Systems	52
		3.1.1	Representation of Voltage Source Converter	53
		3.1.2	Space vector theory and frame representations	54
	3.2	Synch	ronous Reference Frame Phase Locked Loop (SRF-PLL) and	
		Frame	Conversions	56
	3.3	Grid I	Following Control	60
	3.4	Grid I	Forming Control	64
		3.4.1	Grid Stability Issues	64
		3.4.2	Grid Forming Control Topologies	66
	3.5	Small	Signal Modelling	72
		3.5.1	Model of Converter to Grid System	72
		3.5.2	Linearised Small Signal Synchronous Reference Frame Phase	
			Locked Loop	74
		3.5.3	Linearised Reference Frame Transforms	77
		3.5.4	Linearised Current Controller	77
		3 5 5	Linearised Grid Forming Control	79

4	Stal	oility Limits and Tuning Recommendation of the Standard	
	Cur	rent Control Providing Inertia Support	80
	4.1	Motivation	80
	4.2	Introduction	81
	4.3	System Under Study	82
	4.4	Inertia Emulation	84
	4.5	Small Signal Model	85
	4.6	Investigation	86
	4.7	Results	86
		4.7.1 Impact of $K_{in}$ and $F$ with Varying SCR	86
		4.7.2 Kin against $\tau_{PLL}$	87
		4.7.3 Kin against $\tau \alpha$ , Current Controller Time Constant	88
	4.8	Recommendations and Limitations	90
		4.8.1 Inertia Emulation Capability in Fast Operation	90
		4.8.2 Standard Current Controller Operation Region	91
	4.9	Chapter Summary	92
5	Lim	itations and Comparisons of Small Signal Modelling Techniques	
	in C	Converter Dominated Medium Voltage Networks	94
	5.1	Motivation	95
	5.2	$Introduction \dots \dots$	96
	5.3	System Under Study	97
	5.4	Methodology	99
	5.5	Small Signal Model	100
		5.5.1 Full Detail EMT SSM	100
	5.6	Jacobian Model	100
	5.7	Classical Second Order Model	102
	5.8	Results	104
		5.8.1 Overview of Step Response	104
	5.9	Eigenvalue Analysis	107
	5 10	Model Comparison Overview	108

	5.11	Chapt	ser Summary	112
6 Assessing the Capability and Limitations of Small Signal Simplifi				
	Gri	d Foll	owing Models for the Identification of Sub-Synchron	ous
	Osc	illatio	$\mathbf{n}\mathbf{s}$	114
	6.1	Motiv	ation	115
	6.2	Metho	odology	117
		6.2.1	Implementation of Small Signal Models	117
		6.2.2	Identification of Problem Modes	118
		6.2.3	Parametric Overview	119
	6.3	Model	lling	119
		6.3.1	Model Selection Overview	120
		6.3.2	Model 1: Full Detail SSM	122
		6.3.3	Model Two: Model Order Reduction	126
		6.3.4	Model 3: Phasor Simplified Small Signal Model	130
	6.4	Case S	Study	131
		6.4.1	Results	132
	6.5	Summ	nary and Model Suggestions	141
7	Effe	ect of	Grid Forming and Grid Following control on Firev	wall
	Cap	ability	y of MMC-HVDC Systems	144
	7.1	Overv	iew	144
	7.2	Introd	luction	145
	7.3	Syster	m Under Study	147
	7.4	Metho	odology	149
		7.4.1	Small Signal Model Development	149
		7.4.2	Identifying Problem Modes and Participating States	149
		7.4.3	Bode Plot Input-Output Selections	151
		7.4.4	Heat-maps for Screening of Propagation Risk Conditions	151
		7.4.5	Firewall Quantification Metric	151
	7.5	Small	Signal Model	152

		7.5.1	DC Link	158
		7.5.2	MMC Circulating Currents	162
		7.5.3	DC Voltage Droop	162
		7.5.4	Grid Forming Control	163
	7.6	Case S	Study Results	166
		7.6.1	Participating State Identification	166
		7.6.2	Bode Plots	168
		7.6.3	Heat-map Parametric Overview	171
		7.6.4	Frequency and Time Domain Comparison	174
	7.7	Conclu	usion	177
8	The	sis Co	nclusion	180
	8.1	Future	e Work	185
A	Full	Deriv	ration of Small Signal Synchronous Reference Frame Phas	e
		ked Lo	· ·	187
В	Jaco	bian I	Matrix Detail	190
$\mathbf{C}$	Mod	del Or	der Reduction Detailed Expansion	193
D	Par	ticipat	ion Factors	197
		•		
${f E}$	MM	-	uation Derivation Detail	198

2.1	Traditional AC ship distribution systems.(a) propulsion isolated, (b)	
	radial IPS, (c) modern AC zonal distribution system	15
2.2	Generic DC shipboard IPS	17
2.3	DC rail distribution system.	20
2.4	Suggested and implemented applications since year 2000 and associated	
	voltage level	24
2.5	SB2B Soft Open Point configuration. b) Soft Power Bridge $\ \ldots \ \ldots \ \ldots$	26
2.6	Network topologies, a) radial, b) hand-in-hand multiterminal, c) Ring.	30
2.7	MVDC bus structures. a) Mono-polar asymmetric. b) Mono-polar	
	$symmetric.\ c)\ Bipolar\ \dots$	31
2.8	Line commutated converter (LCC)	32
2.9	a) Two-level converter (2-level (2L)). b) Three-level neutral point	
	clamped converter (3L-NPC)	33
2.10	MMC and submodules	34
2.11	Converter Station Configuration of Angle-DC Project	35
2.12	Buck-Boost	36
2.13	Dual Active Bridge (DAB) and DAB Resonant Converter $\ \ldots \ \ldots \ \ldots$	37
2.14	Dual Active Bridge Modular Multilevel Converter	38
2.15	Push-Pull and Tuned Filter MMDC	39
2.16	Example of Smart Transformer architecture	40
2.17	Solid State DC Circuit Breaker	43
2.18	Hybrid DC circuit breaker	44

2.19	inherent reactions. GFM acts as a voltage source with series impedance,	
	GFL acts as current source with high parallel impedance	47
2.20	(a) Traditional control communications compared to (b) AC/DC hybrid	11
2.20	<u>-</u>	40
	grid communications	49
3.1	Converter to Grid System	53
3.2	Converter equivalent averaged model	54
3.3	Relation between $abc$ frame, stationary frame, and synchronous reference	
	frame	55
3.4	Control Structure of SRF-PLL	57
3.5	Relation between stationary and synchronous reference frame and PCC	
	voltage	58
3.6	Simplified Control loop of PLL	59
3.7	Simplified Representation of AC sides of VSC to Grid PCC	60
3.8	Current Controller Model of GFL in $dq$ control	64
3.9	Power synchronisation loop with converter angle output	67
3.10	Simplified Equivalent Synchronous Machine to Grid	69
3.11	Control structure of virtual synchronous machine (VSM) with AC	
	voltage controller and synchronisation loop.	71
3.12	PCC voltage vector, grid global synchronous rotating reference frame,	
	and converter synchronous frame	76
4.1	Current Controller With Inertia Emulation.	83
4.2	Time domain and SSM response	85
4.3	$Kin_{max}$ against $F$ Stability limit for varying SCR, $\tau_{PLL}=0.0045$ s, $\tau_{\alpha}$	
	= 0.002 s	87
4.4	Power [kW] Response to 1 pu ramp increase in frequency: $K_{in}=12,F$	
	= 0.3 s, $F = 0.9$ s	88
4.5	Maximum value of $K_{in}$ that can be provided whilst maintaining stability	
	with increasing $\tau_{PLL}$ at SCR = 5	89

4.6	Maximum value of $K_{in}$ that can be allowed whilst maintaining stability,	
	with increasing $\tau_{\alpha}$ at SCR = 5 with a) $\tau_{PLL} = 2 \mathrm{e/wn} = 0.0045 \; \mathrm{s}$ b) $\tau_{PLL}$	
	$=0.04~\mathrm{s}~\ldots\ldots\ldots\ldots\ldots\ldots$	90
4.7	Maximum $K_{in}$ with large range in $\tau_{\alpha}$ , SCR = 5, $\tau_{PLL} = 0.04$ ,	91
4.8	Maximum $K_{in}$ allowed whilst maintaining system stability with	
	increasing $\tau_{\alpha}$ , $\tau_{PLL}$ for a) SCR = 4, b) SCR = 3, c) SCR = 2	92
4.9	Maximum $K_{in}$ allowed whilst maintaining system stability with	
	increasing F, with tuning recommendations $\tau_{PLL}=0.04\mathrm{s},\ \mathrm{a})\ \tau_{\alpha}=0.1$	
	ms, b) $\tau_{\alpha} = 10$ ms, c) $\tau_{\alpha} = 100$ ms	93
4.10	Power Response for system: $\tau\alpha$ =0.1ms $\tau_{PLL}$ =0.04s, SCR 5, Kin = 585	
	As-2, F = 0.5	94
5.1	Virtual synchronous machine to grid connection	98
5.2	Linearised small signal model system connections	101
5.3	Jacobian representation of grid to converter system with VSM control	102
5.4	Small signal model diagram second order synchronous machine model.	103
5.5	Step of 10 MW (0.03pu) SCR = 1.5, $\zeta$ = 0.1 X/R = 10	105
5.6	Step of 10 MW (0.03pu) SCR = 1.5, $\zeta$ = 0.1 X/R = 5	105
5.7	: Step of 10 MW (0.03pu) SCR = 1.5, $\zeta =$ 0.1 X/R = 1	106
5.8	: Step of 10 MW (0.03pu) d) SCR = 6, $\zeta =$ 0.1, X/R = 10. $\   .$	106
5.9	Comparison of the models with SCR 1.5 =, $\zeta$ = 0.1, H = 5 s, over	
	decreasing X/R ratio (10 to 1)	108
5.10	Percentage error in transient response across SCR and damping ratio at	
	$X/R=10. \ldots \ldots$	110
5.11	Percentage error in transient response across SCR and damping ratio at	
	X/R = 1.	111
6.1	Current controller model of GFL in $dq$ control	120
6.2	Simplified phasor model [1]	130
6.3	Summary of small signal representation of equations and assumptions	
	used in each model	132

6.4	Selected power responses of 0.01 pu disturbance. a) $SCR = 1$ , $X/R =$	
	10, $\tau = 50$ ms. b) SCR = 4, X/R = 10, $\tau = 25$ ms	134
6.5	Eigenvalue plots for varying SCR = $0.5$ - $6$	136
6.6	Eigenvalues for varying $\tau$ , 0.7 pu active power, $\tau=1$ ms to 40 ms, SCR	
	$= 0.7, X/R = 10. \dots$	137
6.7	Parameter conditions at which the full detail model has oscillatory sub-	
	synchronous modes, but are not identified by a) the MOR. b) the	
	simplified phasor. 0.1 pu active power operating point	137
6.8	Parameter conditions at which the full detail model has oscillatory sub-	
	synchronous modes, but are not identified by a) the MOR. b) the	
	simplified phasor. 0.7 pu active power operating point	139
6.9	Parameter conditions the full detail model indicates instability, that are	
	not recognised in a) the MOR. b) the simplified phasor. Operating point	
	of 0.1 pu active power power.	140
6.10	Parameter conditions the full detail model indicates instability, that are	
	not recognised in a) the MOR. b) the simplified phasor. Operating Point	
	of 0.7 pu active power power	142
7.1	AC $grid_{jj}$ to AC $grid_{kk}$ through HVDC-MMC link	148
7.2	Single MMC topology connected to AC grid	150
7.3	AC $Grid_{jj}$ to AC $Grid_{kk}$ through HVDC-MMC link	158
7.4	Grid following current control	161
7.5	Circulating current controller	163
7.6	DC voltage droop, $V - P_{ac}$	163
7.7	Control of implemented grid forming converter	164
7.8	Overview of full SSM of system	166
7.9	Validation of small signal model, power at PCC on $grid_{jj}$ following 0.1	
	pu step in power reference.	167
7.10	Eigenvalue parametric sweep across $SCR_{jj}$ of poles of system. $\zeta=0.1$	
	shown by dashed lines. $SCR_{kk}=2$ , $H=6$ s, Droop = 0.002, Damping	
	= 1000 pu	167

7.11	Bode plot of a) input current disturbance to ac $Grid_{kk}$ current, damping
	600, SCRs = 5, H = 6. b) input Voltage to $MMC_{kk}$ sub-module voltage
	$SCR_{jj} = 5$ , $SCR_{kk} = 5$ , H = 6, Droop = 0.02. c) input voltage
	disturbance to AC $Grid_{kk}$ current. Damping = 400 pu $SCR_{jj}$ = 5,
	$\mathrm{H}=1,\mathrm{droop}=0.002,\mathrm{varying\ damping\ d})$ Input current to voltage zero
	component. $SCR_{jj} = SCR_{kk} = 5$ , $H = 6$ , droop = 0.02, varying damping.170
7.12	Heat-map of peak oscillation in system, per unit output from 1 pu input
	disturbance, $edjj$ to $icdkk,SCR_{kk}=5,\mathrm{GFM}$ damping = 60 pu, H = 2
	s a) GFL/GFL b) GFM/GFL
7.13	Heat Map of Peak Oscillation in Grid Forming System, a) $icd_{jj}$ to
	$VCPy2_{kk}$ , $SCR_{jj} = SCR_{kk} = 5$ , $H = 1s$ b) $icd_{jj}$ to $icd_{kk}$ , $H = 2s$ ,
	droop = 0.002, D = 100 pu
7.14	Heat Map of Peak Oscillation in Grid Forming System, a) $ed_{jj}$ to
	$VCP0kk$ , D = 100 pu, droop = 0.002, $SCR_{kk} = 5$ b) $icd_{jj}$ to $idiffx2_{kk}$ ,
	$D = 60 \text{ pu}, SCR_{kk} = 5, droop = 0.002. \dots 174$
7.15	Response of GFM/GFL and GFL/GFL systems to an input power
	oscillation of 0.05 Hz at 0.1 per unit. Damping = 2000 pu, Droop = $$
	0.02, H = 1 s, $SCR_{jj} = SCR_{kk} = 5$
7.16	Frequency spectrum of voltage across phase $a$ in sub-modules in MMC
	at (a) $grid_{jj}$ . (b) $grid_{kk}$
7.17	Time domain response of PCC voltage at when subject to a 100 Hz $0.2$
	pu voltage disturbance in AC $grid_{jj}$ voltage $ed_{jj}.$ (a) PCC voltage $grid_{jj}$
	(b) PCC voltage $qrid_{kk}$

## List of Tables

2.1	MVDC Applications and Voltage Levels	25
2.2	: MOSFET and IGBT Comparison for MVDC applications $\ \ldots \ \ldots$	41
5.1	System Parameters	97
5.2	Parametric Sweep Range	99
5.3	Real components of eigenvalues of models: SCR = 1.5, $\zeta$ = 1, X/R = 10	107
6.1	Details included in each model	122
6.2	System parameters	133
6.3	Parametric range tested	133
7.1	System Base Parameters	148
7.2	Example identifying participating states of poorly damped modes in	
	GFM/GFL system, for $SCR_{jj}=5$ , DC Voltage Droop = 0.002, D =	
	1000 pu, H = 6s	168

## List of Acronyms

AC Alternating Current

BESS Battery Energy Storage System

**CB** Circuit Breaker

**DAB** Dual Active Bridge Converter

**DC** Direct Current

**DG** Distribtued Generation

**DNO** Distribution Network Operator

**ESO** Energy System Operator

EMT Electromagnetic Transient

 $\mathbf{FFR}$  Fast Frequency Response

FACTS Flexible AC Transmission Systems

FB Full Bridge

**GFL** Grid Following

**GFM** Grid Forming

**HB** Half Bridge

**HVDC** High Voltage Direct Current

IBR Inverter Based Resources

List of Tables

IGBT Insulated Gate Bipolar Transistor

 ${\bf IGCT} \ \ {\bf Integrated} \ \ {\bf gate\text{-}commutated} \ \ {\bf thyristor}$ 

**IPS** Integrated Power System

LCC Line Commutated Converter

**LVDC** Low Voltage Direct Current

MIMO Multi Input Multiple Output

**MMC** Modular Multilevel Converter

MMDC Modular Multilevel DC-DC Converter

MOR Model Order Reduction

MTDC Multi-Terminal Direct Current

MVDC Medium Voltage Direct Current

MVAC Medium Voltage Alternating Current

NPC Neutral Point Clamp

NOP Normally Open Point

**OEM** Original Equipment Manufacturers

**PCC** Point of Common Coupling

PI Proportional Integral

**PLL** Phase Locked Loop

**RMS** Root Mean Square

**ROCOF** Rate of Change of Frequency

SCR Short Circuit Ratio

SISO Single Input Single Output

SM Sub-Module

List of Tables

 $\mathbf{SSM}$  Small Signal Model

 ${f SOP}$  Soft Open Point

 ${f SSO}$  Sub Synchronous Oscillations

 ${\bf STATCOM}\ \ {\bf Static}\ \ {\bf Synchronous}\ \ {\bf Compensator}$ 

 ${\bf TSO}$  Transmission System Operators

**TRL** Technology Readiness Level

VOC Virtual Oscillating Control

 $\mathbf{VSC}$  Voltage Source Converter

 $\mathbf{VSM}$  Virtual Synchronous Machine

2L 2-level

**3L** 3-level

## Preface/Acknowledgements

I have the deepest gratitude for my supervisors of this PhD, Agustí Egea-Àlvarez and Sam Harrison. Their continued support, patience and expertise provided me with the best foundation to build my research off of. Additionally, members of the Power Electronics, Drives and Energy Conversion team in the department of Electronic and Electrical Engineering at the University of Strathclyde, Lie Xu, Ning Yang, Yin Chen, Irene Masenge, Ayse Colak, Euan Macrae, Rui Alvez and everyone else in the group. I have received great support and insight from many other member of the wider department, learning from their extensive knowledge and wide expertise. Additionally, members of the wider community at Strathclyde have provided invaluable support and friendship throughout my PhD, namely Lara Diaz-Garcia.

My family have been understanding, helpful, and my inspiration during this research, and I am forever grateful to them. My mother, Nana and Pappy have always been my biggest supporters and without them I would not have been capable of half of what I have done. They helped me through all of my education, my Pappy inspiring me to become an Electrical Engineer, and my Nana and mother showing me how to achieve what I wanted. I am forever grateful for my siblings, Catherine, Patrick and Martin, who I rely on and always care for me, as well as Nick. Also, thank you to Lukey, Ben, Peter, Lena and Claire, (and the new baby) for inspiring me to work for their future. My Aunt and Uncle, Hilary and Seamus, and my cousin Anna gave me the help and support I needed at the most difficult of times and I owe so much to them. Last, but not least, I owe so much to my partner, Luke, who is the kindest and most genuine person.

## Chapter 1

## Introduction

#### 1.1 Motivation

The climate crisis caused by wide scale anthropogenic emissions, such as CO2 and methane [2] [3], has, is, and will cause significant natural disasters that pose a threat to human life and society. Disproportionately, countries with a low GDP, and people who earn below the global average, are affected more than richer countries that have contributed greater amounts of Greenhouse Gas emissions. Already, the world is close to breaching the 1.5 °C limit of global average temperature rise from pre-industrial levels [3]. Therefore, there is the urgent need to decarbonise the traditional fossil fuel powered industries, with modern grids becoming increasingly populated with renewable based generation. In 2023 European renewable generation reached a new peak of 43% [4], with Sweden having the largest share of 70% [5].

Any generation source that relies on varying and unreliable resources (such as wind, solar, tidal, wave) requires a converter connection, resulting in such generation being referred to as an Inverter Based Resources (IBR). These IBRs differ significantly from traditional synchronous generation, from the connection, distribution, location, and effect on the electric grid system. Converter technology has also become significantly advantageous for Medium Voltage Direct Current (MVDC) and High Voltage Direct Current (HVDC) transmission, especially since the introduction of the

Modular Multilevel Converter (MMC), vastly improving the integration of renewable technologies at differing geographical conditions.

#### 1.2 Research Gaps

Traditional standard systems were dominated with synchronous generation (synchronous machines), which set the voltage source, and self-synchronise to the grid. However, the converter connections used in modern grids are typically implemented in a Grid Following (GFL) structure, which relies on an outside voltage source to synchronise to the grid. Such systems without synchronous generation, and instead increased GFL control, can have low available short circuit currents and Short Circuit Ratio (SCR)s, low inertia, and voltage instability [6].

Several improvements to control topologies have been suggested to combat these grid issues. GFL controllers can be enhanced upon their basic services, with voltage support and fault ride through [7], primary frequency control responses [8] [9] and Fast Frequency Response (FFR) controls [6]. Even with such ancillary controls added to GFL topologies, they have been stated as fundamentally having the disadvantage of acting as a controlled current source relying on external synchronisation. Therefore, Grid Forming (GFM) converter control has been suggested in the literature [10], [11] and has been implemented in many demonstration projects [12], with many available topologies offered from Original Equipment Manufacturers (OEM). It has been argued that the inherent voltage source response of the GFM results in a more "truer" inertial response, however it is now being emphasised in the literature that GFL with added inertial control can provide the same support a GFM can [13]. Therefore, the lack of focus on GFL converters with additional inertial support needs to be addressed, and the recommended tuning conditions must be determined.

Further to this, the problems modern grids are experiencing, originating from increased IBRs, are of significant concern, however there is the additional difficulty of accurately predicting grid performance and issues. Model accuracy has always been of essential importance to power system operators, but increasingly there are disturbances on the

grid that have not been predicted, resulting in significant problems. Transmission System Operators (TSO)s have observed Sub Synchronous Oscillations (SSO)s that were not predicted during the pre-grid connection simulation phase. Such examples occurred in the UK in June and July 2023, where 8 Hz oscillations occurred on 5 separate days, resulting in tripping of generation, an HVDC link, an inter-connector and a transmission circuit [14]. This situation, and similar events, resulted in National Grid creating a system plan for tackling SSOs, citing the need for accurate modelling, compliance, and improved research on causes of the underlying mechanisms [15]. Other cases have also been reported worldwide such as in China and the US which have been severely destructive [16].

These issues highlight the need for accurate modelling. Typically, TSOs model the whole system with Root Mean Square (RMS) modelling. This represents the voltages and currents as phasors, and has the grid modelled in algebraic form. The computational burden of this method is more appropriate for representing very large systems, offering dynamic analysis close to the fundamental frequency [17]. However, significant dynamic detail is excluded from this modelling technique. To capture grid dynamics and fast transients, Electromagnetic Transient (EMT) simulations are typically used, where the non-linear differential equations of the instantaneous signals of the system are solved in the time domain. The instantaneous voltages and currents are calculated across the time frame, which is of great benefit when analysing fast system transients, which are increasingly common with fast responding controllers [18], [19].

Each of these modelling methods have known advantages and disadvantages. EMT simulations are used for fast transient analysis, including significant system detail, and representing high frequency harmonics, at the cost of great computational burden and speed. RMS models are used for their ease of implementation, understanding, lower computational burden, and ability to still represent some SSOs (varying detail can be included in the RMS models, which is discussed in later chapters). However, there is a vast reduction in detail compared to EMT Modelling. TSOs, and other operators, needing to model large systems are requiring more accuracy to represent the more

complex systems being added to the grid. However, using EMT models at such scale is infeasible, and other modelling steps have been taken, such as impedance modelling, or using a Small Signal Model (SSM). There have been several suggested adaptions to SSMs to reduce model complexity, for converter to grid systems in both GFL and GFM control. However, the accuracy of such models has not been tested, especially across varying system parameters.

The limitations of reduced detail models highlight the need for including system dynamics and reducing simplifications of grid-tied converter systems. This will ensure the capture of the aforementioned SSOs. This is pertinent, as HVDC systems have been stated to prevent the propagation of such oscillations, having an "inherent firewall capability" HVDC, due to the high controllability capabilities of the converter controllers [20]. This firewall effect can be described as preventing fault and oscillation propagation from one Alternating Current (AC) grid to another. This is due to the typically "strict" control of power flow and Direct Current (DC) voltage on either side of the HVDC link. However, there have been limited studies on this with different controller topologies with MMCs, and none comparing these controllers whilst including the internal MMC dynamics, with more than one converter and accurate DC link modelling.

#### 1.3 Research Questions, Objectives and Methodologies

To address the identified research gaps, the following hypotheses were developed and investigated.

- Although providing inertia is a desired attribute from a converter control system, there could be limits on the amount of inertial support that can be provided depending on system and control conditions. This thesis suggests that providing this support could affect the system stability. Therefore, the effect of weak grid conditions, and grid following control loop parameters on the maximum inertia that can provided whilst maintaining a stable system is to be investigated.
- As described earlier in this chapter the integration of IBRs is resulting in

variations in grid strength, as well as generation and demand in different geographical locations from the traditional grid, resulting in "extreme" grid parameters. It is suggested that modelling methods of lower dynamic detail will miss key details when representing these extreme conditions. Therefore, systematic methodologies for assessing the capability of small signal models of varying detail are required. It is expected that lower detail models have reduced capability, however the conditions that they can be used in must be ascertained.

• Further to this, the importance of highly detailed models in representing oscillations needs to be demonstrated. When using small signal appropriately detailed models, the impact of converter control on propagation of SSOs between asynchronous grids needs to be assessed. Sufficiently detailed point-to-point MMC-HVDC models with accurate DC links and MMC dynamics have not been evaluated in the literature to conclude what parameter conditions result in the controllers significantly affecting the firewall capability of the system. Furthermore, the impact of different control topologies on the propagation of oscillations between AC grids has not been fully investigated. It is suggested in this thesis that the addition of AC grid ancillary services could greatly inhibit this inherent "firewall" capability of HVDC technology by drawing too much support for its connected AC grid, from the DC side. Therefore, the impact of GFM control producing SSOs between interconnected AC grids will be shown across a series of changing grid parameters.

Throughout this thesis, many of the converter-grid tied systems are represented using small signal modelling, which is the transform of non-linear models into a linearised form. Small signal stability describes the ability of the power system to maintain synchronism when subject to a small disturbance [21]. It informs about the power system's inherent dynamic characteristics and stability.

To obtain the model, the non-linear equations for the full system are represented in the rotating reference frame, presented in state space form [21] and linearised around their operating point. Some of the key analysis techniques used in this thesis are

enabled from small signal modelling, specifically eigenvalue analysis. This tackles the aforementioned difficulties in representing dynamic detail and identifying the source of oscillations and interactions in grid systems. Therefore, throughout this thesis, the systems are represented with small signal modelling, which allows for clear analysis of system instability, oscillatory modes, and frequencies at which interactions may occur.

#### 1.4 Contributions

Having identified the need for accurate modelling assessment and detail, and the gaps in the research applying to this, the key contributions of this thesis are proposed.

- Comprehensive review of medium voltage direct current applications, technologies
  and capabilities, including rail, shipboard structures, and grid systems. An
  assessment of active MVDC projects to present clear trends in architecture,
  utilised technologies, benefits and disadvantages, providing guidance as MVDC
  implementation becomes more popular, cheaper and beneficial.
- An in-depth analysis of the limitations of synthetic inertia utilised in GFL converters, and recommendation of the grid parameter and tuning limits to maintain system stability and reliable response, whilst providing required inertia.
- Comparison of transient response accuracy of small signal GFM models under varying grid parameter conditions.
- Methodology for testing dynamic representation capabilities of small signal models of a GFL grid-tied converter system. Additionally, comparison of GFL SSMs for dynamic representation across parameter variations, for recommendation of model suitability.
- Detailed SSM and large signal model of a point-to-point MMC-HVDC system with GFL and GFM control.
- Analysis of harmonic content of MMC-HVDC systems with sufficiently accurate dynamic detail at a small signal and large signal level.

- Identification method and assessment of oscillatory modes and their link with oscillation propagation between asynchronous AC grids interconnected with MMC-HVDC link.
- Methodology of firewall quantification metric to enable identification of the conditions that cause oscillation propagation.
- Comprehensive overview of effect of changing system and control parameters on firewall capability of MMC-HVDC systems.

#### 1.4.1 Publications

The following texts have been published by the author of this thesis.

#### Published:

- Stability Limits and Tuning Recommendation of the Classical Current Control Providing Inertia Support. S. Coffey, J. F. Morris, & A Egea-Álvarez, 29 July 2021, 2021 IEEE Madrid PowerTech Conference).
- Review of MVDC Applications, Technologies, and Future Prospects. S. Coffey, V. Timmers, R. Li, G. Wu, & A. Egea-Àlvarez, 9 Dec 2021, in Energies. 14, 24, 37 p., 8294.
- Limitations and Comparisons of Small Signal Modelling Techniques in Converter Dominated Medium Voltage Networks. S. Coffey, S. Harrison, A. Egea-Àlvarez, & C. Brozio, 2 Oct 2023, 25th European Conference on Power Electronics and Applications 2023 (EPE'23 ECCE Europe).
- Assessing the Capability and Limitations of Small Signal Simplified Grid Following Models for the Identification of Sub-Synchronous Oscillations. S. Coffey, S. Harrison, A. Egea-Àlvarez, L. Xu, in IEEE Access, vol. 13, pp. 116025-116036, 2025.
- Upgraded Control Strategies to Safeguard Resiliency in Hybrid AC-DC
   Networks. M. Sharma, J. C. Gonzalez, J. L. Ruedatorres, Y. Pang, S.Coffey,

A. Knockaert, IEEE Power and Energy Magazine [ACCEPTED Publication date to be confirmed].

Submitted and Under review

• Effect of Grid Forming and Grid Following Control on Firewall Capability of MMC-HVDC Systems., S. Coffey, S. Harrison, N. Yang, A. Egea-Àlvarez, L. Xu, IEEE Transactions on Power Delivery.

#### 1.5 Thesis Outline

Having detailed the required motivation and context for this thesis in this Chapter, the rest of this thesis is outlined in the following paragraphs.

The historical, contemporary, and future implementations of MVDC systems are discussed in terms of applications and developments in technology in Chapter 2. Common network implementations are highlighted, reviewing MVDC projects and hardware used in these systems.

In Chapter 3, the systems that are modelled throughout this thesis are described and the mathematical equations presented. The background modelling information on frame transforms, small signal model representation, converter control are clearly explained, and are referred back to throughout the following thesis chapters.

Chapter 4 assesses the stability of a standard GFL converter with inertia emulation and the effect of common tuning on the system. Recommendations are given for ensuring a balance between system stability whilst providing the required inertial response.

The importance of model accuracy and representation of low frequency oscillatory modes are highlighted in Chapters 5 and 6. Small signal models of varying dynamic detail are compared in these chapters, in GFM and GFL control respectively, giving a methodology of screening models to determine conditions that they are not sufficiently accurate.

Following the discussions on the importance of model accuracy, a highly detailed

dynamic small signal model of a point-to-point MMC-HVDC system is developed in Chapter 7. The effect of system parameters and converter control on propagating oscillations between the interconnected AC grids is assessed and a metric to quantify the limitation on firewall effect of the HVDC system is presented.

Finally, the overall thesis conclusions and recommendations are discussed in Chapter 8

## Chapter 2

# Review of MVDC Applications, Technologies and Future Prospects

The application of this research has been focusing on MVDC and HVDC connections, and the converters and controllers that enable this technology. Therefore the background literature on the innovations and developments enabling renewable integration needs to be expanded. Additionally, in order to understand the problems the modern grid is facing, the technologies utilised need to be understood.

Considering these issues the modern grid is facing, several of the upcoming chapters analyse different small signal modelling methods, for different control topologies, and their capabilities and the level of detail required in models to accurately represent sub-synchronous oscillations and oscillation propagations. Therefore the background information in this Chapter will expand on HVDC and MVDC technologies and applications.

#### 2.1 Medium Voltage to High Voltage DC

The author has completed and extensive review as part of the published work "Review of MVDC, technologies and future prospects" which provides a detailed analysis of the state of MVDC applications and the technology required for implementation. Within the review, grid design, converter topologies, state of the art equipment, converter and grid control were discussed. The discussed literature from an MVDC perspective will be given here, targeting key contributions such as answering what level is medium voltage, key applications and current demonstration projects, technologies required to implement MVDC, and the role it will play, along with HVDC systems.

#### 2.2 MVDC applications

SINCE the "Current War" between Thomas Edison and Nikola Tesla, AC has been the basis for electricity systems across the world for the last 100 years [22]. DC systems have been used in the past, for some applications, but their benefits could see DC replacing traditional AC systems in many situations. Compared to AC, DC systems have a better transfer capacity, improved flexibility and controllability, and could provide better power supply reliability [23]. Medium Voltage DC (MVDC) could replace AC for several applications due to these benefits, for example, in creating MVDC rail systems, integrated shipboard power systems, offshore renewable collection, distribution grids, electrification of oil and gas rigs, DC homes, electrification of university campuses and mine sites. The first applications (i.e., rail systems, integrated ship board power systems, off-shore renewable collection, and distribution grids) are the most common in implementation and research literature. They were selected in this Chapter to give a significant overview of MVDC applications.

HVDC has been already implemented for transmission [24], but increasingly MVDC is being suggested for distribution in power systems. MVDC links have been implemented successfully between distribution grids [25], [26], and MVDC collection systems could be utilised for offshore renewables, integrating with HVDC transmission links.

#### Chapter 2. Review of MVDC Applications, Technologies and Future Prospects

For rail systems, the lower end of MVDC (750 V to 3000 V) has been used for several decades in urban and suburban traction systems [27]. It has been proposed to firstly increase these systems to higher MVDC voltages and power ratings to improve capacity [28], and also to develop MVDC rail grids to achieve a 25 kV AC line equivalent performance [29].

Shipboard power systems have developed to Integrated Power System (IPS)s, due to the benefits such as flexibility of layout, reduced fuel consumption, maintenance and emissions, and improved reliability [30]. Traditionally these IPSs have been based on AC distribution but the industry is seeing a move towards DC systems [31].

MVDC has been suggested for these applications for the following reasons: firstly, there is an approaching limit of how much the transfer capacity can increase with the AC infrastructure [32]. For example, growing populations in urban areas are resulting in concentrated loads, which increase the distribution capability and power supply reliability requirements.

Furthermore, transportation and heating systems are increasingly using electricity, aiming to reduce CO2 emissions by utilising renewable energies, which brings further stress on the capacity of the distribution networks. In rail systems, increasing traffic in low medium voltage DC systems is causing the system to reach its limits [28]. Compared with the AC cables, DC cables have a higher transfer capacity, and so converting existing AC lines to DC in distribution networks and rail systems would increase capacity [33]. This could also benefit shipboard systems with the reduced weight provided by utilising DC cables [34].

Furthermore, conventional AC systems often have radial and open loop layouts, resulting in a lack of flexibility and controllability. This limits the implementation of Distribtued Generation (DG) as their generated power is in a specific area and it is not able to be supplied back upstream in times of excess power generation. Additionally, this lack of flexibility in AC shipboard system prevents excess capacity being stored [30]. The reliability of power flow is of vital importance in shipboard systems and MVDC offers the ability to improve flexibility with integrated power

Chapter 2. Review of MVDC Applications, Technologies and Future Prospects

systems and improved reliability [35]. The flexibility benefits of MVDC also aide rail systems, especially urban rail networks [36], by improving protection control [37], enabling flexible integration with distribution grids and simplifying onboard energy conversions [37]. AC radial networks in distribution grids with DG could also result in over voltages and congestion [38], however, the ability of the distribution system to respond to uncertainty from supply and demand must be maintained [39]. DC distribution systems have more configurations leading to improved flexibility for these applications.

MVDC grids would improve systems with a high penetration of DC loads and power converters. DC loads are continuously increasing with up to 80% of loads in commerce and residential areas being DC [40], [41], therefore utilising MVDC systems would reduce conversion stages. Modern ship systems also often utilise DC loads and pulse loads; loads that draw a very high current in a short time, over intermittent periods [42]. In rail systems, MVDC supply rails would also reduce the number of conversion stages required to supply the series wound DC motors [28].

Furthermore, power electronic devices are becoming increasingly common in ship power systems [30], rail, and to interface renewable generation in distribution grids, however this results in control interactions with the AC distribution networks [43]. With these renewable sources being connected, their intermittency and uncertainty results in instability and control issues with AC grids [39], [44]. MVDC links with back-to-back power converters creating a Soft Open Point (SOP) are being suggested to combat this instability, reactive power issues and increase the control flexibility [45], [46].

There could be significant improvements in efficiency and cost if MVDC collection systems were utilised to integrate renewables, specifically wind power [47]. Moreover, for the device required to connect to the transmission or distribution grids, the size of collection systems and the conversion stages could be reduced using DC-DC converters, which can enable MVDC systems with high gains to step up to high voltages [48]. Additionally, for shipboard electric systems, the size and weight of the traditional Medium Voltage Alternating Current (MVAC) electric systems would be reduced and

Chapter 2. Review of MVDC Applications, Technologies and Future Prospects

the generators and heavy low frequency transformers can be removed [31], [34].

MVDC technologies have been suggested and/or implemented in rail, ship, distribution grid, and offshore collection systems, however, a comprehensive understanding of the usage of MVDC in the future is lacking in the literature. This paper aims to review a comprehensive set of MVDC applications, the overall network configurations, hardware, topologies required for the application implementation, case studies, future trends and problems of MVDC applications. This paper highlights the maturity of the various MVDC applications, as they are at differing stages or development and Technology Readiness Level (TRL). This paper reviews the uses, advantages, and disadvantages of MVDC and offers a "cross sectional" review of common points to paint a full picture, which has been lacking in the literature.

#### 2.2.1 Sea

In traditional shipboard systems, diesel propulsion systems have a direct mechanical connection between the prime mover and the turbine, with the propulsion area being separate from the main power system [49]. However, in the 20th century, these systems began to be replaced with diesel–electric propulsion [50], where the diesel generator connects to an electric motor, as seen in Figure 2.1. This move towards electric systems was motivated by the flexibility of the layout; reduced fuel consumption, maintenance, and emissions; and improved reliability. However, up until the beginning of the 21st century, the majority of the power in the ships that were using these systems was solely dedicated to propulsion, [51], as well as for cargo ships and refrigeration [52], which required special electrical power system arrangements. In recent years, IPSs have been proposed to replace standard mechanical ship propulsion systems, which use generators and Battery Energy Storage System (BESS) to supply the propulsion system and all other loads, no longer separating propulsion from the rest of the system [30]. IPSs could help pave the way for all electric ships (AES), where all of the onboard equipment and systems are electrical, with generation being provided by electric storage [53].

Schuddebeurs et al., [53], categorises ship systems from diesel-electric to AES,

Chapter 2. Review of MVDC Applications, Technologies and Future Prospects

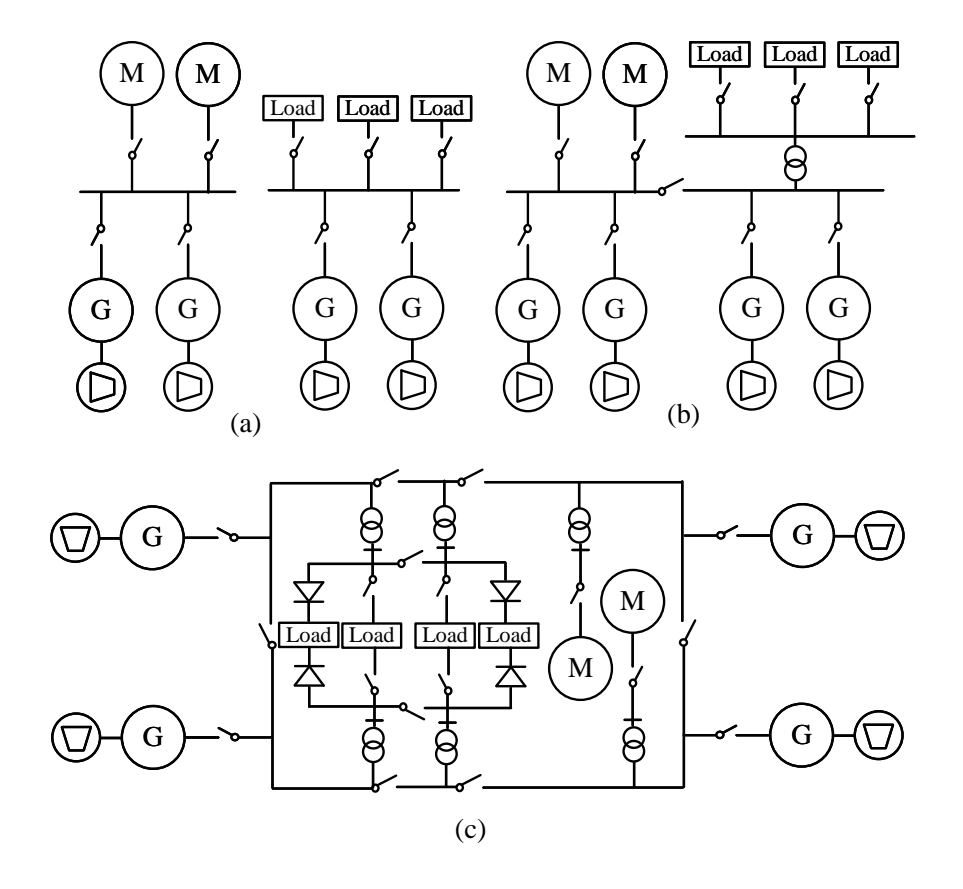


Figure 2.1: Traditional AC ship distribution systems.(a) propulsion isolated, (b) radial IPS, (c) modern AC zonal distribution system

highlighting development and direction in the industry. An IPS could improve flexibility, reduce the number of prime movers that are required, and increase efficiency; additionally, vessels of all sizes can utilise an IPS [52]. Standard AC ship system rated voltages traditionally ranged from 690 V for small ships (e.g., passenger ferries with a generator capacity of 4 MW) to 6 kV, with total generator capacity between 4–20 MW and 11 kV, with a generator capacity above 20 MW (e.g., container ships and larger cruise liners [54]). Initial AC distribution designs had separate propulsion and service load systems to prevent faults propagating. However, the disadvantage of this system is a lack of flexibility, and it is more efficient to amalgamate these systems. IPSs can be further improved with zonal distribution, which has been increasingly suggested in the literature [30] [49] [55] for increased reliability. The development of AC standard shipboard systems is illustrated in Figure 2.1. However, the industry

Chapter 2. Review of MVDC Applications, Technologies and Future Prospects

has seen a move towards DC power systems, specifically towards MVDC [31], for IPSs, as shown in Figure 2.2. AC ship power systems have disadvantages, with bulky transformers taking up important space and weight [34]. Furthermore, in traditional AC systems, the excess capacity from the propulsion power system when travelling at a low speed or when the vessel is stationary cannot be directly used or stored in BESS [30]. Another reason for the move towards DC systems is that power electronic devices are becoming increasingly common in ship power systems [30]. Modern ship systems also often utilise pulse loads, which are loads that draw a very high current in a short time and over intermittent periods [42]. However, gas powered AC generators have a slow response, which does not match the fast response that is required for the emerging pulsed loads [54]. On the other hand, energy storage devices (DC systems) as well as power electronics provide a fast response. DC networks also avoid the issues that are associated with the synchronisation of loads to sources and reduces voltage drops and power losses due to reactive power [56]. Therefore, BESS and possible renewable sources (RES) can be connected to the IPS. In AC grids, power quality issues such as the harmonics and frequency fluctuations that are caused by pulse loads and that are loads interfaced with power electronics are a system concern that require regulation in order to avoid risks to the ship and crew [30]. DC grids do not have frequency issues; however, they do have voltage stability issues [54]. Therefore, appropriate stabilising methods must be considered for MVDC distribution systems and power quality standards for DC grids that need to be defined [57]. A generic DC ship distribution network layout is shown in Figure 2.2 [58, 59].

The network structure could be a radial, ring, or mixed structure [55]. Traditionally, AC ship systems were arranged radially, an orientation that has the benefit of simplicity; however, these structures lack survivability, as if a line is disconnected due to a fault, there are no other connections to the load to power it [30]. Several papers have highlighted the benefit of utilising an open ring bus structure [55] [60]. This structure is capable of isolating a fault with a normally open point, therefore allowing the rest of the system to continue to operate. Furthermore, a ring bus structure ensures that a vital load can be powered from several points, improving security and reliability [54].

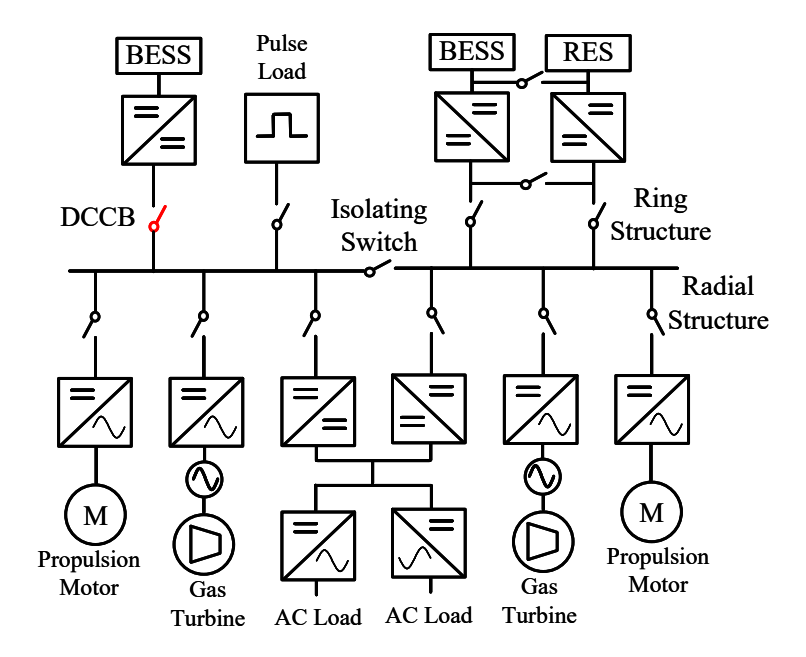


Figure 2.2: Generic DC shipboard IPS

IPSs have been around for the last 30 years, with the Queen Elizabeth II being the first ship with an AC IPS [61]. Other IPS examples are Queen Elizabeth Class Aircraft Carriers [59], the Ellen E-Ferry, and the Yara Birkeland Autonomous container, an AES [62]. The QEC has four 11 kV switchboards and six generators, two at 35 MW, two at 11.3 MW, and 2 at 8.5 MW. The Ellen E-ferry is a 57 m medium sized car and passenger ferry with 4.3 MWh battery capacity with DC operation [63]. The Yara Birkeland is a 79.5 m long ship with an optimal speed of 11 km/h, and it is the first fully battery powered and autonomous container ship. The battery pack of the propulsion system is 7–9 MWh [64]. All electric ships are being suggested due to their better efficiency, fuel economy, power quality, and reliability [65]. Helgesen et al, [64], detail the advancements in electrical energy storage for ships and the extensive progress made in the field. The NORLED MF Ampere Ferry is the world's first electric car ferry, which uses battery storage; however, it is based on an AC distribution system [66].

# 2.2.2 Rail Systems

Since the 1950s, rail systems have been leaning towards electric rail in Europe, China, and Japan [29], [67]. However, diesel and diesel—electric locomotives still exist in North American and some European countries. Electric trains are more efficient and do not produce greenhouse gases [68] and have a greater power to weight ratio than their diesel counterparts [69]. The installation costs of electric rail systems are significant; however, in busy lines, these expenses are negated by the reduced operating costs compared to diesel engines, as the cost of diesel fuel is significantly more than that of electricity [70]. However, in remote areas with little rail traffic, the installation costs are often too much to warrant system electrification. Such areas would have to rely on the development of large scale rail battery storage systems in order to achieve electrification [70, 71].

Electric rail systems across the world have historically been supplied with a mix of Low Voltage Direct Current (LVDC)/MVDC for low speed and urban connections and MVAC for intercity and high speed rail systems. In inner city areas, there are currently several LVDC/MVDC voltage levels for various light rail operations in different countries; trams and subways use voltages between 750 V and 1.5 kV, and medium distance trains use 3 kV DC [27]. With these DC systems, a three phase AC distribution network would traditionally connect to a traction power substation (TPSS) containing a rectifier bridge for DC conversion. However, lower voltage DC systems suffer from increased heavy traffic, preventing operation at nominal power, and the substations are required to be very close together.

For high speed AC rail networks, step down transformers that are connected to the grid provide the catenary with medium voltage AC, e.g., 25 kV/50 Hz, and VSCs on each train supply traction DC induction motors. AC rail distribution grids have been prevalent due to ease of connection to the main national grid through step up transformers to reach higher voltages and to reduce line losses, meaning that fewer substations are required and that AC technology is advanced and reliable, such as in AC Circuit Breaker (CB) [72]. Some European countries, such as Sweden, Germany, and Austria, maintain a low frequency AC catenary voltage of 15 kV at 16.7 Hz [73], while

Chapter 2. Review of MVDC Applications, Technologies and Future Prospects

most other European countries, such as Spain, France, and the UK, adopt an MVAC rated at 25 kV/50 Hz [67] [74]. However, AC supply lines have certain drawbacks: reactive power compensation is required, single phase substations have a high short circuit power in order to avoid voltage imbalance at the Point of Common Coupling (PCC), and the inductive voltage drops [75].

As a natural evolution of existing LVDC/MVDC traction systems, modern MVDC rail systems have been proposed instead of MVAC. High speed DC rail systems were limited due to the significant voltage drops along DC lines, the required high number of expensive substations, and the lack of development of protection, [67] and only the LVDC and the lower end of MVDC voltage ratings could be utilised. However, there have been significant advances in these areas and in MVDC technologies [27], and future MVDC rail distribution grids are increasingly being suggested in the literature. Gómez-Expósito et al., [67], present a multiterminal MVDC network with a single uninterrupted 24 kV DC catenary. The main transmission grid supplies this MVDC distribution grid through a series of equally spaced substations containing multilevel VSCs. In Verdicchio et al. and Caron et al., [28], [75], reviews of similar MVDC distribution structures are presented; however, the systems that are presented use two overhead lines. The former investigated the optimal distance between substations and compared operation to a real 25 kV AC line. The latter reviews the DC voltage levels of a bus system and suggests that a 9 kV DC supply has a comparable performance to that of a traditional 25 kV AC system. Verdicchio et al., [29], also agree with this comparison but adds that the selected DC voltage level must take substation distance, the rail to ground voltage, and the thermal constraint on the overhead line cross section into consideration, increasing costs. Thus, the selected voltage must optimise between thermal constraints and cost. References [76, 77], Tobing et al. and Pereira et al., present optimisation solutions for the placement of DC traction substations to minimise voltage drops and power losses.

An example DC network is shown in Figure 2.3. The TPSS contains disconnectors on the AC side, rectifiers, and DC circuit breakers and disconnectors [27].

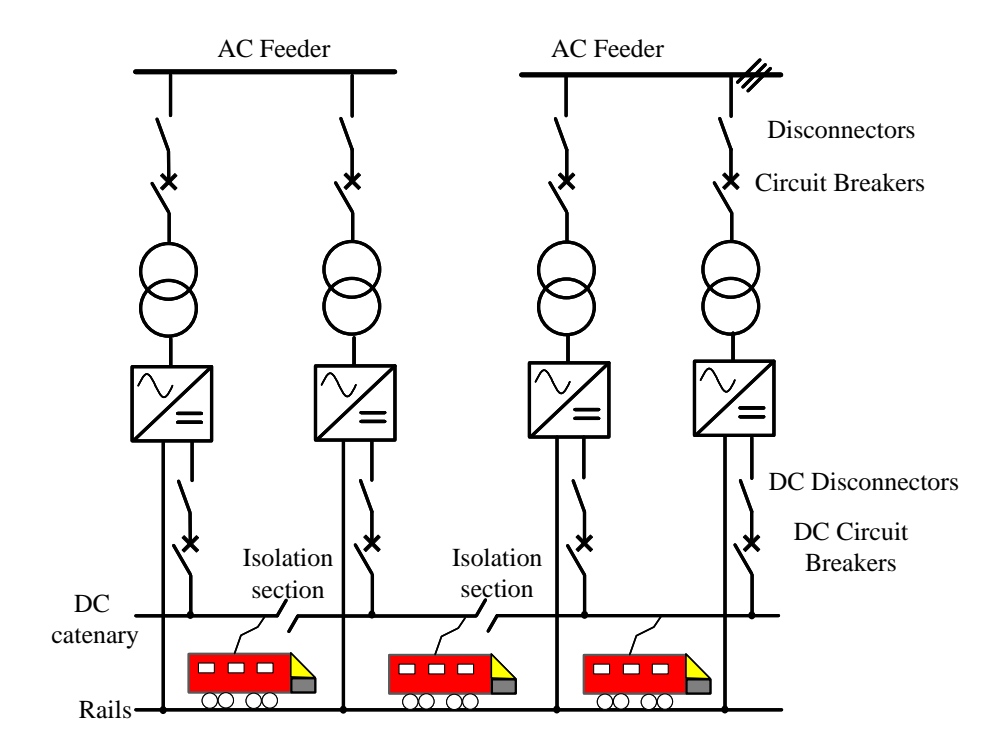


Figure 2.3: DC rail distribution system.

The substation control system controls the reactive power on the AC side as well as the active power and DC voltage. In areas where the lines are close to each other, rectifying stations could be removed and replaced with DC–DC links [67]. Further to this, modern MVDC rail might be reversible and integrate BESS [78]. There are still significant developments that are required in MVDC rail systems, such as those seen in [79]. Arcing in DC rail systems is intense, as the voltage is often lower compared to that of the equivalent AC systems, resulting in the current being higher [80]. Interruption between the pantographs and the overhead line can cause arcing and results in power quality issues, electromagnetic emissions, increased temperature at the contact point, and wear on the contact wire and strip on the pantograph [81]. Fast detection methods might be required to prevent the spread of negative electromagnetic phenomena throughout the rail network [82].

# 2.2.3 Network Distribution Grid Systems

The distribution grid has predominantly been AC since the early 1900s and the "Current Wars" between Edison and Tesla [22]. AC technology has been utilised due to the ease of stepping it up to higher voltages with transformers, allowing for reduced power losses. However, developments in Voltage Source Converter (VSC)s, protection and semiconductor devices has enabled the introduction of HVDC transmission, paving the way for further DC connections, such as MVDC distribution.

The importance of power reliability and quality in cities and urban areas is paramount, but as populations increase and the strain on the power supply is exasperated, extra capacity will be required in the distribution grid. However, the AC system is reaching its limit as the space for new substations and lines is finite. The transfer capacity a DC conductor is about 1.5 to 1.8 times that of an AC cable of the same width and current [83], [84], [85], and also has a higher efficiency [86]. DC also uses full peak voltage capability compared to RMS and DC does not suffer from the skin effect [41]. Therefore, MVDC could provide the increased and capacity required in congested areas, by converting MVAC lines to MVDC.

Another disadvantage of AC systems is the required reactive power compensation. Utilising DC allows for the removal of three phase balance or compensation requirements of AC [44]. DC cables do not consume any reactive power, and power converter connections between DC and AC grids could provide support and voltage control to the AC systems.

Connecting distributed renewable energy sources to AC grids also creates challenges for the distribution grid. DGs are intermittent and unreliable and so BESS are required for excess storage and support; connecting these to MVDC would allow for simpler conversion stages than AC [41]. Controlling voltage disturbances is a significant goal of DG connections, and power converters control with MVDC systems can provide DG voltage control [87].

MVDC is not simply HVDC downscaled. MVDC could significantly aid in areas where

there are no high voltage connections and where high voltage infrastructure could not be easily implemented, for example, densely populated urban areas. Following from this, HV has a large visual impact of high lines and power towers, an getting permits for HV corridors is significantly increasing in difficulty [88]. Furthermore, MVDC has the adaptability to allow for smaller, less expensive converters at the lower voltage ranges [89].

However, MVDC grids have several challenges to overcome; protection systems and DC circuit breakers need further development, there is a general lack of standardisation, and installation costs of DC are currently high due to the power converters required [86]. Power converters are also still not as efficient as AC transformers, and have a lower lifespan [41].

Furthermore, MVDC networks have no current zero crossings, and low DC impedances, [90] and thus the fault current will be high. Dealing with short circuit currents is predicted to be a great difficulty in DC grids [91], and compared to AC systems, the protection in DC will be much more complex [86]. Fault detection and location is a difficulty in DC systems, and detection methods are highlighted in the literature, [82], [92], however there are still developments required. Further to this, the protection methods in DC systems are still to be standardised, and the best prevention methods are still up for debate, for example, the discussion between hybrid and solid-state circuit breakers.

## Applications overview

The four main applications overviewed are briefly summarised below in Table 2.1, detailing the average voltage and power levels, TRL, maturity, case studies, and available technology.

For rail systems, the lower end of MVDC technology is already in use for tram, metro and subways, however long distance travel with MVDC is being suggested at higher voltages of around 10 kV, and high speed of 20-30 kV.

For shipboard IPSs, MVDC power systems are emerging as an alternative to AC

Chapter 2. Review of MVDC Applications, Technologies and Future Prospects

systems with heavy transformers. As reducing weight is highly important in ships, the benefits of MVDC power electronics are being utilised, especially as the voltage of the DC bus required will be 5-35 kV (depending on ship size), therefore not requiring significantly large onboard substations [31], [55], [93].

Distribution grids are beginning to introduce MVDC links and DC grids. There are several examples of DC links, [94], [95], and small DC distribution networks have been developed in South-Eastern China [96], [97]. The technology of distribution grids is available as MVDC systems have the flexibility of utilising 2L and 3-level (3L) VSCs, as well as modular multilevel converters (MMCs). The suggested voltage range for distribution operation varies in the literature, some papers suggesting 1.5 – 100 kV, [85], with others narrowing the range to 5-50 kV, [98], [47]. For projects [99], [26], [25] and [97], the voltage ranges from 10 kV to 27 kV. This will likely be the mean range for distribution but there may be some extension up to 50 kV or even 100 kV for distributed renewable connection.

Offshore wind collection however is still being developed and there are currently no active MVDC collection systems. The lower weight of MVDC collection substations compared to AC collection or HVDC would also significantly reduce capital cost of the system. MMC technology could achieve the high step up ratios required, and has good short term reliability with active redundancy, but there the long term survival of the technology in offshore conditions is still being investigated [100].

The range of MVDC voltages for the various applications have not been standardised. The values that have been suggested in the literature or that have been implemented differ, with Table 2.1 showing these details. To further represent the variation in voltage levels, the suggested and implemented applications are displayed in Figure 2.4, as a function of the year. The trends show that for rail systems, the lower end of MVDC voltages (600-1500 V) have been implemented up to the 2010s, and from 2010 to the present day, higher medium ranges, (9-24 kV) are being suggested to match the 25 kV AC rail systems. With distribution, the most common suggested and implemented voltage was 10 kV, with an outlier of the ANGLE-DC project reaching 27 kV. The

most common implemented voltage for shipboards systems was also 10 kV, however, the suggested values have a larger range due to the variety in ship sizes and required loads. Finally, the suggested wind offshore collection platform voltages are in the higher range of MVDC values (20 kV-35 kV).

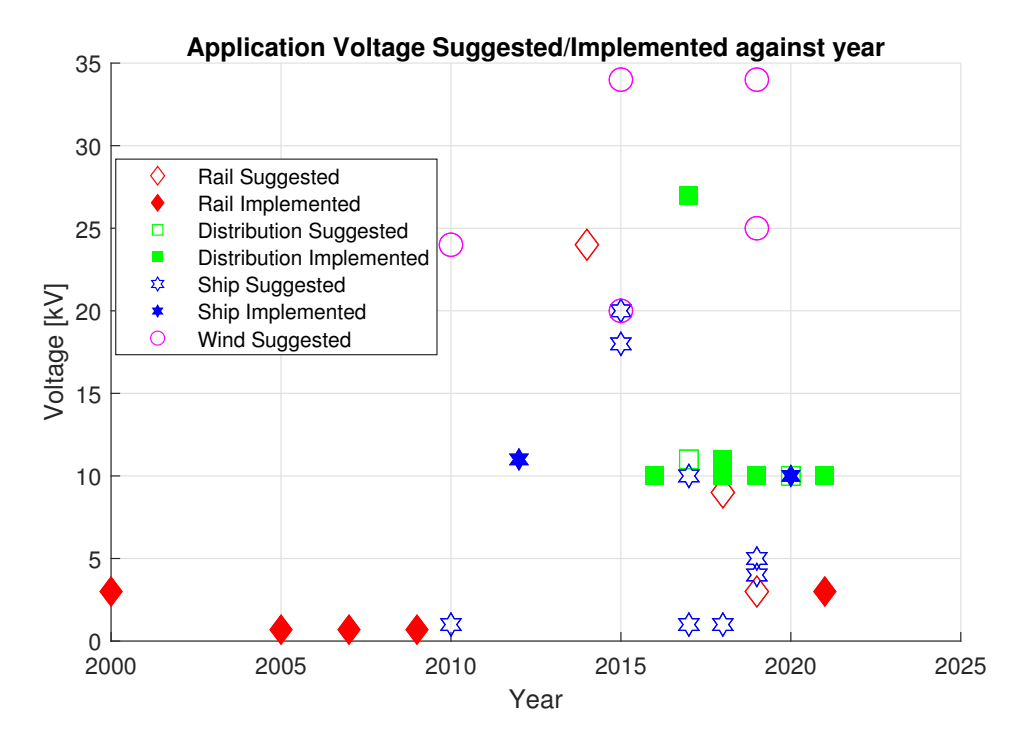


Figure 2.4: Suggested and implemented applications since year 2000 and associated voltage level.

# 2.3 MVDC For Grid Connected Applications

# 2.3.1 Applications

According to CIGRE [85], future MVDC distribution systems will be for interconnection with MVAC grids, and connecting LVDC and HVDC. The AC system will operate with the DC system providing ancillary services and support. There will be a combination of structures; point to point DC connections, multiterminal MVDC grids, microgrids, and distributed generation connections. This section reviews the main applications for grid connected applications.

Table 2.1: MVDC Applications and Voltage Levels

	Railways	MVDC Distribution	Offshore	Shipboard Systems
Voltage levels	600 V - 3 kV (trams, suburb trains) Long distance 9 to 10.5 kV [28, 29] High speed DC 20 - 30 kV [67]	5-50 kV [98], [47], [101], [88] ±10 kV [96], [97], [102], [26], [99] 1.5-100 kV [85], [103], [104] ±10 kV to ±70 kV [105]	Typically ±25 to ±50 kV [106]	5 kV main bus voltage [34] 1-35 kV [93] 10 kV [31], [55]
Power	3 to 5 MW suburban [27] 12 MW higher speed [75]	3 MW - 200 MW [107] [108] Common mid- range 10-20 MW [26] [97]	160 MW to 1200 MW [109], [110], [111]	2-7 MW [58] (smaller ships) 10-20 MW (cruise liners) [54]
Maturity	Already utilised for tram, subway, metro travel. HVDC converters already capable of implementation, with SSCB and improved power semiconductors offering new voltage capabilities.	Utilised in several countries in test phase: UK, China, Finland. Range of developed converter, semiconductor, and control systems by industry	Relying on DCWT development [106], but many countries with large installed offshore capacity and MVDC technologies.	Integrated DC power systems are beginning to dominate the market. Lightweight MMCs and power electronics replacing heavyweight transformers. Improving battery capacity.
Cases	London Underground, Bordeaux-Hendaye intercity line, Paris-Strasbourg high speed line.	ANGLE DC SPEN, Zhuhai Distribution Project, Shenzhen MVDC [96], Suzhouo [97], Hangzhou Jiangdong, Guizhouo [65]	None implemented [106]	ForSea Ferries [112], Yara Birkeland [62], QEC Aircraft Carriers [59]
Available Technology	Siemens MVDC plus [88], RXHK Smart VSC-MVDC transmission	Siemens MVDC Plus, RXHK Smart VSC-MVDC transhission	Siemens MVDC Plus	Energy storage systems, power management systems, voltage drives [112] [113]

# SOPs, Flexible AC Transmission Systems (FACTS) and DC Links

AC distribution systems often utilise a radial structure, where entire sections of the line are isolated after a fault, causing loss of supply downstream [46]. Two adjacent independent feeders might be connected to offer routes of electricity supply in case of an unplanned outage [95]. This can be done using standard mechanical switch-gears also known as a Normally Open Point (NOP). As an alternative, this connection can be realised through a MVDC VSCs back-to-back known as a SOP [114] [45]. A SOP has the advantage that allows AC grids to be decoupled from each other, for example due to power quality of the short circuit ratio [115]. At the same time, it can provide voltage support and active power control [45] [46]. SOPs can be understood as a standard back-to-back topology, Figure 2.5a [46]. SOPs are already being trialled; reference [99] details a 11 kV flexible power link, connecting two 33 kV AC distribution networks with SOPs and SPBs being installed on the network [116] (Figure 2.5b). Following from SOPs, is the soft power bridges (SPBs), which perform a similar function to SOPs however they can process less power reducing the number of power electronics taking advantage of a series-parallel connection [95].

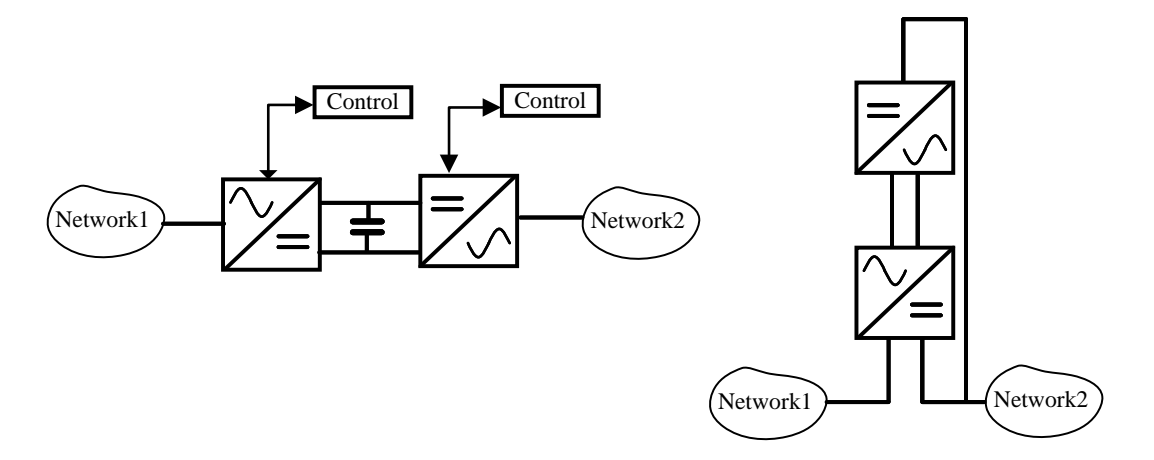


Figure 2.5: SB2B Soft Open Point configuration. b) Soft Power Bridge

FACTS have been traditionally used to improve power balance and voltage regulation in AC transmission power networks. Standard FACTS such as Static Synchronous Compensator (STATCOM)s have been extensively used and have been specifically designed to suit the network needs such as voltage support or power flow control [117]. Medium voltage level power electronics have been suggested to provide the same services for MVAC distribution [46].

MVDC can be also used to interconnect to distant nodes using a DC line or link. Several MVDC links have been suggested between two medium voltage nodes, for example, the ANGLE-DC project, [118], will use a bidirectional MVDC link to improve power flow, allow control, release power capacity and ensure reactive power control [45] [94].

#### DC Distribution Networks

As MVDC technology continues to develop in terms of protection, converters, and reduced cost, full DC grids could be connected to AC systems, instead using single SOP or DC lines [115]. At the same time, MVDC distribution networks might be a convenient solution as the loads are shifting from AC to DC. Consumer loads are increasingly DC, up to 80% of commercial and residential loads are now DC [41]. MVDC networks can easily integrate LVDC loads such as electric vehicles or future electrified transport systems.

MVDC distribution networks have started to be developed, especially in China. In Zhuhai, a  $\pm 10$  kV MVDC distribution system has been implemented [26]. A star network topology with three converters is suggested to improve reliability of the AC distribution network.

There are several further MVDC projects that have been or are currently being developed in China's south-eastern provinces. The Shenshen VSC-DC based multiterminal hand-in-hand distribution system in Shen Zhen has been under development since 2014 [96]. The Hangzhou MVDC project will also utilise a multiterminal structure, as does the Guizhou project [102]. The Suzhou MVDC project has a more complicated system and is designing a single bus double terminal ring structure. This is to combine the traditional ring structure and radial structure benefits [98]. Although the structure of these projects vary, they all utilise MMC converters and operate at a DC voltage of  $\pm 10$  kV. This could suggest a standardisation

Chapter 2. Review of MVDC Applications, Technologies and Future Prospects of voltage in South-East China for MVDC networks.

# Microgrids

Microgrids and smart grids have been proposed to integrate distributed generation to meet local energy demand and to connect to distribution networks without costly expansion of the centralised utility grid. Microgrid grid structures and hardware topologies are very similar to the distribution topologies discussed in the next section, and are often in the lower range of voltages [119]. According to some sources, [22], [119], [91], DC microgrids are set to take dominance of AC microgrids, as the price decreases, due to their ease of integration or renewable sources, with better integration efficiency, integration of DC loads, no harmonic oscillations, no skin effect, and no requirement of synchronisation [119]. MVDC microgrids will be prominent, in offshore oil rings [41], data centres [115], industrial applications, and EV charging stations. Offshore oil drilling often takes place in geographically remote locations, and at these locations offshore wind generation is a significant resource. However, at these locations the lack of electrical collection systems linking generation and transmission prevents the implementation. The oil drilling platforms could be electrified with MVDC architecture and also act as a wind generation collection system [93].

There are however several issues associated with DC grids that are often over looked, particularly in such DC microgrids. Firstly, power quality standards need to be defined for DC microgrids. Reference [57] provides power quality indexes for DC grids, as DC grids can be prone to electromagnetic compatibility issues, source and load interference causing flicker and fluctuations, low frequency oscillations propagating between connected AC grids, and impact of overheating and ageing. Furthermore, DC microgrids require significant protection, differing from that of AC microgrids. DC lines have low impedance resulting in short circuits quickly increasing, and high fault currents and difficulties using traditional current relays from AC grids. AC CBs also cannot be used in DC grids as they interrupt current at the zero crossing, which DC current does not have [91].

# 2.3.2 Grid Topologies

There are several topologies for MVDC distribution systems: radial, meshed, multiterminal hand in hand, and ring [120], or a combination of these (see Figure 2.6). The topology selected depends on the design requirements. Radial topologies are more economical, due to smaller conductor size the further along the feeder [121]. They are however not very reliable, and a fault at the beginning of one feeder will cause supply failure to the rest of the connections leading from it. The power also flows in one direction in a radial configuration, which could limit the flexibility of additional distributed generation [122].

Ring structures have fewer voltage fluctuations at consumer level, and provide a reliable system, as the loads are fed from two feeders. The open ring loop structure has NOPs between the two feeders which separates the loop into two radial feeders. During normal operation, sections are not connected but during a failure, the switch closes, and the section is energised from the other side. Ring structures can provide flexibility and reliability as there are multiple paths for power flow [123]. Further to NOPs, normally closed point (NCP) configurations allow for a load to be balanced between feedings improving power supply reliability [45].

Multiterminal MVDC networks have been proposed in the literature, [47], [124], [125], [126], for use in microgrids, distribution systems and renewable collection systems. Multiterminal networks are systems that don't contain a loop. MVDC networks connecting multiple MVAC grids would provide voltage support, power quality and flexibility [127]. Multiterminal systems can be extended to more readily than ring networks and offer the ability to inter-tie multiple networks at one point [128], [129]. Protection and control of multiterminal MVDC networks need further research and development, due to the inherent instability of Multi-Terminal Direct Current (MTDC) VSC based systems [124].

There are three main bus structures for MVDC networks [130]: mono-polar asymmetric, mono-polar symmetric and the bipolar structure (see Figure 2.7). Mono-polar symmetric systems consist of a single conductor and a ground return, and the symmetric

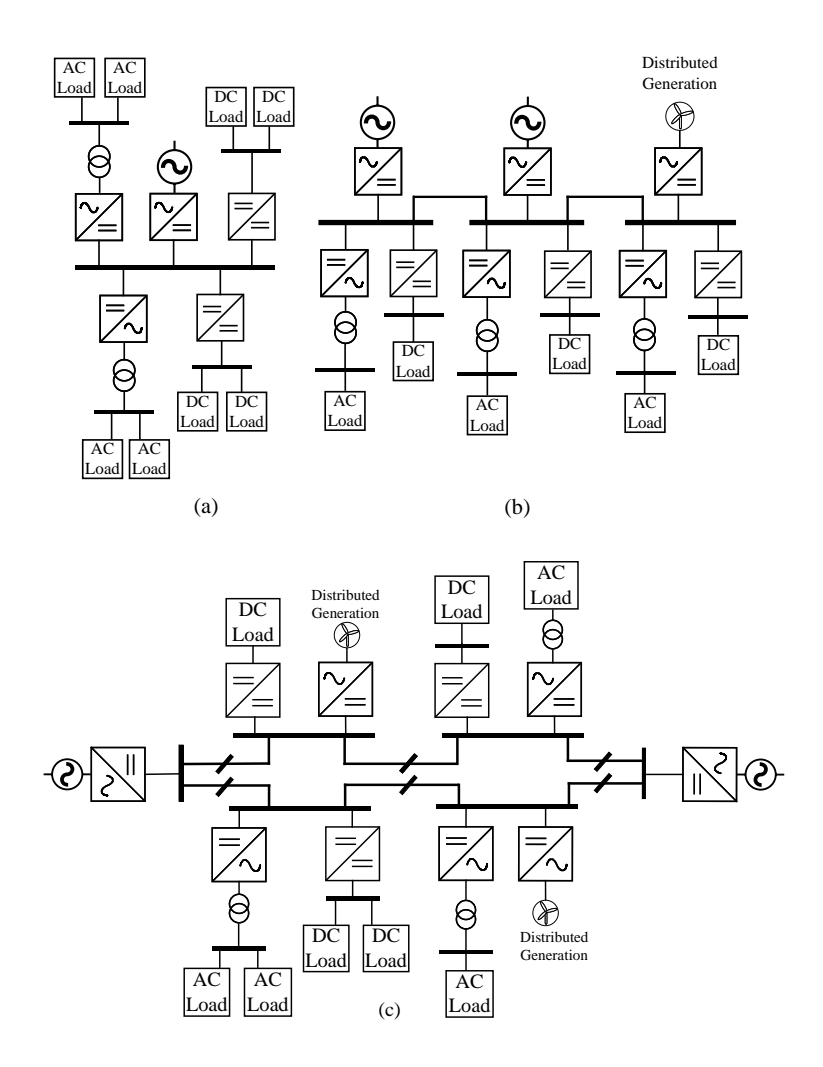


Figure 2.6: Network topologies, a) radial, b) hand-in-hand multiterminal, c) Ring.

structure uses two conductors. This symmetric structure is preferred in MVDC systems. On the other hand, bipolar buses might run with two cables but if one of the poles fails it is possible to keep it running considering a grounded or metallic return.

# 2.4 Hardware

Each MVDC application will have specific hardware requirements, and the development of AC-DC converters, DC-DC converters, solid-state smart transformers, and semiconductor devices are all at varying levels. This section presents the available

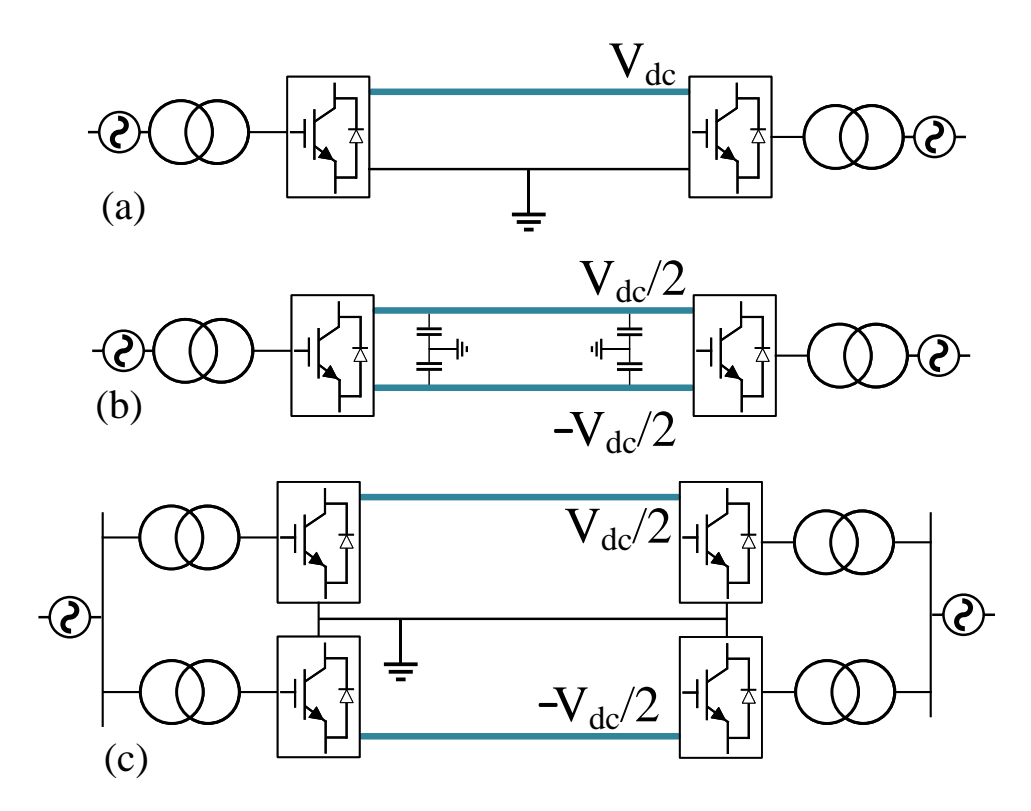


Figure 2.7: MVDC bus structures. a) Mono-polar asymmetric. b) Mono-polar symmetric. c) Bipolar

topologies, the voltage range over which they are considered, the advantages, and the disadvantages of each.

# 2.4.1 Converters

# AC-DC & DC-AC Converters

The topology selected for MVDC converters is dependent on requirements of the intended application. For AC-DC conversions there are several topologies available including; diode rectifiers, 6-pulse and 12-pulse thyristors bridge, Line Commutated Converter (LCC)s (Figure 2.8) 2-level (2L) VSCs, 3-level (3L) Neutral Point Clamp (NPC), (Figure 2.9b) 3-level flying capacitor (3L-FC), [131], alternate arm converters, 5-level converters, and modular multilevel converters (MMC) (Figure 2.10).

Rectifiers have been utilised since the late 19th century for AC-DC conversion. Railway

traction substations have utilised the simple 6 and 12 pulse diode rectifier for decades and this converter is utilised in many rail systems today [36]. This basic diode rectifier however suffers from lack of regenerative braking capabilities, and high harmonic current injections.

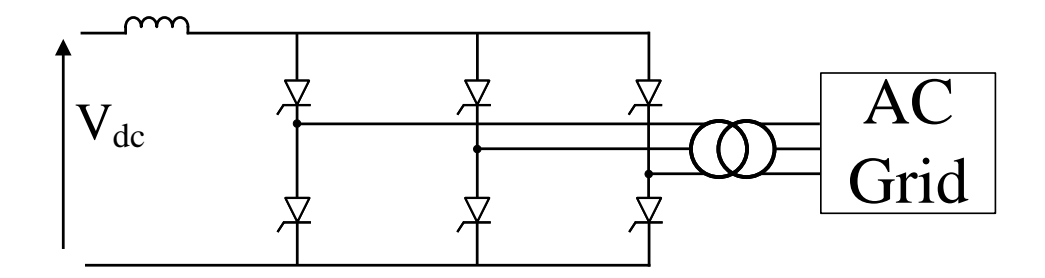


Figure 2.8: Line commutated converter (LCC).

Shipboard systems traditionally used thyristor based rectifiers at the medium voltage level, about 20 kV, due to their significant robustness [105]. Generally, the 12-pulse thyristor rectifier is utilised and it can remove the 5th and 7th harmonic, however the lower order harmonics are still included [132].

For power transmission, LCCs as shown in Figure 2.8, were widely used for long distance high power transmission and asynchronous grid connections [133]. LCC devices were implemented in high power transmission to enable HVDC, however this resulted in poor voltage regulation and commutation failure when operating under weak grids. This lead to the development of the voltage source converter (VSC) for VSC-HVDC links, in 1997, utilising IGBT based switching, instead of thyristor pulse switching [134]. Since then, the modular multilevel converter (MMC) and several other multilevel or cascaded converters have been developed for improved sinusoidal outputs, reduced switching losses and harmonics.

2L and 3L VSCs are the most common in MVDC systems at the lower voltage range, e.g. 3-6 kV [135], due to their significantly lower cost and efficiency, at these voltages, compared to MMCs or other multilevel converters. 2L can be considered up to  $\pm 28$  kV DC [100], and the 3L-NPC even for up to  $\pm 35$  kV, however, generally, MMCs are the best topology for the higher voltage ranges above 10 kV [135], [40], [136], [88], but at

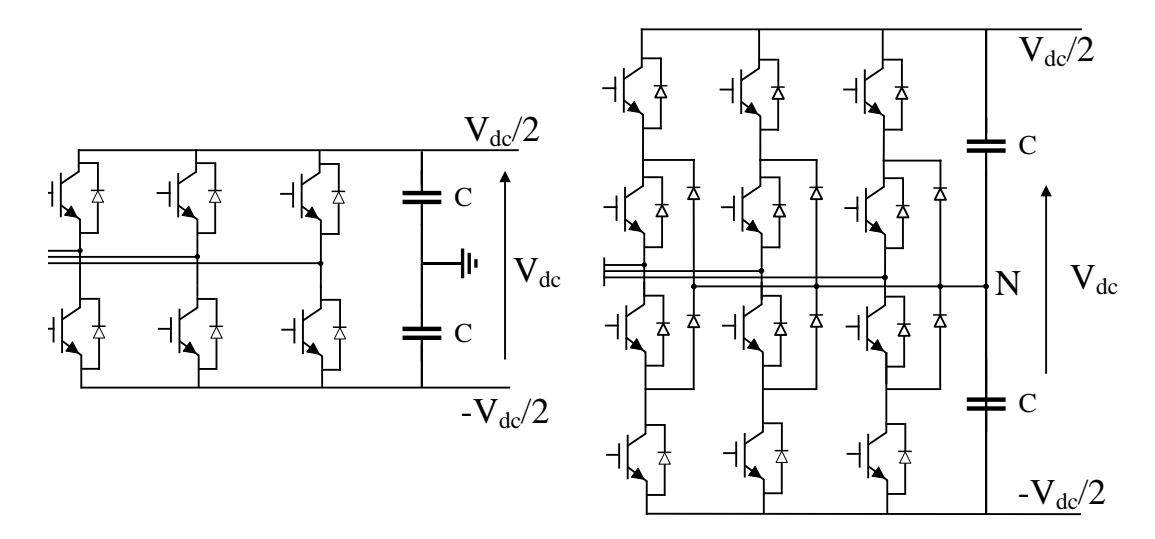


Figure 2.9: a) Two-level converter (2L). b) Three-level neutral point clamped converter (3L-NPC).

this voltage boundary the converter should be selected on a case by case basis. MMCs possess benefits such as low distortion, the modular design providing scalability [137], voltage balancing across switches, reduced harmonics, lower switching frequencies [136], improved fault ride through capability [138], [117], and active redundancy which significantly improves reliability [139], [140]. There are disadvantages however to MMCs, such as cost introduced by sub-module redundancy, and significant losses in the Full Bridge (FB) configuration [105]. In shipboard systems, size and weight of equipment is a crucial factor to be kept as low as possible, and reliability is also required. MMCs in shipboard systems offer scalability with voltage and power, [141], [31]. [31] and [108] review power densities and weight reduction benefits of the standard 12-pulse thyristor rectifier, Integrated gate-commutated thyristor (IGCT) based converters, MMCs and 2L VSCs.

A basic outline of the MMC topology is shown in Figure 2.10 [142], [143], [144]. There are several possible submodule topologies including, the Half Bridge (HB), full-bridge, and five-level cross connected modules. The HB submodule in MMCs has a lower power loss compared to the FB [100], [145], and several papers consider solely HB MMC configurations, [105]. However, the FB module has fault blocking capabilities, [146], [141]. There has also been a focus on the development of advanced semiconductor

devices in converters for reduced power losses. [147] reviews the benefits of hybrid MMCs utilising both SiC and Si semiconductors, and [146] reviews the effects of varying FB-HB configurations for varying switching devices inside the MMC.

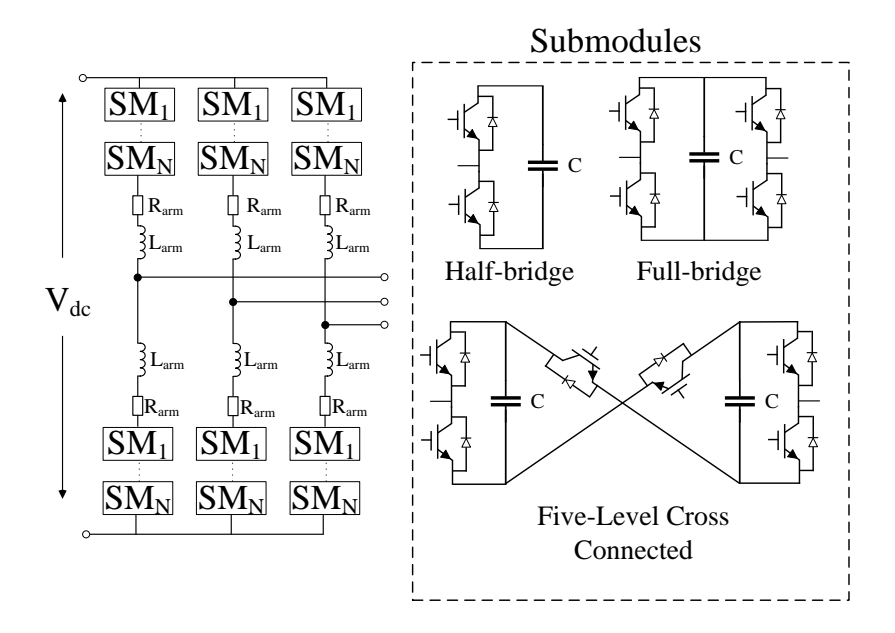


Figure 2.10: MMC and submodules

Commercially, there are many considerations for converter topologies. In the Network Equilibrium FPL project, 3-level 3.3 kV converters based on IGCT technology were utilised to connect the 33 kV DC link [99], and in planning the ANGLE-DC MVDC project, 3L-NPC AC-DC converters were utilised for the connection between the 33 kV AC bus and ± 27 kV DC link [101], as shown in Figure 2.11. To implement this conversion, 12 of these converters were to be installed at each substation, [148], [94], arranged as submodules in the substation achieving the 33 kV AC to 27 kV DC conversion [105] [94]. Comparing this configuration of modular converters to Figure 2.10, the individual transformers and associated power losses could significantly affect total losses and cost. This series of cascaded converters is not the same as the traditional MMC, or ABB's alternative to the MMC, the cascaded two-level converter [149] which was designed for VSC-HVDC transmission.

The planning of an MVDC distribution network in Zhuhai, [26], opted for MMCs,

where the Jishan I substation was not equipped with a DC breaker so an MMC with self-fault clearing ability was required. For this, an IGCT cross-clamped (ICC) MMC was designed with both FB and HB submodules.

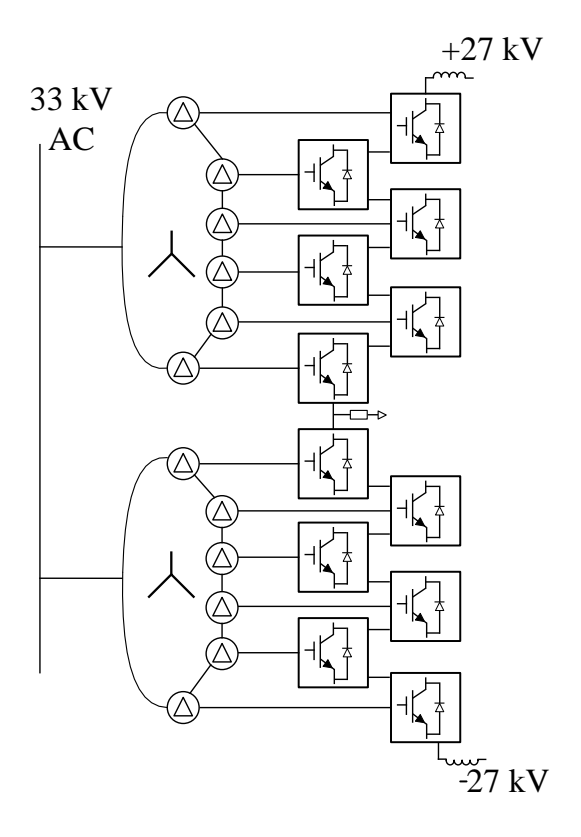


Figure 2.11: Converter Station Configuration of Angle-DC Project

# **DC-DC** Converters

DC-DC converters will have multiple uses in MVDC applications; connections from offshore wind farms, use in smart transformers, stepping up and down from MVDC to HVDC links, in ship systems, and rail connections. MVDC distribution projects are already introducing medium voltage level DC-DC converters, [26], [102], [96].

DC-DC converters can be divided into two groups: isolated and non-isolated. With the former, the input is isolated from the output with coupled inductors or AC transformers offering galvanic isolation by creating a magnetic pairing. This provides protection of the low voltage side from the high voltage side [150]. Isolated converters can offer larger step up or step down ratios, and can allow for multiple DC outputs without significant

cost [151]. Insulated converters can also improve efficiency, reduce switching losses, aid grounding, and result in low voltage and current switching stress [152]. Non-isolated converters remove the transformers and use fewer semiconductor devices, which reduces switching losses, size and cost but they cannot provide large voltage ratios [150].

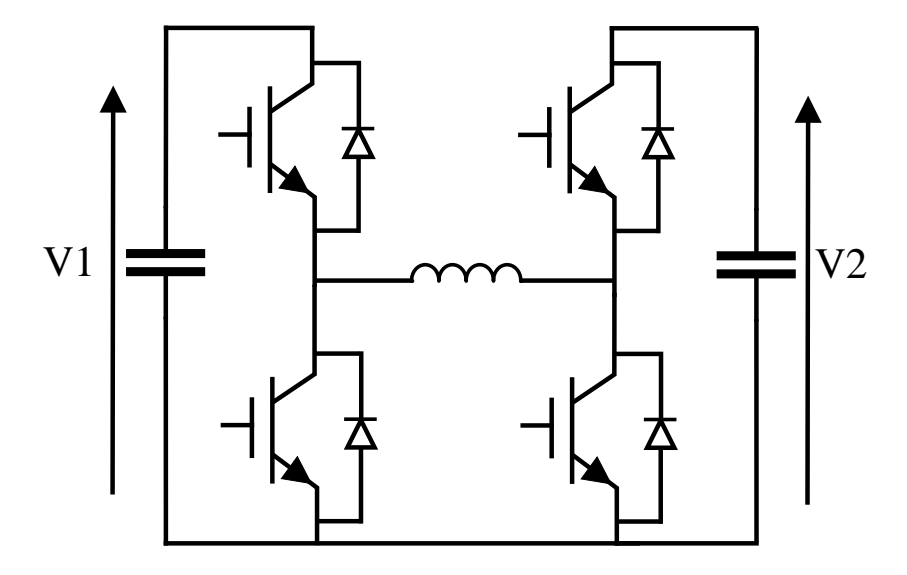


Figure 2.12: Buck-Boost

There are several topology options for DC-DC converters, the main suggested (isolated) topologies are: the Dual Active Bridge Converter (DAB) and the dual active bridge resonant converter (Figure 2.13), cascaded DAB converter, and modular multilevel DAB converter (Figure 2.14,)) and the (non-isolated) Modular Multilevel DC-DC Converter (MMDC), shown in Figure 2.14. The well known non-isolated Buck, Boost, and Buck-boost (Figure 2.15) converters, [152], are also utilised for low voltage DC-DC connections, such as in light rail [78]. For this application, particularly with state-of-the-art battery driven light rail, a bidirectional buck-boost topology is utilised to aid regenerative braking. However, for high power applications, these aforementioned devices are not suited, and cannot achieve high enough step up or down ratios, and as the duty cycle is increased, the efficiency of the device begins to significantly decrease [151].

There are multiple DAB and DAB resonant topologies presented in the literature,

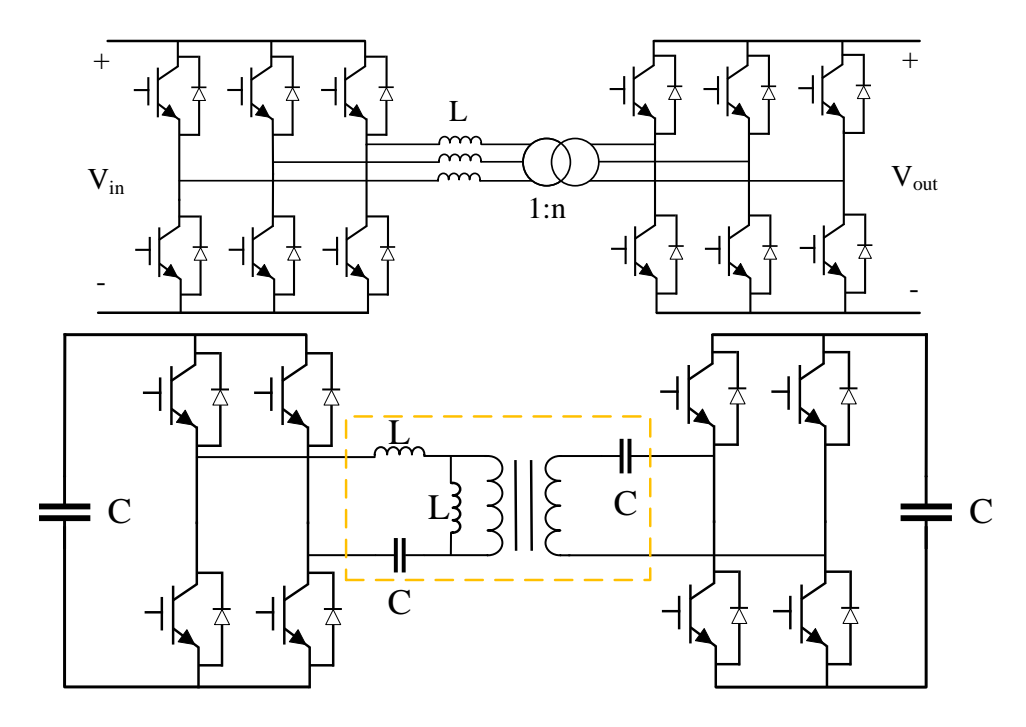


Figure 2.13: Dual Active Bridge (DAB) and DAB Resonant Converter

with varying benefits, e.g.; high efficiency [150], high power densities, and bidirectional flow [153]. [58] and [56] emphasise the importance of the bidirectional capabilities of DC-DC converters for battery storage and ultra-capacitors in ship systems. Furthermore, the DAB resonant converter can operate at high frequencies [154], allowing for reduced magnet and capacitor sizing. Soft switching is achieved with this configuration [155], reducing switching losses and noise [156]. Resonant topologies however, can experience greater stress on switching and passive components [157]. Bidirectional resonant DAB converters have been recommended for connection between the charging station and the MVDC grid, [154], for the soft switching capabilities, galvanic isolation and high efficiency [156].

Multilevel modular DC-DC converters can be implemented with an AC link between the DC-DC input and output, as with the DAB MMC or with a direct DC-DC architecture, as illustrated in Figure 2.14 and Figure 2.15, respectively, where the symbol Sub-Module (SM) signifies the submodule. A multilevel architecture allows for higher voltage gains for connections to distribution systems [48], [157]. DAB MMCs can handle high power

Chapter 2. Review of MVDC Applications, Technologies and Future Prospects

and DC voltage and have DC fault blocking capability, with isolation benefits [158].

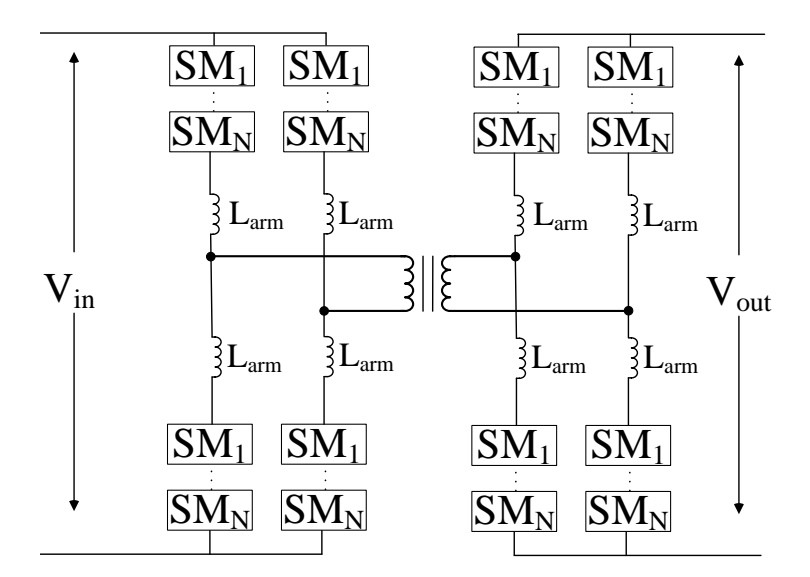


Figure 2.14: Dual Active Bridge Modular Multilevel Converter

The non-isolated MMDC can be separated in two categories; the push-pull and the tuned filter topologies, shown in Figure 2.15, where SM represents the sub-module [159]. The tuned filter requires more filtering than the push-pull [150]. Several papers recommend that high-power application DC-DC converters utilise a modular multilevel structure due to the high step up ratio, [58], [160], enabling near sinusoidal ac waveforms, compact size and low switching losses [157]. Such converters allow for large single stage step up/down conversions, due to their multilevel and modular nature [161], and DC fault blocking capabilities, [157]. The MMDC offers higher efficiency than the DAB-MMC at lower voltage step up ratios, but this efficiency drops as the transformation voltage is increased [157].

Furthermore, MMDCs have significant reliability as they utilise active redundancy, which is important in offshore applications. However, the voltage balancing control of the MMDC is considered complicated [162], and active redundancy results in a significant number of semiconductor devices being required and increased costs. The reliability of the MMDC is significantly greater than that of the DAB, due to active redundancy, however in terms of grid connections the importance of this factor has to be weighed up with the other parameters. Grid substations are easy to access and also

do not face the harsh conditions that an offshore collection platform would, therefore reliability might not be as of the same importance for DC grids [163]. In terms of MVDC to HVDC grid connections, the benefits of both DAB-MMC and the MMDC can recommend them for use in varying scenarios. Galvanic isolation of the DAB-MMC provides guaranteed fault blocking capability, yet the non-isolated MMDC with FB submodules can prevent fault propagation and are recommended generally for lower step up ratios between MVDC and HVDC grids, [157].

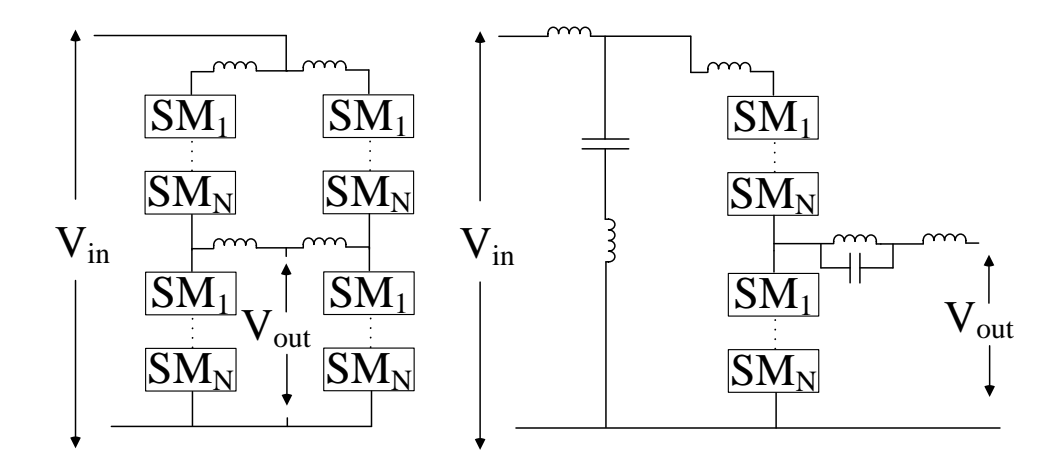


Figure 2.15: Push-Pull and Tuned Filter MMDC

## 2.4.2 Smart Transformer

Smart transformers have been suggested as a method to control hybrid networks and provide ancillary services. According to [164], a smart transformer, or a Solid State Transformer (SST), is a collection of digitally controlled high powered semiconductors and enables control of the network. It can step up or down voltages, with input and output of both AC and DC voltages, can alter frequency levels, and could improve power supply stability [165]. Reference [88] claims the high costs of the proposed STs are justified by these capabilities of operation. An example of a Smart Transformer is shown in ??.

Liserre et al. [166] gives a detailed overview on the possible role of the smart transformer, key architectures and ancillary services it could provide. The SST essentially acts as

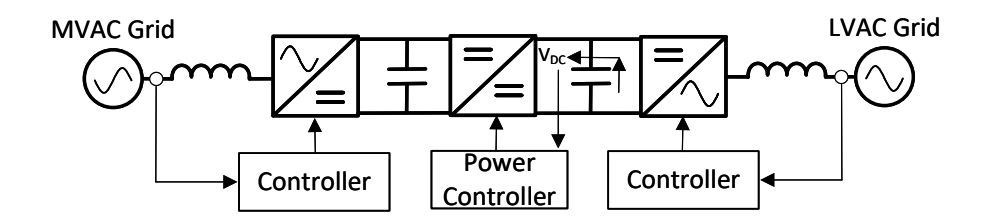


Figure 2.16: Example of Smart Transformer architecture.

the "heart of the system" and its role is to interact with variable power supplies, gather information on demand, priority loads, and provide intelligent control of electric vehicles and other domestic loads. The ST could also interact with local generators, control the grid frequency, and decrease power injections from the DC side to avoid reverse power flow. [167] displays MVDC meshed hybrid grids that can be created with STs and BESS. The ST allows three levels of connections, MVDC, LVDC and LVAC, and provides control systems for each converter ensuring voltage stability is maintained on the voltage buses, during the voltage sag operating mode. The control system compares the active power from the DG and injects the required power from the MVAC grid.

There are several possible ST implementations, SPEN, with funding from OFGEM, have embarked on the LV Engine, a project to aid the uptake of low carbon technologies based on DC [156], one such technology being the smart transformer. As many loads, such as electric vehicles and heat pumps rely on DC, the LV Engine project aims to design a smart transformer which provides a LV DC supply to customers which will increase the transfer capacity of the network. According to SPEN, the ST will allow for: optimum phase voltage regulation at low voltages, optimum substation active power sharing, MV network voltage regulation (11 kV), provision of a LVDC customer supply, modular design and scalability. The Shenzhen MVDC distribution project [96] implemented a DC SST with multiple DAB cell modules. The smart transformers were connected at two points of the distribution system for load connection.

Despite the aforementioned promising application of SSTs, the high cost associated with most topologies has to be considered. [166] predicts that SST will not be mass

Chapter 2. Review of MVDC Applications, Technologies and Future Prospects produced in the near future, and only a few grid nodes would have them installed.

# 2.4.3 IGBT and MOSFETs

For the varying applications of MVDC technologies, there will be many uses of IGBTs and MOSFETs. Heat dissipation and switching losses are an issue with ever increasing power converter penetration, therefore improvements in semiconductor materials will significantly affect the sector [168].

Table 2.2: : MOSFET and IGBT Comparison for MVDC applications

MOSFE	CT (SiC)	IGBT		
Advantage	Disadvantage	Advantage	Disadvantage	
Low switching loss	High conduction loss [169]	Low conduction loss	High switching loss	
Higher switching frequencies	High cost [147]	Low cost	Low switching frequency required	
Improved thermal properties [170]	Forward voltage degradation [171]	Can withstand high short circuit currents	Cannot block high reverse voltages	
Higher voltage blocking [172]	Reliability issues	Low driving power [173] Fast response [91]	Generally unidirectional	

Silicon (Si) IGBTs dominate MMC converters for medium and high voltage applications, but wide bandgap semiconductor devices, e.g., the silicon carbide (SiC) MOSFET, would have superior performance, such as the high frequency capability and lower losses. However, SiC semiconductors have higher costs than their Si based counterparts [147].

IGBTs and MOSFETs also have an important role to play in protection and are primarily used in DC Solid State Circuit Breakers (SSCBs) [91]. The advantages and disadvantages of IGBTs and MOSFETs are highlighted in Table 2.2.

# 2.5 Protection

#### 2.5.1 Overview

Protection in AC systems is very advanced, with IEEE standards having already been implemented for the grid, ship, and rail systems. However, there has been limited research that has been conducted on DC protection [174] and commercially available products. MVDC networks have no current zero-crossings and low DC impedances, [175] meaning that the fault current will be high. Dealing with short circuit currents is predicted to be a great difficulty in DC grids [176], and compared to AC systems, the protection in DC will be much more complex [177]. This is partly due to the fact that in AC systems, power flow is generally in one direction; however, due to bidirectional converters, a DC fault is often propagated to all of the interconnected converters in DC systems [178]. The increase in power electronics also adds to the system complexity in terms of protection. Power converters are more sensitive to over-currents and over voltages that transformers are, and therefore, external protection is required [179]. Protection systems have the following requirements: sensitivity, selectivity, robustness, reliability, and speed [178]. Reliability is of vital importance for all networks, grid distribution, micro-grids, rail, and onboard ship systems [35]; therefore, DC protection must ensure that DC grids are not frequently down due to common short circuit faults. The entire protection system must protect the DC system and prevent any faults from propagating into the connected AC systems.

# 2.5.2 System Protections

The key system protection components for developing DC systems will likely rely on DC circuit breakers, fuses, disconnector switches, and surge arrestors. The DC circuit breaker (DCCB) requires the greatest development in terms of the necessary components. There are three key DCCB structures, i.e., mechanical CBs with active current injection, solid-state CBs (SSCBs), and hybrid CBs [86]. Mechanical DCCBs have low on-state resistance, but their opening speed is slow, and they require maintenance due to moving parts. They create an artificial zero-crossing point for the

current that is flowing through the mechanical breakers by activating the LC resonance circuit [180].

SSCBs are defined by fast clearance times and less maintenance but higher conduction losses due to the semiconductor devices in the main current path. IGBTs are commonly used as the switches, and across the IGBT branch, a metal oxide varistor (MOV), which acts as a surge arrestor, is connected to absorb the discharged energy, as shown in Figure 2.17. Ultimately, the SSCB offers the fastest clearing time and the lowest fault current; however, it has much greater power losses than the other two topologies, as detailed experimentally in [86]. Continued development in semiconductor devices could lead to reduced SSCB power loss. Several papers have investigated improvements to the SSCB, such as [181], which implements an RC buffer branch due to its ability to clear faults quickly and to resist very large currents. Reference [90] proposes an interlinked solid-state MVDC circuit breaker (ISSCB). The author of [165] presents a SSCB for the protection of BESS terminals from over-currents. The SSCB comprises several IGBTs and diodes in series, increasing the cost and the risk of complication.

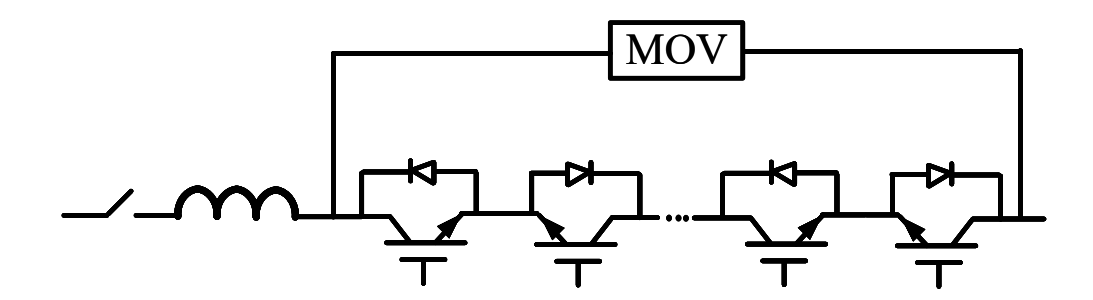


Figure 2.17: Solid State DC Circuit Breaker.

The hybrid CBs that are illustrated in Figure 2.18 have the characteristics of both mechanical and SSCBs, achieving faster response times than mechanical CBs, and have the benefit of lower conduction losses than SSCBs [86]. These CBs do not achieve a clearing time that is as fast as or that a fault current that is as low as that of a solid-state CB. Furthermore, they are also large and require cooling systems [180]. Common topologies are compared in reference [182].

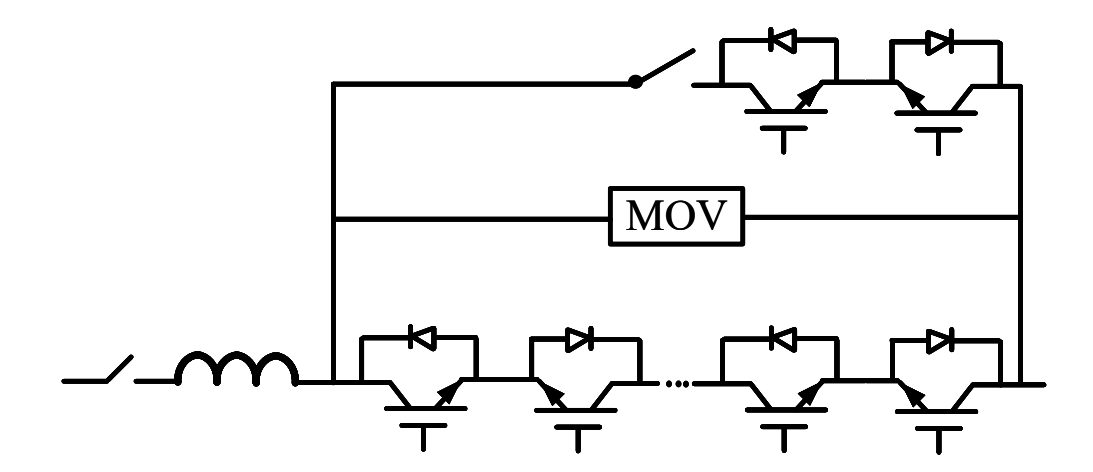


Figure 2.18: Hybrid DC circuit breaker.

Although DCCB technology is relatively new, there are several commercial examples. Reference [26] details the selection process for the DC circuit breaker for the Zhuhai project, where hybrid DCCBs are used. The mechanical switch in the main branch of the CB provided low on-state losses, high reliability, and low maintenance costs. The metal oxide surge arrester configuration branch would then limit over voltage. In the SPEN Angle DC project, the DC circuit was installed with a manual disconnector with a grounding switch to enable the circuit to be isolated. Therefore, a single fault in one of the DC cables would be isolated from the circuit, with the rest of the circuit is still being in service [25].

## 2.5.3 Converter Protection

Converter fault isolation methods will also play a significant role in DC grid protection [123]. Fault currents need to be quickly interrupted to avoid damage to the switches. The author of [136] presents the issue of DC fault handling in MMCs, stating that after a DC fault, the freewheeling diode in the converter acts as an uncontrolled rectifier that prevents DC-fault isolation in a flexible DC system. HB MMCs cannot block DC fault currents nor can 2L-VSCs [178]. Several papers have recommended FB MMCs for DC grids due to their fault blocking capabilities [183, 184]; however, other papers

such as [136] suggest still utilising an HB-SM with a double thyristor in order to reduce investment and power loss. This would isolate AC/DC faults by generating symmetric fault points and short circuits, after which the DC fault current can decay. The authors of [135, 183] suggest hybrid MMC configurations that utilise both HB and FB submodules, allowing for complete fault handling capability whilst also being cost effective.

## 2.5.4 Control for Protection

Systems with DCCBs, FB MMC converter fault protection, and DC isolation switches could all be utilised for DC fault operation with a fast response; however, the costs are still significant in these developing sectors. Furthermore, even with the FB submodule MMCs that block faults, there are associated short-term black outs that occur in the DC network following the fault. Several papers have recommended various control systems to effectively utilise protection devices such as DCCBs whilst controlling the current and voltage, ensuring fault ride through. The author of [109] highlights issues with the ACCBs that are integrated in DC systems as well as with the DCCBs and MMCs in MTDC networks and proposes a control system that enables reduced numbers of DCCBs and that can respond during an MMC substation going offline. Reference [183] also proposes an integrated protection control for limiting current, fault detection, and fault clearance whilst maintaining the operation of healthy lines. In MTDC grids, it is important to maintain network reliability and to enable faults to be detected and cleared quickly.

Protection control systems can also be integrated into other protection technologies, such as DCCBs with current regulation, as detailed in [175]. The paper recommends a current flow controller to prevent post-fault conditions where a faulty DC line is disconnected and where overloading occurs.

# 2.6 Converter Control

The main control topologies for converters are the grid following (GFL), and the grid forming (GFM) controllers. The GFL is the traditional control functionality that has

## Chapter 2. Review of MVDC Applications, Technologies and Future Prospects

been utilised for grid connected converters, however due to the changing grid scenarios, grid forming converters have been developed. In this section, an overview of the control details are highlighted, as well as the fundamental difference between GFL and GFM control.

Fundamentally the difference between GFL and GFM is defined by the former acting as a current source with a high parallel impedance, and the latter as a voltage source with a low series impedance [185], shown in Figure 2.19. There has been discussion on expanding these definitions to include the method of synchronisation. The GFL relies on an external voltage source to synchronise to the external grid, and generates a current at this measured frequency, whilst the GFM uses power(/current) synchronisation, performing self-synchronisation, and sets its own voltage magnitude and frequency [186]. For stable operation, a GFL controlled converter needs to be connected to a stiff voltage source. A GFM controller however can act as a stiff voltage source, meaning that the voltage magnitude and frequency will not be sensitive to current drawn [187].

There are various control topologies for both grid following and forming converters, however the fundamental properties still apply. The GFL acts as a current source in the sub-transient time frame, if there is an active power - frequency droop, the frequency is measured and active power set as constant, voltage is controlled by magnitude or Q-V droop, and current is controlled by fast reference tracking and disturbance rejection. For the GFM, it acts as a voltage source, maintaining P- $\omega$  droop without external  $\omega$  measurement, voltage is controlled by vector control of the magnitude and angle, and any inner current loops are set within the current limit.

In Chapter 3, the derivation of the traditional current control, grid forming virtual synchronous machine control, and models are derived. Ancillary services can be added for additional grid support, however the discussed topologies are those that are used in this thesis.

The utilisation of VSCs in MVDC networks provides significant ancillary services for both the DC and AC interconnected grids. Aithal et al. in [168] proposes the control of an MVDC link, highlighting the benefits of each VSC connection having its own

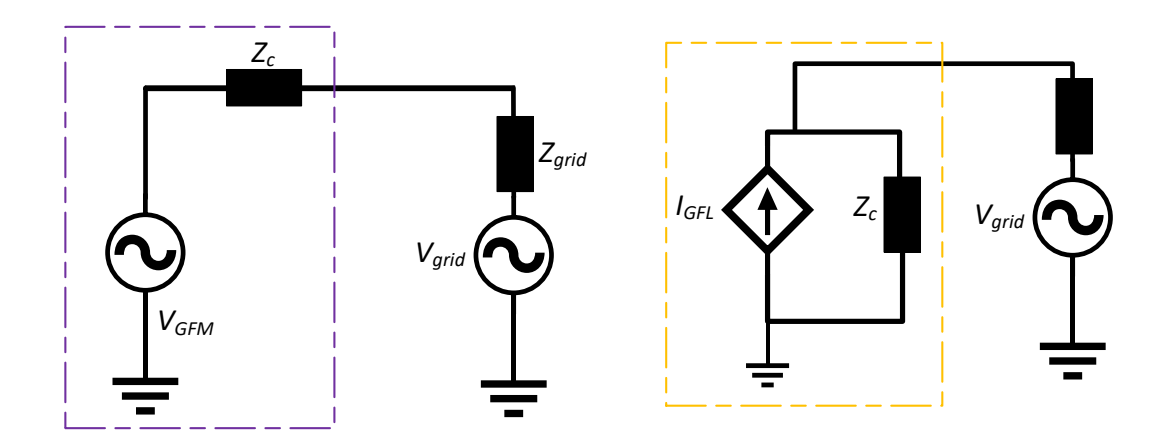


Figure 2.19: Representation of grid forming and grid following control in terms of their inherent reactions. GFM acts as a voltage source with series impedance, GFL acts as current source with high parallel impedance.

separate control system. References [41,43,45,86] and extensive literature agrees with [168] that the VSCs at each node provide flexible control and DC voltage balancing. The operating modes (all four of the P-Q plane quadrants) are all available to the network operator, with continuous control of the set points, all whilst fixing the DC link voltage. Castelo De Oliveria et al. in [188] experimentally tested the flexibility of AC-DC links and claimed that the main priority of DC operation is to provide the ancillary services that are required by the grid (as well as increasing power capacity). The paper concluded that the VSC controlled the DC link effectively and that it was capable of switching from power transmission to shunt FACTS.

# 2.6.1 DC Control

The primary concern of DC control is the ability to maintain a stable DC voltage at the DC bus and in any submodules, arms, and branches in a converter if they are present. In MTDC systems, DC voltage control is achieved with master—slave control, voltage margin control [189], and droop control [190]. Traditionally, the "master—slave" control structure has been adopted [191], which is a centralised DC voltage control method. The master controller operates in constant DC voltage mode and the other controllers, the "slave" terminals, operate under constant power mode. This method can produce

highly accurate operation with the master converter, ensuring that the DC voltage is kept at the reference voltage [192].

Voltage margin control extends the master–slave technique; however, it allows the VSC acting as the DC voltage controller to change [193], and the VSC operates within the P-Vdc characteristic.

However, centralised DC control has several drawbacks, such as poor transients, with just one controller controlling DC voltage level, and it also relies on fast communication [192]. Furthermore, for both the master—slave and voltage margin controls, if there is an outage in the DC voltage controller, the voltage of the whole system becomes unstable; hence, droop control is preferable. Hence, distributed DC voltage control has since been suggested to reduce dependence on fast communication [180]. Each converter has a DC voltage droop controller and one controller controlling the AC active power. Droop control offers better stability during VSC outages on the system compared to voltage margin control. The DC bus voltage is maintained across the DC link, which can be achieved using equation (2.1)

$$P_c = P_{DC_{ref}}^* + k_{droop}(V_{DCref}^* - V_{DC})$$

$$\tag{2.1}$$

where  $P_c$  is the PCC measured power,  $P_{DC_{ref}}^*$  is the reference power,  $k_{droop}$  is the droop gain,  $V_{DC_{ref}}^*$  is the reference DC voltage and  $V_{DC}$  is the measured DC voltage [194].

## 2.6.2 Network Level Control

Traditional AC distribution grids conventionally have power flow in one direction, with the high levels moving down to the AC distribution grid. An AC/DC hybrid grid could enable the AC distribution grid to be interlinked with a DC distribution grid at varying levels, offering flexibility with decentralised control, easing the integration of distributed renewables. Two methods of communication in the AC/DC hybrid grid could exist: the conventional grid communication network and non-utility-based networks such as the IoT, as shown in Figure 2.20 [195]. In a traditional communication reliability and distribution operator (DO) was entirely in control of the distribution reliability and

communication. Increasingly, distribution grids are developing to be able to contain distributed renewables, which might not be controlled directly by the DO but rather by the energy services organisation (ESO). This communication is through the internet and communicates with the DO and an independent system operator (ISO).

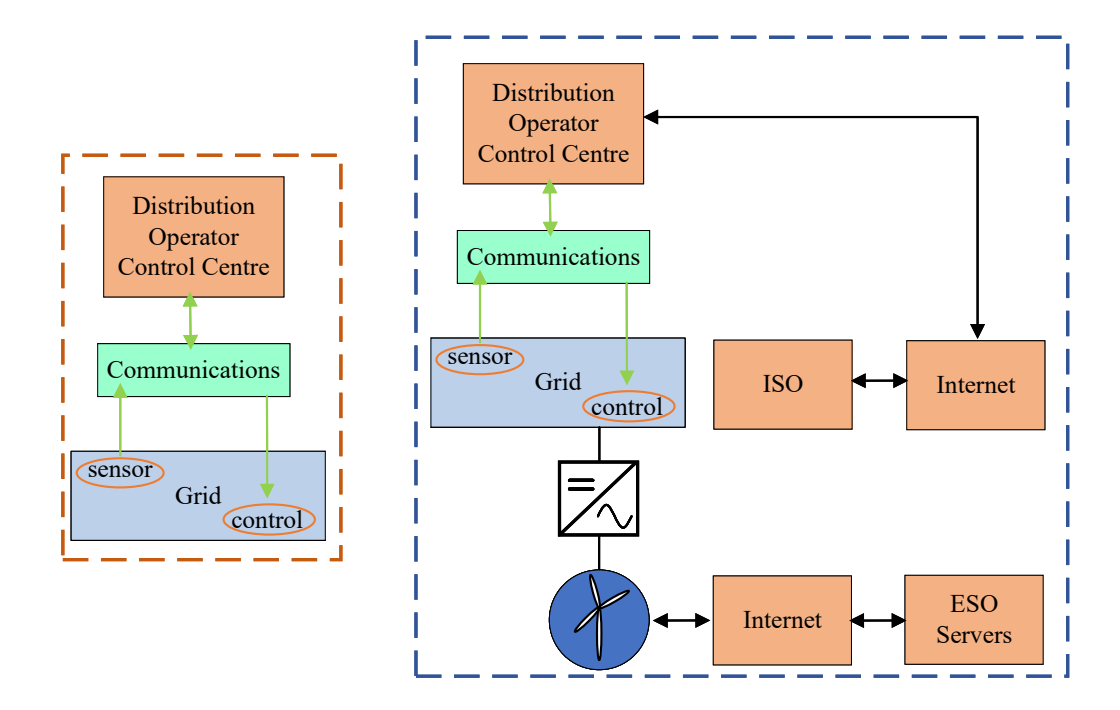


Figure 2.20: (a) Traditional control communications compared to (b) AC/DC hybrid grid communications.

However, these AC/DC systems, with their increased flexibility and power flow complexity, have new demands and dynamic issues [196]. MVDC distribution grids also tend to have an increased geographical range with increased DERs and load and power fluctuations that significantly affect system operation and control [197]. MVDC distribution is also characterised by high converter penetration with extensive voltage and power control. Fast and reliable communication is required for this extensive controllability and requires the use of units such as phase measurement units (PMUs) and synchronous DC Measurement Units (SynDCs) [198]. A central DC re-dispatch to perform recalculations during a DC or AC contingency is essential in multiterminal grids. When a power converter disconnects, the re-dispatch restores power exchange

Chapter 2. Review of MVDC Applications, Technologies and Future Prospects and redirects power flow from one area to another [194].

# 2.7 MVDC Conclusion

This chapter has presented a complete review of the applications of MVDC systems along with the possible benefits that are offered by the adaption of this technology. System topologies, hardware, protection, and control were discussed. The four main MVDC applications that were reviewed in this paper were shipboard systems, rail, offshore wind collection, and distribution grids. For rail systems, the lower end of MVDC technology is already in use for tram, metro, and subway systems; however, long distance travel with MVDC is being suggested at higher voltages of around 10 kV, and the recommended voltage for high speed railways is 20–30 kV. For shipboard IPSs, MVDC power systems are emerging as an alternative to AC systems with heavy transformers. The industry has had IPSs available for several decades; however, the system was traditionally AC based. Further to this, to improve efficiency, fuel economy, and power quality, all electric ships are emerging in the industry [63], as developments in power electronics, namely MMCs, in shipboard systems offer voltage and power scalability [31,142] and FB sub-modules; they also have good fault blocking capability [143]. MVDC systems offer more flexibility in the on-board network structure compared to traditional AC systems, which are often radially distributed. Using an MVDC grid could improve system controllability and could improve security and reliability [54]. Distribution grids are beginning to introduce MVDC links and DC grids. MVDC interties will enable the use of SOPs to provide ancillary services to the grid [46]. There are several examples of DC links [94,95], and small DC distribution networks have been developed in southeastern China [96,97]. Multiterminal DC grids will likely develop in commercial industries, grids, and interties with HVDC systems [47]. The technology that is required for MVDC distribution grids is available, as MVDC systems have the flexibility of utilising 2L and 3L VSCs as well as MMCs. The 2L and 3L converters could be utilised at voltages of up to around  $\pm 10$  kV DC [135], and MMCs could provide the required step that needs to be taken before for higher voltages can be used.

Chapter 2. Review of MVDC Applications, Technologies and Future Prospects

For DC–DC connections, multilevel DAB converters and MMDCs are suggested in the literature. The MMDC has higher efficiency and reliability but no galvanic isolation. For projects [25, 26, 97, 99], the voltage can range from 10 kV to 27 kV. This will likely be the mean distribution range, but there may be an extension of up to 50 kV or to even 100 kV for distributed renewable connection. However, offshore wind collection is still being developed, and there are currently no active MVDC collection systems. The lower weight of MVDC collection substations compared to AC collection or HVDC substations could significantly reduce the capital cost of the system [199]. MMC technology could achieve the high step-up ratios that are required and has good short term reliability with active redundancy, but the long term survival of the technology in offshore conditions is still under investigation [100]. The protection mechanisms that are implemented in DC grids will have to ensure that faults are not propagated from the DC to the AC side and vice versa. Three categories of DC circuit breakers are continually being developed: mechanical, solid state, and hybrid. The SSCBs are the fastest; however, they have significant losses, so hybrid DCCBs have become the most common. The fault propagation from one AC system through a DC link has been highlighted as a concern in the literature [200]. However, it has been suggested that existing AC protection systems can be updated for MVDC protection [201]. Damping the oscillations between multiterminal DC grids with AC connections is also being investigated in the literature [200, 202]. MVDC systems offer several benefits for the applications presented in this paper, from flexibility, controllability, and reliability to increased capacity. Continued developments in DCCB technology are still required to improve costs and power losses in SSCBs. However, the technology is available and is being utilised for rail, shipboard, and distribution systems, and MVDC systems could begin to take prevalence on the electrical stage.

# Chapter 3

# Power Converter Modelling and Control

In this chapter, the theory behind power converter modelling and the vector control representation is explained. Additionally, the models that have been used throughout the thesis are shown. The presented systems are shown with the non-linear EMT equations, then, small signal models are derived from these equations, shown in Section 3.5.

The system modelled in this Chapter is a grid tied VSC connection, described in terms of the non-linear equations, as well as the derivation of grid following and grid forming control. To obtain linear equations utilised in the small signal models, the whole system needs to be represented in the synchronous reference frame [203–205], and then linearised. Therefore the full equations of the system are detailed, along with the background of vector control, and derivation of control topologies used.

# 3.1 Vector Control and Representation of Converters and Grid Systems

The modelling and control of converter systems is expanded upon in this section. A converter to infinite bus system (shown in Figure 3.1) is used as an example to

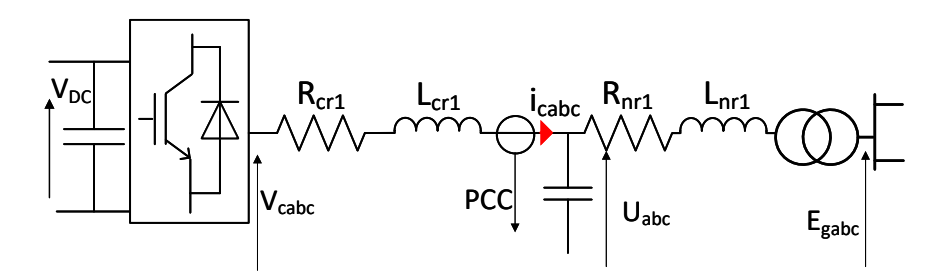


Figure 3.1: Converter to Grid System

explain the implementation and representation of reference frames. The grid voltage is represented with  $E_{gabc}$ , the PCC voltage as  $U_{abc}$ , converter AC side voltage as  $V_{abc}$  and the converter DC side voltage as  $V_{DC}$ . The converter side resistance and inductance is described by  $R_{cr1}$  and  $L_{crc1}$ , and the grid side by  $R_{nr1}$  and  $L_{nr1}$ .

#### 3.1.1 Representation of Voltage Source Converter

Typical converter VSC topologies have been presented in Chapter 2, reviewing the well known two-level and three-level designs. The output voltage of the converter is set by the control system, which applies switching signals to the switches of the converter. The control of the voltage is enabled with space-phasor vector theory, described in the next section [206]. The control system utilises pulse width modulation (PWM), producing the modulation index creating the modulating signal, which is then compared with the carrier signal. The modulating signal is a slow varying waveform, and the carrier signal is a fast periodic sawtooth or triangular waveform. When the modulation signal is greater than the carrier, the switching function changes from 0 to 1. This function is used to control both switches on the one half bridge, with a Not gate producing the opposite signal for the bottom switch [206].

When modelling the converter to grid system of Figure 3.1, the averaged model of the system can be used for simplicity. In this representation, the AC and DC sides of the VSC are decoupled, and the average values of variable taken, with the converter dynamics produced as a function of the modulation signal. The equivalence of a two-level VSC structure in the averaged model representation is shown in Figure 3.2, where

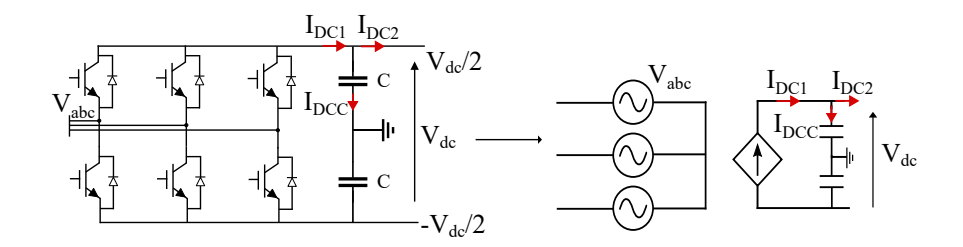


Figure 3.2: Converter equivalent averaged model.

the AC side is represented as a controlled voltage source, and the DC side as a controlled current source.

The desired voltages at each of the three voltage phases is taken from the control system. Then, the current source representing the DC side is calculated from (3.1), assuming no converter losses.

$$I_{DC1} = \frac{P_{AC}}{V_{dc}} \tag{3.1}$$

With this representation, the following sections describe the representation of the VSC to grid system in the synchronous frame, and the derived controller topologies.

#### 3.1.2 Space vector theory and frame representations

The converter to grid system in this chapter is modelled in the  $\alpha\beta$  and dq frames, to simplify control. This is enabled by space vector representation, which relies on the instantaneous values of the system. For the system variables, a complex vector can represent the three-phase components of the system. For a variable  $\mathbf{Y}$ , representation in the abc frame as  $Y_{abc}(t)$  is defined by (3.2) in the instantaneous phasor form.

$$Y_j(t) = Y_m cos(\omega t + \theta_0 - \frac{2\pi k}{3}) \qquad for(j,k) = (a,0), (b,1), (c,2)$$
(3.2)

where  $Y_m$  is the variable magnitude,  $\omega$  the angular frequency and  $\theta$  the initial phase angle [206]. A complex vector of the three-phase vectors is defined by

$$\mathbf{Y}^{s} = \frac{2}{3} (Y_a + Y_b e^{j\frac{2\pi}{3}} + Y_c e^{j\frac{4\pi}{3}})$$
(3.3)

where  $\mathbf{Y}^s$  is in the stationary reference frame: the variables are shown as  $\alpha$ - $\beta$  components, in a frame that does not rotate. The *abc* three phase oscillating signals of each variable can be converted to the stationary frame using the Clarke Transform  $(T^{Clarke})$  [207]. If a vector variable  $\mathbf{Y}^s = T^{Clarke}$   $Y_{abc} = Y_{\alpha} + jY_{\beta}$ , (with subscript s indicating the stationary frame) then it can be represented by equation (3.4) [205] [208] [209], assuming a balanced system.

$$\begin{bmatrix} Y_{\alpha} \\ Y_{\beta} \end{bmatrix} = \frac{2}{3} \begin{bmatrix} 1 & \frac{-1}{2} & \frac{-1}{2} \\ 0 & \frac{-\sqrt{3}}{2} & \frac{\sqrt{3}}{2} \end{bmatrix} \begin{bmatrix} Y_{a} \\ Y_{b} \\ Y_{c} \end{bmatrix}$$
(3.4)

$$Y_{\alpha} = \frac{2}{3} Y_{m} cos(\theta) - \frac{1}{2} Y_{m} cos(\theta - \frac{2\pi}{3}) - \frac{1}{2} Y_{m} cos(\theta - \frac{4\pi}{3}) = \frac{3}{2} Y_{m} cos(\theta)$$
 (3.5)

$$Y_{\beta} = -\frac{\sqrt{3}}{2}Y_{m}cos(\theta - \frac{2\pi}{3}) + \frac{\sqrt{3}}{2}Y_{m}cos(\theta - \frac{4\pi}{3}) = \frac{3}{2}Y_{m}sin(\theta)$$
 (3.6)

For the work completed in this thesis, the systems represented in the SSMs are in the dq reference frame. Typically system control is represented in this synchronous rotating reference frame [210], to enable DC control of the system variables, as opposed to 3 phase sinusoidal signals. This can be achieved by the Park Transform (power variant form), shown in equation (3.7), and the inverse Park Transform shown in (3.8). This

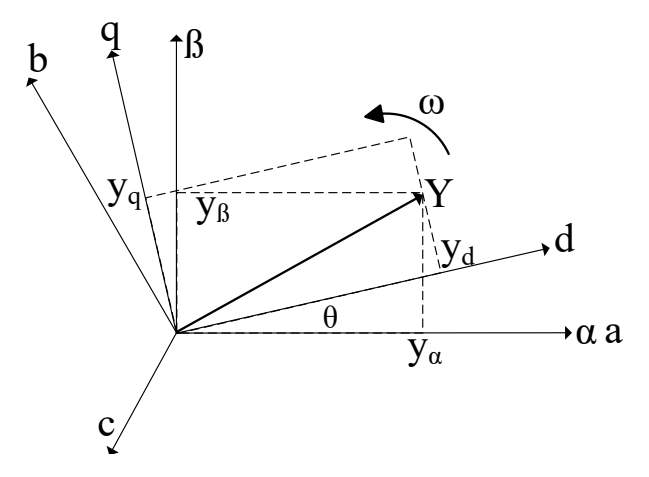


Figure 3.3: Relation between abc frame, stationary frame, and synchronous reference frame.

transform converts the component of the three phase variables in the abc reference frame to a rotating reference frame with "direct, quadrature, and zero components" [211]. The variable  $\theta$  is the angular position of this rotating reference frame, and when utilising the transform to obtain constant steady state variables, the input angle is the electrical angle of the voltage at the PCC. In this thesis, the Park Transform used has the d component aligned with the a-axis, and the q component leading 90°, as seen in Figure 3.3 [203].

For the same variable in equation (3.2), it can be transformed into the dq components,  $Y_{dq} = Y_d + jY_q$ , by the Park Transform using (3.7) and the inverse with (3.8). The power variant form is used, indicated by the  $\frac{2}{3}$  term in equation (3.7). This results in power calculation from the dq components requiring multiplication by  $\frac{3}{2}$ .

$$\begin{bmatrix} Y_d \\ Y_q \\ Y_0 \end{bmatrix} = \frac{2}{3} \begin{bmatrix} \cos(\theta) & \cos(\theta - \frac{2\pi}{3}) & \cos(\theta + \frac{2\pi}{3}) \\ -\sin(\theta) & -\sin(\theta - \frac{2\pi}{3}) & -\sin(\theta + \frac{2\pi}{3}) \\ \frac{1}{2} & \frac{1}{2} & \frac{1}{2} \end{bmatrix} \begin{bmatrix} Y_a \\ Y_b \\ Y_c \end{bmatrix}$$
(3.7)

$$\begin{bmatrix} Y_a \\ Y_b \\ Y_c \end{bmatrix} = \begin{bmatrix} \cos(\theta) & -\sin(\theta) & 1 \\ \cos(\theta - \frac{2\pi}{3}) & -\sin(\theta - \frac{2\pi}{3}) & 1 \\ \cos(\theta + \frac{2\pi}{3}) & -\sin(\theta + \frac{2\pi}{3}) & 1 \end{bmatrix} \begin{bmatrix} Y_d \\ Y_q \\ Y_0 \end{bmatrix}$$
(3.8)

The relation between the abc, dq and  $\alpha\beta$  frames is visualised in Figure (3.3). With this transform, the measured voltage and currents from the PCC, can be represented as two DC signals (and zero component), as opposed to the three phase sinusoidal waveforms, enabling converter control, with active and reactive power decoupled.

# 3.2 Synchronous Reference Frame Phase Locked Loop (SRF-PLL) and Frame Conversions

The system variables can be represented in the abc, stationary  $\alpha\beta$ , and synchronous reference dq frames. When modelling the full system, there are multiple synchronous reference frames, typically, the converter and global reference frame. In GFL control,

the Phase Locked Loop (PLL) provides voltage based synchronisation between the converter and grid. The basic structure of the PLL is shown in Figure 3.4

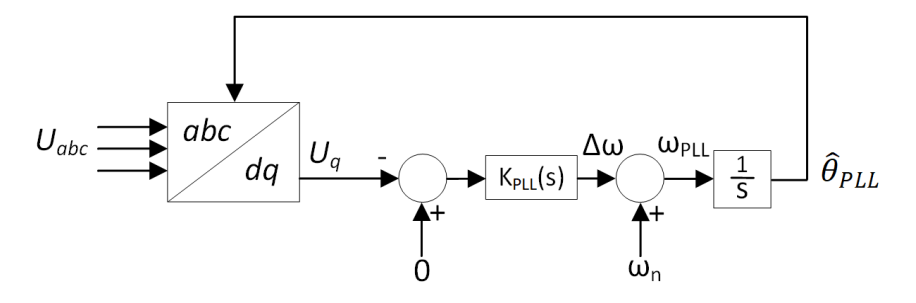


Figure 3.4: Control Structure of SRF-PLL.

The synchronous reference frame PLL aligns the PCC voltage with the converter frame d-axis, with the goal being to extract the grid angle [212]. If the actual PCC angle is defined as  $\theta_{PLL}$ , the PCC angle estimated by the PLL is defined as  $\hat{\theta}_{PLL}$ . Considering this control structure in Figure 3.4, the relation between the PLL angle estimate and the input q axis voltage can be defined by (3.9).

$$\hat{\theta}_{PLL} = \int \left( \omega_n + K_P * u_{PCCq} + K_i \int (u_{PCCq}) \right) dt$$
 (3.9)

The relation between the reference frames and the PCC voltage can be seen in Figure 3.5. The stationary reference frame,  $\alpha\beta$ , has  $\alpha$  aligned with the a-axis. The PCC voltage is defined by  $U_{PCC}$ , with an angle,  $\theta_{PLL}$ , and the estimation of the PLL angle, is  $\hat{\theta}_{PLL}$ . It is often assumed there is no error between the actual angle and the estimation of the angle, primarily during steady state [213] [214]. However, there will be a difference between the actual PCC angle and the estimate of the angle during transients and disturbances, which can be defined by  $\delta$ , shown in Figure 3.5.

$$\delta = \theta_{PLL} - \hat{\theta}_{PLL} \tag{3.10}$$

The derivation of the standard GFL control, tunings, and PLL tunings can now be explained using the synchronous reference frame representation. The PLL gains defined

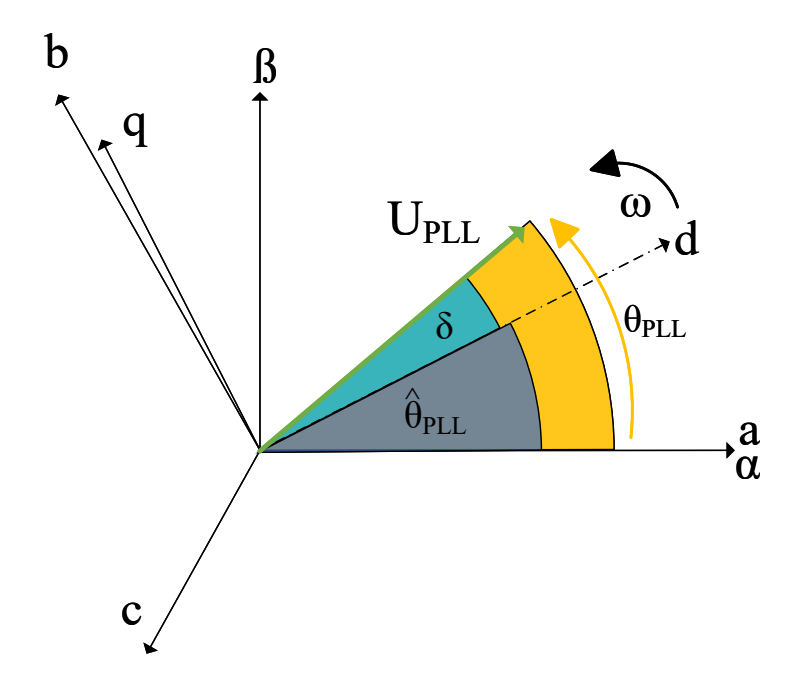


Figure 3.5: Relation between stationary and synchronous reference frame and PCC voltage.

in equation (3.9) are typically tuned by considering the transfer function of grid angle to estimation of the angle. Referring back to Figure 3.4 and to Figure 3.5, the relation between these two angles,  $\theta_{PLL}$  and  $\hat{\theta}_{PLL}$  is observed. If the PCC voltage is represented in the  $\alpha\beta$  frame, detailed in equations (3.4), (3.5) and (3.6) as  $Y_{\alpha} = Y_{m}cos(\theta)$  and  $Y_{\beta} = Y_{m}sin(\theta)$ , the voltage can then be represented in the dq frame. It has been established that the PCC angle  $\theta_{PLL}$  is estimated by the PLL as  $\hat{\theta}_{PLL}$ . The instantaneous dq voltages can then be defined by (3.11).

$$U_d = U_m cos(\theta_{PLL} - \hat{\theta}_{PLL}) \tag{3.11}$$

$$U_q = U_m sin(\theta_{PLL} - \hat{\theta}_{PLL}) \tag{3.12}$$

Ideally, the angle difference between  $\hat{\theta}_{PLL}$  and  $\theta_{PLL}$  should be negligible, as the goal of the PLL is for the error between the estimated angle and the actual angle to zero [214]. Additionally, for simplification, if the angle error between  $\theta_{PLL} - \hat{\theta}_{PLL}$  is controlled to

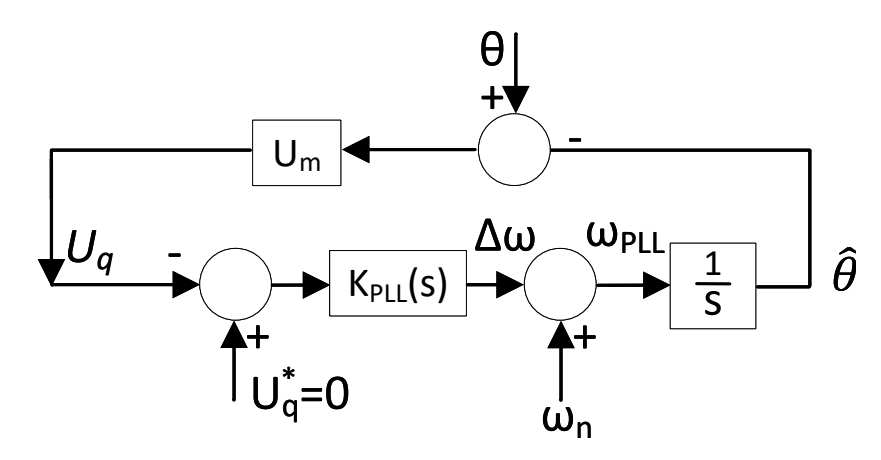


Figure 3.6: Simplified Control loop of PLL.

be zero, then  $U_q = 0$ , and if the angle difference is very small, using the approximation of a small angle  $\theta_{small}$ , then  $sin(\theta_{small}) \approx \theta_{small}$ 

$$U_q = U_m sin(\theta_{PLL} - \hat{\theta}_{PLL}) \approx U_m(\theta_{PLL} - \hat{\theta}_{PLL})$$
(3.13)

and the PLL control can be considered linear. This simplified control is seen in Figure 3.6. This results in the transfer function (3.14)

$$\frac{\hat{\theta}_{PLL}}{\theta_{PLL}} = \frac{K_{PLL}(s)V_{nom}}{s + K_{PLL}(s)V_{nom}}$$
(3.14)

which can be related to a second order transfer function in (3.15). It should be noted that  $\omega_n$  is the natural frequency of the filter (not the grid synchronous frequency).

$$H(s) = \frac{2\zeta\omega_n s + \omega_n^2}{s^2 + 2\zeta\omega_n s + \omega_n^2}$$
(3.15)

Comparing 3.14 and 3.15 the following tuning relations can be found [215], [216], [217], [218].

$$Kp_{PLL} = \frac{2\omega_n}{V_{nom}}, \quad \tau_{PLL} = \frac{2\zeta}{\omega_n}, \quad Ki_{PLL} = \frac{Kp_{PLL}}{\tau_{PLL}}$$
 (3.16)

with  $V_{nom}$  as the nominal input voltage,  $\zeta$  is the damping ratio of the response, and

 $\tau_{PLL}$  as the PLL time constant.

The tuning of the traditional GFL parameters presented in this section is typically used throughout this thesis. However, these typical parameter values are tested throughout the chapters when assessing their impact on small-signal and dynamic stability.

The small signal representation of the PLL is derived in the small signal modelling part of this chapter in Section 3.5.2.

# 3.3 Grid Following Control

GFL converters act as a controlled current source with a high parallel impedance [185]. A common GFL implementation is a standard current controller, with outer power and voltage loops for creating the current references. The system contains an LC filter between the grid and converter voltages, with the voltage at the PCC being used as an input to the PLL to obtain the grid angle. The control of the converter contains the outer power and AC voltage control loops, and the inner current control containing proportional and integral gains dependent on the converter side inductance and resistance [204].

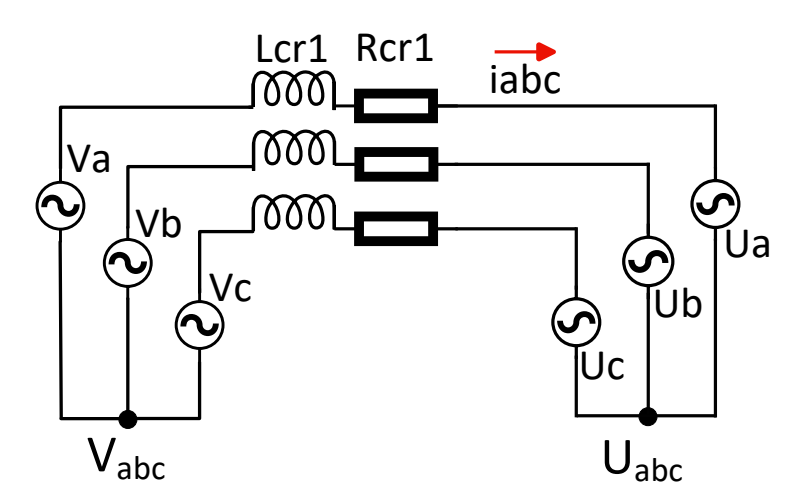


Figure 3.7: Simplified Representation of AC sides of VSC to Grid PCC.

The basis of current vector control can be described by considering the equations that define the converter to grid system [210], [205]. The system represented in Figure 3.7 is

the AC equivalent circuit of the VSC to PCC, to obtain the desired control structure. The equations for this system in the abc, representing the three phase instantaneous variables of the voltage and current are in (3.17). In this system, the converter side impedance is defined by,  $R_{cr1}$  and  $L_{cr1}$ .

$$\begin{bmatrix} V_{a} \\ V_{b} \\ V_{c} \end{bmatrix} - \begin{bmatrix} U_{a} \\ U_{b} \\ U_{c} \end{bmatrix} - (V_{0} - U_{0}) \begin{bmatrix} 1 \\ 1 \\ 1 \end{bmatrix} = \begin{bmatrix} R_{cr1} & 0 & 0 \\ 0 & R_{cr1} & 0 \\ 0 & 0 & R_{cr1} \end{bmatrix} \begin{bmatrix} i_{a} \\ i_{b} \\ i_{c} \end{bmatrix} + \begin{bmatrix} L_{cr1} & 0 & 0 \\ 0 & L_{cr1} & 0 \\ 0 & 0 & L_{cr1} \end{bmatrix} \frac{d}{dt} \begin{bmatrix} i_{a} \\ i_{b} \\ i_{c} \end{bmatrix}$$

$$(3.17)$$

In the stationary reference frame the representation is (3.18).

$$\mathbf{V}^s - \mathbf{U}^s = R\mathbf{i}^s + L\frac{d\mathbf{i}^s}{dt} \tag{3.18}$$

In this system it was assumed that the zero components of the grid and converter are equivalent, where  $V_0 - U_0 = 0$ . Additionally, the current zero component,  $i_0$ , is assumed to be equivalent to zero, 0, therefore when the Park transform of (3.7) is applied to (3.17), the resulting in matrix only comprises the d and q components.

$$\begin{bmatrix} V_d \\ V_q \end{bmatrix} - \begin{bmatrix} U_d \\ U_q \end{bmatrix} = \begin{bmatrix} R_{cr1} & -\omega L_{cr1} \\ -\omega L_{cr1} & R_{cr1} \end{bmatrix} \begin{bmatrix} i_d \\ i_q \end{bmatrix} + \begin{bmatrix} L_{cr1} & 0 \\ 0 & L_{cr1} \end{bmatrix} \frac{d}{dt} \begin{bmatrix} i_d \\ i_q \end{bmatrix}$$
(3.19)

where the converter and grid, direct and quadrature voltages are  $V_d$ ,  $V_q$ ,  $e_d$ ,  $e_q$ , the converter dq currents are  $i_d$  and  $i_q$ , and the electrical frequency is  $\omega$ . It should be noted that a cross coupling term is introduced when converting from the abc frame, to  $\alpha\beta$  stationary frame, to the dq synchronous rotating frame. Referring to equation (3.4),  $\mathbf{Y^s} = Y_\alpha + jY_\beta$ , and for a derivative term, if the relation of stationary to dq frame in (3.64) is considered, then the cross coupling term is produced in (3.21), with  $\mathbf{Y}$  indicating the vector in the dq frame [219], [208] [205].

$$\mathbf{Y}^{\mathbf{s}} = e^{jwt}\mathbf{Y} \tag{3.20}$$

$$\frac{d\mathbf{Y^s}}{dt} = \frac{d}{dt}(e^{jwt}\mathbf{Y}) = jwt\mathbf{Y}e^{jwt} + \frac{d\mathbf{Y}}{dt}e^{jwt}$$
(3.21)

Therefore if the equations for the converter to PCC grid voltages are transformed from the stationary reference frame to the dq frame, by (3.22).

$$\mathbf{V}^s = \mathbf{V}e^{jwt}, \mathbf{U}^s = \mathbf{U}e^{jwt}, \mathbf{i}^s = \mathbf{i}e^{jwt}$$
(3.22)

Then (3.22) can be substituted into (3.18), and expanding into the dq components  $(\mathbf{Y} = Y_d + jY_q)$  and comparing the real and imaginary parts, the cross coupling terms are derived.

$$\mathbf{V}e^{jwt} - \mathbf{U}e^{jwt} - R\mathbf{i}e^{jwt} = L\frac{d\mathbf{i}e^{jwt}}{dt} = L(\mathbf{i}jwte^{jwt} + \frac{d\mathbf{i}}{dt}e^{jwt})$$
(3.23)

$$\mathbf{V} - \mathbf{U} - R\mathbf{i} = L(\mathbf{i}jwt + \frac{d\mathbf{i}}{dt})$$
(3.24)

To design the inner control loop, it is important to highlight design requirements:

- active and reactive power decoupling
- appropriate time response, such as fast current response [220]
- accurate control of current flowing through the converter impedance.

Considering these points, the vector control should enable the independent control of the dq variables by decoupling them. The current will be controlled to generate the desired voltage references to be applied to the gate drives of the VSC, by controlling the voltage drop across the converter impedance [221]. The reference voltage to be applied to the VSC can be controlled by the current Proportional Integral (PI) with

$$\begin{bmatrix} V_d \\ V_q \end{bmatrix} = \begin{bmatrix} V_d^{in} - \omega L_{cr1} + U_d \\ V_q^{in} + \omega L_{cr1} + U_q \end{bmatrix}$$
(3.25)

where

$$V^{in} = Ri + L\frac{di}{dt} (3.26)$$

If (3.26) is rearranged in transfer function form of voltage to current, and the LaPlace [222] transform applied, then a 1st order controller function for the dq variables can be

defined by:

$$\frac{i_d(s)}{V_d^{in}(s)} = \frac{1}{L_{cr1}s + R_{cr1}} \tag{3.27}$$

$$\frac{i_q(s)}{V_q^{in}(s)} = \frac{1}{L_{cr1}s + R_{cr1}}$$
 (3.28)

This controller in turn can be related to the equation of the proportional integrator (PI), using the Internal Model Control technique which is described in [223].

$$G_{PI}(s) = \frac{K_P s + K_i}{s} \tag{3.29}$$

where for both the dq controllers the gains can be defined by

$$K_P = \frac{L_{cr1}}{\tau_{cc}} \tag{3.30}$$

$$K_i = \frac{R_{cr1}}{\tau_{cc}} \tag{3.31}$$

The time constant  $\tau_{cc}$  is selected to generally be 10 times slower than the switching frequency [222]. The overview of a typical GFL model can be observed in Fig. 3.8. The grid side inductance and resistance are defined by  $L_{nr1}$  and  $R_{nr1}$ , and the converter side defined by  $L_{cr1}$  and  $R_{cr1}$ . Each control component will be expanded upon in this section.

The outer loop controls typically are to control active power and voltage/reactive power, seen in Figure 3.8, with control transfer functions  $K_p(s)$  and  $K_U(s)$  control active power and AC voltage respectively. The time constant of the active power controller typically should be 10 times slower than the inner current control loop [224]. In this control loop, the variables are considered as peak phase-to-phase.

Due to the changing requirements of the grid, there have been several suggestions for amendments to GFL topologies to provide supporting services to the grid. GFL converters can typically provide essential services such as reactive power control, resulting in voltage support and control. Active and reactive power is controlled via an outer loop, as seen in Figure 3.8. However, there have been increasing desires for more

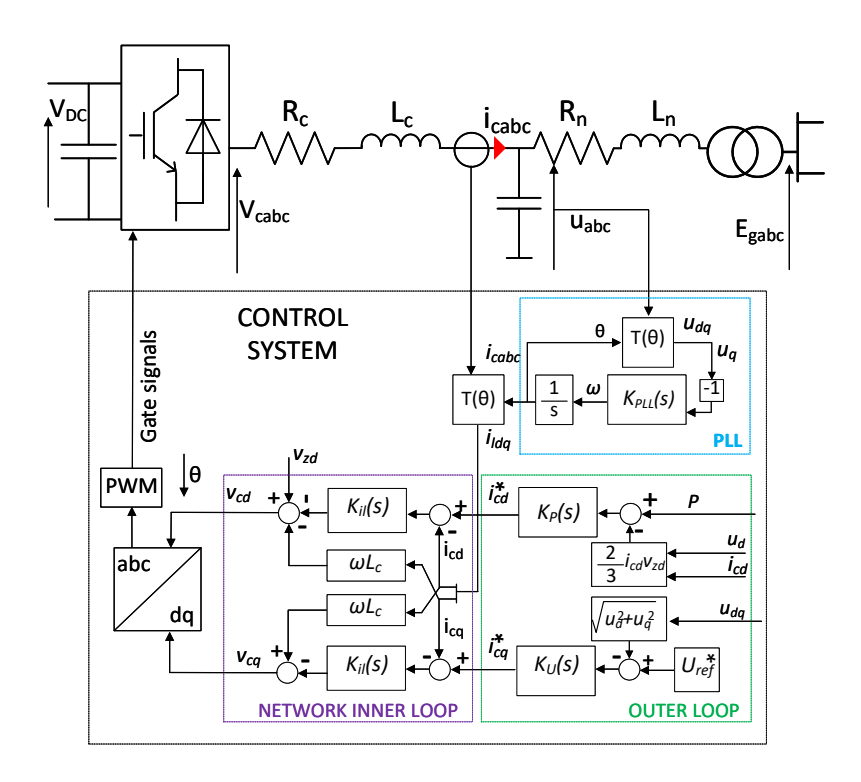


Figure 3.8: Current Controller Model of GFL in dq control.

advanced grid supporting features, for example, control can be amended to provide frequency and Rate of Change of Frequency (ROCOF) support [9], [13]. The effects and limitations of providing grid support through GFL control with ROCOF support is assessed in Chapter 4.

# 3.4 Grid Forming Control

#### 3.4.1 Grid Stability Issues

The move from traditional standard grid systems of large, synchronous generation, to IBR with grid *following* control has produced the some key concerns, namely, instability from resonance, converter driven instability, rotor angle, voltage, and frequency [225].

Considering frequency stability, it has been suggested that system inertia lost from decommissioning synchronous machines should be replaced with inertia provided by converters, usually called "emulated inertia", "digital inertia" or "synthetic inertia"

[226]. This can be offered from GFL converters acting in grid "supporting mode", however it has been debated over whether inertial response provided from GFLs can be a "true" inertia response, as it is considered as a grid forming inherent response. The UK grid code states, "for avoidance of doubt, Inertia Active Power is an inherent capability of a Grid Forming Plant to respond naturally, within less than 5 ms, [226]." However, papers such as [13] show that there are parameter conditions where inertia enhanced GFL converters can provide this "true" inertial response as well as a GFM.

Traditionally, the short circuit level to the nominal power of a device is the short circuit ratio SCR, and has been the index of traditional system strength (although newer quantifications of system strength are required [227]). With a low SCR, the system is considered weak and, therefore, sensitive to active and reactive power changes, making it difficult to control. In a weak grid, standard GFL converters might become unstable, forcing the converter to disconnect. The grid needs to maintain the voltage waveform in steady state, and during disturbance transients [228].

In general, voltage fluctuations at a large and local level are increasingly of concern for the grid. The integration of renewable energy at distances far from demand areas [229] result in a weakened connection and difficulty in controlling voltage. Voltage stability is desired to maintain values at acceptable levels during steady state and transients, and can be maintained with reactive power. Additionally, voltage stability needs to be maintained at a local level, and so adequate reactive power reserves are required [230].

To tackle these challenges, GFM converters have been proposed to provide stability and support. GFM converters are capable of providing inertia support, frequency support, black start, voltage source behaviour for grid strength and reactive power support, oscillation damping, and acting as a sink for harmonics [185] [231]. Not all of these capabilities would be provided at once, and the active and reactive power required must be available in order to support the system. Some of these grid issues can be tackled with enhanced controller support in GFL control, for example, GFL based inertial controls, reactive power support and FFR.

#### 3.4.2 Grid Forming Control Topologies

GFM converters act as a controlled voltage source with a low series impedance. There are several characteristic capabilities of GFMs, but this is the only commonly used definition. However, one of the fundamental differences between GFL and GFM converters is the synchronisation technique. As described in Section 3.3, the traditional current controlled GFL synchronises to the grid relying on the external voltage source. Grid forming converters however have a self-synchronisation capability, based on active power flow and not external voltage signals.

There are several key GFM topologies, and various combinations, however the current main designs are:

- Droop Control [185]
- Virtual Synchronous Machine (Virtual Synchronous Machine (VSM)) [232]
- Power Synchronisation Control [233]
- Matching Control [234]
- Virtual Oscillating Control (VOC) and dispatchable VOC (dVOC) [235]

#### Droop

The most "basic" implementation of GFM control is droop control, which is emulating the active power-speed droop of a synchronous machine. The change in frequency is related to the change in measured power and reference power, as shown in (3.32)

$$\omega = \omega^* + K_{droop}(P^* - P) \tag{3.32}$$

where  $\omega$  is the converter frame frequency,  $\omega^*$  is the reference frequency,  $P^*$  is the reference PCC active power, and P is the measured PCC power. With this simplistic control, changes in frequency are balanced with power absorption or generation, with the droop component being equivalent to power damping in the swing equations. The angle of the converter is the integral of the output frequency in (3.32).

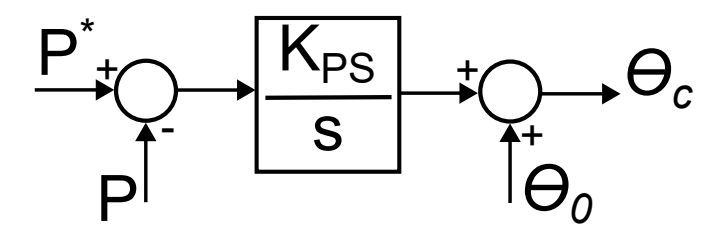


Figure 3.9: Power synchronisation loop with converter angle output.

#### Power synchronisation

Power synchronisation control is very similar to droop control, however instead of relating the error in angular frequency to the power error, the integral of the power error is related to the error in angle. The output  $\theta_c$  is the controller reference angle, with the initial angle defined by  $\theta_0$  [236].

$$(P - P^*)\frac{K_{PS}}{s} + \theta_0 = \theta_c$$
 (3.33)

### Virtual oscillating control (VOC)

The inspiration for VOC (and dispatchable VOC) control is the synchronisation theory from non-linear control [237]. The dynamics of a weakly non-linear limit-cycle oscillator are produced, which enables the converters to synchronise together from random initial conditions, without requiring external communication [185]. VOCs can be based on differing oscillators, a common one being the Van der Pol oscillator. Scaling constants are selected for equations of voltage and current, based on capacitor and inductor equations, which can be tuned to emulate typical droop control [238]. Although, higher performance than standard droop control is expected as VOC control utilises instantaneous time-domain signals, opposed to phasor electrical variables [185].

#### Matching control

The basis of this control technique is "matching" the electromechanical energy exchange patterns in synchronous machines [234]. As with the VOC, an oscillator is utilised with the converter dynamics (matching converter dynamics to synchronous

machine dynamics), with the oscillator frequency tracking the value of the DC voltage measurement. Therefore, for GFM control, the dynamics of the synchronous machine are matched by the oscillator producing the PWM signals for the switching gates.

#### Virtual synchronous machine

Throughout this work the main GFM control used has been the VSM, the full modelled system being a VSM converter connected to an infinite bus through an LC filter. Therefore the control topology, parameters and tunings of the VSM will be described in this section. The function of the VSM is to emulate the behaviour of a synchronous generator, to improve support to modern grid systems. The derivation of the control is described here, based on the characteristics on a synchronous machine.

The first proposed control structure of a VSM form was the VISMA, [10], with several developments to the control structure presented in the literature since [232], [239], [185], [240]. In this control the power measurement,  $P_e$ , is obtained at the point of common coupling (PCC) and controlled to the reference power,  $P_m$ , through the swing equation, (3.34) with the damping, D, inertia, J, the rotor frequency,  $\omega_r$ , and the grid frequency,  $\omega_g$ .

$$P_m - P_e = J\frac{d\omega_r}{dt} + D(\omega_r - \omega_g)$$
(3.34)

J is equivalent to 2H, the mechanical time constant representing inertia of the virtual rotor, with the relation shown in (3.35). J is the moment of inertia in  $(kgm^2)$ , which traditionally was calculated from synchronous machine parameters [11],  $\omega_b$  is the base frequency and  $S_b$  is base power. For virtual synchronous machines, H is selected based on how much power is available to be delivered during set ROCOF changes [241], it can be tuned based on desired application and is not constrained by physical characteristics of the machine [242], rather than the available stored energy.

$$H = \frac{1}{2}J\frac{\omega_b^2}{S_b} \tag{3.35}$$

The derivation of the VSM model can be obtained from assessing a simplified

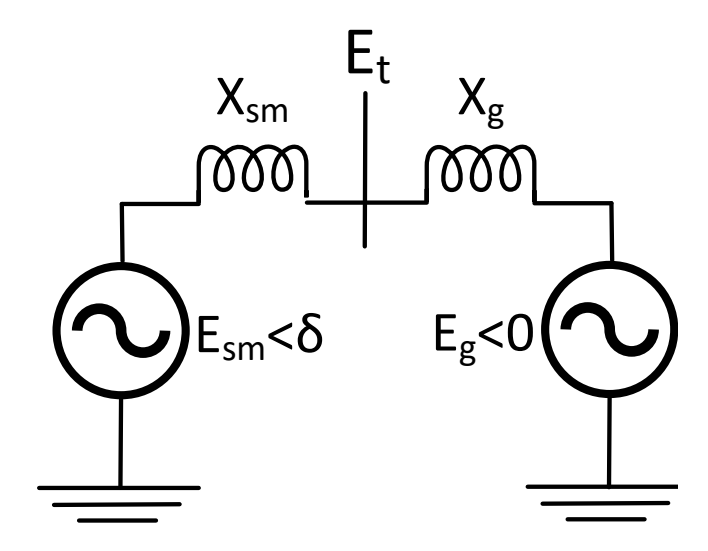


Figure 3.10: Simplified Equivalent Synchronous Machine to Grid.

synchronous machine to grid system, with neglected resistance, shown in Figure 3.10. It should be noted that this is the classical model, with simplifications in the representation, assuming neglected resistance, for ease of representation. The grid voltage is  $E_g \angle 0$ , converter voltage is  $E_{sm} \angle \delta$ , and if the total inductance is defined by  $X_T = X_{sm} + X_g$ , then the complex power behind  $X_{sm}$ , assuming neglected resistance, and can be defined by (3.36)

$$S = P + jX = E_{sm}I_t^* = \frac{E_{sm}E_g sin(\delta)}{X_T} + j\frac{E_{sm}(E_{sm} - E_g cos(\delta))}{X_T}$$
(3.36)

where  $I_t$  is the current through the impedance and  $I_t^*$  is the complex conjugate of the current. From (3.36), the active power is defined by

$$P = \frac{E_{sm}E_g sin(\delta)}{X_T} \tag{3.37}$$

If this linearised around the initial angle,  $\delta = \delta_0$ , (in per unit, with T representing torque) then the relation can be defined.

$$\Delta T = \frac{E_{sm}E_g}{X_t}cos(\delta_0)(\Delta\delta)$$
 (3.38)

The relation between  $\Delta T$  and  $\Delta \delta$  is called the synchronising torque coefficient  $K_s$ . This is derived from the synchronising power, which is equivalent to the theoretical maximum value of the power transferred between the two voltage sources [242]. This is the power a machine can provide or absorb from and to the grid when there are disturbances. A high synchronising power ensure the machine is capable of maintaining synchronism with the grid, ensuring stability.

$$K_s = \frac{E_{sm}E_g}{X_t}cos(\delta_0) \tag{3.39}$$

The per unit linearised representation of the swing equation can be now seen in 3.40, where the electrical power/torque has been replaced with the synchronising torque and rotor angle, and the damping term defined by D

$$\frac{d}{dt}\Delta\omega = \frac{1}{2H}(\Delta T_m - K_s \Delta \delta - D\Delta\omega) \tag{3.40}$$

where rotor angle and grid frequency are related by equation (3.41).

$$\frac{d}{dt}\Delta\delta = \omega_0 \Delta\omega \tag{3.41}$$

In terms of the rotor angle only, and if the Laplace transform is taken, the following representation is obtained

$$s^{2}(\Delta\delta) + \frac{D}{2H}s(\Delta\delta) + \frac{K_{s}}{2H}\omega_{0}(\Delta\delta) = \frac{\omega_{0}}{2H}T_{m}$$
(3.42)

giving the characteristic equation

$$s^2 + \frac{D}{2H}s + \frac{K_s}{2H}\omega_0 = 0 (3.43)$$

which can be related to the general form of

$$s^2 + 2\zeta\omega_n s + \omega_n^2 \tag{3.44}$$

Therefore, an indication of appropriate tuning values can be concluded from comparing (3.43) and (3.44), and the selected damping, D, can be obtained.

$$\omega_N = \sqrt{\frac{\omega_b K_s}{2H}} \tag{3.45}$$

$$D = 2\zeta \sqrt{2H\omega_b K_s} \tag{3.46}$$

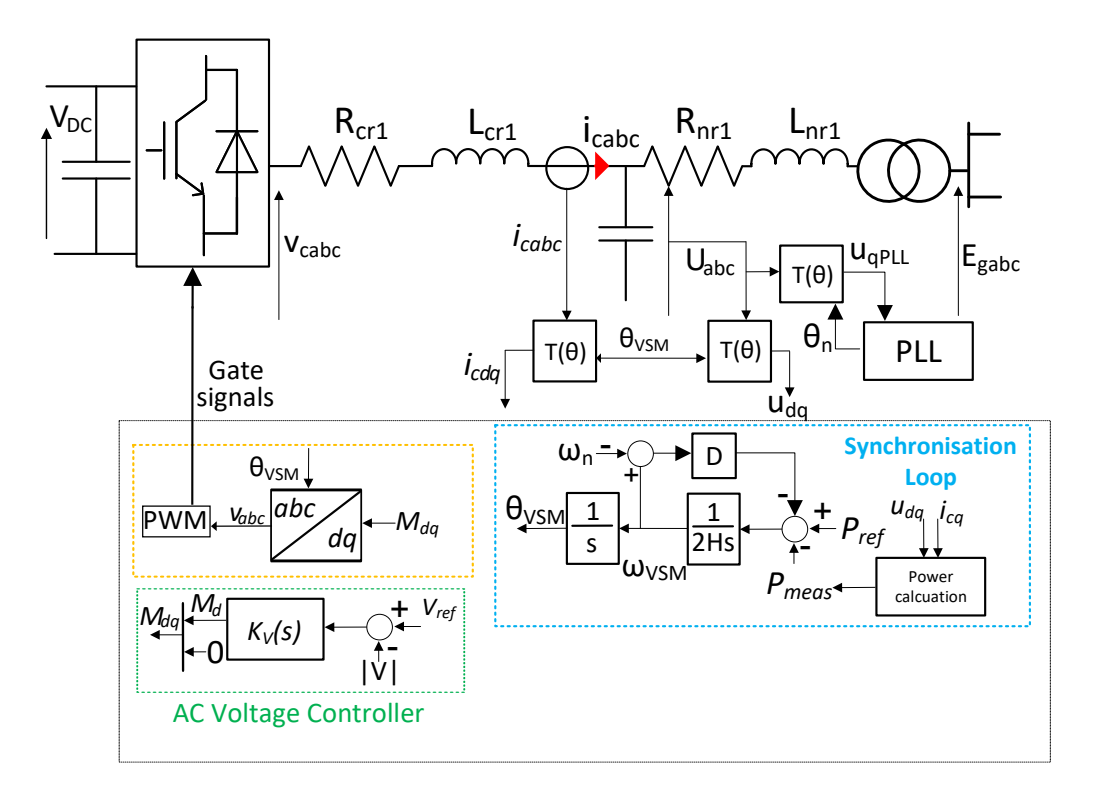


Figure 3.11: Control structure of virtual synchronous machine (VSM) with AC voltage controller and synchronisation loop.

A basic control of the VSM converter is implementation of the swing equation, with the power directly relating to the angle set by the controller creating the power synchronization. The AC voltage is maintained by a PI controller which sets the magnitude of the voltage, which is fed into the averaged model of the converter to return the converter side voltage. The system and control diagram are shown in Figure 3.11, with the direction of current considered from the converter to the grid, modelled in the dq reference frame with the d-axis aligned to the a-axis, and the q-axis leading

90° to it. The grid, PCC, and converter voltages are  $E_g \angle 0$ ,  $U_{PCC} \angle \theta_U$  and  $V_c \angle \theta_V$ . The grid and converter side impedances are  $R_{nr1}$ ,  $L_{nr1}$ , and  $R_{cr1}$ ,  $L_{cr1}$ , respectively. The reference frequency  $\omega_{REF}$  can be set at the system nominal value (50 Hz), or is frequently taken from a PLL to remove initial offset ( $w_g$  in Figure 3.11) [243].

# 3.5 Small Signal Modelling

#### 3.5.1 Model of Converter to Grid System

Classically, power systems have been subject to either small, or large disturbances [244]. Small signal stability describes the ability of the power system to maintain synchronism when subject to a small disturbance [21]. It informs about the power system's inherent dynamic characteristics and stability.

Small signal modelling is used to transform non-linear EMT equations into a linearised form. To obtain the model, the non-linear equations for the full system are represented in the rotating reference frame, presented in state space form [21] and linearised around their operating point.

These equations and final linearised state space form can be expressed with the following representation. The state, input and output variables are  $\Delta x$ ,  $\Delta u$ , and  $\Delta y$ , and A, B, C and D are the state, input, output, and feed-through matrices [21].

$$\frac{d\Delta x}{dt} = A\Delta x + B\Delta u \tag{3.47}$$

$$\Delta y = C\Delta x + D\Delta u \tag{3.48}$$

For all systems in this work, the equations are divided into subsystems, described by the forms in equations (3.47) and (3.48). Considering Figure 3.1, the grid equations in the SSM are shown by equations (3.49) to (3.55).

Chapter 3. Power Converter Modelling and Control

$$A_{grid} = \begin{bmatrix} \frac{-R_{cr1}}{L_{cr1}} & \omega & \frac{-1}{L_{cr1}} & 0 & 0 & 0\\ -\omega & \frac{-R_{cr1}}{L_{cr1}} & 0 & \frac{-1}{L_{cr1}} & 0 & 0\\ \frac{1}{C_f} & 0 & 0 & \omega & \frac{-1}{C_f} & 0\\ 0 & \frac{1}{C_f} & -\omega & 0 & 0 & \frac{-1}{C_f}\\ 0 & 0 & \frac{1}{L_{nr1}} & 0 & \frac{-R_{cr1}}{L_{cr1}} & \omega\\ 0 & 0 & 0 & \frac{1}{L_{nr1}} & -\omega & \frac{-R_{cr1}}{L_{cr1}} \end{bmatrix}$$
(3.49)

$$B_{grid} = \begin{vmatrix} \frac{1}{L_{cr1}} & 0 & 0 & 0\\ 0 & \frac{1}{L_{cr1}} & 0 & 0\\ 0 & 0 & \frac{-1}{L_{nr1}} & 0\\ 0 & 0 & 0 & \frac{-1}{L_{nr1}} \end{vmatrix}$$

$$(3.50)$$

$$D_{arid} = zero(4x4) \tag{3.52}$$

where the state, input, and output variables are defined by  $x_g$ ,  $u_g$  and  $y_g$ . The converter and grid voltages are  $V_c$  and  $E_g$  respectively, and the converter and grid currents,  $i_c$  and  $i_n$ . As described in Section 3.2, there is a global reference frame and converter reference frame. The grid system is modelled in the global frame, indicated by  $x_g$ , and converter frame by  $d_g$ . Therefore, the grid side current is indicated by  $i_{nx}$ ,  $i_{ny}$ , grid side voltage by  $E_{gx}$ ,  $E_{gy}$ , and converter side currents and voltage by  $i_{cx}$ ,  $i_{cy}$ , and  $V_{cx}$  and  $V_{cy}$ .

$$\Delta x_q = [\Delta i_{cx}, \Delta i_{cy}, \Delta U_{cx}, \Delta U_{cy}, \Delta i_{nx}, \Delta i_{ny},]$$
(3.53)

$$\Delta u_q = [\Delta V_{cx}, \Delta V_{cy}, \Delta E_{qx}, \Delta E_{qy}] \tag{3.54}$$

$$\Delta y_q = [\Delta i_{cx}, \Delta i_{cy}, \Delta U_{cx}, \Delta U_{cy}] \tag{3.55}$$

From this sub-system, the voltage at the PCC can be obtained, as well as PCC currents. These output components are in the global grid frame (here on represented by xy frame), but then are passed through the linearised reference frame to transform from the variables from grid frame to the converter frame. Additionally from these dq voltages and currents, the three phase active power is calculated based on the dq instantaneous power theory [245]. The Park transform has been described earlier in this chapter, with a three-phase variable being transformed to two orthogonal signals,  $Y_{dq} = Y_d + jY_q$ .

$$S = P + jQ = 3V^{dq}I^{dq*} = 3(\frac{U_d + jU_q}{\sqrt{2}})(\frac{i_{cd} - ji_{cq}}{\sqrt{2}})$$
(3.56)

$$P = \frac{3}{2}(U_d i_{cd} + U_q i_{cq}) \tag{3.57}$$

Linearising around the operating point gives a relation between input voltage and currents to compute the small signal measured active power,  $\Delta P_{meas}$ .

$$\Delta P_{meas} = \Delta U_d i_{cd0} + \Delta i_{cd} U_{d0} + \Delta U_g i_{cg0} + \Delta i_{cg} U_{d0}$$
(3.58)

Additionally, the calculation of measured voltage at the PCC can be calculated by (3.59) and linearised to (3.60).

$$U_{meas} = \sqrt{U_d^2 + U_q^2} (3.59)$$

$$\Delta U_{meas} = \Delta U_d \frac{U_{d0}}{\sqrt{U_{d0}^2 + U_{q0}^2}} + \Delta U_q \frac{U_{q0}}{\sqrt{U_{q0}^2 + U_{d0}^2}}$$
(3.60)

# 3.5.2 Linearised Small Signal Synchronous Reference Frame Phase Locked Loop

The relation between grid voltage and the converter synchronisation relies on the angle estimated at the PCC, as described in Section 3.2. The method of grid synchronisation differs between converters operating in GFL and GFM control, for the former, the PLL is used. The converter aims to synchronise to the PCC voltage, ideally minimising the error between the estimated PLL angle and the real value, to zero. Therefore, rotating

the converter dq frame at the same frequency and angle as the input voltage state space vector. For the further small signal modelling sections, the full system needs to be modelled in the dq component equations and then linearised. However, to do this, a global reference frame needs to be defined and the relation to the converter reference frame.

The relation between voltage vector and the PLL estimate angle was displayed in Figure 3.5. If a global reference frame is introduced, the new relations can be shown in Figure 3.12, with this global frame defined by  $dq_g$  and rotating at  $\omega_g$  rad/s. The converter frame is defined by  $dq_c$ , rotating at  $\omega_{PLL}$ .  $\mathbf{U_{PLL}^s}$  is the measured PCC voltage in the stationary frame,  $\mathbf{U_{PLL}}$  is in the global frame, and  $\hat{\mathbf{U}_{PLL}}$  in the local converter frame. The angles in Figure 3.12 are the actual PCC angle,  $\theta_{PLL}$ , the estimated angle from the PLL,  $\hat{\theta}_{PLL}$ , the global reference frame angle,  $\theta_g$ , and the difference between the converter synchronous reference frame and the global reference frame,  $\tilde{\theta}$ .

$$\tilde{\theta} = \hat{\theta}_{PLL} - \theta_q \tag{3.61}$$

Considering the defined angles and reference frames, the following relations in (3.62) and (3.63) apply [214].

$$\mathbf{U_{PLL}} = e^{-j\theta_g} \mathbf{U_{PLL}^s} \tag{3.62}$$

$$\hat{\mathbf{U}}_{\mathbf{PLL}} = e^{-j\hat{\theta}_{PLL}} \mathbf{U}_{\mathbf{PLL}}^{\mathbf{s}} \tag{3.63}$$

The stationary reference frame can be removed and the equations related in only the global grid frame and the converter frame where  $\tilde{\theta} = \hat{\theta}_{PLL} - \theta_g$ .

$$\hat{\mathbf{U}}_{\mathbf{PLL}} = e^{-j\hat{\theta}_{PLL}} \mathbf{U}_{\mathbf{PLL}}^{\mathbf{s}} = e^{-j\hat{\theta}_{PLL}} e^{\theta_g} \mathbf{U}_{\mathbf{PLL}} = e^{-j\tilde{\theta}} \mathbf{U}_{\mathbf{PLL}}$$
(3.64)

Following this relation, if  $\Delta \tilde{\theta}$  is the error between the two reference frames, then the relation,  $\hat{\mathbf{U}}_{\mathbf{PLL}} = e^{-j\tilde{\theta}}\mathbf{U}_{\mathbf{PLL}}$ , established by (3.64), can be linearised as in equation (3.65).

$$\Delta \hat{\mathbf{U}}_{\mathbf{PLL}} = -je^{-j\tilde{\theta}_0} \mathbf{U}_{\mathbf{PLL}_0} \Delta \tilde{\theta} + e^{-j\tilde{\theta}_0} \Delta \mathbf{U}_{\mathbf{PLL}}$$
(3.65)

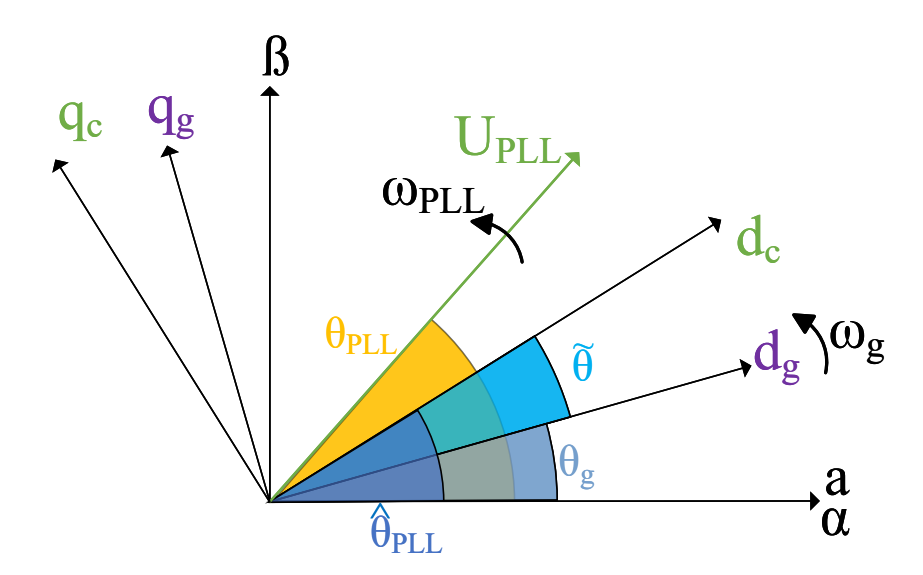


Figure 3.12: PCC voltage vector, grid global synchronous rotating reference frame, and converter synchronous frame.

Referring back to the control diagram in Figure 3.4, the relation between input voltage and PLL angle estimation is considered again in (3.66).

$$\hat{\theta}_{PLL} = \int \left( \omega_n + K_P * \hat{U}_{PCCq} + K_i \int (\hat{U}_{PCCq}) \right) dt$$
 (3.66)

The equation is in terms of the PLL estimate, therefore, if (3.65) is substituted in, the transfer function between input angle and global reference frame voltage can be produced. Considering  $\frac{d}{dt}(\hat{\theta}_{PLL}) = \frac{d}{dt}(\tilde{\theta}) + \frac{d}{dt}(\theta_g)$ , and assuming the  $\omega_n$  is equivalent to the global rotational speed,  $\frac{d}{dt}(\theta_g) = \omega_g$  the voltage and angle can be represented in the global reference frame. By collecting real and imaginary components, the q components, the transfer function of input  $\Delta U_{PLLq}$  to  $\Delta \tilde{\theta}$  is produced by (3.67),

$$\frac{\Delta \tilde{\theta}}{\Delta U_q} = \frac{Kp_{PLL}s + Ki_{PLL}}{s^2 + a_0s + b_0} \tag{3.67}$$

where  $a_0$  and  $b_0$  are comprised of the proportional and integral gains of the PLL (shown in (3.16)) and are defined in (3.68). The full expansion of the substitution in shown in

the Appendix A.

$$a_0 = Kp_{PLL}cos(\theta_0)U_{d0} + Kp_{PLL}sin(\theta_0)U_{q0}$$
(3.68)

$$b_0 = Ki_{PLL}cos(\theta_0)U_{d0} + Ki_{PLL}sin(\theta_0)U_{d0}$$
(3.69)

#### 3.5.3 Linearised Reference Frame Transforms

As the previous subsection described, the system equations are in the global reference frame, or the converter reference frame. Therefore, the frame changes need to be linearised, resulting in the transforms of (3.70) and (3.71), where  $\theta$  is the angle between the two frames, and subscript  $_0$  indicates linearisation point.

$$\Delta Y_f^c = \begin{bmatrix} \cos(\theta_0) & \sin(\theta_0) & -Y_{x0}\sin(\theta_0) + Y_{y0}\cos(\theta_0) \\ -\sin(\theta_0) & \cos(\theta_0) & (-Y_{x0}\cos(\theta_0) - Y_{y0}\sin(\theta_0) \end{bmatrix} \Delta Y_f$$
(3.70)

$$\Delta Y_f = \begin{bmatrix} \cos(\theta_0) & -\sin(\theta_0) & (-Y_{d0}^c \sin(\theta_0) - Y_{q0}^c \cos(\theta_0)) \\ \sin(\theta_0) & \cos(\theta_0) & (Y_{d0}^c \cos(\theta_0) - Y_{q0}^c \sin(\theta_0)) \end{bmatrix} \Delta Y_f^c$$
(3.71)

#### 3.5.4 Linearised Current Controller

Passing the grid and converter voltages through the frame transforms, the linearised current controller can be presented. Again, the converter frame representation is signified by  $Y_{dq}^c$ .

$$A_{cc} = 0 (3.72)$$

$$B_{cc} = \begin{bmatrix} 1 & 0 & -1 & 0 & 0 & 0 \\ 0 & 1 & 0 & -1 & 0 & 0 \end{bmatrix}$$
 (3.73)

$$C_{cc} = \begin{bmatrix} K_{iCC} & 0\\ 0 & K_{iCC} \end{bmatrix} \tag{3.74}$$

$$D_{cc} = \begin{bmatrix} K_{pCC} & 0 & -K_{pCC} & -\omega L_c & 1 & 0 \\ 0 & K_{PCC} & \omega L_c & -K_{pCC} & 0 & 1 \end{bmatrix}$$
(3.75)

Where the state, input and output variables are defined by  $\Delta x_{cc}$ ,  $\Delta u_{cc}$  and  $\Delta y_{cc}$ 

$$\Delta x_{cc} = [\Delta e i_d^c, \Delta e i_g^c] \tag{3.76}$$

$$\Delta u_{cc} = [\Delta i_{cd}^*, \Delta i_{cg}^*, \Delta i_{cd}^c, \Delta i_{cg}^c, \Delta u_{d}^c, u_{g}^c]$$
(3.77)

$$\Delta y_{cc} = [\Delta v_d^c, \Delta v_q^c] \tag{3.78}$$

The proportional and integral gains of the current loop PI controllers are  $K_{pCC}$  and  $K_{iCC}$  respectively, and  $\Delta e i_d^c$  and  $\Delta e i_q^c$  are the errors between reference current and measured current for the d and q components respectively.

The outer loop power and voltage controllers are shown in Fig. 3.8, with the PI controllers defined by  $K_P(s)$  and  $K_U(s)$  for the power and voltage controller respectively. Outer power and voltage loop state matrices are defined by state variables, input variables, and output variables ( $\Delta x_{out}$ ,  $\Delta u_{out}$ ,  $\Delta y_{out}$ ) in (3.79) to (3.81).  $\Delta e_P$  and  $\Delta e_U$  are the error between reference and measured power and PCC voltage.

$$\Delta x_{out} = [\Delta e_P, \Delta e_U] \tag{3.79}$$

$$\Delta u_{out} = [\Delta P^{ref}, \Delta P_{meas}, \Delta U^{ref}, \Delta U_{meas}]$$
 (3.80)

$$\Delta y_{out} = [\Delta i_d^{ref}, \Delta i_q^{ref}] \tag{3.81}$$

with the state matrices defined by  $A_{out}$ ,  $B_{out}$ ,  $C_{out}$  and  $D_{out}$  which contain power loop proportional and integral gains,  $K_{pPC}$  and  $K_{iPC}$ , and the voltage loop proportional and integral gains,  $K_{pUC}$  and  $K_{iUC}$ .

$$A_{out} = 0 (3.82)$$

$$B_{out} = \begin{bmatrix} 1 & 0 & -1 & 0 \\ 0 & 1 & 0 & -1 \end{bmatrix} \tag{3.83}$$

$$C_{out} = \begin{bmatrix} K_{iPC} & 0\\ 0 & K_{iUC} \end{bmatrix}$$
 (3.84)

$$D_{out} = \begin{bmatrix} K_{pPC} & 0 & -K_{pPC} & 0\\ 0 & K_{pUC} & 0 & -K_{pUC} \end{bmatrix}$$
 (3.85)

#### 3.5.5 Linearised Grid Forming Control

The linearised angle is obtained from the output of the power synchronisation loop in GFM control. In the VSM structure used in this work, the small signal representation is detailed with the following state matrices, state and input variables. Referring back to equations (3.40) (3.41), the synchronisation loop is shown in the state space form. The matrices are shown by  $A_{swing}$ ,  $B_{swing}$ ,  $C_{swing}$  and  $D_{swing}$ , with state, input and output variables defined by  $x_{swing} = [\Delta \omega, \Delta \theta]^T$ ,  $u_{swing} = [\Delta P_m, \Delta P_{meas}]^T$ ,  $y_{swing} = [\Delta \omega, \Delta \theta]^T$ .

$$A_{swing} = \begin{bmatrix} \frac{-K_d}{2H} & 0\\ \omega_0 & 0 \end{bmatrix} \tag{3.86}$$

$$B_{swing} \begin{bmatrix} \frac{1}{2HSbase} & \frac{1}{2HSbase} \\ 0 & 0 \end{bmatrix}$$
 (3.87)

$$C_{swing} = \begin{bmatrix} \omega_0 & 0\\ 0 & 1 \end{bmatrix} \tag{3.88}$$

$$D_{swing} = zero(2x2) (3.89)$$

The voltage applied to the converter is controlled by applying a PI controller to the difference of the reference voltage and measured voltage magnitude. The output of the controller is applied directly to the d component of the modulation index, which is in turn, transformed to the grid frame with the output voltage angle, and return as an input to the grid system.

# Chapter 4

# Stability Limits and Tuning Recommendation of the Standard Current Control Providing Inertia Support

#### 4.1 Motivation

The drastic increase in renewable energy sources in power grids has raised stability concerns. A particular concern exists in the ability of the converters to preserve frequency stability, due to their inherent lack of inertia provision. Grid forming converters have been presented as a solution to this issue, however there have been multiple suggestions of improvements to GFL control and that the emulated inertia can be comparable to GFM capabilities [13]. The standard current controller with a PLL can be modified to provide inertia by including an additional control loop that injects active power in the case of a frequency event. This Chapter presents a detailed stability study, using a small signal model, and a set of controller tuning recommendations for the standard current controller with inertia emulation capability. The investigation found that the standard current loop time constant tuning causes instability in the

Chapter 4. Stability Limits and Tuning Recommendation of the Standard Current Control Providing Inertia Support

control structure with the inertia emulation loop. Reducing this time constant can allow for stable inertia emulation with classical vector current control.

## 4.2 Introduction

The standard current controller used in the major part of grid-connected applications is a grid following converter [246], [247] [248], which relies on a strong grid to operate. Grid following converters use a phase locked loop (PLL) to measure the grid electrical angle from the point of common coupling (PCC) and cannot provide inertia in its basic implementation.

One solution presented to provide inertia using power converters, are grid forming Virtual Synchronous Machines (VSMs), a particular type of grid forming converter. They provide inertia by emulating the behaviour of conventional synchronous machines during a frequency disturbance [249].

However, the VSM control structure, with the grid forming capabilities it provides, is significantly different to the traditional current controller, which is currently widespread and utilized by most manufacturers [240]. Another solution is to add an additional loop to the standard current control to provide inertia emulation without modifying the present control structure [9]. The benefit of using this model would be that the control structure would not need to be changed much and existing installed control mechanisms can be used. Furthermore, the conventional current controller has a faster transient response than that of a typical grid forming converter (e.g. a VSM) which is a greatly desirable feature [250], [251], [237]. Additionally, the difference between inertial support in grid following and forming converters has been up for debate in much of the literature. In [13], grid following and grid forming converters are compared for their inertial response with varying grid voltage in acceptable ranges (0.9 pu to 1.1 pu), active power set points 0.1 pu to 0.9 pu, and grid SCR from 1.5 to 5, i.e., a weak to strong range. Additionally, sweeps are performed for control settings that would not "explicitly impact the magnitude of the inertia response", but do affect the stability and dynamics of the system. The paper concludes that across several system

conditions, the grid following controller maintains the grid frequency as well as the grid forming. Therefore, the additional inertia emulation in GFL control, can act as this "true" inertial response typically attributed to GFM control [252]. Therefore, the benefit of adding inertial response in grid following control needs to be assessed and stability tuning recommendations given. This Chapter investigates the limitations and optimal tuning for a current controller with inertia emulation, including the PLL and current loop, for different grid strengths.

# 4.3 System Under Study

The system investigated is a 3 MW, 690 V grid connected two-level VSC converter, connecting a source such as a wind turbine (such as the doubly fed induction generator (DFIG)) or an energy storage system (Figure 4.1). The converter is connected to the grid through an RL filter and a shunt capacitor  $C_f$ . In this study a constant DC link has been assumed. The grid is modelled as the Thevenin equivalent [204] and will be studied for varying SCR values; 2-5. The system is modelled in the dq frame, with the equations described in Chapter 3.

As described in Chapter 3, the inner current controller consists of two PI controllers, two decoupling terms and a voltage feed-forward. The PI controller for the current loop,  $K_{CC}(s)$ , is tuned initially with the modulus optimum tuning technique [222], [224].

$$K_{cc}(s) = \frac{Kp_{cc}s + Ki_{cc}}{s} \tag{4.1}$$

$$Kp_{cc} = \frac{L_{cr1}}{\tau_{\alpha}} \tag{4.2}$$

$$Ki_{cc} = \frac{R_c}{\tau_{\alpha}} \tag{4.3}$$

where  $\tau_{\alpha}$  is the current loop time constant, recommended to be 5 to 10 times slower than the switching frequency [204], which is in the range 1-2 kHz [253], up to 10 kHz [254]. Therefore, for the standard current controller, the optimal time constant has been considered to be 1-5 ms.

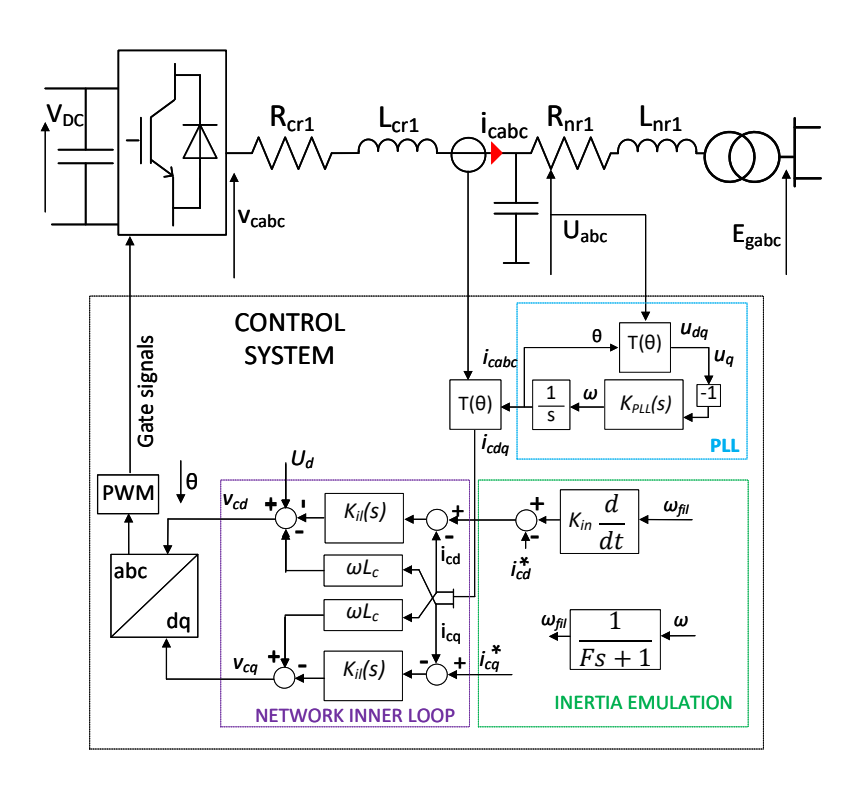


Figure 4.1: Current Controller With Inertia Emulation.

The derivation of PLL control structure has been explained in Chapter 3. The gain  $K_{PLL}(s)$  is defined as

$$K_{PLL}(s) = \frac{Kp_{PLL}s + Ki_{PLL}}{s} \tag{4.4}$$

$$Kp_{PLL} = \frac{2\omega_n \zeta}{E_m} \tag{4.5}$$

$$Ki_{PLL} = \frac{Kp_{PLL}}{\tau_{PLL}} \tag{4.6}$$

where  $E_m$  is the admitted voltage,  $\zeta$  is the damping ratio, and  $\tau_{PLL}$  is the PLL bandwidth. This was described, again in Chapter 3, but it should be noted again, that the variable  $\omega_n$  in the natural bandwidth of the PLL filter, not the frequency of the grid system. The initial  $\tau_{PLL}$  has traditionally been tuned using [210]:

$$\tau_{PLL} = \frac{2\zeta}{\omega_n} \tag{4.7}$$

which is used in turn, to tune the proportional and integral PLL gains. Initially, the current loop was tuned with a current loop time constant of 2 ms, and the PLL time constant to 4.5 ms.

#### 4.4 Inertia Emulation

Inertia is emulated by the the control loop in (4.8) the output of which is added to the reference  $i_d^*$  current to form the total reference current [9]. A gain,  $K_{in}$  amplifies the rate of change of frequency and adds it to the current reference  $i_d^*$ . The frequency of the grid is provided by the PLL, which is then passed through a derivative term and then a low pass filter to improve the system stability. The inertia controller can therefore be defined as

$$i_{dfreq} = s \frac{K_{in}}{Fs + 1} \Delta \omega \tag{4.8}$$

where F is the first order filter time constant. The inertia gain  $K_{in}$  also determines the required power to be delivered to the grid during a frequency disturbance [241]. The gain of the inertia controller can be obtained from the synchronous generator swing equation and therefore maximum power delivery required for a particular rate of change of frequency (ROCOF) [255], which can be simplified to

$$P_{emulationmax} = \frac{2HS_{base}}{\omega_s} \omega_{max}$$
 (4.9)

where  $S_{base}$  is the rated power of the turbine, H is the inertia constant emulated (seconds),  $\omega_s$  is the synchronous frequency and  $\omega_{max}$  is the maximum allowable ROCOF (Hz/s).

The required inertia emulation power should be divided by the nominal voltage and ROCOF to obtain the gain  $K_{in}$ . The inertial branch gain is therefore derived in (4.10).  $V_{nom}$  is the line-to-line RMS voltage.

$$K_{in} = \frac{P_{emulationmax}}{V_{nom}\omega_{max}} = \frac{2HS_{base}}{\omega_s V_{nom}\sqrt{\frac{3}{2}}}$$
(4.10)

A typical required inertia constant, H, for a 3 MW system ranges from approximately 1-5 s [256], [257].

# 4.5 Small Signal Model

The full system modelled has been described in section 4.3 and is represented in Figure 4.1. The small signal model for the converter to grid voltages, is the same as that described in Chapter 3, by equations (3.49) to (3.55). The linearised PLL, reference frame changes, and inner current loops are expressed in equations (3.70) to (3.78).

The inertia response of this small-signal system was implemented by the transfer function previously shown in equation (4.8). A no-linear EMT time domain model was designed and simulated to validate the results of the small-signal model, with SCR values ranging from 2 to 5. The time domain and SSM response to a power step is shown in Figure 4.2. As it can be seen, both models overlay, validating the SSM.

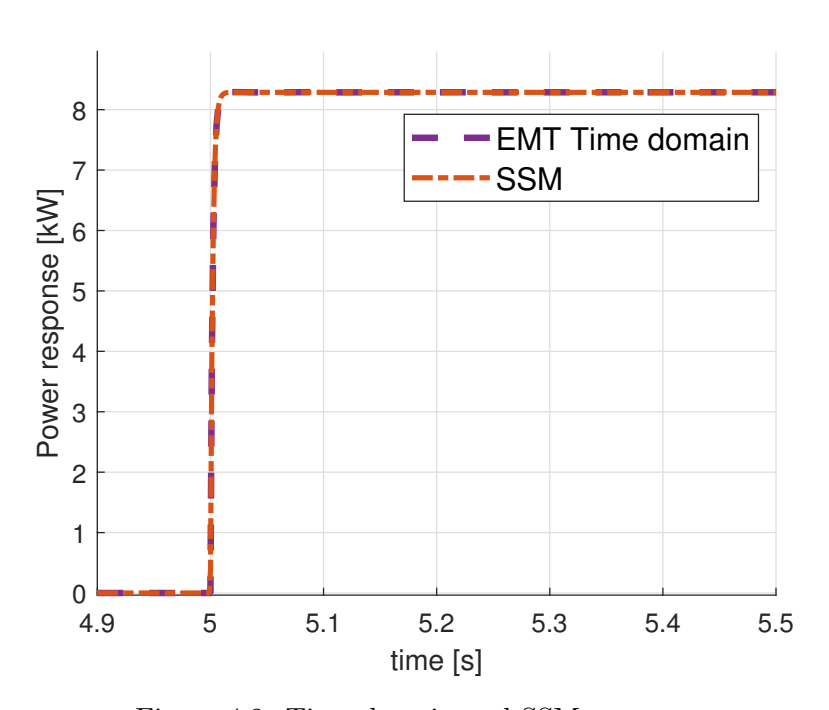


Figure 4.2: Time domain and SSM response

# 4.6 Investigation

The small-signal model is used to perform a parametric sweep for increasing values of  $K_{in}$  and F in order to identify the impact of each parameter on stability. This produces the stability limits of the system under varying conditions and isolated the optimum PLL and current loop tunings. The small signal instability is determined by the eigenvalues of the system. In Chapter 3, small signal representation and stability has been described. The eigenvalues of the A matrix of the state space representation, are assessed, and for a complex pair of poles, if they move into the right hand plane, then the system is unstable. The specific investigations carried out are as follows:

- Determining the maximum  $K_{in}$  gain whilst maintaining stability with increasing F filter value for changing SCR.
- Investigate the effect of changing PLL time constant,  $\tau_{PLL}$ , on stability.
- Assess the impact of the current controller time constant,  $\tau_{\alpha}$ , and its effect on system when delivering inertial power.

#### 4.7 Results

# 4.7.1 Impact of $K_{in}$ and F with Varying SCR

The first investigation was to observe the maximum value of  $K_{in}$  and F which had a stable condition when standard PLL and current control tuning were considered for different SCR values from 2 to 5. The initial tuning of the converter has been obtained from well-established tuning rules resulting in a current loop time constant,  $\tau_{\alpha}$  of 2 ms, and a PLL time constant,  $\tau_{PLL}$ , of 0.0045 s [210].

Figure 4.3 shows the stability limit for different SCR and F values, a linear relationship between the maximum value of  $K_{in}$  and F is observed. Also, it can be seen that as the SCR is decreased, the maximum inertial gain for a stable system at a given filter constant reduces.

The line of stability continues as both  $K_{in}$  and F increase, however, there reaches a

Chapter 4. Stability Limits and Tuning Recommendation of the Standard Current Control Providing Inertia Support

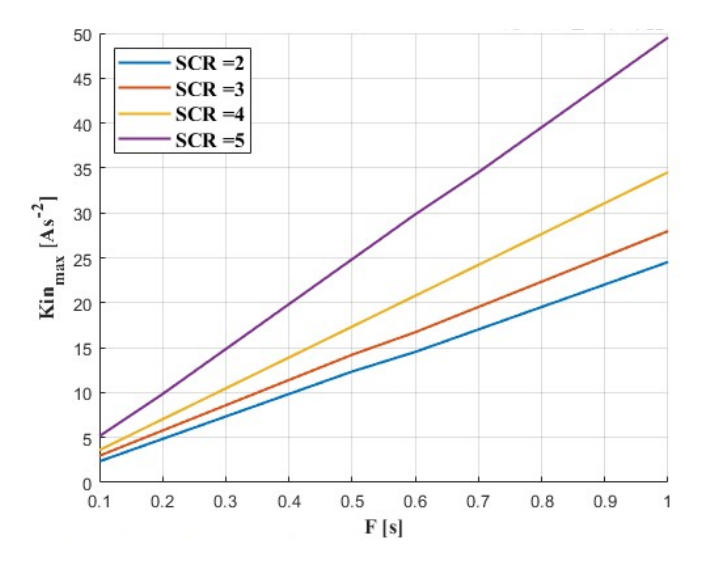


Figure 4.3:  $Kin_{max}$  against F Stability limit for varying SCR,  $\tau_{PLL} = 0.0045$  s,  $\tau_{\alpha} = 0.002$  s

point where the filter value is too great and degrades the dynamic response of the power injection during a frequency disturbance.

The limiting effect of the filter constant can be observed in Figure 4.4, which shows that for a constant value of  $K_{in}$  (12  $As^{-2}$ ), F significantly affects the performance. An F of 0.3 s produces an acceptable dynamic performance, however, when F is increased to 0.9 s, the dynamic performance is much slower. Equation (4.9) is used to calculate the power required to be transferred by the converter. If a value of 24 kW is required, Figure 4.4 shows that this is not achieved by the system with F = 0.9 s. Therefore, it is recommended that the filter is tuned to be fast enough for an appropriate dynamic response but slow enough to filter out standard frequency deviations that the system is not required to respond to.

#### 4.7.2 Kin against $\tau_{PLL}$

The effect of increasing  $\tau_{PLL}$  on the stability of the system was studied for varying F values. Figure 4.5 shows the maximum  $K_{in}$  that can be employed as  $\tau_{PLL}$  is increased, with  $\tau_{\alpha}$  kept constant at 2 ms. For all values of F, the maximum  $K_{in}$  gain that can be achieved, increased with increasing  $\tau_{PLL}$  and then plateaus off. The plateau begins at 0.04 s for F = 0.1 s,  $\tau_{PLL} = 0.15$  s for F = 0.5 s.

Chapter 4. Stability Limits and Tuning Recommendation of the Standard Current Control Providing Inertia Support

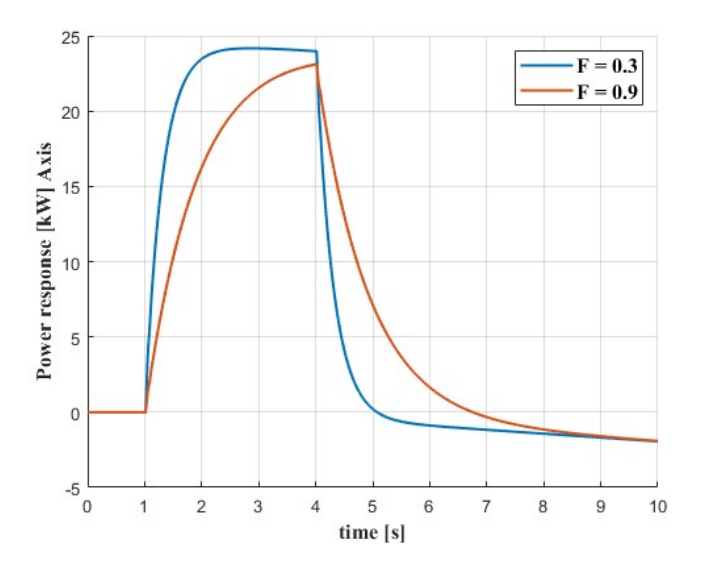


Figure 4.4: Power [kW] Response to 1 pu ramp increase in frequency:  $K_{in} = 12$ , F = 0.3 s, F = 0.9 s.

As expected, increasing the filter time constant increased the maximum  $K_{in}$  gain that could be achieved for a stable system. As the PLL time constant is increased, the stability limit increases at first, but then reaches a plateau. Based on the location of this plateau, a new  $\tau_{PLL}$  constant of 0.04 s was selected, 10 times slower than the previously defined optimal tuning. Figure 4.5 demonstrate that increasing the time constant past this value would have no further impact on stability. It was therefore concluded that the optimal PLL time constant to be selected for this system was 0.04 s.

#### 4.7.3 Kin against $\tau \alpha$ , Current Controller Time Constant

The maximum value of  $K_{in}$  that can be achieved as the current controller time constant is varied was simulated at multiple values of F. Note that (4.2) and (4.3) are considered to give optimal tunings for vector current control, typically with a current control time constant in the range  $\tau \alpha = 2$ -5 ms. Equation (4.7) is considered the optimal PLL bandwidth.

Figure 4.6a shows the effect on the maximum value of  $K_{in}$ , that can be enabled whilst maintaining system stability, with increasing  $\tau_{\alpha}$ , with  $\tau_{PLL}$  fixed at the assumed

Chapter 4. Stability Limits and Tuning Recommendation of the Standard Current Control Providing Inertia Support

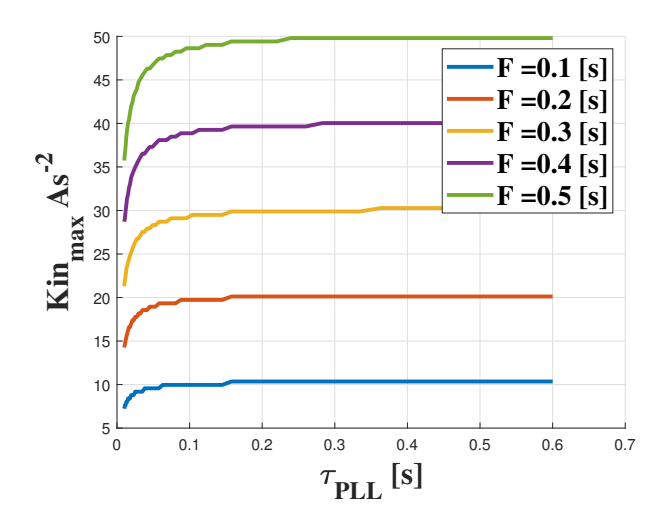


Figure 4.5: Maximum value of  $K_{in}$  that can be provided whilst maintaining stability with increasing  $\tau_{PLL}$  at SCR = 5.

optimum value of 0.0045 s, and in a grid with SCR = 5. Figure 4.6b shows the same system simulation but with  $\tau_{PLL}$  fixed at the new optimum value, found in the previous section, i.e.  $\tau_{PLL} = 0.04$  s. A significant increase in the maximum  $K_{in}$  that maintains stability can be seen with the new value of  $\tau_{PLL}$ . Figure 4.6 also shows that, for a set value of  $K_{in}$ , the controller is most stable with either a very fast  $\tau_{\alpha}$ , or a slow value. There is a dip in stability at 1.5 ms – 10 ms, above which the system stability begins to rise again allowing for increased  $K_{in}$ . The stability recovers with a  $\tau_{\alpha}$  of 0.1 s or greater for SCR 5, shown in Figure 4.7, especially with F > 0.1. However, with SCR 5 and F of 0.1 s, the system requires a much larger time constant for stability with an increased  $K_{in}$ . The system can achieve high inertial gains for current loop time constants less than 1 ms, but then begins to deteriorate, dipping to a minimum at around 2 ms. The system then recovers, and the gain begins to increase again, but the time constant,  $\tau_{\alpha}$ , has to be to about 0.1 s to achieve a high  $K_{in}$ .

The analysis was repeated at SCR = 4, 3 and 2, as shown in Figure 4.8. As the SCR decreases, the dip in stability begins at a slightly lower  $\tau_{\alpha}$ . Furthermore, for the same F, reducing the SCR reduces the maximum  $K_{in}$  at the given  $\tau_{\alpha}$ .

This analysis shows that the standard choice of a current loop time constant in the

Chapter 4. Stability Limits and Tuning Recommendation of the Standard Current Control Providing Inertia Support

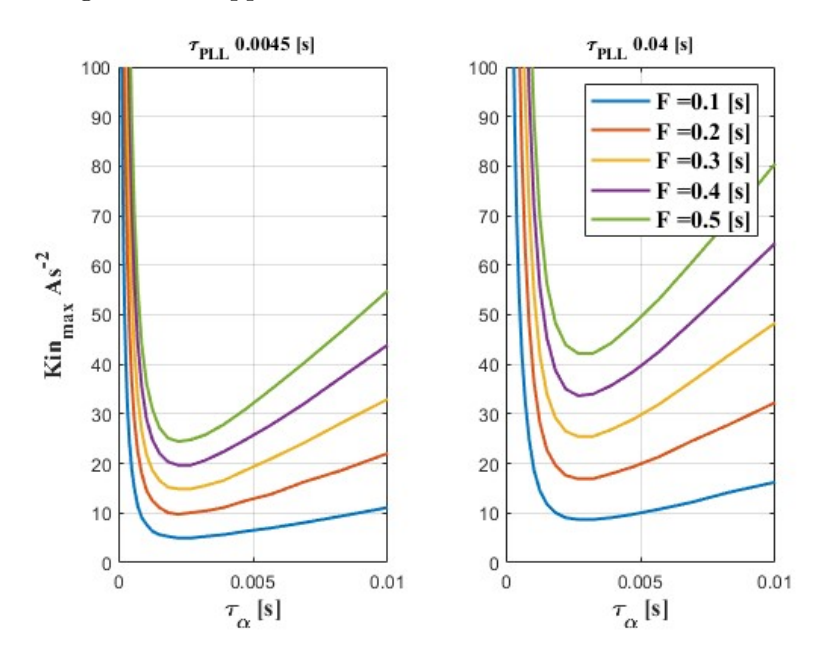


Figure 4.6: Maximum value of  $K_{in}$  that can be allowed whilst maintaining stability, with increasing  $\tau_{\alpha}$  at SCR = 5 with a)  $\tau_{PLL} = 2e/wn = 0.0045$  s b)  $\tau_{PLL} = 0.04$  s

range 1-5ms gives the lowest possible maximum inertial gain. Therefore, a much faster or much lower time constant is recommended, which is discussed in the following section.

# 4.8 Recommendations and Limitations

#### 4.8.1 Inertia Emulation Capability in Fast Operation

From this investigation, it was determined that for the set system parameters, the ideal system tuning can be determined from running parametric sweeps of  $K_{in}$  against  $\tau_{PLL}$  and against  $\tau_{\alpha}$ . A PLL time constant of 0.04s was recommended. However, from the figures shown, it would appear that the optimal regions for current controller time constant would be 0.1 ms, or a value of 0.1 s or more. This would allow the  $K_{in}$  gain to be increased to achieve the required power transfer required to emulate inertia. However, this needs to be considered with converter switching limitations, which is covered in the next sub-section. Figure 4.9 shows the response of the system with  $\tau_{\alpha}$  = 0.1 ms, 10 ms, and 100 ms. The 0.1 ms and 100 ms systems allow high inertial gains, but with  $\tau_{\alpha}$  = 10 ms the system cannot reach gains higher than 100  $A_s^{-2}$ . The

Chapter 4. Stability Limits and Tuning Recommendation of the Standard Current Control Providing Inertia Support

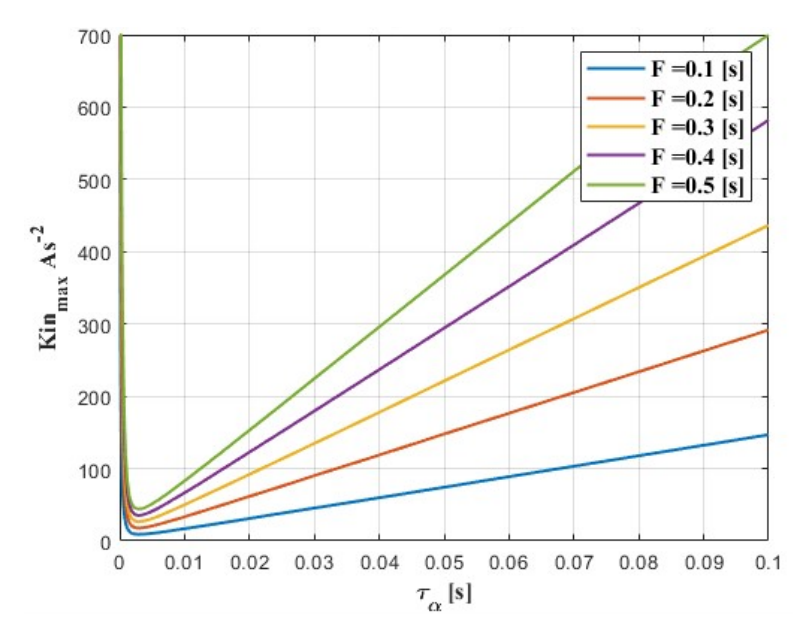


Figure 4.7: Maximum  $K_{in}$  with large range in  $\tau_{\alpha}$ , SCR = 5,  $\tau_{PLL} = 0.04$ ,

implication of this means the maximum inertial power is reduced. The SCR 5 provides the highest possible inertial gain, but any SCR lower than this has a significant drop in maximum possible  $K_{in}$ .

Figure 4.10 shows the dynamic response of the system with a Kin of approximately 586  $A_s^{-2}$  and a filter constant of 0.5 s. The required power to be delivered was calculated from requiring an inertia constant of 4 s, a ROCOF of 2.5 Hz/s, and the system base power 3 MW. Using (4.9), the power calculated was 1200 kW, corresponding to an inertial gain of 568  $A_s^{-2}$ . Using the new optimum tunings developed in this section, it can be seen that the system responds effectively and is capable of delivering the power required by the frequency disturbance with a suitable inertia constant, H, with appropriate dynamic performance.

## 4.8.2 Standard Current Controller Operation Region

Current controller time constants are limited by the switching time of the converter; they should be 5 to 10 times slower than the converter switching frequency. The average switching frequency for a 3 MW wind turbine to grid converter connection is about 1-2 kHz, up to about 10 kHz [254].

Chapter 4. Stability Limits and Tuning Recommendation of the Standard Current Control Providing Inertia Support

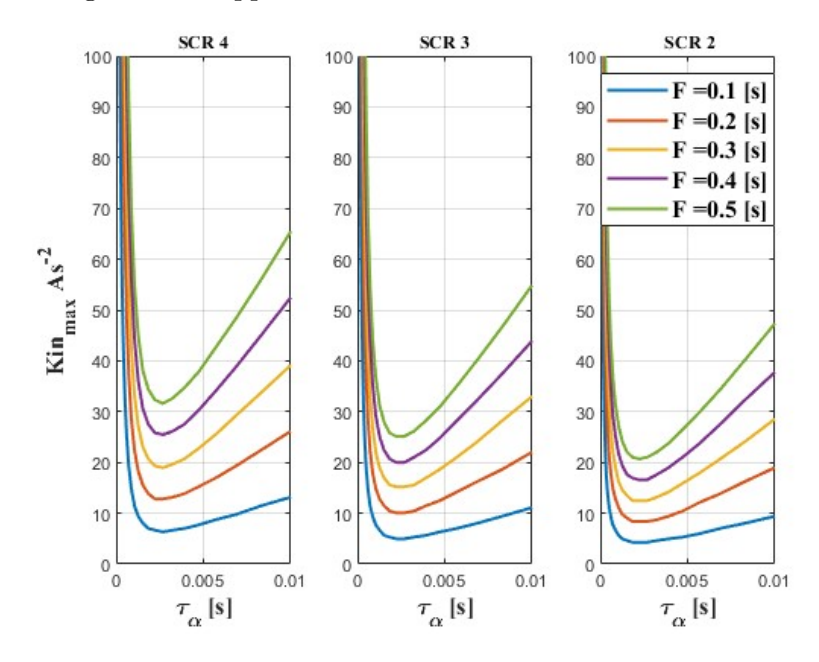


Figure 4.8: Maximum  $K_{in}$  allowed whilst maintaining system stability with increasing  $\tau_{\alpha}$ ,  $\tau_{PLL}$  for a) SCR = 4, b) SCR = 3, c) SCR = 2.

Therefore, to comply with switching limitations, the fastest response of the current controller should be about 1 ms. This is 10 times slower than the value of 0.1 ms (or faster) that was recommended from this study to ensure stability. The standard current controller value is around 2-5 ms, which the graphs in Figure 4.6 to Figure 4.8 show is the least stable region of operation. Therefore, it is recommended, that for current controller inertial emulation, the current controller time constants must be reduced to increase stability during frequency disturbances to obtain a high inertial gain that can deliver or absorb power during the disturbance. The standard current controller time constant region of operation is very limited for this type of inertia emulation.

# 4.9 Chapter Summary

In this study, inertia capabilities were replicated successfully in the traditional current controller by adding an inertial gain amplifying the rate of change of frequency of the system, and a filter. A series of parametric sweeps were performed for varying filter constants and current controller and PLL time constants. This investigation highlighted that in the normal area of tuning,  $\tau_{\alpha}$  of 1-5 ms, the inertia emulation performs poorly,

Chapter 4. Stability Limits and Tuning Recommendation of the Standard Current Control Providing Inertia Support

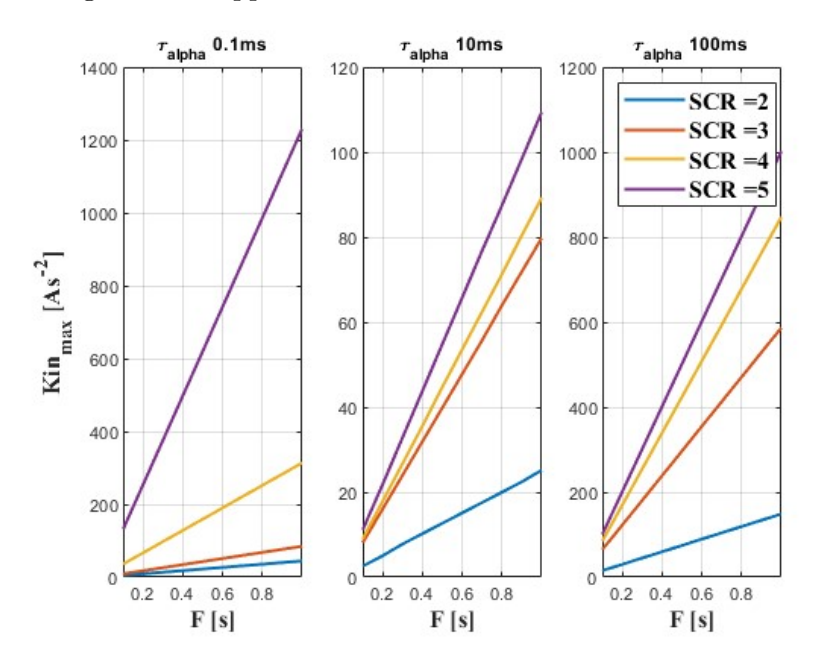


Figure 4.9: Maximum  $K_{in}$  allowed whilst maintaining system stability with increasing F, with tuning recommendations  $\tau_{PLL} = 0.04$ s, a)  $\tau_{\alpha} = 0.1$  ms, b)  $\tau_{\alpha} = 10$  ms, c)  $\tau_{\alpha} = 100$  ms.

unable to reach the gains required for emulating inertia. If  $\tau_{\alpha}$  is reduced to fast values of around 0.1 ms, then stable inertia emulation with classical vector current control can be achieved, however this is encroaching on the converter switching frequency range of 1-10 kHz range, and so is not an acceptable value. At much slower current loop time constants,  $\tau_{alpha} > 10ms$ , the maximum  $K_{in}$  that can be achieved whilst maintaining stability is increased, however this begins to slow the current controller losing its ideal fast response.

Using the classical PLL tuning methods with this system would produce a  $\tau_{PLL} = 0.004s$ , however to enable a larger inertial gain, the PLL time constant should be increased to 0.04 s. Increasing the time constant ever further slightly improves the range of allowed  $K_{in}$ , but loses the fast PLL tracking.

Finally, the filter the grid frequency is passed through should be selected to maintain a reasonable response, whilst enabling the required  $K_{in}$ . An F greater than 0.6 s begins to significantly slow and limit the power response. However, with a very low F constant (< 0.3), then the maximum  $K_{in}$  that can be achieved is reduced.

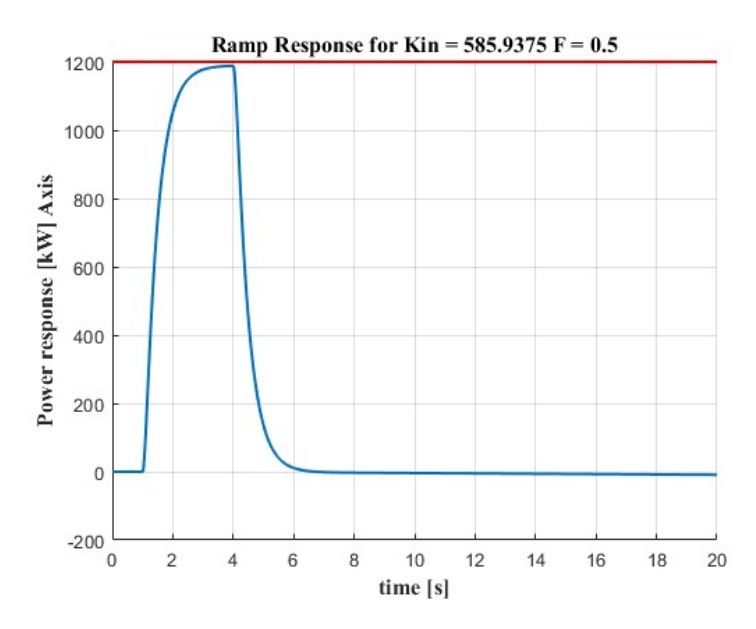


Figure 4.10: Power Response for system:  $\tau\alpha{=}0.1 \text{ms}~\tau_{PLL}{=}0.04 \text{s},$  SCR 5, Kin = 585 As-2, F = 0.5

# Chapter 5

Limitations and Comparisons of Small Signal Modelling Techniques in Converter Dominated Medium Voltage Networks

## 5.1 Motivation

This chapter assesses several common grid forming small signal modelling techniques of varying computational complexity for their accuracy. As discussed in Chapter 1, modern grids are seeing changing SCRs, due to increased power converter penetration. Additionally, generation is increasingly being connected at a distribution level or areas of the grid far from demand, therefore with different levels of X/R ratios. Each model is tested for its transient accuracy limitations in response to a power disturbance for varying grid SCRs and X/R ratios and controller damping for distribution networks.

#### 5.2 Introduction

The power system has seen significant changes over the last few decades as traditional fossil fuel power plants are being phased out and replaced with converter-based generation resources [258]. Traditional generation sites use synchronous machines to create a stiff voltage source, however, grids are now seeing converter dominated networks, which bring their own problems, with new device dependent and control interactions emerging [259]. Additionally, the short circuit ratio (SCR) is increasingly differing at points across the grid, and so the effect of SCR on model accuracy needs to be reviewed. Furthermore, the Distribution Network Operator (DNO)s are seeing more renewable generation integrated into the distribution grid, instead of transmission grids, and at a medium voltage level [130]. Distributed grids have a much lower X/R ratio compared to transmission grids [260], and so the effect of changing X/R ratios on model accuracy should also be investigated.

Utilisation of extensive large signal EMT models can provide in depth information regarding power system stability and interactions [258], [259]. However, in some instances they may be more detailed than is required, impractical to implement when there are many converters, and computationally intensive [261], [262].

In standard power networks, sub-synchronous oscillations (SSO) have been caused by interactions with the generator rotors, in series compensated transmission lines [21]. The swing equation has been commonly used to model synchronous machines connected to the grid, and to represent the interaction of the torsional modes causing the SSOs [21]. The new converter induced interactions require varying resolution of models to fully understand stability [263], [261] in the ever-changing grid of differing SCR and X/R levels.

Increasingly there have been several instances of sub-synchronous oscillations that have caused stability issues to many grids, and were not predicted or could not be modelled [225] [264]. As such, understanding the limitations of (and suggesting improvements to) existing modelling techniques is vital. It has long been discussed in the literature

Chapter 5. Limitations and Comparisons of Small Signal Modelling Techniques in Converter Dominated Medium Voltage Networks

Table 5.1: System Parameters

Parameter	Value
Base Power	$350 \; \mathrm{MW}$
Nominal L-L RMS AC Voltage	$230~\mathrm{kV}$
Grid frequency $\omega_n$	$50~\mathrm{Hz}$
Grid Resistance	0.1 pu / SCR
Grid Inductance	1 pu / SCR
Converter Resistance	0.01 pu
Converter Inductance	0.08 pu
Inertia Constant, H	5 s
Converter Damping pu, $K_D$	$2 \zeta \sqrt{K_s 2H\omega_0}$
Voltage Proportional Gain, $K_{vp}$	0.1
Voltage Integral Gain $K_{vi}$	50

[265], [266], these limitations, and the detail of information required in the model to accurately represent stability, transients and oscillations. Consequently, this Chapter offers an insight into the limitations of commonly used GFM modelling approaches from a small-signal perspective. The full detailed small signal [204], the Jacobian implementation [205], and the classical model [21] will be assessed for transient accuracy compared to the full detail non-linear EMT model. The effect of the SCR, damping ratio, and X/R ratio of the grid on the model transient accuracy will be investigated for each modelling method.

# 5.3 System Under Study

A grid forming converter, based on a virtual synchronous machine (VSM) topology is represented in the three modelling techniques [249], [267]. The full modelled system is a VSM converter connected to an infinite bus through an LC filter. The power measurement is calculated from the measured AC voltage and current at the point of common coupling (PCC) and controlled to the reference power through the swing equation, described in Section 3.4, and presented again below

$$P_m - P_e = \frac{Jd\omega}{dt} + D\omega \tag{5.1}$$

Chapter 5. Limitations and Comparisons of Small Signal Modelling Techniques in Converter Dominated Medium Voltage Networks

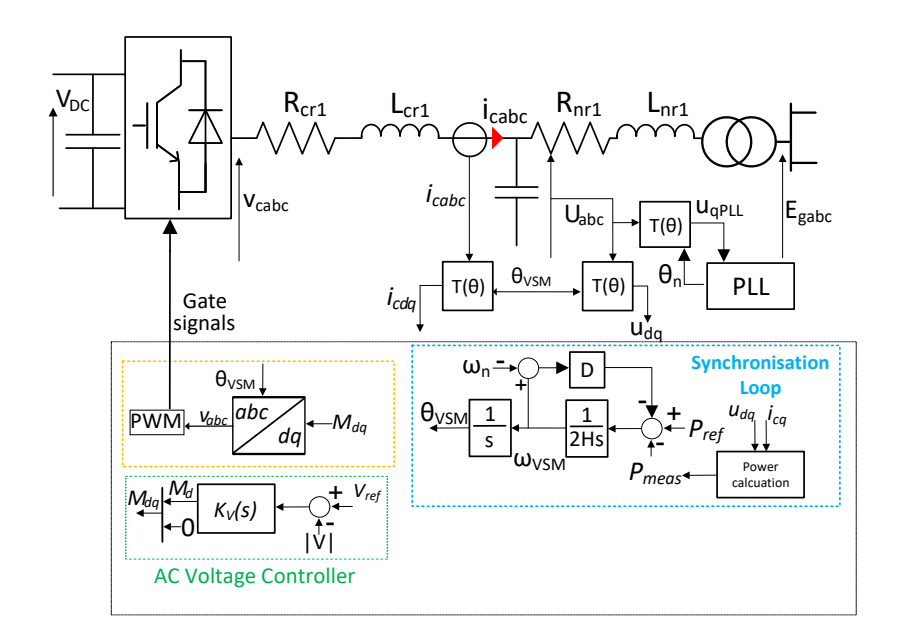


Figure 5.1: Virtual synchronous machine to grid connection

with the damping, D, and inertia, J, set following the parameters given in Table 5.1, with the damping calculated using the synchronising torque coefficient (derived in Section 3.4.2) and the damping factor,  $\zeta$ . The control of the converter is the second order implementation of the VSM swing equation, with the power directly relating to the angle set by the controller creating the power synchronization. The AC voltage is maintained by a PI controller which sets the magnitude of the voltage, which is fed into the averaged model of the converter to return the converter side voltage. This converter control was implemented in a non-linear EMT model in Simulink, to obtain the accurate, detailed baseline to compare the other models against.

The system and control diagram are shown in Figure 5.1, with the direction of current considered from the converter to the grid, modelled in the dq reference frame with the d-axis aligned to the a-axis, and the q-axis leading 90° to it. The grid, PCC, and converter voltages are  $E_g \angle 0$ ,  $U_{PCC} \angle \theta_U$  and  $V \angle \theta_V$ . The grid and converter side impedances are  $R_{nr1}$ ,  $L_{nr1}$ , and  $R_{cr1}$ ,  $L_{cr1}$ , respectively.

Chapter 5. Limitations and Comparisons of Small Signal Modelling Techniques in Converter Dominated Medium Voltage Networks

Table 5.2: Parametric Sweep Range

Parameter	SCR	X/R ratio	$ \zeta $
lower limit	1	1	0.1
upper limit	6	10	1

# 5.4 Methodology

As described in Section 5.2, the increase in power converter connected devices and the change in site generation geographical location is resulting in several variations to the grid parameters at connection, namely in SCR and X/R ratio [130]. For example, the short circuit ratio (SCR) is changing at many points across the grid, and decreasing beyond traditionally "low" values (<2) [268], [269]. Additionally, distribution grids have a lower X/R ratio compared to transmission grids [260], and renewable generation is increasingly being added to distribution networks [268]. Simplified models have been used for basic load flows and analysis of very large systems, however with the changes to the modern grid, it is important to represent the effect of these changing parameters on the models' accuracy, especially at the more "extreme" values we are seeing.

A series of parametric sweeps were performed on each of the models to investigate the effect of short circuit ratio, damping ratio,  $\zeta$ , and X/R ratio on the accuracy of the models. The upper and lower range of the parameter values are given in Table 5.2. A step input of 0.03 pu (10 MW) active power reference is observed for each model as the first case study, with key examples selected to represent the transient inaccuracies introduced by each model. Following this, the effect of varying the X/R ratio, SCR, and GFM damping factor, is shown on the eigenvalue detail of each model. A selected sweep of reducing X/R ratio is used to highlight the distinction in mode detail between the models. Finally, to show the parameter conditions that result in the largest transient inaccuracy of each model, the error of each model during the power disturbance, compared to the EMT non-linear model, is calculated and displayed in a series of heat-maps.

# 5.5 Small Signal Model

Following the implementation of the non-linear EMT model in the time domain, the three small signal models of varying detail complexity were derived, to be later compared to the non-linear model for accuracy. The three tested models are the full detail SSM, the Jacobian representation from [205], and the classical model.

#### 5.5.1 Full Detail EMT SSM

The first small signal model derived, is the full detail SSM representation. The method of creating the SSM requires the linearization of all of the non-linear EMT equations representing the grid and control system. This derivation is described in Chapter 3. The grid to converter system is shown in equations (3.49) to (3.55), the power and AC voltage calculations in (3.58) and (3.59). The linearised frame changes are shown in (3.70) and (3.71), and finally, the grid forming control is represented by (3.86) and (3.89). The value of damping selected is determined from the calculation of the damping torque, which is further explained in Section 5.7. Additionally, the outer loop AC voltage control is shown by the voltage components in (3.79) to (3.85) An overview of the linearised systems with the defined state variables is shown in Figure 5.2.

The voltages obtained from the voltage controller are passed through the linearised reference frame transformation from the converter frame to the grid frame [204]. The full EMT SSM considers the dynamics of the network, the full converter impedance, and the filter capacitor ensuring full detail of the represented system.

#### 5.6 Jacobian Model

The next small signal model of a VSM to grid system investigated is the static Jacobian matrix, which has traditionally been utilized for power flow and voltage stability analysis, despite the latter being a dynamic phenomenon. However, [205] argues that the Jacobian can still be used to observe the system dynamics if the frequency range is "quasi-static". It is based on the four transfer functions between inputs of

Chapter 5. Limitations and Comparisons of Small Signal Modelling Techniques in Converter Dominated Medium Voltage Networks

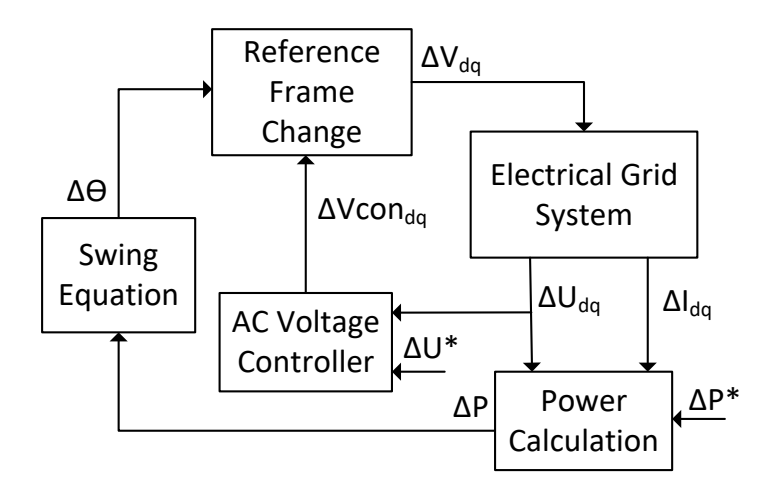


Figure 5.2: Linearised small signal model system connections.

angle disturbance and PCC voltage disturbance, to change in output power and PCC voltage [205], with the matrix representing the AC network and the vector control of VSCs connected to the grid. It is derived from the voltage and current equations from the grid to converter circuit, represented in the dq frame, and substituting the linearised equations into the state space dq representation of the power equation [205]. However, in certain parts of the equation substitution, the resistance is neglected to simplify the equations, and this representation with the transfer functions neglects the filter capacitor and so its dynamics.

The motivation behind using the Jacobian is to be able to represent a synchronous AC power system as "one multivariable feedback control system", with feedback controllers defined [205]. The idea is that various VSCs, synchronous machines, and loads, can be added to the system as inputs to the matrix control. However, these simplifications to make the matrix could result in important dynamics not being included. The relationship between the power, angle, and voltage, resulting in the Jacobian matrix

$$\begin{bmatrix} \Delta P \\ \Delta U \end{bmatrix} = \begin{bmatrix} J_{P\theta} & J_{PV} \\ J_{U\theta} & J_{UV} \end{bmatrix} \begin{bmatrix} \Delta \theta_v \\ \frac{\Delta V}{V} \end{bmatrix}$$
 (5.2)

Chapter 5. Limitations and Comparisons of Small Signal Modelling Techniques in Converter Dominated Medium Voltage Networks

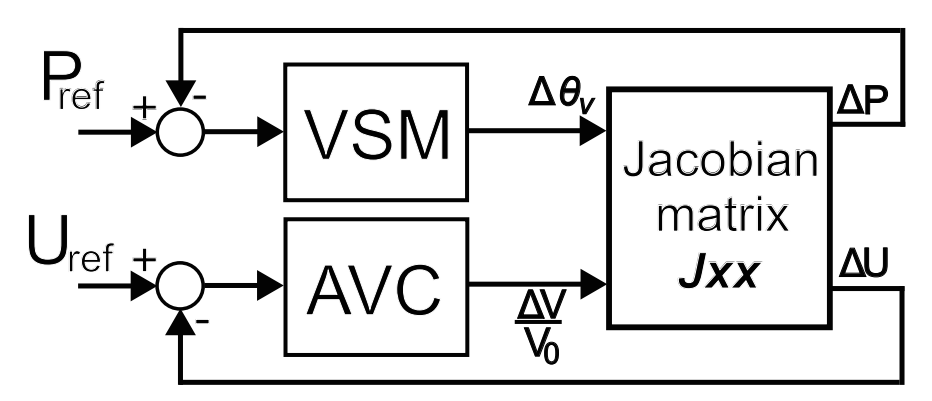


Figure 5.3: Jacobian representation of grid to converter system with VSM control.

With each  $J_{XX}$ , being the derived transfer function relating each variable from the equations of the system and contain the grid dynamics representing the inputs to outputs in the Laplace transform [205]. Each of these transfer functions contain dynamic information of the converter to grid model. The expanded detail of this matrix is described in the Appendix B, with a description of some of the simplifications and assumptions.

Once the derivation of the Jacobian matrix has been achieved, the additional control function can be added, as shown in Figure 5.3. The outputs from the VSM control block, and the AC voltage controllers are input to the matrix, with the voltage controller differing from that in the previous section, 5.5.1, and being divided by the voltage magnitude.

# 5.7 Classical Second Order Model

The simplest representation of a virtual synchronous machine connected to an infinite bus involves the swing equation and synchronising torque coefficient [21], as shown in Figure 5.4. The swing equation is the same VSM control structure used in the full EMT SSM and the Jacobian model, however in the Classical model, the grid is represented only by the synchronising torque,  $K_s$ . The electromagnetic torque can be separated into the synchronising torque and the damping torque, with their coefficients defined by  $K_s$  [pu torque/ radians] and  $K_d$  [pu torque/pu speed deviation] respectively. As

Chapter 5. Limitations and Comparisons of Small Signal Modelling Techniques in Converter Dominated Medium Voltage Networks

presented in Chapter 5, the coefficient  $K_s$  is defined by

$$K_s = \frac{EV}{X_T} \cos \delta_0 \tag{5.3}$$

and takes into account the infinite bus voltage, E, synchronous machine output voltage, V, reactance between the two,  $X_T$  and the initial angle,  $\delta_0$ . The damping coefficient is calculated by (5.4), where  $\zeta$  is the damping ratio, H is the selected inertia constant, and  $\omega_0$  the base frequency.

$$K_D = 2\zeta \sqrt{K_s 2H\omega_0} \tag{5.4}$$

Equation (5.3) does not take into consideration the resistance between the infinite bus and synchronous machine, and is based on algebraic equations so lacks any related dynamic information [1]. The synchronising torque coefficient indicates system stability, with a negative value showing unstable non-oscillatory modes, and negative damping torque coefficient indicating unstable oscillatory modes [270]. In Figure 5.4, the representation is in per unit, with  $\Delta T_m$  and  $\Delta T_e$  the per unit reference and electrical torque respectively. The VSM frequency is represented by  $\Delta \omega_r$ .

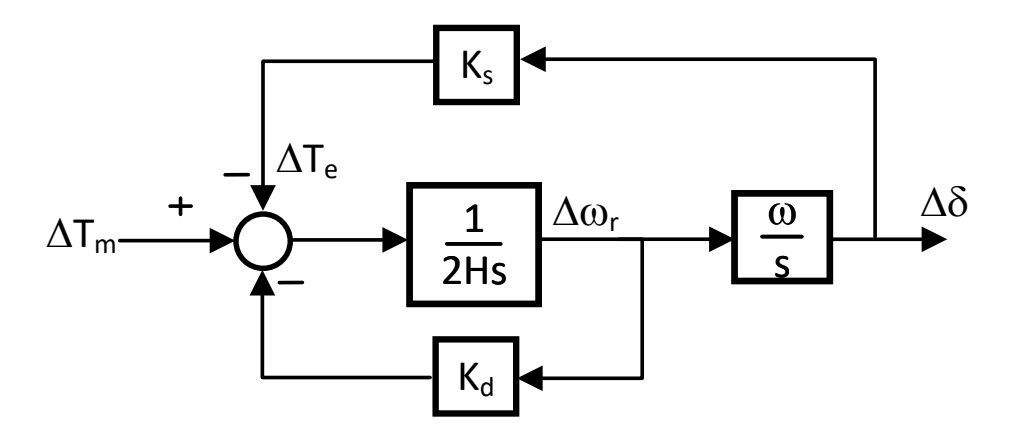


Figure 5.4: Small signal model diagram second order synchronous machine model.

The limitations of this model depend on what information is required. There are several higher order and more complex control structures of the VSM, however they

Chapter 5. Limitations and Comparisons of Small Signal Modelling Techniques in Converter Dominated Medium Voltage Networks

can be difficult to use for analytical dynamic analysis. The "importance" of some of the electromagnetic phenomena has also been debated in the literature [271], the relevance of neglecting electromagnetic dynamics is less clear in the presence of converter interfaced generation. The full small signal and Jacobian models have cross coupling terms representing the dynamics of the impedances which are not included in the classical model. This is a significant limitation of the basic Classical model, and the impact of this can be observed in the results section with the reduction in X/R ratio.

#### 5.8 Results

#### 5.8.1 Overview of Step Response

A series of parametric sweeps were performed on each of the models to investigate the effect of short circuit ratio, damping ratio,  $\zeta$  (and therefore grid forming damping), and X/R ratio on the accuracy of the models. The response to an active power step input of 0.03 pu (10 MW) is observed for each model as the first case study. The three implemented small signal GFM models were compared for their transient power response across the parametric sweeps, to the non-linear EMT time domain response, with some select examples shown here.

The higher the X/R ratio, the greater the decoupling between active and reactive power [260] and so a step in the reference power should control the measured power without significant effect on the voltage. However, decreasing the X/R ratio results in the Classical model and Jacobian models having reduced accuracy. For the Classical model, this is also partly due to the lack of inclusion of voltage control dynamics. This can be observed between Figure 5.5 and Figure 5.6, where the X/R ratio is reduced from 10 to 5, at SCR of 1.5, and the Classical model loses accuracy slightly, but not significantly. Further reducing the X/R ratio to 1, as in Figure 5.7, shows significant error in both the Classical and Jacobian models, deviating from the EMT model, showing longer lasting oscillations.

Chapter 5. Limitations and Comparisons of Small Signal Modelling Techniques in Converter Dominated Medium Voltage Networks

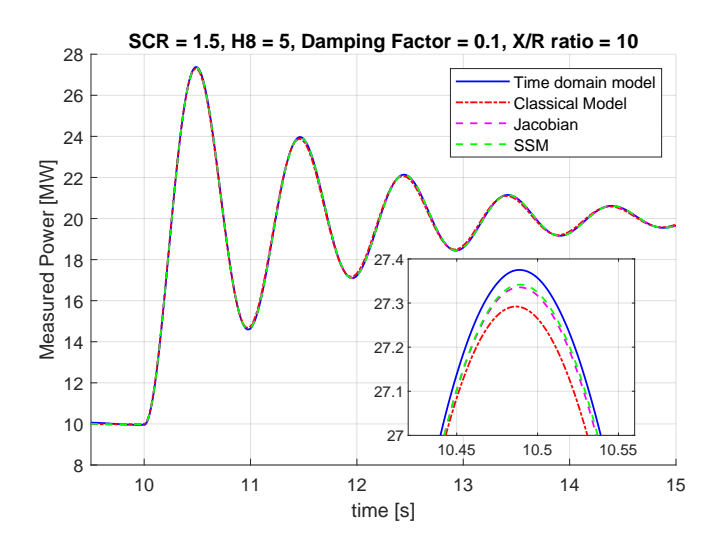


Figure 5.5: Step of 10 MW (0.03pu) SCR = 1.5,  $\zeta$  = 0.1 X/R = 10.

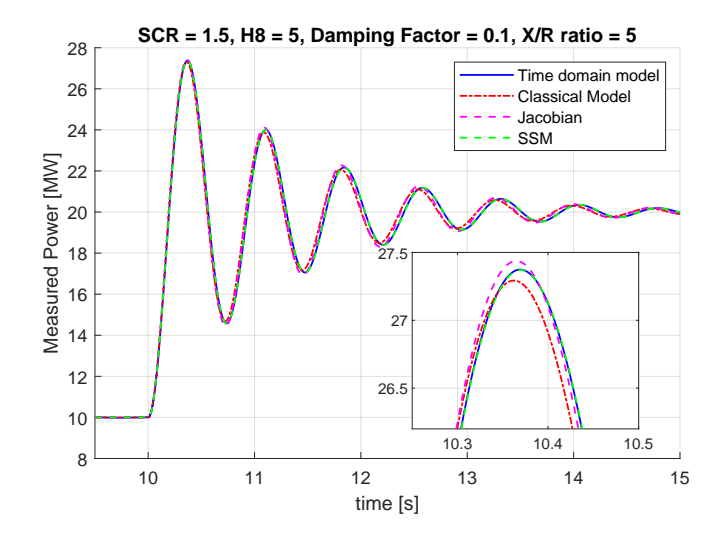


Figure 5.6: Step of 10 MW (0.03pu) SCR = 1.5,  $\zeta$  = 0.1 X/R = 5.

The effect of reducing the X/R ratio is most critical at lower SCRs, as well as low damping ( $\zeta <= 0.1$ ). Comparing Figures 5.7 and 5.8, if the SCR is increased from 1.5 to 6, for the same X/R=1 and  $\zeta$ =0.1, the Jacobian and Classical model match the time domain model slightly better than at the lower SCR. The model can suitably represent small changes around the equilibrium point, however lower SCRs and X/R ratios result in larger inaccuracies. Furthermore, this Classical model cannot reflect the changes in voltage reference as the voltage control loop is not included in the model. With

Chapter 5. Limitations and Comparisons of Small Signal Modelling Techniques in Converter Dominated Medium Voltage Networks

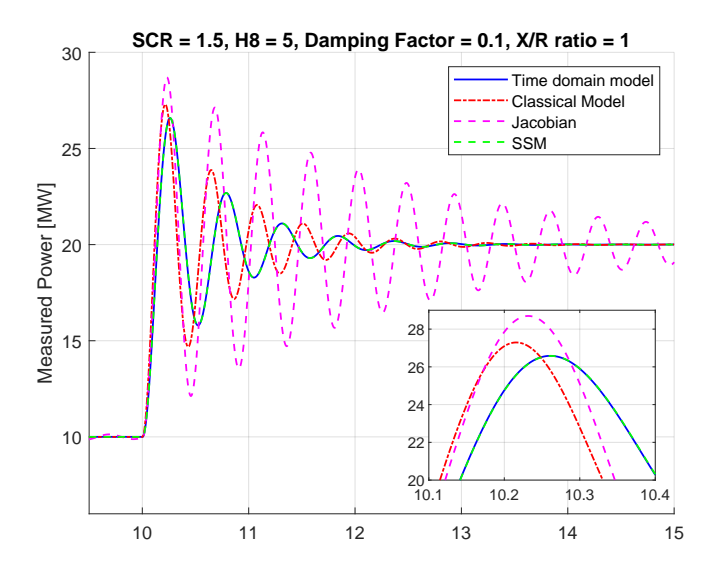


Figure 5.7: : Step of 10 MW (0.03pu) SCR = 1.5,  $\zeta$  = 0.1 X/R = 1.

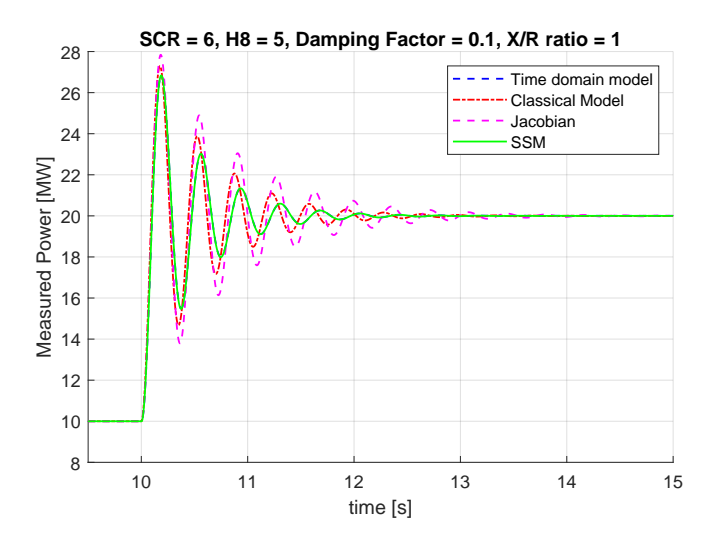


Figure 5.8: : Step of 10 MW (0.03pu) d) SCR = 6,  $\zeta$ = 0.1, X/R = 10.

the lower SCR, the frequency of the oscillations differs for the Jacobian and Classical models, compared to each other and the EMT, resulting in the waveforms being out of phase with each other.

The full range of parameter values tested, in each of the three small signal models are defined in Table 5.2. To illustrate the the effects of changing SCR, X/R ratio and  $\zeta$  on the models, a brief overview of the trends in the eigenvalue movement, and then overall percentage error in transient accuracy calculated, in the following sections.

Chapter 5. Limitations and Comparisons of Small Signal Modelling Techniques in Converter Dominated Medium Voltage Networks

# 5.9 Eigenvalue Analysis

For the full range of investigated SCRs, X/R ratios and damping ratios, the full EMT SSM model completely matched the non-linear EMT model. Therefore, the eigenvalues of the full detail SSM model were used as the accuracy baseline for the model small signal comparisons. For the same parameters investigated, detailed in Table 5.2, the eigenvalues were analysed. The voltage controller and network modes are represented by the full detail SSM and the Jacobian models, but they are much more heavily damped than the electromechanical modes and so will dissipate much faster. In Table 5.3, the full range of the real parts of the eigenvalues are shown, and the electromechanical modes are emphasized in bold. As the Classical model only represents the electromechanical modes, they will be briefly analysed for comparison amongst the three models. The electromechanical modes match well across the models for this parameter selection.

Table 5.3: Real components of eigenvalues of models: SCR = 1.5,  $\zeta = 1$ , X/R = 10

Full SSM	Jacobian	Classical
-0.6339	-0.6358	-0.6486
-12.4488	-30.9007	
-32.2373	-32.2574	
-41.2439	-41.0783	
-5.3925		

For a constant SCR of 1.5, and damping ratio of 0.1, the X/R ratio was reduced from 10 to 1, with modes for each model shown in Figure 5.9. As the X/R ratio is decreased, the electromechanical modes become more damped for the full SSM model, but the Classical and Jacobian modes move further apart in frequency (imaginary axis) from the full SSM model, causing them to become out of phase with each other and the full SSM model. They also deviate in terms of damping (time constant), due to the deviations in the real axis.

Chapter 5. Limitations and Comparisons of Small Signal Modelling Techniques in Converter Dominated Medium Voltage Networks

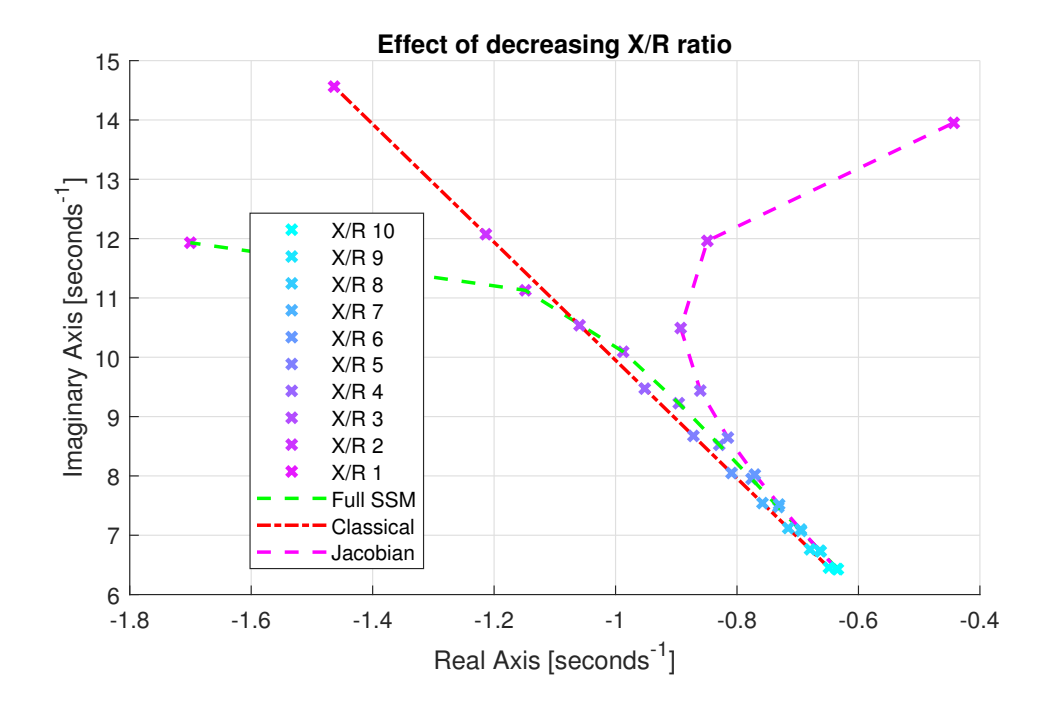


Figure 5.9: Comparison of the models with SCR 1.5 =,  $\zeta = 0.1$ , H = 5 s, over decreasing X/R ratio (10 to 1).

Towards the lower end of the X/R ratio range, the Jacobian modes are significantly different from the full SSM electromechanical modes, which was observed in the oscillations of the model in Figure 5.8. The modes of each model begin to significantly diverge from each other from X/R < 3. Increasing the SCR, at a low X/R ratio, results in the modes becoming more damped again but with closer together frequencies and so this phase shifting is not as pronounced.

# 5.10 Model Comparison Overview

The limits of the converter modelling methods in regards to accuracy are subjective in a sense of what is an acceptable deviation. Referring back to Figures 5.5 to 5.8, the full detail small signal model matches the EMT model incredibly well for the range of investigated parameters, SCR, damping ratio and X/R ratio. For high X/R ratios, the Classical and Jacobian models follow the EMT response very well, combined with SCRs greater than 3 and damping factors above than 0.3. For the lower X/R ratios of

Chapter 5. Limitations and Comparisons of Small Signal Modelling Techniques in Converter Dominated Medium Voltage Networks

< 1, when SCR = 6, the initial response is acceptable but begins to get out of phase, and deviate in terms of damping. Then, as the SCR is reduced, the lower detail models begin to lose accuracy significantly for all damping ratios.

The general conclusions of the effect of the parameters on model accuracy can be displayed in the heat-maps of Figure 5.10 and Figure 5.11. For the three modelling techniques, the system was implemented as a linear time-invariant block with the corresponding state space system selected, and the output of each compared to the EMT model. The sum of the squares of the error for each point of the response after the step was then calculated compared to the EMT response following

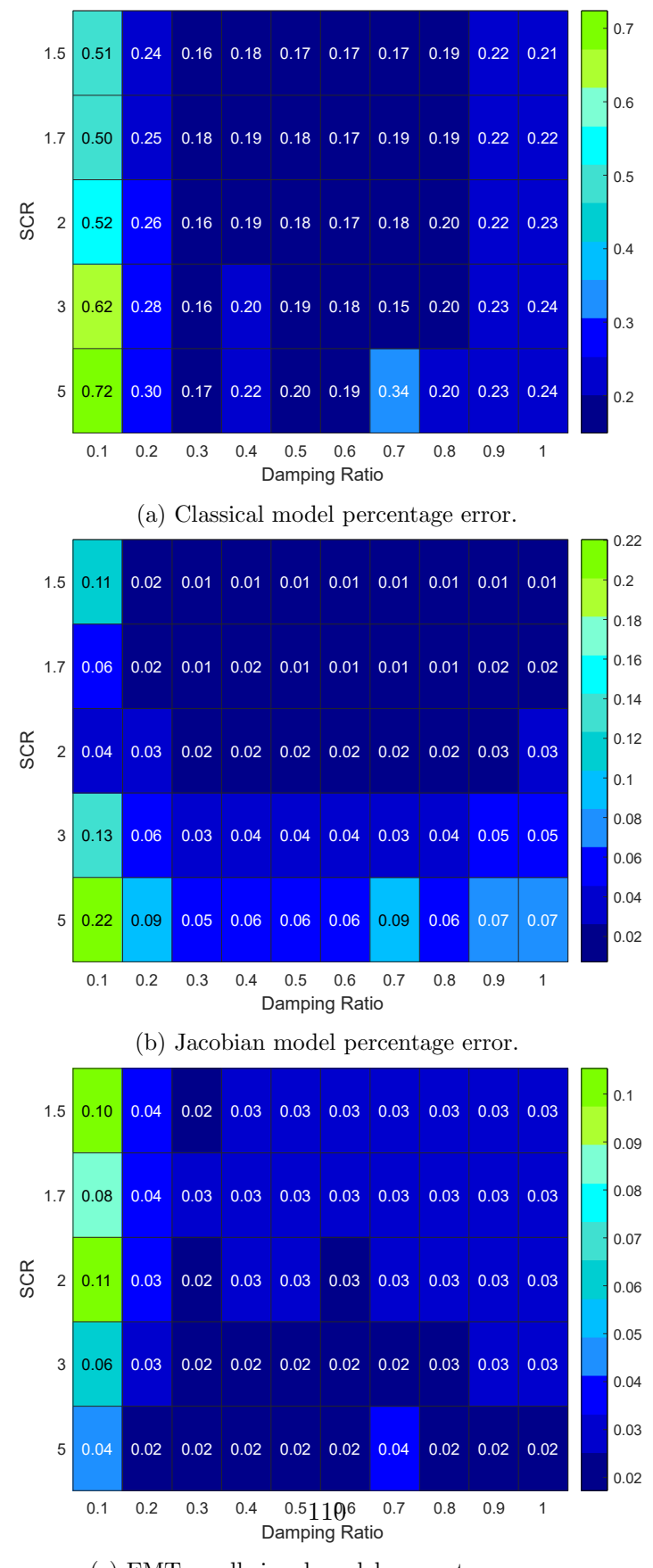
$$\%Error = 100\sqrt{\frac{\sum_{i=0}^{n} (P_{mi} - P_{sim_i})^2)}{\sum_{i=0}^{n} P_{sim_i})^2}}$$
 (5.5)

Where  $P_{sim}$  is the EMT Simulink response at point i, and  $P_m$  is the investigated model at time i. Therefore, Figure 5.10 and Figure 5.11 are heat-maps showing for each modelling technique, the percentage error in accuracy compared to the non-linear EMT model, across the parameters investigated.

For the range of SCRs and damping ratio, the sum of the squares of the error was calculated for each X/R ratio. For the X/R ratio of 10, Figure 5.10, the greatest error was with the classical model at SCR 5 and damping ratio of 0.1. The exact percentage error of this value is only 0.72%, which is very insignificant. Considering this is the highest error for this parametric sweep, the other errors for the remaining models, SCRs and  $\zeta$ , are even smaller and so show great accuracy. As the overall error is very small, for a small signal power disturbance, any three of the models would be capable of accurate representation, and the classical model has the lowest computational burden and so could be used very effectively for this type of investigation for the given parameters.

When the X/R ratio is reduced to 1, a significant change is observed in the accuracy of the Classical and Jacobian models, shown in heat-maps of Figure 5.11. The greatest error observed across the parametric sweeps was 20.5%, using the Jacobian model at SCR = 1.5 and damping  $\zeta = 0.1$ . For the Classical model with the aforementioned

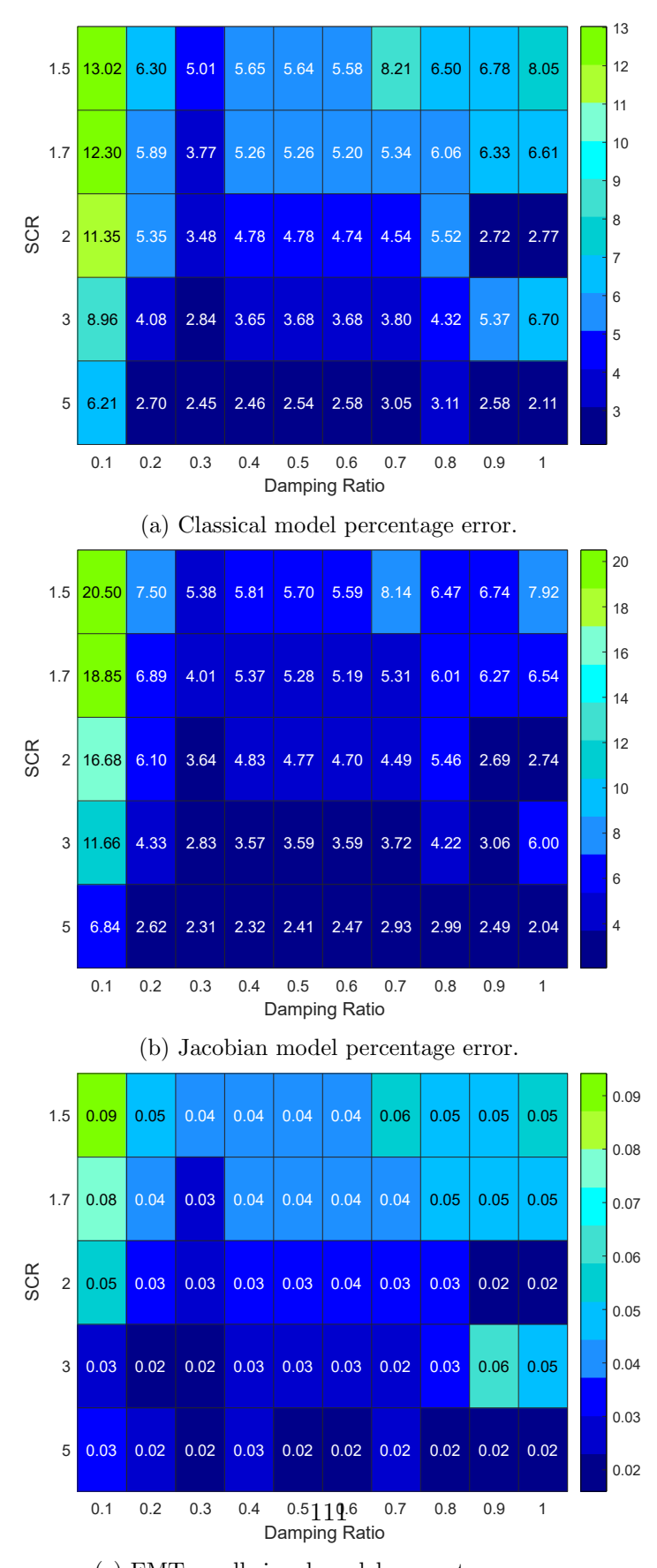
Chapter 5. Limitations and Comparisons of Small Signal Modelling Techniques in Converter Dominated Medium Voltage Networks



(c) EMT small signal model percentage error.

Figure 5.10: Percentage error in transient response across SCR and damping ratio at X/R = 10.

Chapter 5. Limitations and Comparisons of Small Signal Modelling Techniques in Converter Dominated Medium Voltage Networks



(c) EMT small signal model percentage error.

Figure 5.11: Percentage error in transient response across SCR and damping ratio at X/R = 1.

Chapter 5. Limitations and Comparisons of Small Signal Modelling Techniques in Converter Dominated Medium Voltage Networks

parameters, the error is 13%, and for the full EMT SSM, the error is only 0.09%. For the Jacobian and Classical models at this X/R ratio of 1, across all SCRs and damping ratios the percentage error is significantly increased compared to the same parameters but with a higher X/R. The EMT SSM however still maintains a very good accuracy across all parameters.

The Jacobian model can accurately represent the dynamic response of a power step with an X/R > 3, as seen in the graphs of Figure 5.9 to Figure 5.11. However, at lower X/R ratios, the response is increasingly inaccurate, especially at SCR < 2 and  $\zeta < 0.2$ . The Classical model has the same limitations for each parameter. Therefore in terms of accuracy, the Classical model has a slightly higher percentage transient accuracy compared to the Jacobian, however they both have increased percentage error with low X/R (< 3) and low damping factor, ( $\zeta < 0.3$ ). The EMT SSM is accurate in all instances, and fully matches the non-linear EMT, and the classical and Jacobian models could be sufficient in representing a power step change with X/R > 3.

# 5.11 Chapter Summary

The modelling of converter dominated networks, and identification of interactions within, is becoming increasingly complex. As such, maintaining the balance between accurate, detailed models, and an appropriate computational burden is paramount. Non-linear EMT modelling provides the most accurate response, yet is limited by having the highest computational cost, and the full small signal model is incredibly useful for converter interaction and sub-synchronous oscillation analysis however at a high complexity with limited scalability. Simplified models such as the Jacobian representation or the Classical second order model allow for simple analysis but do not always appropriately show the dynamics of the grid/converter, and at lower SCRs and non-moderate damping ratios, they show an increased error, especially at lower X/R ratios. For the range of short circuit ratios of 2 to 6, and damping ratios of 0.1 to 1, the Classical and Jacobian models are as accurate as a full small signal model, when at a high X/R ratio. However, with an X/R < 3, the Jacobian and Classical models

Chapter 5. Limitations and Comparisons of Small Signal Modelling Techniques in Converter Dominated Medium Voltage Networks

have a much lower accuracy compared to the full EMT SSM, especially combined with SCR < 2 and damping ratio  $\zeta$  < 0.3. The inclusion of the full converter to grid impedances as well as filter capacitance is key for the EMT small signal model, enabling accurate representation of the grid. The Classical model only includes the equivalent inductance between the grid and converter, ignoring the resistance and capacitance. The Jacobian model mainly considers the grid impedance, but makes some simplifications in some of the internal transfer functions by neglecting the grid resistance in some cases. These simplifications allow for ease of implementation and simplicity, but result in lack of dynamic detail and damping. These limitations of the Jacobian and Classical model result in significantly reduced accuracy for the increasingly seen "extreme" grid parameters.

# Chapter 6

# Assessing the Capability and Limitations of Small Signal Simplified Grid Following Models for the Identification of Sub-Synchronous Oscillations

Electricity grids are seeing dramatic changes due to increased power converter penetration, causing variations in grid strength, X/R ratio, and new dynamic bandwidths, which present stability challenges that need to be captured in models. The use of appropriate modelling techniques is critical to achieve an accurate stability assessment, however, it is also important to balance this accuracy with computational burden. This chapter compares three key small signal models of a grid following converter; a full detail small signal model, a Model Order Reduction (MOR) method, and a simplified phasor model. They are compared for their ability to represent transient accuracy, eigenvalue stability and identifying the presence of key modes that could cause sub-synchronous oscillations. Previous literature has failed to define the

bandwidth and accuracy of the different modelling approaches in specific conditions. This chapter addresses the need for parametric sensitivity studies, and presents a methodology of evaluation of lower detail models, for highlighting instability, and the sub-synchronous, oscillatory modes that low detail models fail to capture, even when they are expected to. Results show that the MOR performs slightly better than the simplified phasor model, however, both fail to capture critical stability information regarding oscillatory modes at sub-synchronous frequencies in certain parameter conditions. Additionally, they both have reduced accuracy in representing system instability, especially at low SCRs, when the full detail model should be used.

# 6.1 Motivation

The urgent threat of the climate emergency has resulted in a dramatic change in the power system, with traditional synchronous generation being replaced with power converter interfaced renewable generation [3]. The most widely used converter control is the grid following (GFL) structure, which utilises a phase locked loop (PLL) to synchronise to the grid voltage at the point of common coupling (PCC), [272], [12].

System operators have observed sub-synchronous oscillations (SSOs) that were not predicted during the grid connection simulation phase. Such examples occurred in the UK in June and July 2023, where 8 Hz oscillations occurred on 5 separate days, resulting in tripping of generation, an HVDC link, an inter-connector and a transmission circuit [14]. Other cases have been reported worldwide, such as in China and the USA, which have been severely destructive [16]. These issues highlight the difficulties system operators are experiencing, and the need for accurate modelling and identification of oscillatory modal phenomena.

CIGRE [273] stresses that SSO screening methods are important and should be simple and easy to understand. This is complicated considering that model accuracy could be impacted by low SCR (values <2) [268], [269], variable X/R ratio (depending on generation connection point) [260], and variable controller gains. This Chapter aims to provide the required screening to identify the ability of the models to accurately

Chapter 6. Assessing the Capability and Limitations of Small Signal Simplified Grid Following Models for the Identification of Sub-Synchronous Oscillations predict SSOs across the range of relevant conditions.

Non-linear electromagnetic transient (EMT) time domain models offer the highest accuracy of modelling but are associated with significant computational burden and simulation time, the need for detailed understanding of the power system parameters and dynamics, and difficulty in identifying the source of oscillations and/or instability. Small signal models (SSM) can offer a compromise between accuracy and computational demand, as well as offering classic control theory tools to assess oscillations and their instability mechanisms [21]. Different SSMs of GFL converters have been proposed, however there are problems that exist for each model, ranging from computational burden, to lack of accuracy [1,262,274–276].

The literature has compared different models for accuracy and representation, such as the extensive descriptions in [1,274] and [277], which compare EMT models, to some phasor, small signal and simplified models of differing dynamic detail. However they give a theoretical overview of the modelling capabilities and not a practical analysis of the contained dynamic modes and instability indications across realistic parameter conditions, as this paper aims to. Large signal model order reduction methods and comparisons have been presented in papers such as [278], [279] and [280], showing a good match in response for a reduced 6th and 4th order models, with a moderate reduction in accuracy for a 2nd order model. The authors of [281] give an extensive comparative review of small signal models in terms of state space, transfer functions, and impedance models. However, again the models are not compared across a combination of parametric conditions.

Therefore, this chapter compares three small signal models of varying detail, and identifies the conditions under which each model can be used, and when the full detail SSM is required. This is achieved by assessing if each model can identify problematic conditions, such as sub-synchronous oscillations, and instability. The three models assessed are the full detail SSM, such as in [204], a Model Order Reduction (MOR) method, from [282], and a simplified phasor model [274]. The motivation behind selecting each model is provided in Section 6.3.1, with the complexity of each model

Chapter 6. Assessing the Capability and Limitations of Small Signal Simplified Grid Following Models for the Identification of Sub-Synchronous Oscillations described and the derivation of the equations.

The key contributions of this chapter are: a methodology for screening models for their modal accuracy and capabilities of identifying oscillatory sub-synchronous modes, and comparing the accuracy of three common small signal modelling techniques, to assess what system and tuning conditions result in a degradation of model accuracy. It is expected that the simpler models will not be as accurate as the full detail model, however it needs to be studied what parameter conditions exacerbate these issues, and if they do not recognise dynamic detail in the sub-synchronous range, which they would be expected to. To the best of the authors' knowledge this is the first study to complete such a sensitivity analysis. The models are investigated under changing SCR, X/R, and outer power loop time constant. Using the eigenvalue analysis across the range of relevant conditions, this paper defines the conditions that each model-type can be used by Transmission System Operators (TSO)s to accurately identify and describe SSOs.

# 6.2 Methodology

The case studies presented in the results in Section 6.4 were completed with the following methodology.

#### 6.2.1 Implementation of Small Signal Models

The motivation of this work, described in the introduction, is to give a clear understanding of what degree of model complexity is required across varying system and control parameter conditions. The first step in this method is to implement each of the small signal models, which entails the linearisation of the full VSC system and control equations. The linearised equations are expressed in state space form, from (6.1) and (6.2)

$$\Delta \dot{\boldsymbol{x}} = A \Delta \boldsymbol{x} + B \Delta \boldsymbol{u} \tag{6.1}$$

$$\Delta y = C\Delta x + D\Delta u \tag{6.2}$$

where  $\boldsymbol{x}$  is the state variables vector,  $\boldsymbol{u}$  is the input vector, and  $\boldsymbol{y}$  is the output vector. The matrices A, B, C and D are the state space, input, output, and feed-forward matrix. The derivation of each linearised state space set of equations is detailed in Section 6.3.

#### 6.2.2 Identification of Problem Modes

The purpose of reducing the detail in complex models is to improve computational burden, and increase simplicity. It is assumed that there will be detail missing, such as high frequency modes, however many models aim to retain lower frequency modal information, such as the aforementioned MOR method, and accurately represent instability. Therefore, it is important to test the limits of detail that can be represented by the MOR and simplified phasor model compared to the full detail SSM.

To understand the limitations of models, eigenvalue analysis is used to identify cases where the full detail SSM represents key features of the system but the MOR and phasor model do not. The eigenvalues of the overall system **A** matrix [21] are defined by  $\lambda$  in (6.3), and from this the damping of each mode can be defined by (6.4). The damping ratio,  $\zeta$ , indicates when a system is critically damped ( $\zeta = 1$ ), over-damped ( $\zeta > 1$ ), or under damped ( $\zeta < 1$ ). The frequency of each  $i_{th}$  eigenvalue, defined by  $f_i$ , is equivalent to  $b_i$  in (6.3)

$$\lambda_i = a_i + jb_i \tag{6.3}$$

$$\zeta = \frac{a_i}{\sqrt{a_i^2 + b_i^2}} \tag{6.4}$$

From this eigenvalue analysis, it will be identified when the MOR and simplified phasor models do not represent key information that is in the full detail model, such as:

- 1. when the system is unstable  $(a_i > 0)$
- 2. when there are "modes of concern": poorly damped modes, with  $\zeta < 0.2$ , that occur in the sub-synchronous  $(f_i < 100\pi rad/s)$  range.

By reviewing eigenvalue plots of the systems, modes of concern that are missing from the lower detail models are identified. The damping ratio of each mode has been

calculated with (6.4), and where the damping is less than 0.2 the mode is highlighted. A value of 0.2 damping ratio has been selected as outside of this range, in the literature, has been stated as being poorly damped [21], [226]. Additionally, modes that indicate instability that are included in the full detail SSM, but not the lower detail models are identified.

#### 6.2.3 Parametric Overview

TSOs, vendors, equipment manufacturers and project owners are highlighting the importance of simplicity of modelling, whilst balancing accuracy. Therefore, the industry needs methods to give indications of what conditions simplified models can be used to accurately represent sub-synchronous oscillations.

In Section 6.4.1, for each parametric condition, the full detail SSM is analysed to see if it contains "modes of concern", or instability (defined in the previous sub-section). The MOR and simplified phasor are then checked to see if they also contain this modal detail, and if they do not, the parametric value is plotted. Therefore, in these plots, the xyz coordinates of each point are the SCR,  $\tau$ , and X/R value, and so any plotted point indicates at those values, the lower detail model is not accurate.

# 6.3 Modelling

In this Section, the three small signal models are described in detail for their defining equations and assumptions made.

The modelled grid-following current controller is pictured in Figure 6.1. It contains the outer power and AC voltage control loops, and the inner current control containing proportional and integral gains dependent on the converter side inductance and resistance [204], based on the modulus optimum tuning technique [224]. The power loop controller  $K_p(s)$  has proportional and integral gains,  $K_{pPC}$  and  $K_{iPC}$  respectively, and for the voltage controller  $K_U(s)$  the gains are  $K_{pUC}$  and  $K_{iUC}$ . The phase locked loop (PLL) is defined by  $K_{PLL}(s)$  with the proportional and integral gains being  $K_{pPLL}$  and  $K_{iPLL}$ . The grid side inductance and resistance are defined by  $L_n$  and  $R_n$ , and

the converter side defined by  $L_c$  and  $R_c$ . The DC voltage is assumed to be constant, as the purpose of the models the authors are analysing is for the identification of SSOs in the AC grid. Some of the lower detail models do not contain DC voltage feedback, and the goal is to test that claims of the detail included in the simpler models, therefore the effect of the DC link is not assessed. The operating points of the system have been calculated using MatPower [283].

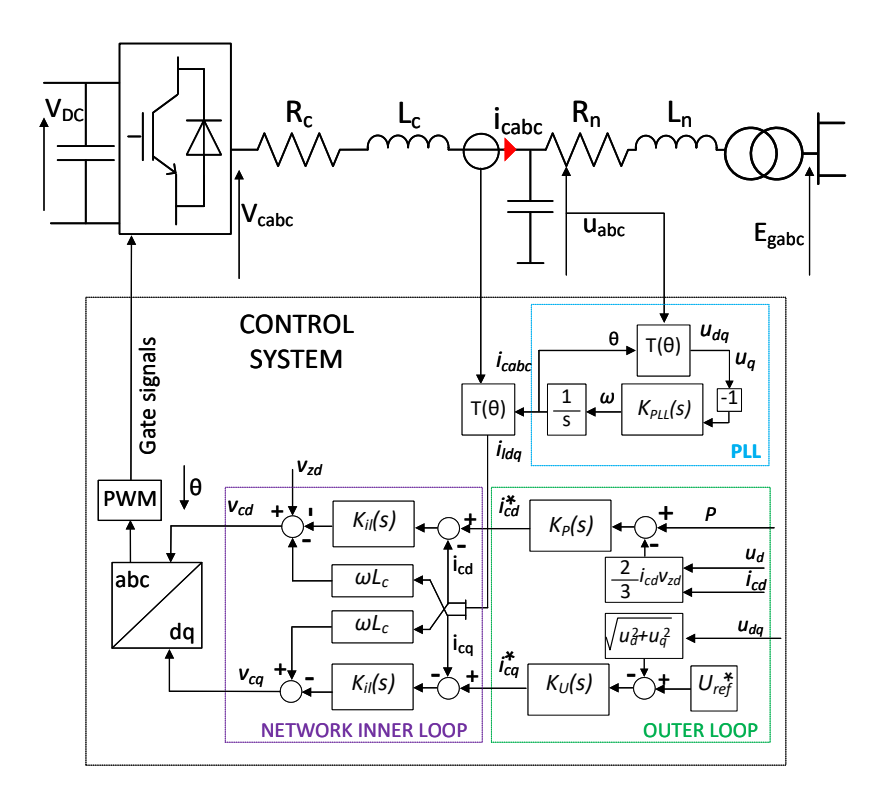


Figure 6.1: Current controller model of GFL in dq control.

#### 6.3.1 Model Selection Overview

The three small signal models analysed in this section are the full detail SSM, the selected Model Order Reduction method from [284], and a simplified phasor model. The reasoning behind the model selections have been briefly described in the introduction, and are expanded upon here, highlighting the known benefits and draw backs of each model.

Chapter 6. Assessing the Capability and Limitations of Small Signal Simplified Grid Following Models for the Identification of Sub-Synchronous Oscillations

The full detail SSM contains the dynamics of the grid, which entails representing the system as the currents, voltages and impedances in first order differential equations. This accurately shows the non-linear characteristics of the voltage and currents flowing through the representative grid impedance. The full detail model also includes the outer, and inner current control (CC) loops, and accurately represents the small disturbance characteristics of the system, sub-synchronous oscillations, small transients and instability [21, 285]. It is presented in a state space representation, with a large number of system states. This extensive state detail gives the ability to obtain great insight into the cause of oscillations or disturbances, by the use of eigenvalue analysis and participation factors. However, a detailed knowledge of the system is required, and the implementation of deriving all the equations of larger systems can be impractical for system operators.

The second model assessed in this study is the MOR implemented from [282] and [284], and has been chosen as it is a very popular simplification method utilised in [286–289], and is deemed to be a good "intermediate" simplification step between the full detail SSM and the simplest modelling method. It is implemented in state-space form as a Multi Input Multiple Output (MIMO) system of transfer functions, allowing the use of classical control theory tools to analyse the represented dynamics. The MOR is stated to be used for analysis of dynamic behaviour and system stability considering sub-synchronous modes in weak grids (pertaining to low SCR) [284].

The simplest representation of a grid-tied GFL converter is a phasor implementation, where the differential equations of grid dynamics are represented algebraically, and the converters are represented as a current source with magnitude and angle defined by the controller. Typically they have been employed due to the assumption that the system frequency will remain close to the rated synchronous frequency, and that the dynamics of the grid do not need to be represented [1,274]. The simplicity of this method is highly beneficial to TSOs and those developing large system models, however it lacks information of system dynamics and some converter interactions.

The full detail SSM contains the grid dynamics and all of the current controller

Table 6.1: Details included in each model.

Detail	Full Detail	MOR	Simplified Phasor
Grid Dynamics	Included	Included	Not Included
PLL Dynamics	Included	Included	Not Included, angle taken directly from phasor
Inner CC	Included	$I_c = I_c^{ref}$	$I_c = I_c^{ref}$

dynamics. The selected MOR is derived from linearised system differential equations, but is simplified to multiple Single Input Single Output (SISO) transfer functions. The method also involves further simplifications, such as assuming the inner current loop is fast enough that the measured current follows the reference current exactly. The simplified phasor model contains no grid dynamic detail, as it models the grid algebraically. Like the MOR, it also assumes the current follows the reference exactly, however it does not represent the grid synchronisation with a PLL, instead it directly uses the angle from the PCC voltage phasor, losing all detail of the PLL dynamics. Additionally, the reference frame conversion in the MOR is simplified to neglect the initial angle deviation. An initial overview of model detail is given in Table 6.1 and a summary later, in Figure 6.3.

# 6.3.2 Model 1: Full Detail SSM

The first small signal GFL model tested is the full detail SSM. The AC grid to converter network can be represented by the matrices,  $\Delta A_g$ ,  $\Delta B_g$ , and  $\Delta C_g$ , shown in (6.5) to (6.8), which are defined by the impedance between the converter and grid voltages ( $v_{dq}$  and  $e_{dq}$ ), and the system frequency,  $\omega$ .  $\Delta D_g$  is a null matrix, in this case. In the

following sections, the variables are in either the grid frame, or the converter frame.

$$\Delta A_g = \begin{bmatrix} \frac{-R_c}{L_c} & \omega & \frac{-1}{L_c} & 0 & 0 & 0\\ \omega & \frac{-R_c}{L_c} & 0 & \frac{-1}{L_c} & 0 & 0\\ \frac{1}{C_f} & 0 & 0 & \omega & \frac{-1}{C_f} & 0\\ 0 & \frac{1}{C_f} & -\omega & 0 & 0 & \frac{-1}{C_f}\\ 0 & 0 & \frac{1}{L_n} & 0 & \frac{-R_n}{L_n} & \omega\\ 0 & 0 & 0 & \frac{1}{L_n} & -\omega & \frac{-R_n}{L_n} \end{bmatrix}$$

$$(6.5)$$

$$\Delta B_g = \begin{bmatrix} \frac{1}{L_c} & 0 & 0 & 0\\ 0 & \frac{1}{L_c} & 0 & 0\\ 0 & 0 & \frac{-1}{L_n} & 0\\ 0 & 0 & 0 & \frac{-1}{L_n} \end{bmatrix}$$

$$(6.6)$$

$$\Delta C_g = \begin{bmatrix} 1 & 0 & 0 & 0 \\ 0 & 1 & 0 & 0 \\ 0 & 0 & 1 & 0 \\ 0 & 0 & 0 & 1 \end{bmatrix} \tag{6.7}$$

$$\Delta D_g = zero(4x4) \tag{6.8}$$

Where the state variables and inputs,  $\Delta \mathbf{x}_{g}$  and  $\Delta \mathbf{u}_{g}$ , are defined in terms of the converter side currents,  $\Delta \mathbf{i}_{cd}$ ,  $\Delta \mathbf{i}_{cq}$ , grid side currents,  $\Delta \mathbf{i}_{nd}$ ,  $\Delta \mathbf{i}_{nq}$ , and PCC voltage  $\Delta \mathbf{u}_{d}$ ,  $\Delta \mathbf{u}_{q}$ :

$$\Delta x_g = \begin{bmatrix} \Delta i_{cd} & \Delta i_{cq} & \Delta u_d & \Delta u_q & \Delta i_{nd} & \Delta i_{nq} \end{bmatrix}$$
(6.9)

$$\Delta u_g = \begin{bmatrix} \Delta v_d & \Delta v_q & \Delta e_d & \Delta e_q \end{bmatrix}$$
 (6.10)

A key feature of the grid following converter is its reliance on a PLL to synchronise with the grid and follow the voltage. The grid angle,  $\theta$ , is obtained from 6.11, where

 $G_{PLL}$  is the PLL transfer function.

$$\frac{\Delta\theta}{\Delta U_q} = \frac{G_{PLL}}{s} = \frac{K_{pPLL}s + K_{iPLL}}{s^2 + a_0s + b_0} \tag{6.11}$$

where  $a_0 = (Kp_{PLL}cos(\theta_0)U_{d0} + Kp_{PLL}sin(\theta_0)U_{q0})$ 

 $b_0 = (Ki_{PLL}cos(\theta_0)U_{d0} + Ki_{PLL}sin(\theta_0)U_{q0}$  with the subscript, 0, indicating initial operating point of the variable.

The outer loop controls and inner current loop are modelled using the dq components to form the voltage references to be applied to the gate drives. The grid dq currents and voltages are converted into the converter reference frame from the grid frame, by the linearised frame transformation [83] and the angle given in equation (6.11). If a component X is defined in the grid frame by  $X_f$ , and in the converter frame by  $X_f^c$ , then the relation can be expressed by (6.12) and (6.13) (where the superscript c indicates the converter frame), and  $\theta$  is the angle difference between the frames.

$$X_f^c = X_f e^{j\theta} (6.12)$$

$$X_f = X_f^c e^{-j\theta} (6.13)$$

The transfer matrix from grid to converter frame needs to be linearised, and is defined by T, and by  $T^{-1}$  for the converter to grid frame, which are explained in Chapter 3. For a variable  $\mathbf{X}$ , the linearised transform between each frame is defined by  $\mathbf{T}$ , with the linearisation around  $X_0$ , and  $\theta_0$ .

$$T = \begin{bmatrix} \cos(\theta_0) & \sin(\theta_0) & -x_{d0}\sin(\theta_0) + x_{q0}\cos(\theta_0) \\ -\sin(\theta_0) & \cos(\theta_0) & -x_{d0}\cos(\theta_0) - x_{q0}\sin(\theta_0) \end{bmatrix}$$
(6.14)

With the linearised inverse transform defined by  $T^{-1}$ 

$$T^{-1} = \begin{bmatrix} cos(\theta_0) & -sin(\theta_0) & -x_{d0}^c sin(\theta_0) - x_{q0}^c cos(\theta_0) \\ sin(\theta_0) & cos(\theta_0) & x_{d0}^c cos(\theta_0) - x_{q0}^c sin(\theta_0) \end{bmatrix}$$
(6.15)

The inner current loop can then be expressed, with the state space representation shown

by (6.16) to (6.19).

$$A_{cc} = zero(2x2) \tag{6.16}$$

$$B_{cc} = \begin{bmatrix} 1 & 0 & -1 & 0 & 0 & 0 \\ 0 & 1 & 0 & -1 & 0 & 0 \end{bmatrix}$$
 (6.17)

$$C_{cc} = \begin{bmatrix} K_{iCC} & 0\\ 0 & K_{iCC} \end{bmatrix} \tag{6.18}$$

$$D_{cc} = \begin{bmatrix} K_{pCC} & 0 & -K_{pCC} & -\omega L_c & 1 & 0 \\ 0 & K_{PCC} & \omega L_c & -K_{pCC} & 0 & 1 \end{bmatrix}$$
 (6.19)

Where the state, input and output variables are defined by  $\Delta x_{cc}$ ,  $\Delta u_{cc}$  and  $\Delta y_{cc}$ 

$$\Delta x_{cc} = [\Delta e i_d^c, \Delta e i_a^c] \tag{6.20}$$

$$\Delta u_{cc} = [\Delta i_{cd}^*, \Delta i_{cg}^*, \Delta i_{cd}^c, \Delta i_{cg}^c, \Delta u_{d}^c, u_{g}^c]$$
(6.21)

$$\Delta y_{cc} = [\Delta v_d^c, \Delta v_a^c] \tag{6.22}$$

The proportional and integral gains of the current loop PI controllers are  $K_{pCC}$  and  $K_{iCC}$  respectively, and  $\Delta ei_d^c$  and  $\Delta ei_q^c$  are the errors between reference current and measured current for the d and q components respectively. The outer loop power and voltage controllers are shown in Figure 6.1, with the PI controllers defined by  $K_P(s) = K_{pPC} + \frac{K_{iPC}}{s}$  and  $K_U(s) = K_{pUC} + \frac{K_{iUC}}{s}$  for the active power and AC voltage controller respectively. The integral gain of the power controller is defined by  $K_{iPC}$ , which is defined by the proportional gain, and the time constant of the controller,  $\tau$ ; one of the parameters varied in the study case in Section 6.4. The outer loop of power and AC voltage is defined by (6.23) to (6.26), where the state variables are the error between reference and measured values,  $\Delta x_e = [\Delta e P, \Delta e V]$ , and input variables are the reference and measured power and AC voltage  $\Delta u_{ol} = [\Delta P_{ref}, \Delta P_{meas}, \Delta U_{ref}, \Delta U_{meas}]$ . The measured PCC power and voltage can be calculated from the equations shown in the next section in (6.50) to (6.51). In this study, the DC voltage is not included as an input disturbance, and there is no DC

voltage droop control to the outer loop, as typically this control is in either active power control or DC Voltage, switching between the two [290], and in this study, the small signal response is assessed with active power outer loop.

$$\Delta A_{ol} = zero(2x2) \tag{6.23}$$

$$\Delta B_{ol} = \begin{bmatrix} 1 & -1 & 0 & 0 \\ 0 & 0 & 1 & -1 \end{bmatrix} \tag{6.24}$$

$$\Delta C_{ol} = \begin{bmatrix} K_{iPC} & 0\\ 0 & K_{iUC} \end{bmatrix} \tag{6.25}$$

$$\Delta D_{ol} = \begin{bmatrix} K_{pPC} & -K_{pPC} & 0 & 0\\ 0 & 0 & K_{pUC} & -K_{pUC} \end{bmatrix}$$
 (6.26)

#### 6.3.3 Model Two: Model Order Reduction

The reduced order model uses multiple SISO transfer functions, derived from [282] [284], to provide an input-output relation between power and voltage references and measured values. Reference [282] justifies this as a sufficiently accurate yet simplified model for eigenvalue analysis, however this only is stated for lower SCRs, and needs to be assessed across further parameters. The following section presents an overview of the derivation of the MIMO transfer function, however, the reader is directed to [282] and [284] for full model descriptions.

The plant equations of the VSC, PCC and grid voltage are defined by, (6.27) and (6.30). This is similar to the system equations in Section (6.3.2), however the filter capacitance is not considered. The grid inductance and resistance are indicated by  $L_g$  and  $R_g$ , and the combined grid and converter impedance by  $L_{eq}$  and  $R_{eq}$ .

$$\Delta u_d - \Delta e_d = (sL_a + R_a)\Delta i_{cd} - \omega L_a \Delta i_{ca}$$
(6.27)

$$\Delta u_q - \Delta e_q = (sL_q + R_q)\Delta i_{cq} + \omega L_q \Delta i_{cd}$$
(6.28)

$$\Delta v_d - \Delta u_d = (sL_{eq} + R_{eq})\Delta i_{cd} - \omega L_{eq}\Delta i_{cq}$$
(6.29)

$$\Delta v_q - \Delta u_q = (sL_{eq} + R_{eq})\Delta i_{cq} + \omega L_{eq}\Delta i_{cd}$$
(6.30)

If the initial angle difference is assumed to be 0, the PLL angle can be represented as (6.31). This transfer function is referred to as  $G_{PLL}$ .

$$\frac{\Delta \theta}{\Delta U_q} = \frac{K p_{PLL} s + K i_{PLL}}{s^2 + U_{d0} s + U_{d0}} \tag{6.31}$$

If (6.28) is substituted into the linearised PLL equation given in (6.31), it can be expanded, resulting in the grid angle being represented by (6.32). Note, the grid side voltages,  $\Delta e_{gd}$  and  $\Delta e_{gq}$ , are neglected.

$$\Delta \theta_{PLL} = G_{PLL}((sL_q + R_q)\Delta i_{cq} + \omega L_q \Delta i_{cd})$$
(6.32)

The grid voltages and currents are then transformed between the grid and converter frame. In the full detail model, this is achieved using the linearised transforms in (6.14) and (6.15). However, for this MOR, the transform is simplified to the equations in (6.33) and (6.34), as the initial angle deviation is assumed to be negligible. For this transform, a variable F is in the grid frame, and  $F^c$  in the converter frame.

$$\begin{bmatrix} \Delta f_d \\ \Delta f_q \end{bmatrix} = \begin{bmatrix} 1 & 0 & -f_{q0}^c \\ 0 & 1 & f_{d0}^c \end{bmatrix} \begin{bmatrix} \Delta f_d^c \\ \Delta f_q^c \\ \Delta \theta \end{bmatrix}$$
(6.33)

$$\begin{bmatrix} \Delta f_d^c \\ \Delta f_q^c \end{bmatrix} = \begin{bmatrix} 1 & 0 & f_{q0} \\ 0 & 1 & -f_{d0} \end{bmatrix} \begin{bmatrix} \Delta f_d \\ \Delta f_q \\ \Delta \theta \end{bmatrix}$$
 (6.34)

As the current control is assumed to be fast enough to follow the reference directly, the transient is ignored, and the inner current loop controller is not included in the model (resulting in the controller in (6.35),  $G_{cl}(s) = 1$ ). These linearised reference currents

are substituted into the equations for the inner current control loop, with the converter frame denoted by  $^c$  and the grid frame without any superscript.

$$\Delta v_{cd}^{c*} = \Delta u_d^c + G_{cl}(s)(\Delta i_{refcd}^c - \Delta i_{cd}^c - \omega L_c \Delta i_{cq}^c)$$
(6.35)

$$\Delta v_{cq}^{c*} = \Delta u_q^c + G_{cl}(s)(\Delta i_{refcq}^c - \Delta i_{cq}^c + \omega L_c \Delta i_{cd}^c)$$
(6.36)

The converter voltage equations, transformed currents, voltages, and linearised PLL equations are substituted into the VSC-PCC equations of (6.29) and (6.30). The steps of substitution of this stage are expanded upon in Appendix C.

After this substitution, the system can be represented in terms of current reference, converter currents, and change in angle. The change in angle can be represented solely in current terms, leading to the current reference to current output representation given by (6.37).

$$\begin{bmatrix} \Delta i_{cd} \\ \Delta i_{cq} \end{bmatrix} = \begin{bmatrix} A & B \\ C & D \end{bmatrix} \begin{bmatrix} \Delta i_{cd}^* \\ \Delta i_{cq}^* \end{bmatrix}$$
(6.37)

In [284], the grid inductor dynamics are neglected, resulting in even more system simplification. However, they can be included, as in [282], with the simplification of the matrices to give an input current reference, to output measured current, which is detailed in [282], shown in (6.37). The relation between the measure power and PCC voltage, to input dq current references is defined in (6.38).

$$\begin{bmatrix} \Delta P \\ \Delta u \end{bmatrix} = \begin{bmatrix} m & n \\ p & q \end{bmatrix} \begin{bmatrix} A & B \\ C & D \end{bmatrix} \begin{bmatrix} \Delta i_{cd}^* \\ \Delta i_{cq}^* \end{bmatrix}$$
(6.38)

Where the matrix entries A, B, C, and D are transfer functions defined as

$$A = \frac{1}{1 + G_{PLL} X_a I_{ca0}} \tag{6.39}$$

$$B = 0 \tag{6.40}$$

$$C = \frac{G_{PLL} X_g I_{cd0}}{1 + G_{PLL} X_g I_{ca0}} \tag{6.41}$$

$$D = 1 \tag{6.42}$$

and m, n, p and q defined by

$$m = 1.5[e_{d0} + i_{ca0}X_a + i_{cd0}R_a], p = 0$$

$$n = 1.5[-i_{cd0}X_g + i_{cq0}R_g], q = -X_g$$

In the matrix defined by m, n, p and q, the q-axis aligned voltage is simplified to zero, and the d-axis voltage is equivalent to  $-X_gI_{cq}$  (as the q-axis current through an inductor is d-axis aligned). A further simplification, is the infinite bus voltage,  $e_q$ , is assumed to be negligible, as is the grid resistance. The full MIMO system of input Power and Voltage reference to  $\Delta P$  and  $\Delta u$  is given by (6.43). Measured active power and PCC voltage are shown in (6.48) and (6.49).

$$\begin{bmatrix} \Delta P \\ \Delta u \end{bmatrix} = \begin{bmatrix} \frac{GPC0}{1+GPC0} & \frac{Y}{1+X} \\ \frac{M}{1+N} & \frac{GAC0}{1+GAC0} \end{bmatrix} \begin{bmatrix} \Delta P^* \\ \Delta u^* \end{bmatrix}$$

$$(6.43)$$

where the intermediate variables X, Y, M, N, GPC0 and GPC0 are defined by

$$X = K_p(s)(mA + nC), Y = K_U(s)(mB + nD)$$
(6.44)

$$M = K_p(s)(pA + qC), N = K_U(s)(pB + qD)$$
 (6.45)

$$GPC0 = X - \frac{YM}{(1+N)}$$
 (6.46)

$$GAC0 = N - \frac{YM}{(1+X)}$$
 (6.47)

The magnitude of the PCC Power and Voltage can be calculated with (6.48) and (6.49).

$$P_{meas} = \frac{3}{2}(u_d i_{cd} + u_q i_{cq}) \tag{6.48}$$

$$U = \sqrt{u_d^2 + u_q^2} (6.49)$$

$$\Delta P_{meas} = \frac{3}{2} (i_{cq0} \Delta u_{cq} + i_{cd0} \Delta u_{cd} + u_{q0} \Delta i_{cq} + u_{d0} \Delta i_{cd})$$
 (6.50)

$$\Delta U = \frac{u_{q0}\Delta u_q}{\sqrt{u_{d0}^2 + u_{q0}^2}} + \frac{u_{d0}\Delta u_d}{\sqrt{u_{d0}^2 + u_{q0}^2}}$$
(6.51)

#### 6.3.4 Model 3: Phasor Simplified Small Signal Model

The simplest modelling approach does not model the system as a series of differential non-linear equations but represents the grid algebraically [274]. Additionally in this presented model, it is assumed that the current loop accurately tracks its references and the grid voltage is shown as a static gain  $e_g$ , as in [274] and [1]. The simplified phasor model is shown below in Figure 6.2.

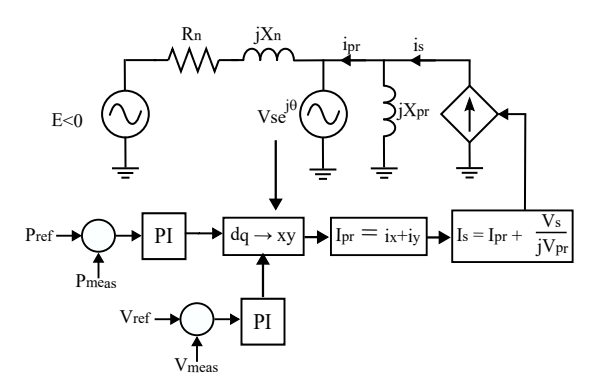


Figure 6.2: Simplified phasor model [1].

The angle from the PCC voltage phasor, The angle from the PCC voltage phasor,  $V_s$ , is used to convert the dq currents to their cartesian x-y grid frame [274], [1], using the linearised frame transformation, T. The output current from this transformation is  $I_{PR} = i_x + ji_y$ , and together with the current derived from  $V_s$ , across the parallel converter inductance,  $X_{PR}$ , the source current  $(I_s = i_{sx} + ji_{sy})$  can be calculated.

$$I_s = I_{PR} - j \frac{V_s}{X_{PR}} \tag{6.52}$$

Where the PCC voltage is derived by

$$V_s \angle \theta = E \angle 0 + (i_x + ji_y)(R_n + j\omega L_n) \tag{6.53}$$

The simple phasor model is then linearised to create the state space small signal representation, giving the simplified phasor small signal model. Collecting the real parts of the equation, these can be set equal to the cartesian x component of the equation, and the imaginary parts of the equation are equal to the y component.

$$\begin{bmatrix} \Delta V_{sx} \\ \Delta V_{sy} \end{bmatrix} = \begin{bmatrix} R_n & -\omega L_n \\ \omega L_n & R_n \end{bmatrix} \begin{bmatrix} \Delta i_x \\ \Delta i_y \end{bmatrix}$$
(6.54)

$$\begin{bmatrix} \Delta i_{sx} \\ \Delta i_{sy} \end{bmatrix} = \begin{bmatrix} 1 + \frac{\omega L_n}{X_{PR}} & \frac{R_n}{X_{PR}} \\ \frac{-R_n}{X_{PR}} & 1 + \frac{\omega L_n}{X_{PR}} \end{bmatrix} \begin{bmatrix} \Delta i_x \\ \Delta i_y \end{bmatrix}$$
(6.55)

The PCC voltage and power are calculated with the same method as the full SSM, however using the x-y coordinates. Although the PI controllers or system dynamics are not included up to this point in the simplified phasor model, several papers have cited the use of outer loop controllers even in RMS or phasor modelling, such as in [1] and [274] due to their slower speed. Therefore the outer power and voltage loops with PI control are included in this model, with the same proportional and integral gains as shown in Figure 6.1. The summary of the equations and simplifications used in the three models can be viewed in Figure (6.3).

# 6.4 Case Study

The three modelling techniques were tested for their accuracy across varying parameters and control gains to observe the limits of each model, using them to implement the system in Figure 6.1. The base system parameters are defined in Table 6.2.

The varied range of parameters, the SCR, the X/R ratio, and the time constant of the outer power controller,  $\tau$  are presented in Table 6.3. These parameters, especially the latter two, lack prior study of their effect on the validity of the reduced order models, when trying to identify poorly damped modes, SSOs, or instability. The range of each parameter, specified in Table 6.3, have been decided upon as the probable expected range each parameter could be. Traditionally a high SCR is anything above 3, and

Chapter 6. Assessing the Capability and Limitations of Small Signal Simplified Grid Following Models for the Identification of Sub-Synchronous Oscillations

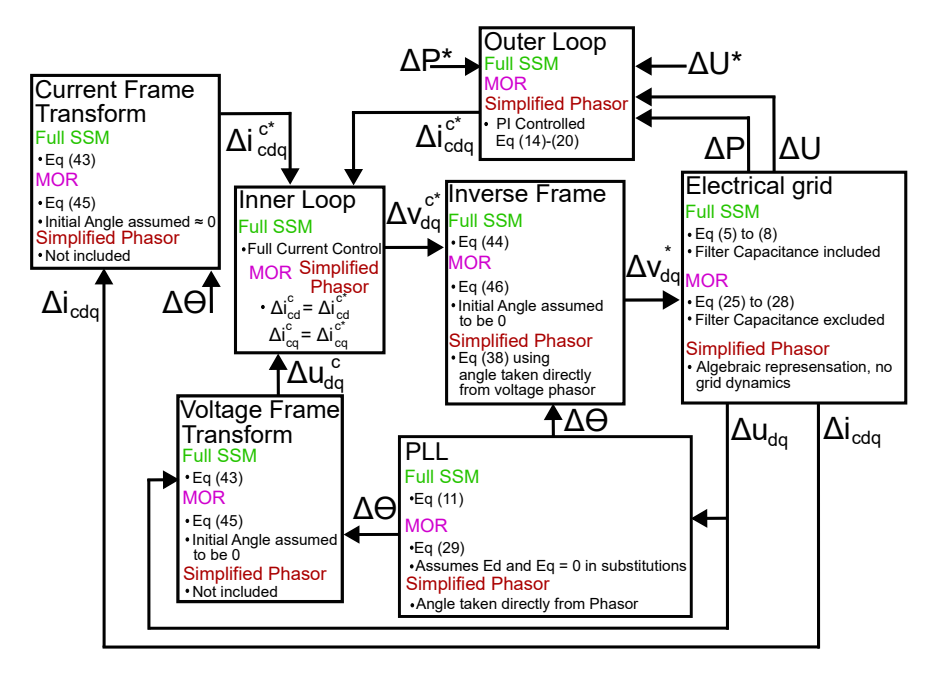


Figure 6.3: Summary of small signal representation of equations and assumptions used in each model.

anything below 2 as low [269]. Therefore a suitable encapsulating range of SCR = 0.4 to 5 has been investigated. The range of X/R selected was to test across a full range of possible lower values in distribution and transmission grids, with low values of 1 [291], and high values of up to 20. The outer loop time constant is varied between extremes of 1ms and 500 ms.

The eigenvalues of each model are assessed at each parameter condition to compare how each model represents sub synchronous modes and system instability. The eigenvalues are checked to see if the under-damped oscillatory modes present in system (as shown by the full detail SSM), are identified in the lower detail models.

#### 6.4.1 Results

The validation of the power responses is shown in Figure 6.4a and Figure 6.4b. The models are compared to the step response (0.01 pu active power) of an EMT time domain model of the same system. The accuracy of the full detail SSM is validated for both sets of parameter conditions in Figure 6.4a and Figure 6.4b. The MOR and

Table 6.2: System parameters

Parameter	Value	
Base Power	$350 \; \mathrm{MW}$	
Nominal AC L-L RMS Voltage	230  kV	
Grid Resistance, $R_n$	0.1 pu / SCR	
Grid Inductance, $L_n$	1 pu / SCR	
Converter Resistance, $R_c$	0.01 pu	
Converter Inductance, $L_c$	$0.08~\mathrm{pu}$	
Current Loop Time Constant	$20~\mathrm{ms}$	
$Kp_{PLL}$ [204]	0.002	
$Ki_{PLL}$	0.0045	
$Kp_{UC}$	0.001	
$Ki_{UC}$ 0.5		
$Kp_{PC}$ 1.0722 × 10		
$Ki_{PC}$ $\frac{Kp_{PC}}{\tau}$		

Table 6.3: Parametric range tested

Parameter	Lower Limit	Upper Limit
Short Circuit Ratio, SCR	0.4	5
X/R	1	20
Time Constant, $\tau$	1 ms	$500~\mathrm{ms}$

simplified phasor maintain good accuracy in Figure 6.4a, with SCR = 1,  $\tau = 50ms$ , and X/R = 10. However, in Figure 6.4b, with an increase in SCR = 4, and reduced time constant to  $\tau = 25ms$ , the response of the MOR and simplified phasor model are much less accurate in transient response. The source of the change in accuracy between Figure 6.4a and Figure 6.4b, is difficult to discern for the wide range of potentially significant parameters. Considering this, and the lack of information regarding mode damping and instability available from the time-domain response, a more thorough approach is required to clarify the impact of system condition on model accuracy. Therefore, a comprehensive technique is required to give an overview of the effect of varying parameters on model accuracy.

Chapter 6. Assessing the Capability and Limitations of Small Signal Simplified Grid Following Models for the Identification of Sub-Synchronous Oscillations

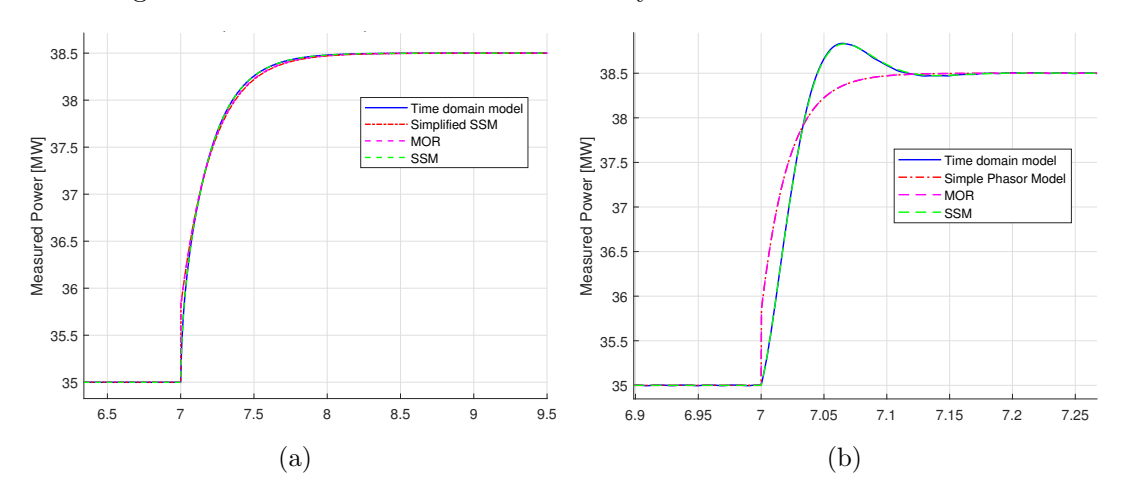


Figure 6.4: Selected power responses of 0.01 pu disturbance. a) SCR = 1, X/R = 10,  $\tau = 50$  ms. b) SCR = 4, X/R = 10,  $\tau = 25$  ms.

#### Eigenvalue Parametric Sweeps

The following section provides examples of plots of the eigenvalues of the three small signal models, across a series of parametric sweeps, comparing the dynamic detail each model represents. Instability is indicated by poles in the right hand plane, and the poorly damped modes with damping (6.4) of lower than 0.2. These eigenvalues that have a low damping factor, are highlighted in blue circles. In Figure 6.5 to Figure 6.6, the full detail SSM is represented by the "x", the MOR by the triangle, and the simplified phasor model by the square. The colour of each key in the legend indicates the first value of the parametric sweep (for example, in the case of Figure 6.5a, an SCR = 0.5), and changes as the variable (SCR) is increased (to 6). The arrows on the figure represent the direction of the increasing variable.

Figure 6.5a shows an example of eigenvalues of the system for each model, at 0.1 pu active power with  $\tau=0.04$  s, X/R=20, and iterating across SCR = 0.5 to 6. The modes of concern are highlighted with blue circles, indicating eigenvalue damping ( $\zeta$ ) is below 0.2. They can be seen at  $-50s^{-1}$  to  $-100s^{-1}$  in the full detail SSM, but they are not represented in the MOR, or simplified phasor. There are several of these modes that are above 314 rad/s (50 Hz), however there is a sub-synchronous mode that is only shown in the full detail, seen at  $-50s^{-1}$  damping. This is important to

Chapter 6. Assessing the Capability and Limitations of Small Signal Simplified Grid Following Models for the Identification of Sub-Synchronous Oscillations

note, as the MOR and simplified phasor model are expected to not include all the higher frequency dynamics, however this is a clear case of even sub-synchronous modes not being represented in the lower detail models. There are sub-synchronous modes close to 300 rad/s shown in Figure 6.5a, from  $-350s^{-1}$  to  $-150s^{-1}$ , that are present in both the MOR and full detail, however they are very well damped and would quickly dissipate. As expected, the simplified phasor model does not include much oscillatory modal detail, across the sweeps, which can be observed in the pole plot. Figure 6.6, shows further examples of "modes of concern" only represented in the full detail model, highlighted by the blue circles.

In Figure 6.5b, the power operating point is increased to 0.7 pu, with the same SCR range, and X/R ratio as in Figure 6.5a, but  $\tau$  of 0.001 s. At this operating point, the MOR contains modes of concern at around 300 rad/s, but it cannot show any higher frequency modes that are seen in the full detail model.

An example of the conditions where the full detail, and simplified phasor show instability, but the MOR does not can be seen in Figure 6.6, with system modes observed across increasing  $\tau$ . The simplified phasor model and full detail show a very unstable mode for the  $\tau$  of 1 ms, which is not accurately represented in the MOR. In this sweep, there are other unstable modes that the MOR does not reflect yet the simplified phasor does, and also modes of concern that only the full detail SSM includes. Although the specific modes in the full detail and simplified phasor model indicating instability are not of the same damping or frequency.

Considering the examples given in Figures 6.5 to 6.6, it is evident that there are conditions in which the MOR and simplified model do not represent sufficient detail of the modes of concern and instability. Therefore, a complete insight needs to be given to show under which parameters these happen. The next section presents an overview of the SCR, X/R ratio, and time constant and their effect on the models' abilities to represent oscillatory modes, and instability.

Chapter 6. Assessing the Capability and Limitations of Small Signal Simplified Grid Following Models for the Identification of Sub-Synchronous Oscillations

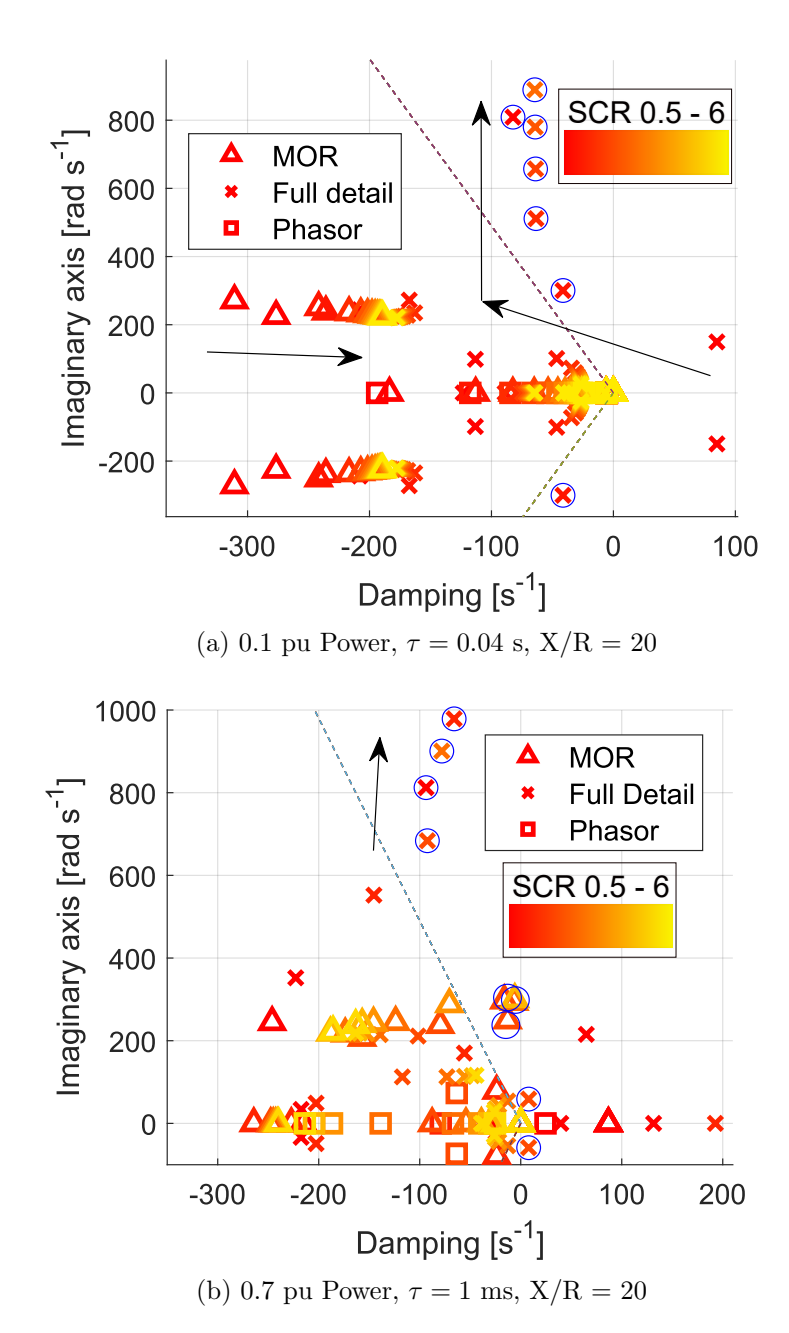


Figure 6.5: Eigenvalue plots for varying SCR = 0.5 - 6

Chapter 6. Assessing the Capability and Limitations of Small Signal Simplified Grid Following Models for the Identification of Sub-Synchronous Oscillations

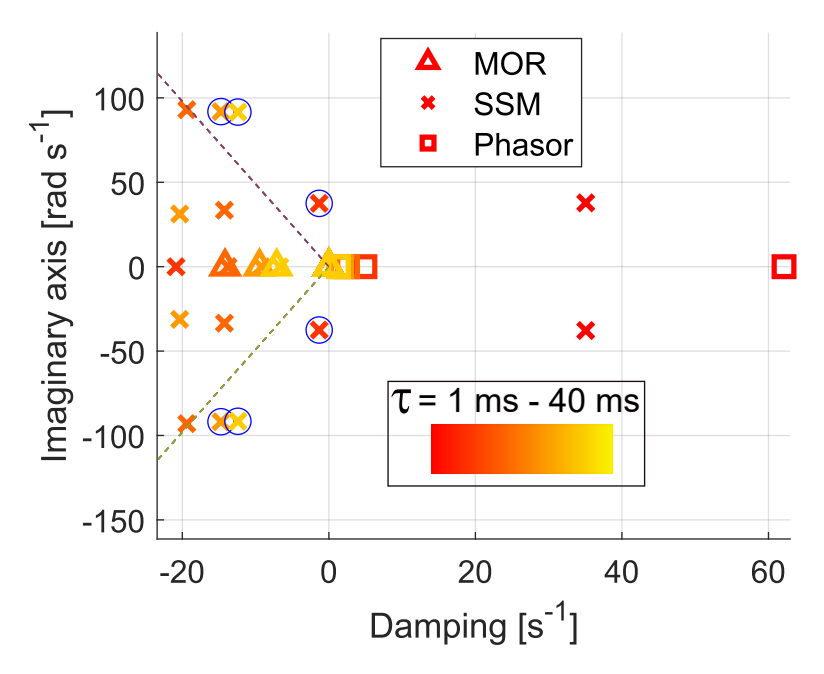
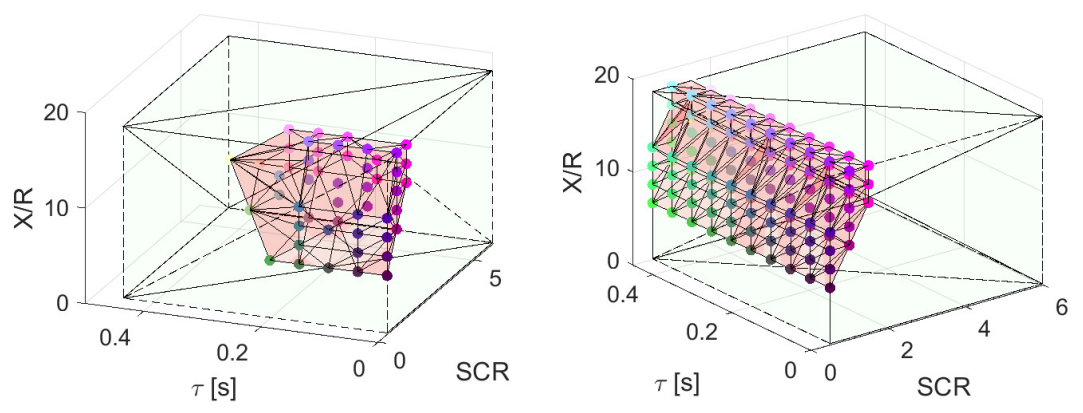


Figure 6.6: Eigenvalues for varying  $\tau$ , 0.7 pu active power,  $\tau = 1$  ms to 40 ms, SCR = 0.7, X/R = 10.



(a) Modes of concern represented in full detail (b) Modes of concern represented in full detail SSM not in MOR 0.1 pu Power Model not in Phasor 0.1 pu Power

Figure 6.7: Parameter conditions at which the full detail model has oscillatory subsynchronous modes, but are not identified by a) the MOR. b) the simplified phasor. 0.1 pu active power operating point.

Chapter 6. Assessing the Capability and Limitations of Small Signal Simplified Grid Following Models for the Identification of Sub-Synchronous Oscillations

#### Parameter Overview

For the three models, the SCR, X/R ratio and  $\tau$  were varied across the range given in Table 6.3. At each parameter condition, the full detail model was checked for modes showing instability, and poorly damped sub-synchronous modes, with the identification process described in Section 6.2.2. The figures in this section show the parameter conditions where the MOR or simplified phasor do not contain the modal detail that the full detail model does. Each point is the X/R, SCR and  $\tau$  value that indicates the condition where the lower detail models fail to capture modal detail. In each figure the green shaded areas show the full range of parameters that were swept through, and the pink shaded area shows the bounded area of parameters which don't show the modal detail in the lower detailed models.

Figure 6.7a shows the parameters where there are modes of concern represented in the full detail model that were *not* present in the MOR, at 0.1 pu active power. The MOR is capable of representing them across slower time constants, in general, above 0.3 s. However, between 0.2 s to 0.3 s, and increasingly below 0.2 s, the MOR is not capable of accurate mode representation with X/R = 6 to 14, and SCR = 0.5 to 1.5. The modes of concern represented by the full detail model, and not the simplified phasor, are shown in Figure 6.7b, at 0.1 per unit active power. At this operating point, the simplified phasor model does not represent *any* of the modes of concern, across the full range of X/R ratio, SCR and time constant, and so is not suitable for identifying possible poorly damped modes. However, the MOR is capable or representation of some sub-synchronous poorly damped modes, but only above an outer power loop time constant of 0.3 s.

If the operating point is now increased to 0.7 pu active power, looking at Figure 6.8a, the MOR fails to represent modes of concern across a larger parameter range than at 0.1 pu active power. In Figure 6.7a, the MOR highlighted modes of concern for time constants greater than 0.3 s, and recognised more for 0.2 s - 0.3 s compared to the simplified phasor model. However, in Figure 6.8a, across the full range of  $\tau$  there are cases where the MOR fails to recognise the modes of concern. This is more prevalent

Chapter 6. Assessing the Capability and Limitations of Small Signal Simplified Grid Following Models for the Identification of Sub-Synchronous Oscillations

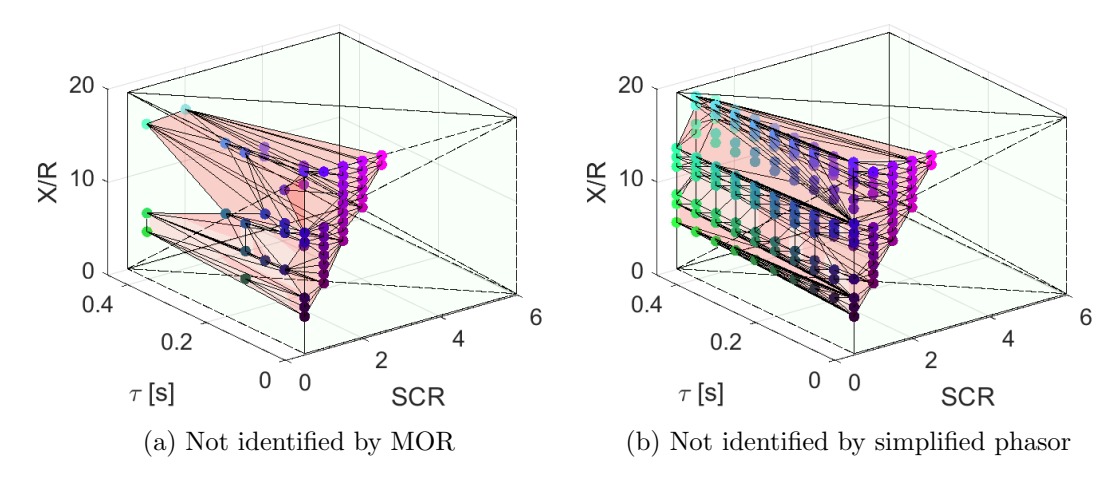


Figure 6.8: Parameter conditions at which the full detail model has oscillatory subsynchronous modes, but are not identified by a) the MOR. b) the simplified phasor. 0.7 pu active power operating point.

for fast  $\tau$  (below 0.1 s), SCR = 0.5 to 2, and X/R = 4 to 20. At this higher active power operating point, the MOR does not recognise modes of concern at very slow time constants, up to  $\tau = 0.4s$ , between X/R = 5 to 17, and SCR = 0.5 to 1.5. This is significant as  $\tau > 0.1s$  is a typical tuning value, about 10 times slower than the inner current controller, [224], and therefore the MOR is expected at typical tunings to accurately identify poorly damped sub-synchronous modes. Figure 6.8a shows that this cannot be assumed.

Figure 6.8b shows the conditions where the simplified phasor, fails to represent the poorly damped sub-synchronous modes. As with Figure 6.7b, the points plotted entirely coincide with all of the conditions where the full detail model has modes of concern. That is to say, the phasor model has been incapable of recognising the modes of concern in any of these conditions, even the cases in the sub-synchronous range.

The modelling methods were then compared for accurate representation of system instability. The full detail SSM highlights the conditions under which the system would be unstable, and the MOR and simplified model are compared to it for recognising instability, by identifying modes in the right hand plane. The full range of parameters identified in Table 6.3 were tested, however only SCR < 2 is shown in the following

Chapter 6. Assessing the Capability and Limitations of Small Signal Simplified Grid Following Models for the Identification of Sub-Synchronous Oscillations

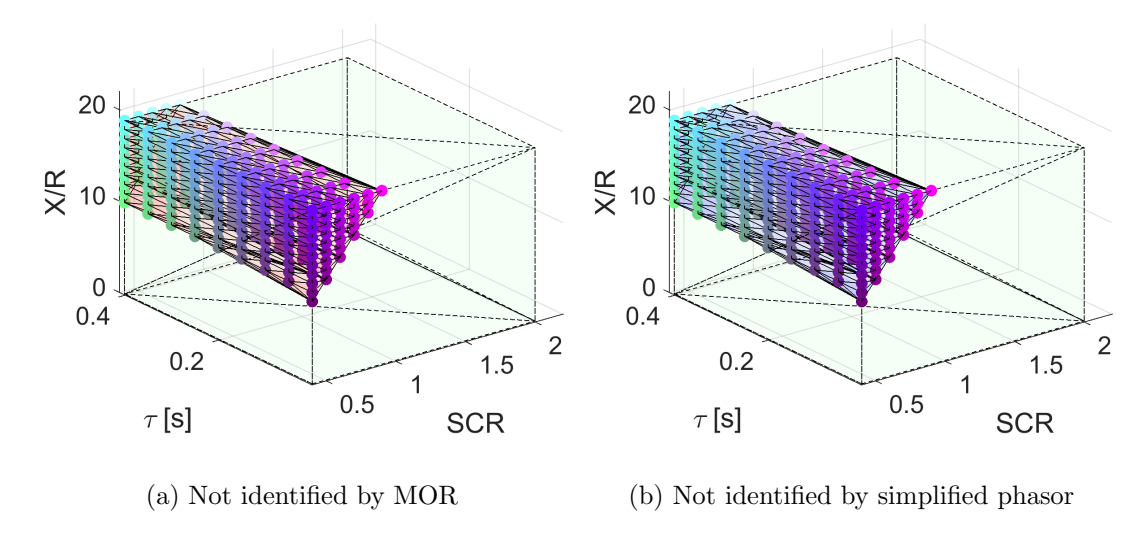


Figure 6.9: Parameter conditions the full detail model indicates instability, that are not recognised in a) the MOR. b) the simplified phasor. Operating point of 0.1 pu active power power.

figures as there were no instances of instability above this. Figure 6.9a and 6.9b show that for the lower power operating point of 0.1 pu, the MOR and the simplified phasor have very similar conditions for which they don't represent instability when the full detail model does. Therefore, it could be concluded that at 0.1 pu active power operating point, for stability indication, there is no benefit to using the MOR over the simplified phasor model at these parametric conditions. However, some caveats to this conclusion arise when considering Figures 6.10d and 6.10e.

However, if the power operating point is increased to 0.7 pu, the modelling methods differ in their ability to represent instability across the parametric range. From Figure 6.10a and Figure 6.10b, the figures show when the simplified phasor and then MOR do not show instability that is represented by the full detail SSM. The MOR and simplified phasor have similar capabilities to each other across the parameters, however there is some variance. Across the full range of  $\tau$ , at SCR = 0.4 to 2 and X/R = 6 to 20, the models are frequently inaccurate. At lower X/R ratios (5 to 8), and lower SCR (0.5 to 1), the simplified phasor model is more accurate than the MOR. Figure 6.10c and 6.10d show when the MOR recognises instability but the simplified phasor does not, and vice versa. The simplified phasor model appears to identify when the system will

be unstable in more situations compared to the MOR method. However the caveats to this are discussed in the next paragraph.

Figure 6.10e shows conditions when the simplified phasor model indicates instability, but the full detail model does not. The full detail model obviously is more accurate than the simplified phasor model (which can be seen in the validation Figure 6.4), and so these parameters show conditions where the simplified phasor model is inaccurate, showing a false positive. This leads to the conclusion also that the simplified phasor model recognising more instability in Figure 6.10c and 6.10d compared to the MOR is not a sign of greater accuracy, but the indication of false positives.

Therefore, it can be concluded that the MOR method can represent when the system has poorly damped modes that could cause unwanted interactions, much more effectively that the simplified phasor model. The simplified phasor can be slightly more suitable for identifying areas of instability at the lower SCR ranges, however this model is more inclined to producing false positives highlighting instability. Ultimately, the full detail SSM is advised for anything below SCR = 2, especially at lower  $\tau$  and X/R 15 to 20.

# 6.5 Summary and Model Suggestions

In this chapter three small signal modelling methods were reviewed for their accuracy compared to the non-linear time domain model and their ability to predict poorly damped oscillatory modes, and unstable operating regions. A series of parametric sweeps were performed across SCR, X/R ratio, and outer power loop time constant, identifying the conditions where only the full detail SSM is capable of accurately representing modes of concern and instability.

The MOR and simplified phasor models both fail to predict instability in low SCR cases, therefore the full detail SSM is required to describe instability in these conditions. If the grid is known to be strong, since the MOR is not more accurate than the simplified phasor, then the latter should be used.

Chapter 6. Assessing the Capability and Limitations of Small Signal Simplified Grid Following Models for the Identification of Sub-Synchronous Oscillations

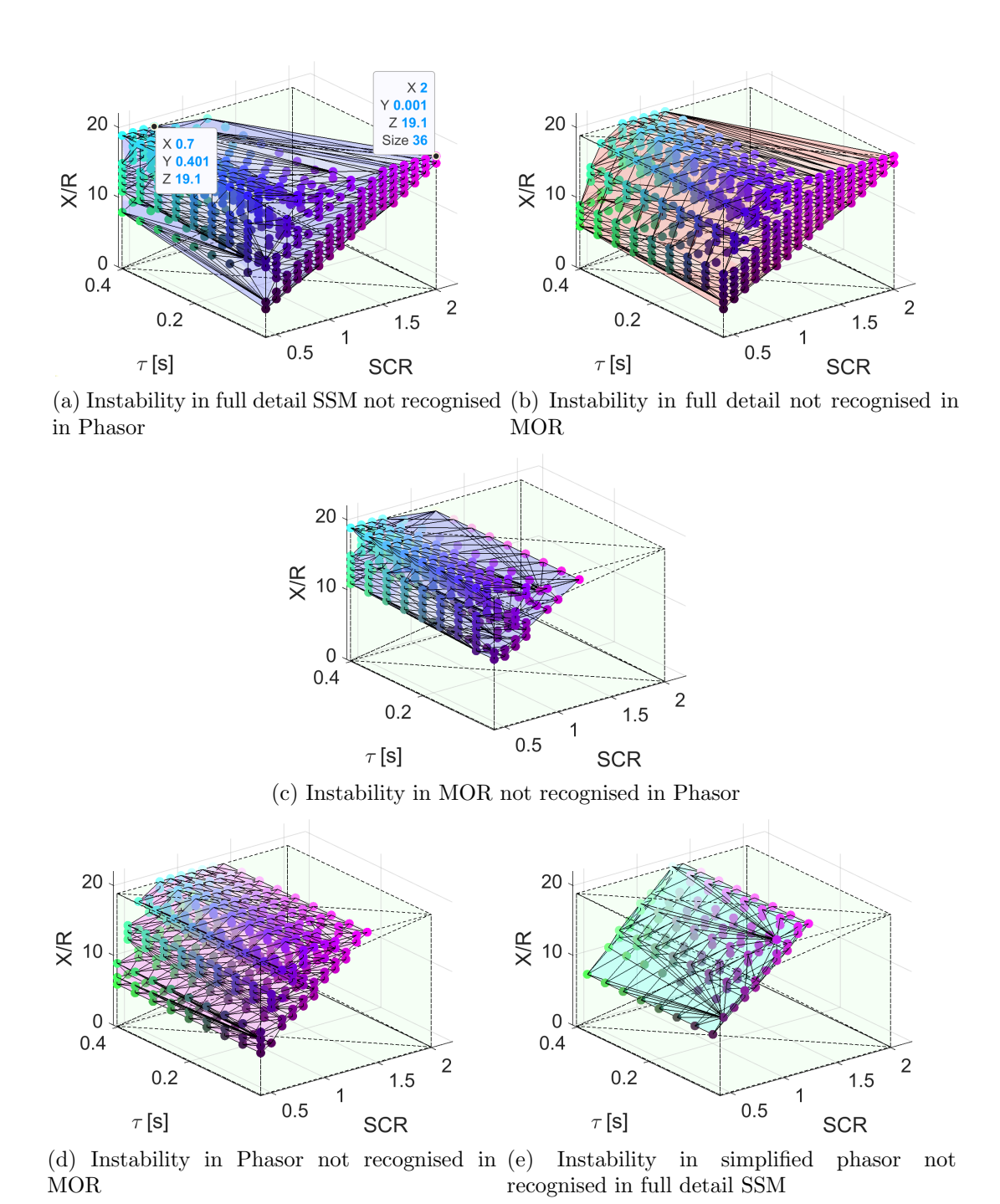


Figure 6.10: Parameter conditions the full detail model indicates instability, that are not recognised in a) the MOR. b) the simplified phasor. Operating Point of 0.7 pu active power power.

Chapter 6. Assessing the Capability and Limitations of Small Signal Simplified Grid Following Models for the Identification of Sub-Synchronous Oscillations

At 0.1 pu active power, the simplified phasor model, across the full range of parameters, had very low accuracy in identifying modes of concern. However, with  $\tau > 0.3$  s, the MOR should be suitable to highlight enough oscillatory mode detail. With low SCR (< 2) and faster time constants,  $\tau < 0.3$ , the full detail model should be used. Increasing the active power to 0.7 pu results in the MOR losing some capability of identifying modes of concern even with slower time power loop time constants up to  $\tau = 0.4$  s. This indicates that even with "typical tuning", at weaker grid conditions of low SCR, the MOR is not viable for model usage, likely due simplification of the inner current controller, and the full detail model should be used.

It is expected that lower detail models will have limitations and will not represent high frequency oscillations. However, it is expected that they will be accurate in indicating instability, and lower frequency oscillatory modes. This study highlights the parameter conditions where the lower detail models fail to capture this detail, and the full detail model should be used in these situations.

# Chapter 7

# Effect of Grid Forming and Grid Following control on Firewall Capability of MMC-HVDC Systems

#### 7.1 Overview

HVDC-VSC/MMC systems have been stated to have an inherent "firewall" capability, which is conventionally described as the prevention of unwanted oscillations between interconnected AC systems, due to the controllability on either side of the link. Typically the control of the converters has been with grid following (GFL) control, however grid forming (GFM) control has become increasingly popular for grid support and these control methods could affect the inherent firewall capability. This Chapter uses electromagnetic transient and small signal models of a point-to-point HVDC-MMC link to identify and verify the firewall capabilities of GFL and GFM controllers in a range of control and grid conditions. Notably, MMC dynamics have been derived and incorporated within these models, which are often neglected for HVDC studies. Critical state dependencies are identified using eigenvalues and participation factors,

which informs parametric selection and worst case scenarios. Although most tunings and conditions do not result in problematic propagation, the GFM was identified to amplify oscillations more than the GFL, highlighting a downside of the grid-supporting outlook, particularly at higher damping and higher droop constants. The conditions under which there exists risk of oscillation propagation between AC grids is highlighted using a novel firewall quantification metric.

#### 7.2 Introduction

Transmission and distribution grids are seeing drastic changes in generation, load sites, stability and reliability of supply. Many sites of renewable generation are located far from demand centres, and so the use of HVDC technology has seen a distinct rise in the last 20 years [292], as well as converter-interfaced generation (CIG).

Early HVDC technology was enabled by Line commutated-converter (LCC) connection, but since the 1970s there have been several updates to converter technology, resulting in Voltage Source Converters (VSC)-HVDC and now, modular multilevel converters (MMC)-HVDC [293]. HVDC has been stated to have an inherent "firewall capability" due to the enhanced controllability of the converters [294] enabling good control of power flow and DC voltage [268]. This has been shown to prevent fault and oscillation propagation from one AC grid to another, producing the "firewall". VSC-HVDC systems offer this capability, as can MMCs, provided the energy balancing control of the sub-module capacitors does not prevent a voltage ripple. The industry is moving towards MMC based systems, which allow for higher voltage step ups, reduced harmonic distortions, and better controllability, with improved scalability and modularity [295,296]. However, there are limitations with MMCs, as internal circulating currents and sub-module capacitor voltages need to be controlled to reduce their 100 Hz harmonic content [297]. Therefore, accurate modelling of these variables and their harmonic content is required.

VSC-HVDC and MMC-HVDC systems have typically employed grid-following (GFL) control strategies, which lack the inherent capabilities of self-synchronization and

Chapter 7. Effect of Grid Forming and Grid Following control on Firewall Capability of MMC-HVDC Systems

voltage support that synchronous generators (SGs) naturally provide [185]. Grid forming (GFM) controllers have been proposed to combat some of these issues, by setting their own frequency, being capable of self-synchronisation [298], acting as a controlled voltage source with a low series impedance, and in some topologies providing inertia [185]. The goal of the GFM converter is to support the AC grid it is interfacing and typically provide more supporting ancillary services compared to GFL converters. Depending on the magnitude and speed of the support, the HVDC firewall capability could be degraded.

There has been research into the limits of firewall capability, however not to the full extent required. Further investigations are needed into MMC-HVDC systems with GFM control, accurate modelling of the HVDC link, and MMC dynamics. For example, much of the literature focuses on the use of grid following, as in [299], or basic gridforming capabilities, such as solely P-f droop control in [300], which also only models one converter, similar to [301]. [302] provides an extensive model overview of MMC-HVDC transmission systems, however they model the MMCs as connected to an ideal DC voltage source. Reference [303] presents a detailed GFM-MMC system, and focuses on the stability of the directly connected AC grid, however, it does not assess the impact of the GFM on the propagation of oscillations to the AC grid on the other side of the HVDC link, and only the virtual inertia and damping coefficient are varied in the parametric sweeps. In [231], a detailed analysis is provided of energy-based control structures in grid-forming converters connected through an MMC-HVDC link to a GFL converter. However, they do not vary the parameters of the system. Sufficiently detailed point-to-point MMC-HVDC models with accurate DC links and MMC dynamics have not been evaluated in the literature to conclude what parameter conditions result in the controllers significantly affecting the firewall capability of the system.

This chapter assesses the research gap, by showing the impact of a virtual synchronous machine (VSM) [232] GFM controller on the firewall capability of a point to point (P2P) MMC-HVDC link. Two small signal systems are compared, the first with a GFM-MMC connected to one grid and a GFL-MMC connected to the second grid

(referred to as the GFM/GFL), and a system with both converters in GFL control (GFL/GFL). They are assessed across various parametric sweeps for the propagation of oscillations from one AC grid, through the HVDC link, to the next. The key control parameters investigated for their impact on firewall capability are the GFM inertia and damping, and DC voltage droop control (on GFL side). The effect of SCR on converter stability has been extensively researched; however, the combination of these parameters with varying SCRs needs to be investigated. The small-signal models will give information on the participation of the system states and their influence on modes that are poorly damped, and of frequencies of concern, such as MMC zero and second harmonic components. From this, the system bode plots with the states of interest can be analysed to find what parameters result in significant oscillation propagation.

The key contributions of this Chapter are, a detailed small signal model (SSM) and large signal model of MMC-HVDC (P2P) system with grid following and grid forming control. Analysis of harmonic content with sufficiently accurate detail at a small signal, and large signal level. A method for identification of oscillatory modes that pose a risk of propagation, as well as a methodology of screening for significant oscillation propagation and participating system states. Also, a firewall quantification metric to identify the conditions that could cause oscillation propagation, and a comprehensive overview of the effect of changing system and control parameters on firewall capability of the HVDC system.

# 7.3 System Under Study

The modelled system is a mono-pole P2P MMC-HVDC system. Two controller systems are implemented: one configuration with GFL controllers on both converters, (referred to as the GFL/GFL), and one with GFM control on terminal 1, and GFL on terminal 2 (GFM/GFL). This is shown in Figure 7.1, showing the equivalent model of the HVDC link, with the two control system tests. Both systems utilise the second GFL to maintain DC voltage control, as there can be difficulties of DC voltage control with inertia emulation on the same controller [304], [305]. Additionally, both control systems utilise

Table 7.1: System Base Parameters

$V_{nom}$	Nominal L-L RMS Voltage $Grid_{jj} = Grid_{kk}$	360 kV
$S_{base}$	Nominal Power	1000 MW
$Z_{b1}$	Base Impedance	$V_n^2/(S_{base1})$
$R_T$	Transformer Resistance	$1.3~\Omega$
$L_T$	Transformer Inductance	$0.033~\Omega$
$R_{cr1}$	Converter Resistance	$\frac{R_m}{2} + R_T$
$L_{cr1}$	Converter Inductance	$\frac{L_m}{2} + L_T$
$R_{nr1}$	Grid Resistance	$\frac{0.1Z_{b1}}{SCR}$
$L_{nr1}$	Grid Inductance	$\frac{Z_{base1}}{2\pi\omega SCR}$
$R_m$	Arm Resistance	$0.08~\Omega$
$L_m$	Arm Inductance	0.084~mH
$C_m$	MMC Sub-Module Capacitance	$31.42\mu C$
$L_{DC}$	DC Link Inductance	1.5 mH
$L_{Link}$	DC Reactor	1.5 mH

circulating current suppression, and not energy balancing control, to not restrict the voltage ripple in the sub-module capacitance. Table 7.1 gives an overview of system parameters, with Section 7.5 detailing system modelling. The representation of one grid-connected MMC topology is shown in Figure 7.2.

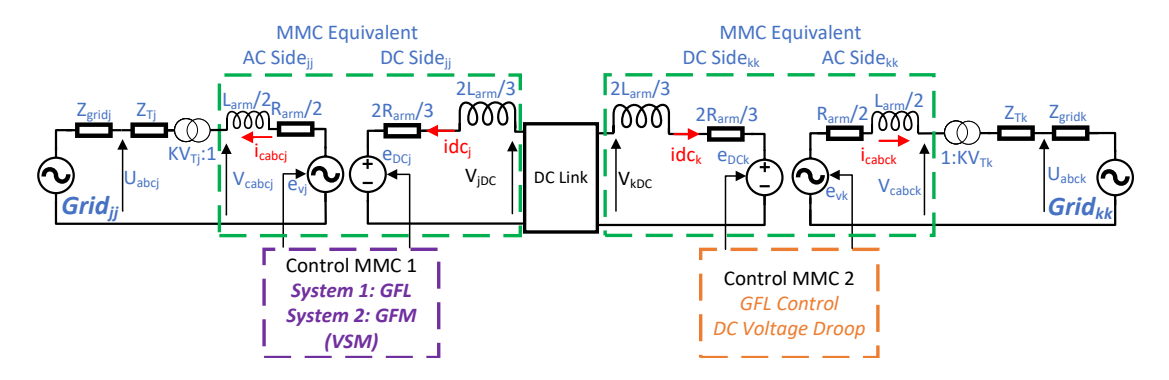


Figure 7.1: AC  $grid_{jj}$  to AC  $grid_{kk}$  through HVDC-MMC link.

The equivalent model of the point-to-point system is shown in Figure 7.1, and the full detail of one grid-connected MMC topology can be observed in Figure 7.2. The grid side resistance and inductance,  $R_{nr1}$  and  $L_{nr1}$ , vary depending on the SCR, the MMC arm impedance is  $R_m$  and  $L_m$ , and average sub-module capacitance is  $C_m$ . The mathematical representation of the MMC is fully described in Section 7.5, and then

linearised to make the small signal model.

## 7.4 Methodology

The goal of this research is to highlight parameter conditions where the implementation of converter control (GFL and GFM) inhibits the firewall effect of MMC-HVDC systems, as well as presenting a comprehensive method of assessing when the firewall effect is limited. The methodology is presented in this section.

#### 7.4.1 Small Signal Model Development

Full detail EMT models are built to verify time-domain behaviour of the systems, while a small signal model of the system is derived to enable the use of classic control methods [21]. To obtain the SSM, the non-linear equations for the full system, shown in Figure 7.1, are represented in the rotating reference frame and linearised around their operating point. The linearised state space representation is expressed by

$$\frac{d\Delta x}{dt} = A\Delta x + B\Delta u \tag{7.1}$$

$$\Delta y = C\Delta x + D\Delta u \tag{7.2}$$

Where the state, input and output variables are  $\Delta x$ ,  $\Delta u$ , and  $\Delta y$ , and A, B, C and D are the state, input, output, and feed-through matrices [21].

#### 7.4.2 Identifying Problem Modes and Participating States

For the two tested systems (GFM/GFL and GFL/GFL), the eigenvalues of the small signal model will be analysed to highlight poorly damped modes in the systems across a range of parameters. The parameters varied in this study are: SCR of both AC grids, GFM inertia (H), GFM damping (D), DC voltage droop, and grid SCRs. The SCR is varied from 1 to 6, (weak grid, SCR < 2, to strong grid, SCR > 2) [269]. VSM inertia is varied, from low values,  $0 \le H < 1 \le [306]$ , to large H = 10 s [307], [308]. Damping is tested from very low values of below 10 pu [309], up to  $10^4$  pu [310].

Chapter 7. Effect of Grid Forming and Grid Following control on Firewall Capability of MMC-HVDC Systems

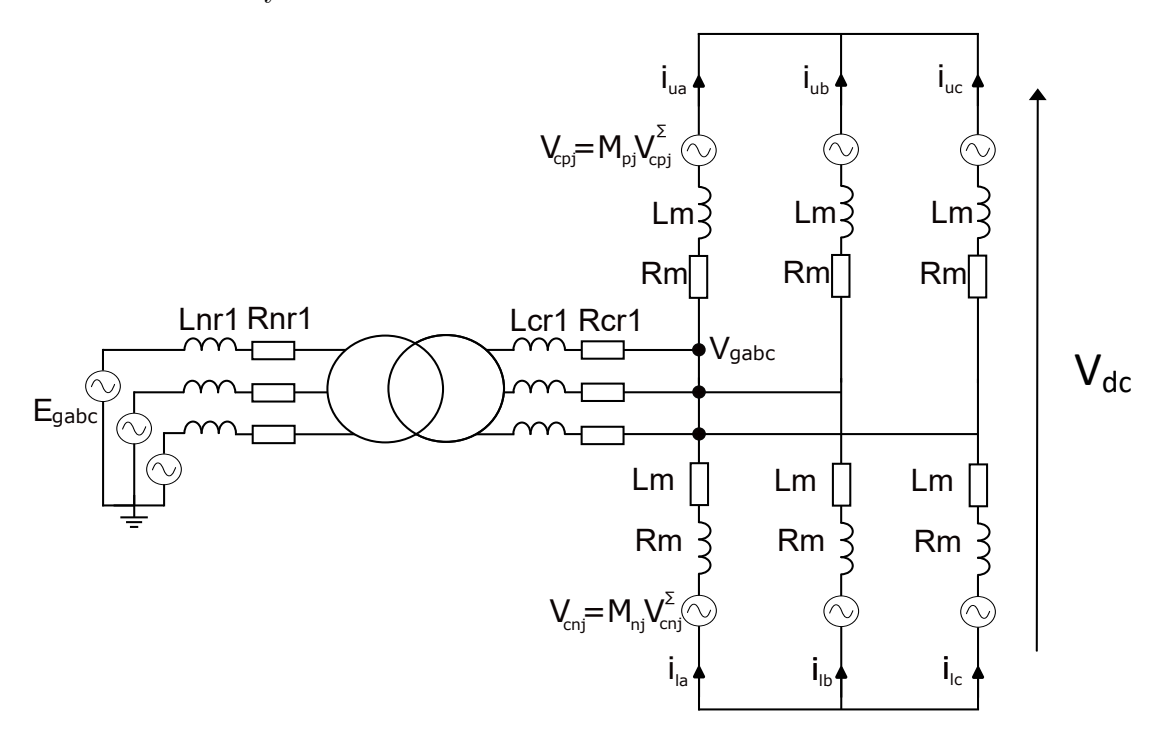


Figure 7.2: Single MMC topology connected to AC grid.

The eigenvalues of the system are defined by (7.3), and the damping of each eigenvalue,  $\zeta$ , is derived using (7.4). In this study, a value of  $\zeta < 0.1$  damping ratio has been selected as the limit of a poorly damped mode, as a value outside of this range, in the literature, has been stated to be poorly damped [21], [226].

$$\lambda_i = a_i + jb_i \tag{7.3}$$

$$\zeta = \frac{a_i}{\sqrt{a_i^2 + b_i^2}} \tag{7.4}$$

The states that participate in these modes are identified using participation factors, shown in equation (7.5). The derivation is described in Appendix D, but in brief, they are quantification of the amount each state participates in an identified mode. If  $\lambda_i$  is the  $i^{th}$  eigenvalue in the system, then  $p_{ki}$  is the participation factor of the  $k^{th}$  state variable of the A matrix in the mode being analysed.  $p_{ki}$  is calculated with  $w_{ki}$  and  $v_{ki}$ , which are the  $k_{th}$  entries in the left and right eigenvector of the  $i_{th}$  eigenvalue [311].

This is to reduce the number of states to be reviewed in the bode plots (described in the next subsection). The most relevant states from  $grid_{jj}$  (input) to  $grid_{kk}$  (output) are selected to create the bode plots.

$$p_{ki} = \frac{|v_{ki}||w_{ki}|}{\sum_{k=1}^{n} |v_{ki}||w_{ki}|}$$
(7.5)

#### 7.4.3 Bode Plot Input-Output Selections

Once the participating states of the problem modes have been identified, this information can be used to obtain relevant state input-output (I/O) bode responses, to analyse the amplification of oscillations. In this study, the input disturbances will be injected on  $grid_{jj}$ , and the output will be observed on  $grid_{kk}$ . The selected responses are reviewed across the full parametric range, and from the bode plots it will be identified at what parameters the grid following only system is more effective as a "firewall", and when the system with the GFM negatively impacts this, and vice versa.

#### 7.4.4 Heat-maps for Screening of Propagation Risk Conditions

To give an overall screening method to quickly establish the parameters that might mitigate firewall response, heat-maps of the peak magnitude of the bode plots, across the parametric sweeps will be created. This gives a comprehensive overview of the effect of parameters on oscillation propagation. The heat-maps can act as a screening method, then the bode plots can be assessed in more detail for the frequencies of poorly damped oscillations and to visualise the trends. In this paper, the heat-maps are presented after the bode plot analysis to give a comprehensive overview of the effect of system parameters and tunings on magnitude propagation.

#### 7.4.5 Firewall Quantification Metric

For different I/O variable types, the threshold for a magnitude response that amplifies an oscillation is not intuitive from a bode plot, in decibels. Therefore, to express the passing of oscillations between different I/O signal combinations, a firewall metric is defined. The calculated gain response is normalised by the per unit input and output

variables. For example, for an input variable type X disturbance to an output variable type Y, the normalised gain,  $G_{nom}$ , is expressed as the product of the gain of the bode G (in ratio not dB), with the ratio of the nominal input and output (7.6).

$$G_{nom} = G \frac{X_{nominal}}{Y_{nominal}} \tag{7.6}$$

It is expected that there will be power transfer from one grid to the other, however, with this representation, any  $G_{nom}$  greater than 1 pu is amplifying the response, indicating firewall capability is being greatly inhibited. Ultimately, effective firewall behaviour would be indicated by a  $G_{nom} = 0$ , for zero oscillation transfer. Therefore, even though a normalised  $G_{nom}$  less than one (but greater than zero) would represent a small normalised oscillation transfer, it could still represent an undesirable passing of oscillations from one system to another. For representation in the heat-maps, the peak magnitude presented will be in this per unit normalised gain, to better understand the propagation of the oscillation.

## 7.5 Small Signal Model

The full system can be seen in Figure 7.1, (with the DC link shown in Figure 7.3. The sub-sections are explained in this section, and the system equations are transformed into the synchronous reference frame. Throughout this paper, the grid frame is represented by xy, and the converter frame as dq, with  $\theta$  being the angle difference between these two frames [299], transformed by:

$$d + jq = (x + jy)e^{-j\theta} \tag{7.7}$$

$$x + jy = (d + jq)e^{j\theta} (7.8)$$

#### **AC Grid Equations**

The AC side of the system from Figure 7.2 can be represented in state space form, with the state variables and input variables defined by  $\Delta x_{grid}$  and  $\Delta u_{grid}$ . The grid

state matrices are  $A_{grid}$ ,  $B_{grid}$ ,  $C_{grid}$  and  $D_{grid}$ , with output variables  $\Delta y_{grid}$  defined by (7.11).

$$\Delta x_{qrid} = [\Delta i_{qcx}, \Delta i_{qcy}, \Delta U_{cx}, \Delta U_{cy}, \Delta i_{nx}, \Delta i_{ny}]^T$$
(7.9)

$$\Delta u_{grid} = [\Delta V_{cx}, \Delta V_{cy}, \Delta E_{cx}, \Delta E_{cy}]^T$$
(7.10)

$$\Delta y_{grid} = [\Delta i_{gcx}, \Delta i_{gcy}, \Delta u_{cx}, \Delta u_{cy}]^T$$
(7.11)

$$A_{grid} = \begin{bmatrix} \frac{-R_{cr1}}{L_{cr1}} & \omega & \frac{-1}{L_{cr1}} & 0 & 0 & 0\\ -\omega & \frac{-R_{cr1}}{L_{cr1}} & 0 & \frac{-1}{L_{cr1}} & 0 & 0\\ \frac{1}{C_f} & 0 & 0 & \omega & \frac{-1}{C_f} & 0\\ 0 & \frac{1}{C_f} & -\omega & 0 & 0 & \frac{-1}{C_f}\\ 0 & 0 & \frac{1}{L_{nr1}} & 0 & \frac{-R_{cr1}}{L_{cr1}} & \omega\\ 0 & 0 & 0 & \frac{1}{L_{nr1}} & -\omega & \frac{-R_{cr1}}{L_{cr1}} \end{bmatrix}$$
(7.12)

$$B_{grid} = \begin{bmatrix} \frac{1}{L_{cr1}} & 0 & 0 & 0\\ 0 & \frac{1}{L_{cr1}} & 0 & 0\\ 0 & 0 & \frac{-1}{L_{nr1}} & 0\\ 0 & 0 & 0 & \frac{-1}{L_{gr1}} \end{bmatrix}$$
 (7.13)

$$C_{grid} = \begin{bmatrix} 1 & 0 & 0 & 0 \\ 0 & 1 & 0 & 0 \\ 0 & 0 & 1 & 0 \\ 0 & 0 & 0 & 1 \end{bmatrix}$$
 (7.14)

$$D_{grid} = zero(4x4) (7.15)$$

#### MMC Dynamics

For each system the AC grid to MMC connection is modelled as shown in Figure 7.2. The current through the AC side can be defined by  $i_{gc}$ , which flows through grid side resistance and inductance,  $R_{nr1}$  and  $L_{nr1}$ , transformer with turns ratio  $K_T$ , and through the converter side impedance,  $R_{cr1}$  and  $L_{cr1}$ . The upper and lower arm currents are defined by  $i_{uacb}$  and  $i_{labc}$  respectively. The voltage across the combined submodules

can be defined by

$$V_{cuabc} = M_{uabc} V_{cuabc}^{\Sigma} \tag{7.16}$$

where  $V_{cuabc}$  is the output arm voltage,  $M_{abc}$  is the modulation index and  $V_{cuabc}^{\sum}$  is the sum of the capacitor voltages across the sub-modules. From Figure 7.2, the equations for circulating currents, voltage across the MMC submodules, and grid currents and voltages can be derived.

$$V_{gabc} + \frac{L_m di_{uabc}}{dt} + R_m i_{uabc} + V_{uabc} = \frac{V_{dc}}{2}$$

$$(7.17)$$

$$V_{gabc} - \frac{L_m di_{labc}}{dt} - R_m i_{labc} + V_{labc} = \frac{-V_{dc}}{2}$$
(7.18)

$$C_m \frac{dV_{cuabc}^{\Sigma}}{dt} = m_{uabc} i_{uabc} \tag{7.19}$$

$$C_m \frac{dV_{clabc}^{\Sigma}}{dt} = m_{labc} i_{labc} \tag{7.20}$$

where the upper and lower arm currents can be combined to define the circulating current,  $i_{diff}$ , and the grid current,  $i_{gc}$  from

$$i_{diff_{abc}} = \frac{i_{uabc} + i_{labc}}{2} \tag{7.21}$$

$$i_{gcabc} = \frac{i_{uabc} - i_{labc}}{2} \tag{7.22}$$

From equations 7.17 to 7.20, and considering equations 7.21 and 7.22, the circulating and grid currents can be expressed in state space representation

$$\frac{di_{gcabc}}{dt} = -\frac{R_m}{L_m} i_{gcabc} - \frac{m_{uabc} v_{cuabc}^{\Sigma}}{2L_m} + \frac{m_{labc} v_{clabc}^{\Sigma}}{2L_m} + \frac{2V_n}{L_m} - \frac{2V_{gabc}}{L_m} K_T$$
 (7.23)

$$\frac{di_{diff_{abc}}}{dt} = -\frac{R_m}{L_m} i_{diff} - \frac{m_{uabc} v_{cuabc}^{\Sigma}}{2L_m} - \frac{m_{labc} v_{clabc}^{\Sigma}}{2L_m} + \frac{V_{dc}}{2L_m}$$
(7.24)

and the voltage across sub-modules can be expressed as

$$\frac{dV_{cuabc}^{\sum}}{t} = \frac{m_{uabc}}{C_m} i_{diff} + \frac{m_{uabc}}{2C_m} i_{gcabc}$$
 (7.25)

$$\frac{dV_{clabc}^{\sum}}{t} = \frac{m_{labc}}{C_m} i_{diff} - \frac{m_{labc}}{2C_m} i_{gcabc}$$
 (7.26)

where the positive and negative modulation indices are defined by the outputs of the inner control loops. For each phase, the  $\mathbf{m_u}$  and  $\mathbf{m_l}$  are defined by (7.27). The  $2\omega t$  term is introduced to represent the 2nd order harmonic dq term, required to represent the dynamic detail of the circulating currents and sub-module voltages in the MMC [312].

$$\mathbf{m_u} = \frac{1}{2} \left( 1 - M\cos(\omega t) - M_2 \cos(2\omega t) \right) \tag{7.27}$$

$$\mathbf{m_l} = \frac{1}{2} \left( 1 + M\cos(\omega t) - M_2\cos(2\omega t) \right) \tag{7.28}$$

where M and  $M_2$  are the outputs from the inner and circulating current control loops. A generic oscillating signal, X(t), can be represented in terms of its zero, fundamental, and 2nd harmonic components as in equation (7.29).

$$X(t) = X_0 + X_X cos(\omega t) + X_Y sin(\omega t) + X_{X2} cos(2\omega t) + X_{Y2} cos(2\omega t)$$

$$(7.29)$$

If the modulation index signals from (7.27) and (7.28) are considered in their xy components, as

$$\mathbf{m_a} = M\cos(\omega t) = M_x \cos(\omega t) - M_y \sin(\omega t) \tag{7.30}$$

$$\mathbf{m_{2a}} = M_2 cos(2\omega t) = M_{x2} cos(\omega t) - M_{2u} sin(\omega t) \tag{7.31}$$

the applied modulation to the upper and lower arms can be represented in the xy frame, for zero component, fundamental frequency and 100 Hz component. This is achieved by equating the expanded xy terms in (7.27) and (7.28) to the expanded signal in (7.29).

$$\mathbf{m_u} = (\frac{1}{2})_0 + (\frac{-M_x}{2})_x cos(\omega t) + (\frac{M_y}{2})_y sin(\omega t) + (\frac{-M_{x2}}{2})_{x2} cos(2\omega t) + (\frac{M_{y2}}{2})_{y2} sin(2\omega t)$$
(7.32)

$$\mathbf{m_l} = (\frac{1}{2})_0 + (\frac{M_x}{2})_x cos(\omega t) + (\frac{-M_y}{2})_y sin(\omega t) + (\frac{-M_{x2}}{2})_{x2} cos(2\omega t) + (\frac{M_{y2}}{2})_{y2} sin(2\omega t)$$
(7.33)

If equations 7.25 and 7.26 (the upper and lower voltages) are expanded for their fundamental components, then the tre representation in the xy frame is shown as

such.

$$V_{clx} = \frac{1}{\omega C} \left( \frac{M_y}{2} I_{diff0} - \frac{M_y}{4} I_{diffx2} + \frac{M_x}{4} I_{diffy2} - \frac{i_{gy}}{4} \right)$$
 (7.34)

$$V_{cly} = \frac{1}{\omega C} \left( \frac{-M_x}{2} I_{diff0} - \frac{M_x}{4} I_{diffx2} - \frac{M_y}{4} I_{diffy2} - \frac{i_{gx}}{4} \right)$$
 (7.35)

$$V_{cux} = \frac{1}{\omega C} \left( \frac{-M_y}{2} I_{diff0} + \frac{M_y}{4} I_{diffx2} - \frac{M_x}{4} I_{diffy2} + \frac{i_{gy}}{4} \right)$$
 (7.36)

$$V_{cuy} = \frac{-1}{\omega C} \left( \frac{-M_x}{2} I_{diff0} - \frac{M_x}{4} I_{diffx2} - \frac{M_y}{4} I_{diffy2} + \frac{i_{gx}}{4} \right)$$
 (7.37)

Comparing the upper and lower arm expanded equations, it can be concluded that they are negative of each other.

$$V_{cux} = -V_{clx} (7.38)$$

$$V_{cuy} = -V_{cly} (7.39)$$

For the fundamental component of voltage, the zero component of the  $i_{diff}$  equation (7.24), is expanded, and the equivalence between upper and lower fundamental component of the voltage can be defined by

$$V_{UC0}^{\sum} = V_{LC0}^{\sum} \tag{7.40}$$

with the relation of the lower arm voltage components to the upper voltages, the equations from (7.17 to 7.20) can be expanded and put in state space representation. The state and input variables  $\Delta x$  and  $\Delta u$  are defined by

$$\Delta x = [\Delta i_{diffx2}, \Delta i_{diffy2}, \Delta i_{diff0}, \Delta V_{CUx2}, \Delta V_{CUy2}, \Delta V_{CUx}, \Delta V_{CUy}, \Delta V_{CUy}]^T \quad (7.41)$$

$$\Delta u = [\Delta i_{gx}, \Delta i_{gy}, \Delta M_x, \Delta M_y, \Delta M_{x2}, \Delta M_{y2}, \Delta V_{DC}]^T$$
(7.42)

with the state and input matrices,  $A_{MMC}$  and  $B_{MMC}$ , defined by (7.43) and (7.44).

$$\begin{bmatrix} \frac{-R_m}{L_m} & 2\omega & 0 & \frac{-1}{2L_m} & 0 & \frac{M_{x0}}{4L_m} & \frac{-M_{y0}}{4L_m} & \frac{M_{x20}}{2L_m} \\ -2\omega & \frac{-R_m}{L_m} & 0 & 0 & \frac{-1}{2L_m} & \frac{M_{y0}}{4L_m} & \frac{M_{x0}}{4L_m} & \frac{M_{y20}}{2L_m} \\ 0 & 0 & \frac{-R_m}{L_m} & \frac{M_{x20}}{4L_m} & \frac{M_{y20}}{4L_m} & \frac{M_{x0}}{4L_m} & \frac{M_{y0}}{4L_m} & \frac{-1}{2L_m} \\ \frac{1}{2C_m} & 0 & \frac{-M_{x20}}{2C_m} & 0 & 2\omega & 0 & 0 & 0 \\ 0 & \frac{1}{2C_m} & \frac{-M_{y20}}{2C_m} & -2\omega & 0 & 0 & 0 & 0 \\ \frac{-M_{x0}}{4C_m} & \frac{-M_{y0}}{4C_m} & \frac{M_{x0}}{2C_m} & 0 & 0 & \omega & 0 \\ \frac{M_{y0}}{4C_m} & \frac{-M_{x0}}{4C_m} & \frac{-M_{y0}}{2C_m} & 0 & 0 & -\omega & 0 & 0 \\ \frac{-M_{x20}}{4C_m} & \frac{-M_{y20}}{4C_m} & \frac{1}{2C_m} & 0 & 0 & 0 & 0 & 0 \end{bmatrix}$$

$$(7.43)$$

$$\begin{bmatrix} 0 & 0 & \frac{V_{UCx0}^{\Sigma}}{4L_m} & \frac{-V_{UCy0}^{\Sigma}}{4L_m} & \frac{V_{UC00}^{\Sigma}}{-2L_m} & 0 & 0\\ 0 & 0 & \frac{V_{UCy0}^{\Sigma}}{4L_m} & \frac{V_{UCx0}^{\Sigma}}{4L_m} & 0 & \frac{V_{UC00}^{\Sigma}}{4L_m} & 0\\ 0 & 0 & \frac{V_{UCx0}^{\Sigma}}{4L_m} & \frac{V_{UCy0}^{\Sigma}}{4L_m} & \frac{V_{UCx20}^{\Sigma}}{4L_m} & \frac{V_{UCy20}^{\Sigma}}{4L_m} & \frac{1}{2L_m} \end{bmatrix}$$

$$(7.44)$$

#### Converter Side Voltages

The equivalent converter side voltages can be defined by

$$\frac{-V_{uabc} + V_{labc}}{2} = V_{cabc} \tag{7.45}$$

where  $V_{cabc}$  is the converter AC voltage. This is now represented in the rotating reference frame

$$V_{cx} = \frac{1}{2} (m_l V_{LC}^{\epsilon})_d - \frac{1}{2} (m_u V_{UC}^{\epsilon})_d$$
 (7.46)

$$V_{cy} = \frac{1}{2} (m_l V_{LC}^{\epsilon})_q - \frac{1}{2} (m_u V_{UC}^{\epsilon})_q$$
 (7.47)

$$V_{cx} = \frac{((2M_x V_{UC0}^{\Sigma}) + (-2 + M_{x2})(V_{UCx}^{\Sigma})}{4} + \frac{M_y 2(V_{UCy}^{\Sigma})}{4} + \frac{M_x V_{UCx2}^{\Sigma}}{4} + \frac{M_y V_{UCy2}^{\Sigma}}{4})$$
(7.48)

$$V_{cy} = \frac{(M_y V_{UC0}^{\Sigma})}{2} - (\frac{2}{4} + \frac{M_{x2}}{4})(V_{UCy}^{\Sigma}) + (\frac{M_{y2}}{4})(V_{UCx}^{\Sigma}) - (V_{UCx2}^{\Sigma})(\frac{M_y}{4}) + (V_{UCy2}^{\Sigma})(\frac{M_x}{4})$$

$$(7.49)$$

which are then linearised around the operating point and the small signal model can be obtained, given in Appendix E.

The DC side converter voltage is defined by  $E_{DC}$  which is the same of the three positive and negative arm phase voltages,

$$E_{DC} = \frac{1}{3} \sum_{j=A,B,C} (V_{CU_j} + V_{CL_j})$$
 (7.50)

and then take the zero component of this equation to obtain the DC only component.

$$E_{DC} = V_{UC0}^{\sum} - \frac{M_{x2}}{2} V_{UCx2}^{\sum} - \frac{M_{y2}}{2} V_{UCy2}^{\sum} - \frac{M_{x}}{2} V_{UCx}^{\sum} - \frac{M_{y}}{2} V_{UCy}^{\sum}$$

$$(7.51)$$

#### 7.5.1 DC Link

The DC Link structure is shown in Figure 7.3. From this, the output voltage from the converters can be related to the voltage and currents at either end of the DC link. The DC link voltage,  $V_{DC}$ , input to the converter MMC equations shown in equation (7.42) is obtained from the equations below, with the final derivation in equation (7.56). In this instance, the voltage obtained from the DC link is on the  $grid_{jj}$  side, therefore for the converter MMC equations  $V_{DC} = V_{jDC}$ . When obtaining the MMC equations for the converter at  $grid_{kk}$ , the DC link voltage  $V_{kdc}$  must be obtained and input to (7.42).

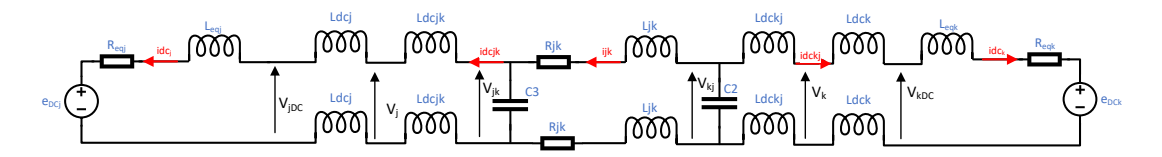


Figure 7.3: AC  $Grid_{jj}$  to AC  $Grid_{kk}$  through HVDC-MMC link.

$$\frac{dV_{jk}}{dt} = \frac{1}{C_1} i_{jk} - \frac{1}{C_1} i_{dcj} \tag{7.52}$$

$$\frac{dV_{kj}}{dt} = \frac{-1}{C_2} i_{jk} - \frac{1}{C_2} i_{dck} \tag{7.53}$$

$$\frac{di_{jk}}{dt} = \frac{-1}{2L_{jk}}V_{jk} + \frac{1}{2L_{jk}}V_{kj} - \frac{R_{jk}}{L_{jk}}$$
(7.54)

$$\frac{di_{dcj}}{dt} = \frac{V_j - V_{jDC}}{2L_{dcjk}} \tag{7.55}$$

$$V_{jDC} = \frac{2L_{dc}}{2L_{dc} + \frac{2}{3}L_{arm}} (e_{dc} + \frac{2R_{arm}}{3}i_{dcj})$$
 (7.56)

$$V_{j} = \frac{1}{2L_{dcj} + \frac{2}{3}L_{arm}} \left(e_{dcj} + \frac{2R_{arm}}{3}i_{dcj}\right) + \frac{\frac{(2L_{arm}}{3} + 2L_{DCj})V_{jk}}{2L_{dcjk}}$$
(7.57)

Following the derivation of the equations, the state space representation is shown by  $A_{DC}, B_{DC}, C_{DC}$  and  $D_{DC}$ .

$$A_{DC} = \begin{bmatrix} \frac{-R_{dc}}{L_{dc}} & \frac{1}{2L_{dc}} & \frac{-1}{2L_{dc}} \\ \frac{-1}{C_2} & 0 & 0 \\ \frac{1}{C_1} & 0 & 0 \end{bmatrix}$$
 (7.58)

$$B_{DC} = \begin{bmatrix} 0 & 0 \\ \frac{-1}{C_2} & 0 \\ 0 & \frac{-1}{C_1} \end{bmatrix}$$
 (7.59)

$$C_{DC} = \begin{bmatrix} 0 & 1 & 0 \\ 0 & 0 & 1 \\ 1 & 0 & 0 \end{bmatrix} \tag{7.60}$$

$$D_{DC} = 0 (7.61)$$

With the state and input variables defined by  $\Delta x_{dc}$  and  $\Delta u_{dc}$  respectively.

$$\Delta \mathbf{x_{dc}} = [\mathbf{i_{jk}}, \mathbf{V_{kj}}, \mathbf{V_{jk}}]^{\mathbf{T}}$$
 (7.62)

$$\Delta \mathbf{u_{dc}} = [\mathbf{i_{dck}}, \mathbf{i_{dci}}]^{\mathbf{T}} \tag{7.63}$$

The only inputs to the DC link required are the DC currents flowing out of each DC side of the converter, which are calculated from the zero component of the circulating current,  $i_{dc} = 3i_{diff0}$ . From the DC link, and equation (7.57), the DC Voltage outputs required,  $V_{jdc}$  and  $V_{kdc}$ , for the internal MMC dynamics can be obtained.

#### Grid Following Current Controller

For the grid following controller the inner current loop is used to control the voltage at the applied terminals. The control structure is shown in Figure 7.4. The current controller state space representation is given by

$$A_{cc} = 0 \tag{7.64}$$

$$B_{cc} = \begin{bmatrix} 1 & 0 & -1 & 0 & 0 & 0 \\ 0 & 1 & 0 & -1 & 0 & 0 \end{bmatrix}$$
 (7.65)

$$C_{cc} = \begin{bmatrix} K_{iCC} & 0\\ 0 & K_{iCC} \end{bmatrix} \tag{7.66}$$

$$D_{cc} = \begin{bmatrix} K_{pCC} & 0 & -K_{pCC} & -\omega L_c & 1 & 0 \\ 0 & K_{PCC} & \omega L_c & -K_{pCC} & 0 & 1 \end{bmatrix}$$
 (7.67)

Where the state, input and output variables are defined by  $\Delta x_{cc}$ ,  $\Delta u_{cc}$  and  $\Delta y_{cc}$ 

$$\Delta x_{cc} = [\Delta e i_d^c, \Delta e i_a^c]^T \tag{7.68}$$

$$\Delta \boldsymbol{u_{cc}} = [\Delta \boldsymbol{i_{cd}^*}, \Delta \boldsymbol{i_{cq}^*}, \Delta \boldsymbol{i_{cd}^c}, \Delta \boldsymbol{i_{cq}^c}, \Delta \boldsymbol{u_d^c}, \boldsymbol{u_q^c}]^T$$
(7.69)

$$\Delta \boldsymbol{y_{cc}} = [\Delta \boldsymbol{v_d^c}, \Delta \boldsymbol{v_q^c}]^T \tag{7.70}$$

The proportional and integral gains of the current loop PI controllers are  $K_{pCC}$  and  $K_{iCC}$  respectively, and  $\Delta e i_d^c$  and  $\Delta e i_q^c$  are the errors between reference current and measured current for the d and q components respectively.

The reference currents are produced but the outer loop equations. In the GFL/GFL, the control on  $grid_{jj}$  produces the references using the same control shown in Chapter 6 Section 6.3.2. For both the GFL/GFL and GFM/GFL, the control on  $grid_{kk}$  uses the same AC voltage control on the outer loop, and the DC voltage droop control described in Section (7.5.3).

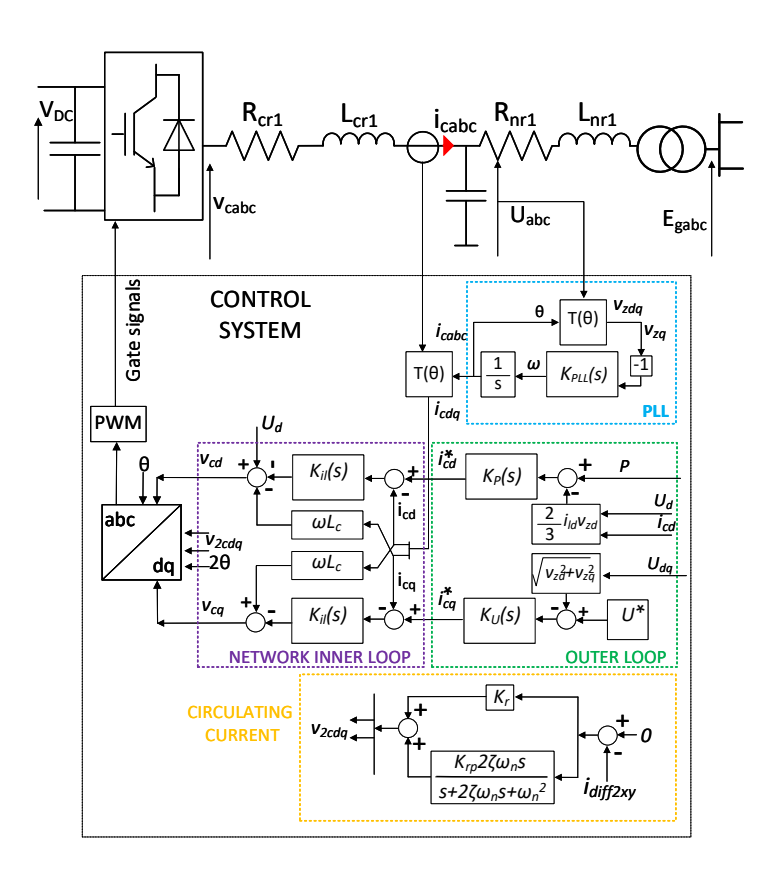


Figure 7.4: Grid following current control.

A key feature of the grid following converter is its reliance on a PLL to synchronise with the grid and follow the voltage. The grid angle is obtained from

$$\theta = \frac{(K_{PLL}U_q)}{s} \tag{7.71}$$

Which can be linearised and used in conjunction with the park transform. A full

description of the PLL and its derivation is given in Chapter 3

$$\frac{\Delta\theta}{\Delta U_q} = \frac{Kp_{PLL}s + Ki_{PLL}}{s^2 + a_0s + b_0} \tag{7.72}$$

where  $a_0 = (Kp_{PLL}cos(\theta_0)U_{d0} + Kp_{PLL}sin(\theta_0)U_{q0})$ ,  $b_0 = (Ki_{PLL}cos(\theta_0)U_{d0} + Ki_{PLL}sin(\theta_0)U_{q0})$ , with the proportional and integral gains of the PLL defined by  $Kp_{PLL}$  and  $Ki_{PLL}$ .

$$Kp_{PLL} = \frac{2\omega_n}{E_m}, \quad \tau_{PLL} = \frac{2\zeta}{\omega_n}, \quad Ki_{PLL} = \frac{Kp_{PLL}}{\tau_{PLL}}$$
 (7.73)

with  $E_m$  as the nominal input voltage,  $\zeta$  is the damping ratio of the response, and  $\tau_{PLL}$  as the PLL time constant.

#### 7.5.2 MMC Circulating Currents

The MMC circulating currents also need to be limited by the circulating suppression control. The input measured circulating currents are passed through the equation in (7.74), producing the output modulation indices  $M_{2xy}$ . The full details of this suppression control is given in [313].

$$K(s) = \frac{-2}{V_{dc}} \frac{K_{rp}s^2 + (K_{rp}K_{rr}2\omega\zeta_c)s + K_{rp}\omega_n^2)}{(s^2 + 2\omega\zeta_cs + \omega_n^2)}$$
(7.74)

where  $\omega_n$  is the frequency of the circulating currents, 100 Hz, and  $K_{rp}$  and  $K_{rr}$  are proportional gains. The selected damping ratio of the transfer function is defined by  $\zeta_c$ .

#### 7.5.3 DC Voltage Droop

The DC voltage droop control [314], [315] is in both systems, on the converter connected to  $grid_{kk}$  (as seen in Figure 7.1). This control maintains the DC voltage across the HVDC link, and was implemented on the converter that is always operated in GFL control across both systems (on  $grid_{kk}$ ), as inertia emulation in a GFM can counteract

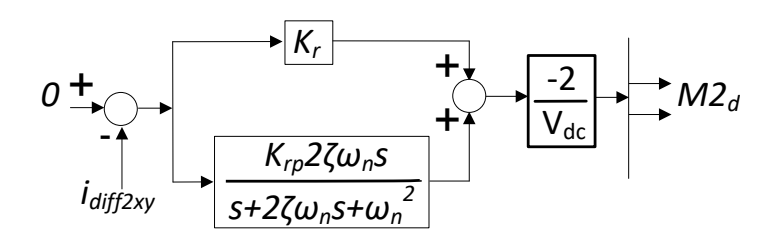


Figure 7.5: Circulating current controller.

the DC voltage control [304], [305].

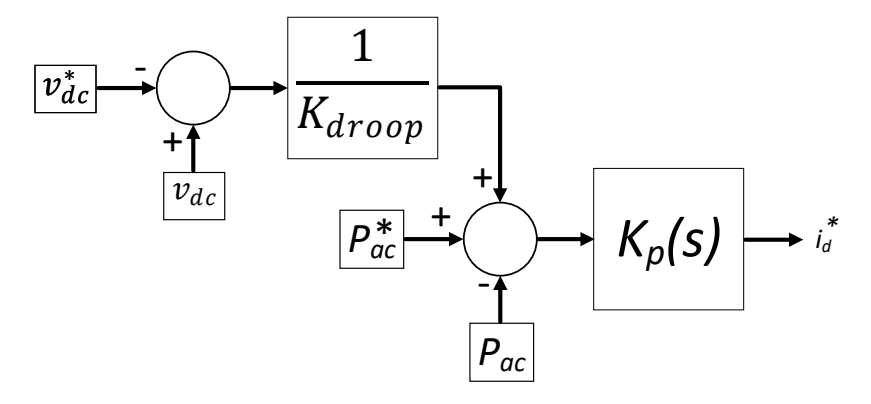


Figure 7.6: DC voltage droop,  $V - P_{ac}$ .

#### 7.5.4 Grid Forming Control

The control of the grid forming converter is the Virtual Synchronous Machine (VSM), emulating the swing equation, defined by (7.75)

$$P_{ref} - P_e = J\frac{d\omega}{dt} + D(\omega_{VSM} - \omega_n)$$
 (7.75)

where  $P_{ref}$  is the reference power,  $P_e$  is the electrical power, J is the moment of inertia  $(\frac{kgm^2}{MVA})$ , 2H = J, H is the inertia constant (in seconds), D is the damping constant (per unit) and  $\omega_{VSM}$  is the virtual angular velocity, and  $\omega_n$  is the rated velocity (or can be estimated grid frequency from a PLL). This power synchronisation loop sets the converter angle. It also introduces a virtual inertia and a damping term, which draw power from the DC side of the converter during a frequency or angle disturbance on the

connected AC grid. The converter voltage is directly set with the magnitude controlled by a PI controller, and the magnitude and angle from the synchronisation loop is used to set the voltage source.

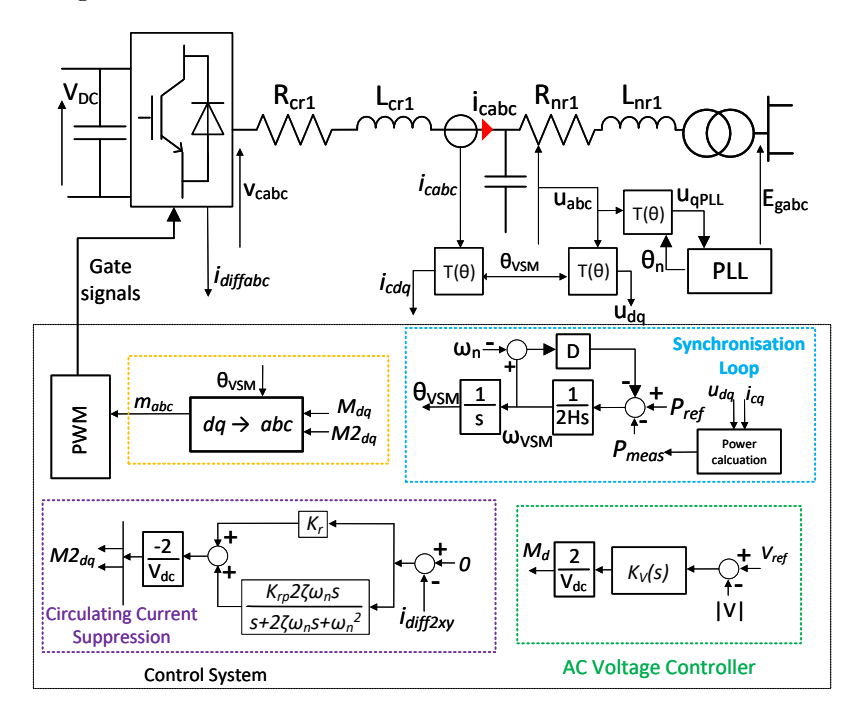


Figure 7.7: Control of implemented grid forming converter.

The synchronisation loop state representation is shown by

$$A_{VSM} = \begin{bmatrix} \frac{-Dpu}{2H} & 0\\ \omega & 0 \end{bmatrix} \tag{7.76}$$

$$B_{BSM} = \begin{bmatrix} \frac{1}{2H} & \frac{-1}{2H} \\ 0 & 0 \end{bmatrix} \tag{7.77}$$

$$C_{VSM} = \begin{bmatrix} 1 & 0 \\ 0 & 1 \end{bmatrix} \tag{7.78}$$

$$D_{VSM} = 0 (7.79)$$

where the state variables,  $\Delta x_{VSM}$  and inputs  $\Delta u_{VSM}$  are defined by

$$\Delta x_{VSM} = [\Delta \omega_{VSM}, \Delta \delta_{VSM}]^T$$
 (7.80)

$$\Delta u_{VSM} = [\Delta P^*, \Delta P]^T \tag{7.81}$$

$$\Delta y_{VSM} = [\Delta \omega_{VSM}, \Delta \delta]^T$$
 (7.82)

The voltage magnitude of the grid former is controlled by the outer AC voltage PI loop, with gain  $K_{VAC}(s) = K_{PVAC} + K_{i_{VAC}}$ ,  $\Delta u_{VAC} = [V_{ref}, V_{meas}]^T$  (reference AC voltage and measured AC voltage magnitude),  $\Delta x_{VAC} = [eV]$  (AC voltage error),  $\Delta y_{VAC} = [V_{mag}]$  (voltage magnitude reference to be applied to  $M_d$ ).

$$A_{AC} = 0 \tag{7.83}$$

$$B_{AC} = \begin{bmatrix} 1 & -1 \end{bmatrix} \tag{7.84}$$

$$C_{AC} = \left[\frac{2Ki_{VAC}}{V_{dc}}\right] \tag{7.85}$$

$$D_{AC} = \begin{bmatrix} \frac{2Kp_{VAC}}{V_{dc}} & -\frac{2Kp_{VAC}}{V_{dc}} \end{bmatrix}$$
 (7.86)

Each subsystem was connected to create a full detail SSM, as shown in Figure 7.8, in which the relations between the global reference and converter reference frames are also shown. The components in the global reference frame are output from the AC Grid sub-system, and transformed into the converter frame, to the power and voltage control loops, and circulating current controller. The outputs of this are the modulation indices, which are then transformed to the global reference frame again to be applied to the internal MMC dynamics, that produces the converter side AC and DC voltages. The two systems were also built as EMT Simulink models to validate the small signal models, shown in Figure 7.9, where the SSM matches the EMT time domain model when subject to an input power disturbance.

Chapter 7. Effect of Grid Forming and Grid Following control on Firewall Capability of MMC-HVDC Systems

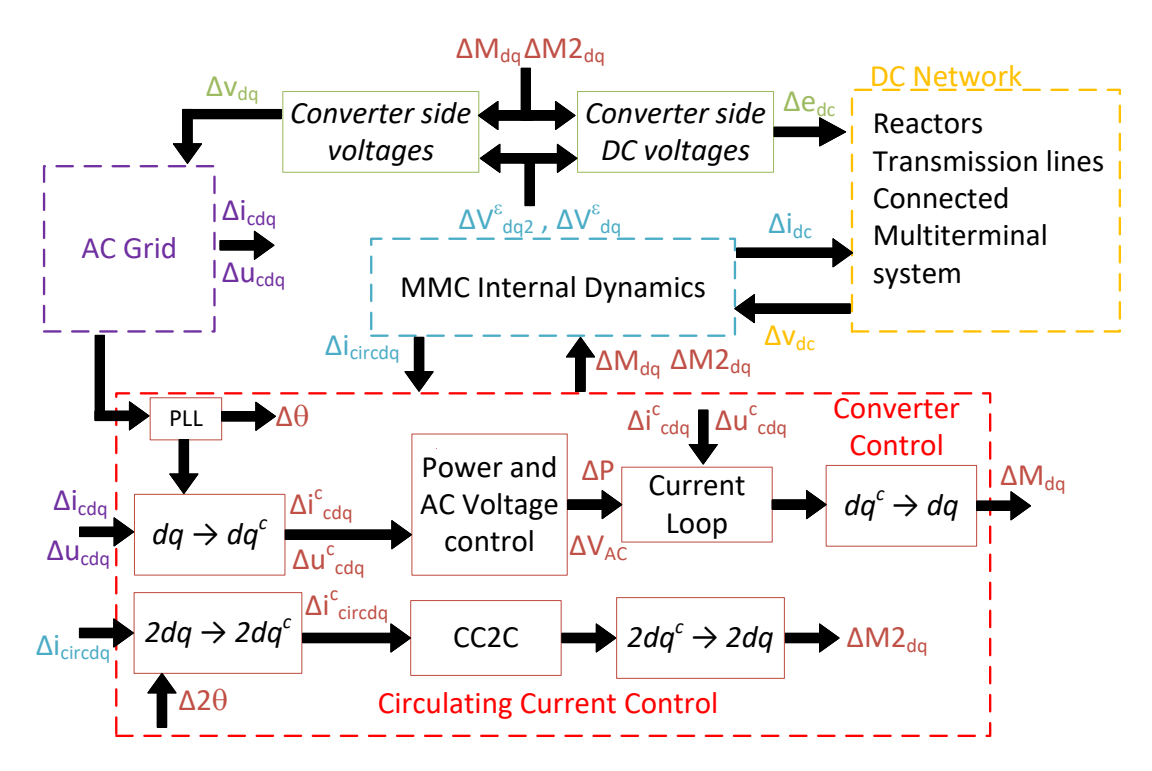


Figure 7.8: Overview of full SSM of system.

### 7.6 Case Study Results

This section presents the results obtained by following the methodology of Section 7.4, using the model from Section 7.5. The base system parameters from Table 7.1 are used in the model, and operating points from the EMT large signal model at steady state are used for the linearisation of the SSM. The validation of the small signal model following the EMT time domain response is shown in Figure 7.9.

#### 7.6.1 Participating State Identification

The small signal model is used to identify conditions producing poorly damped oscillatory modes. Any eigenvalue with  $\zeta < 0.1$ , is considered to be poorly damped, and the states participating in these modes are identified by (7.5). An example is given in Figure 7.10, showing the eigenvalues across varying SCR, and Table 7.2, showing the identified poorly damped modes of the system, and their participating states. In Figure 7.10, any eigenvalue above the dashed line representing  $\zeta = 0.1$  is assessed for

Chapter 7. Effect of Grid Forming and Grid Following control on Firewall Capability of MMC-HVDC Systems

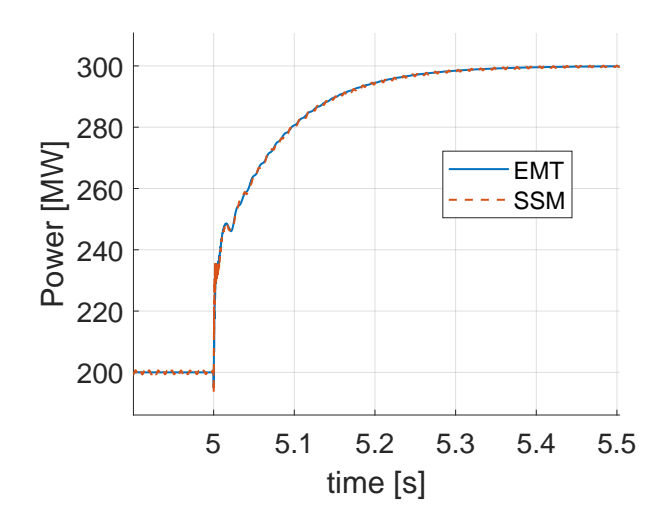


Figure 7.9: Validation of small signal model, power at PCC on  $grid_{jj}$  following 0.1 pu step in power reference.

the participating states. For the final sweep value of  $SCR_{jj} = 5$ , the participating states are shown in Table 7.2.

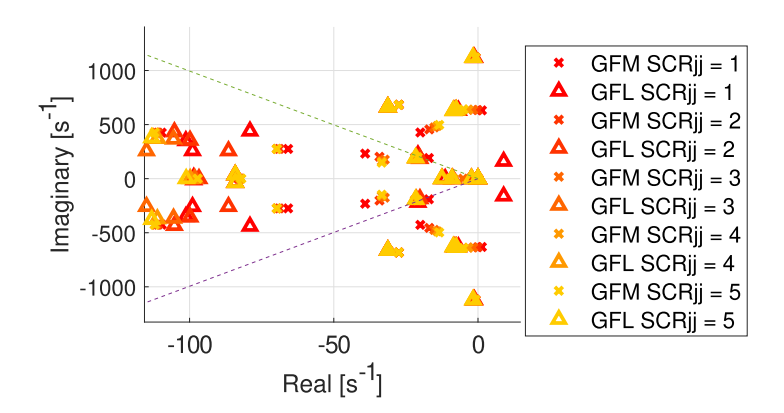


Figure 7.10: Eigenvalue parametric sweep across  $SCR_{jj}$  of poles of system.  $\zeta = 0.1$  shown by dashed lines.  $SCR_{kk} = 2$ , H = 6 s, Droop = 0.002, Damping = 1000 pu.

The MMC circulating currents and sub-module voltages participate in most of the poorly damped modes. The states participating in any poorly damped modes, across *all* of the parametric sweeps, were identified, and then selected to be I/O variables for the bode plots. This method reduces the bulk of the data needing analysed. In this study, the main states participating in poorly damped modes are detailed by the example in Table 7.2. The voltage and current on  $grid_{jj}$  have been identified as participating

Table 7.2: Example identifying participating states of poorly damped modes in GFM/GFL system, for  $SCR_{jj} = 5$ , DC Voltage Droop = 0.002, D = 1000 pu, H = 6s

Mode	Damping	States
-20.17 + j209.86	-0.0945	$VCP0_{jj} \ VCP0_{kk} \ VCPxy_{kk} \ idiff0_{jj} \ idiff0_{kk}$
-27.46 + j682.48	-0.0402	$idiffxy2_{jj}$
-31.15 + j662.47	-0.0470	$idiffxy2_{kk}$
-3.30 + j638.40	-0.0052	$idiffxy2_{jj}, VCP2xy_{jj}$
-8.58 + j629.66	-0.0136	$idiff_{kk}\ VCP2xy_{kk}$
-14.1217+ $j486.603$	-0.0290	$VCPxy_{jj}\ VCP2xy_{jj}\ icdq_{jj}$

in poorly damped modes, so they will be the input variables for the bode plots. The remaining participating states are selected as the output: the converter side currents  $i_{cxykk}$ , MMC Voltage Sub-module 100 Hz and zero component,  $VCPxy_{kk}$  and  $VCP0_{kk}$ , and MMC circulating currents,  $idiff2_{xykk}$ .

#### 7.6.2 Bode Plots

Some key bode plots are shown here to highlight the main differences in magnitude response of the GFM/GFL and GFL/GFL systems. All of the I/O combinations specified in section 7.6.1 were reviewed, however, for the sake of brevity only key examples are given here. The magnitude responses are different for all parameter and tuning combinations, but there are key trends to observe. The general trends of Figures 7.11a -7.11d, highlighted in the following paragraphs are: the GFM/GFL has two sharper resonant peaks, compared to the GFL/GFL system. The first peak occurs at 0.01 Hz - 1 Hz, and the second at 100 Hz (highlighted by the red circles). The figures also show the GFL/GFL is not as affected by the tuning and parameter conditions, having a more consistent oscillation magnitude, without the large resonant (or with more reduced) peaks seen in the GFM/GFL.

These peaks in the GFM/GFL vary dependent on the parametric values and tuning.

Chapter 7. Effect of Grid Forming and Grid Following control on Firewall Capability of MMC-HVDC Systems

For example, shown in Figure 7.11a, as the DC voltage droop decreases, the first peak increases to just below the 1 pu threshold, indicating a larger transfer of low frequency oscillations. Although a larger DC voltage droop corresponds to a smaller oscillation transfer at this lower frequency, a value above 0.2 can lead to instability, so the two objectives must be compromised. Increasing the damping also increases the magnitude of the first peak in the GFM/GFL system, leading to a a larger oscillation transfer, and therefore reduction in firewall capability. However, as shown by Figure 7.11b and Figure 7.11d, this is typically only at very high damping (> 2000pu). This first peak is also affected by  $SCR_{jj}$ , shown in Figure 7.11c, with an increase resulting in a larger magnitude response in the GFM/GFL. Conversely, in the GFL/GFL, in this frequency range, the magnitude is slightly reduced, as the  $SCR_{jj}$  increases.

The second peak seen in the bode plots in the GFM/GFL, occurs at 100 Hz, and like the first peak, is also affected by the  $SCR_{jj}$  and DC voltage droop. Figure 7.11a shows for the GFM/GFL the first peak increases if droop is decreased, however this second peak at 100 Hz slightly increases as dc voltage droop is increased. In Figure 7.11c, increasing the  $SCR_{jj}$  also increases the second peak at 100 Hz. This is due to the higher SCR corresponding to a lower coupling impedance, and therefore, driving a higher resultant current magnitude. Across the full range of  $SCR_{jj}$ , the GFM/GFL has a larger second peak than the GFL/GFL, however the latter still exhibits a 100 Hz peak, increasing as the SCR is increased above 2. With  $SCR_{jj} < 2$ , the peak decreases, but the GFL/GFL system is unstable at this weak grid value.

Throughout the bode plots, and evidenced by the figures shown in this section, some clear trends are apparent. Namely, that the GFM/GFL system does tend to have a greater magnitude response compared to the GFL/GFL, particularly at low droop and high damping at lower frequencies. The first magnitude peak in the GFM/GFL responses typically is between 0.01 Hz to 1 Hz, the bandwidth of which being dependent generally on the inertia constant. In both systems, a peak is also seen at 100 Hz, due to the 2nd fundamental components seen particularly in MMCs. The firewall metric for each I/O combination has been discussed in Section 7.4. This is implemented in

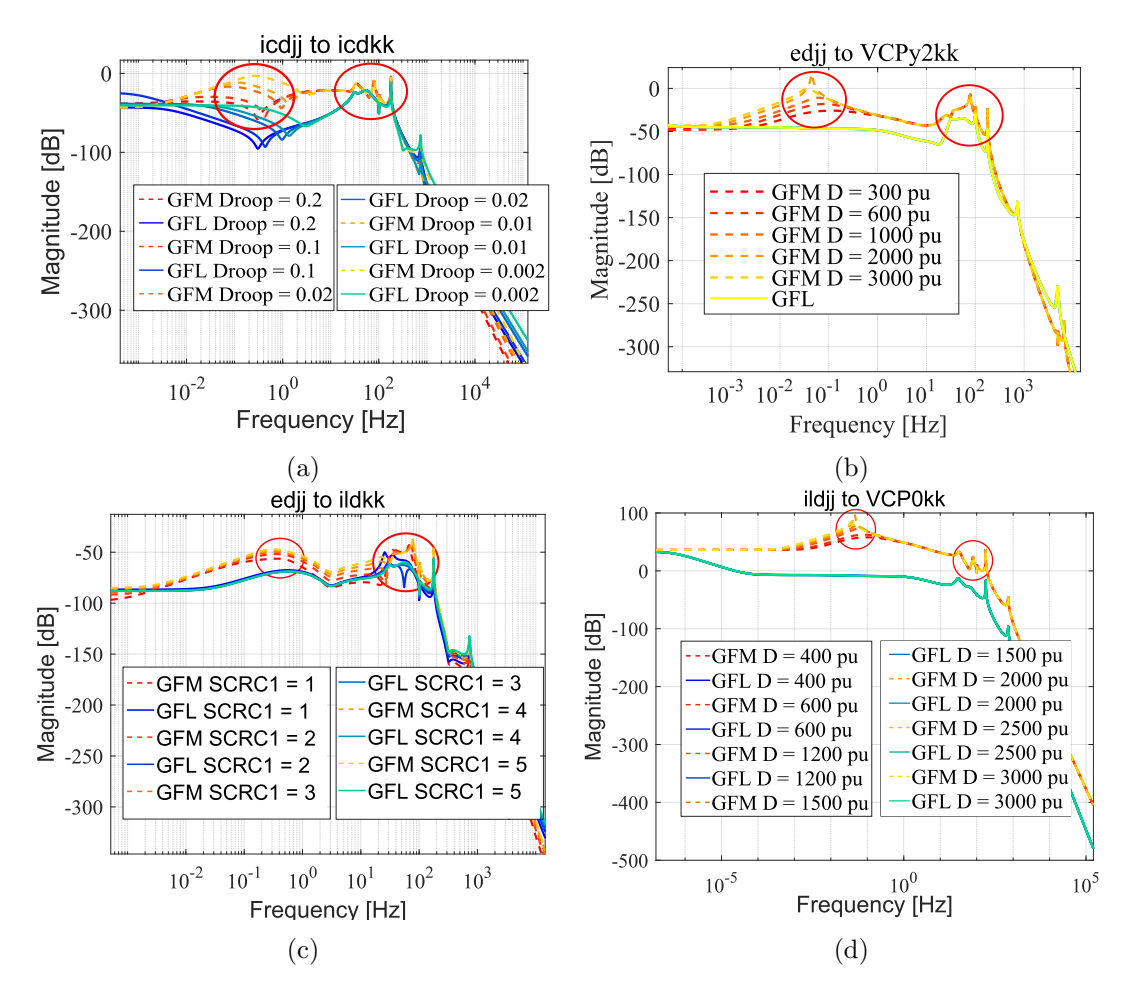


Figure 7.11: Bode plot of a) input current disturbance to ac  $Grid_{kk}$  current, damping 600, SCRs = 5, H = 6. b) input Voltage to  $MMC_{kk}$  sub-module voltage  $SCR_{jj}$  = 5,  $SCR_{kk}$  = 5, H = 6, Droop = 0.02. c) input voltage disturbance to AC  $Grid_{kk}$  current. Damping = 400 pu  $SCR_{jj}$  = 5, H = 1, droop = 0.002, varying damping d) Input current to voltage zero component.  $SCR_{jj}$  =  $SCR_{kk}$  = 5, H = 6, droop = 0.02, varying damping.

the heat-maps of the next section, which show the peak magnitude of a bode response, in per unit.

#### 7.6.3 Heat-map Parametric Overview

It is evident from the bode plots that for a disturbance on  $grid_{jj}$ , to  $grid_{kk}$ , the GFM/GFL frequently has a slightly larger magnitude response, with peaks at 0.01 Hz - 1 Hz, and 100 Hz. However, it is difficult to interpret all of the parameter effects from multiple bode plots at once. Therefore, to summarise the data:

- Heat-maps of the peak magnitude response for each I/O bode plot, are produced to find the parameters that amplify oscillations. The peak magnitude is represented in per unit to give a more intuitive way of interpreting the firewall limit (described in Section 7.4.5).
- The parameters that result in large oscillation propagation will be emphasised by key examples, not all I/O pairs and parameter conditions can be shown.

The per unit representation indicates any value over 1 pu will amplify a response and indicate the firewall effect is inhibited. However, anything above a zero gain, still shows an oscillation transfer from one grid to the other, which could still be undesirable, especially at these "peak" frequencies seen in the bode plots. Any NaN spaces in the following heat-maps indicate that for that parameter, the system is unstable.

The first key trend to be noted, observable in Figures 7.12a and 7.12b, is that the GFL/GFL is unstable in more conditions across these parametric sweeps, compared to the GFM/GFL. These figures show the peak magnitude response of a disturbance on  $grid_{jj}$  voltage,  $ed_{jj}$ , to converter current,  $icd_{kk}$ , for the GFL/GFL and GFM/GFL systems respectively, across DC voltage droop and  $SCR_{jj}$ . For both systems, the peak per unit disturbance is at 100 Hz. For the GFL/GFL the peak is between 0.2 pu - 0.3 pu, however there are many parameter conditions that result in instability. For the GFM/GFL, the peak is much higher, varying between 1.7 pu to 2.3 pu, increasing as  $SCR_{jj}$  is increased, however this system maintains stability across more parameter conditions compared to the GFL/GFL. Therefore, the GFM/GFL amplified

the response more than the GFL/GFL, but maintains stability more often across the sweeps.

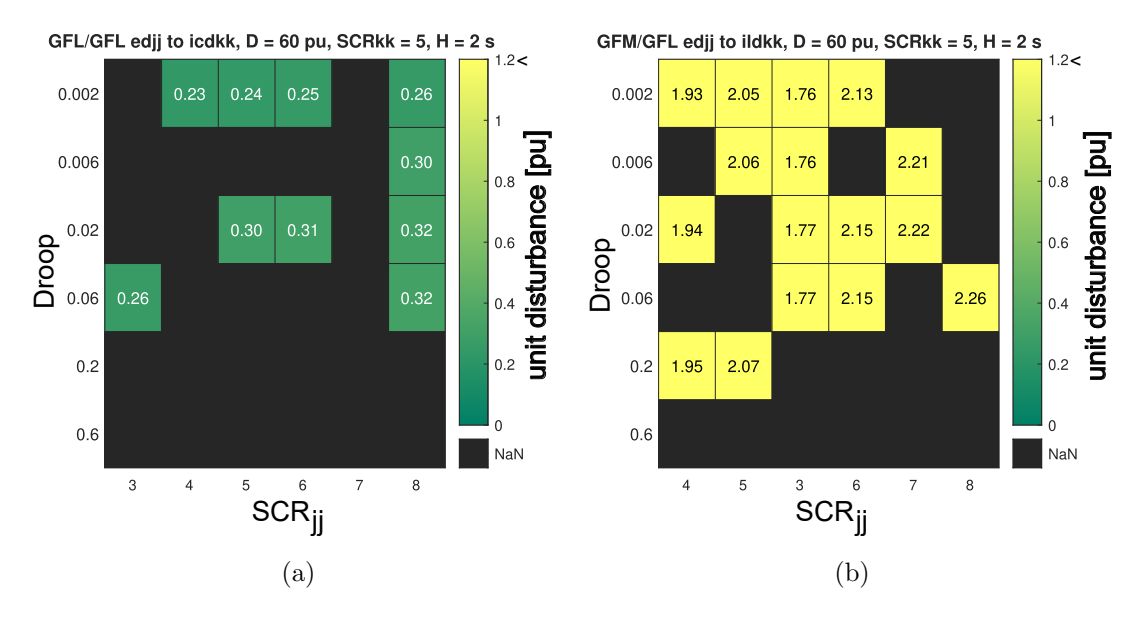


Figure 7.12: Heat-map of peak oscillation in system, per unit output from 1 pu input disturbance, edjj to icdkk,  $SCR_{kk} = 5$ , GFM damping = 60 pu, H = 2 s a) GFL/GFL b) GFM/GFL.

The effect of DC voltage droop can be observed in the heat-maps, confirming the results presented in the bode plots. In Figure 7.12b, there is a slight increase in peak magnitude as droop is increased, however this increase is more prominent in Figure 7.13a, which shows a current  $icd_{jj}$  disturbance to sub-module voltage component on  $grid_{kk}$ . For both of these heat-maps, the peak is at 100 Hz for the lower value damping scenarios, and as discussed and shown in Figure 7.11a, increasing the DC voltage droop, increases this second peak. For the higher damping conditions, the peak magnitude is can be at the lower 0.1 Hz - 1 Hz frequency range, when combined with the higher DC voltage droop.

Considering GFM damping, in Figure 7.13a, the oscillations are typically (< 0.1pu) and so can be considered as maintaining firewall capability. With damping greater than 1200 pu, and DC voltage droop above 0.02, the peak magnitude begins to increase. In general, with very high damping, and larger DC voltage droop, the magnitude of both peaks increases significantly. The peak magnitude response with damping above 1600

pu, occurs in the  $0.01~\mathrm{Hz}$  to  $1~\mathrm{Hz}$  frequency range. Any amplification is unwanted for this I/O pair, especially at  $100~\mathrm{Hz}$  as the second harmonic component is being amplified.

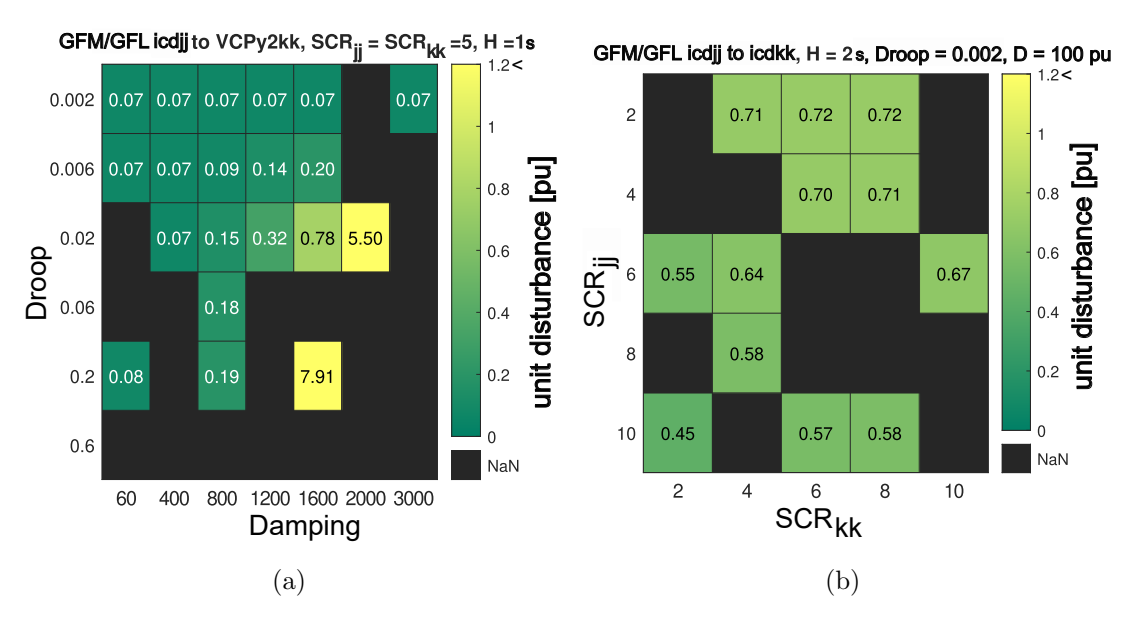


Figure 7.13: Heat Map of Peak Oscillation in Grid Forming System, a)  $icd_{jj}$  to  $VCPy2_{kk}$ ,  $SCR_{jj} = SCR_{kk} = 5$ , H = 1s b)  $icd_{jj}$  to  $icd_{kk}$ , H = 2s, droop = 0.002, D = 100 pu.

The effect of increasing  $SCR_{jj}$  on the GFM/GFL system is shown by Figures 7.12b, 7.13b, and 7.14a. As highlighted by the bode plots in Figure 7.11c, increasing the  $SCR_{jj}$ , results in the 100 Hz peak increasing. Figure 7.13b shows converter current disturbance from  $grid_{jj}$  to  $grid_{kk}$ , varying both grid SCRs. The SCR does affect the response across the full range of frequencies, but this peak oscillation, which in this instance occurs at 100 Hz, is not varied significantly by either grid SCR. Increasing  $SCR_{jj}$  from 2 to 10, slightly reduces the peak, whilst increasing  $SCR_{kk}$  slightly increases the peak. This peak in oscillation propagation at 100 Hz highlights a cause for concern for the GFM/GFL system, even though the magnitude is less than 1 pu; 0.7 pu propagation at 100 Hz is a large oscillation at an unwanted second harmonic.

Figure 7.14a shows the effect of increasing  $SCR_{jj}$  and inertia, on a grid voltage disturbance to MMC sub-module voltage output. The inertial power provided with

Chapter 7. Effect of Grid Forming and Grid Following control on Firewall Capability of MMC-HVDC Systems

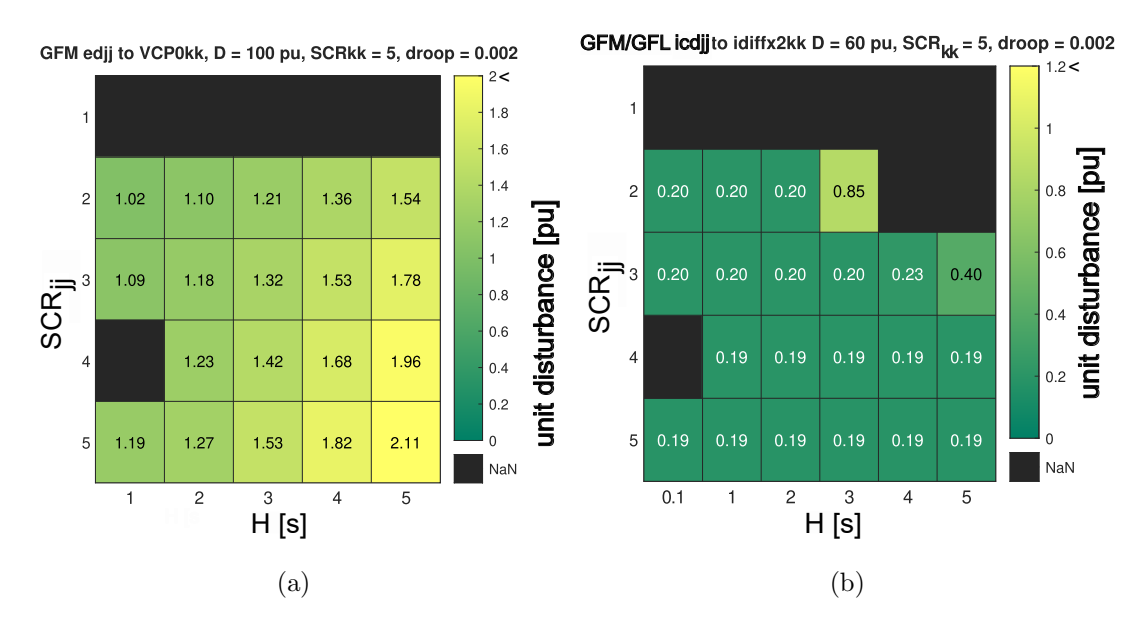


Figure 7.14: Heat Map of Peak Oscillation in Grid Forming System, a)  $ed_{jj}$  to VCP0kk, D = 100 pu, droop = 0.002,  $SCR_{kk} = 5$  b)  $icd_{jj}$  to  $idiffx2_{kk}$ , D = 60 pu,  $SCR_{kk} = 5$ , droop = 0.002.

an H > 3s, results in the converter at  $grid_{kk}$  experiencing a peak increasingly greater than 1 pu at low frequencies, inhibiting the firewall response. Therefore, the support of adding inertia power must be balanced with its negative effect on firewall capability, especially with H > 3s. The effect of  $SCR_{jj}$  and inertia can also be observed in Figure 7.14b showing current on  $grid_{jj}$  to circulating current on  $grid_{kk}$ . The effect of the inertia in this figure is less prevalent, as this peak occurs at 100 Hz (frequency of the circulating current) and the inertia effects the response mostly in the low frequency range.

#### 7.6.4 Frequency and Time Domain Comparison

Some selected non-linear EMT case studies are compared in the frequency spectrum and time domain to highlight the propagation of unwanted oscillations between AC Grids. A time domain Simulink model, used for validation of the small signal models, was used to demonstrate the characteristics of the two systems. The Fourier transform was taken of the time domain data points to obtain the amplitude of the frequencies propagated, to confirm the predicted frequencies of concern indicated by the small

Chapter 7. Effect of Grid Forming and Grid Following control on Firewall Capability of MMC-HVDC Systems

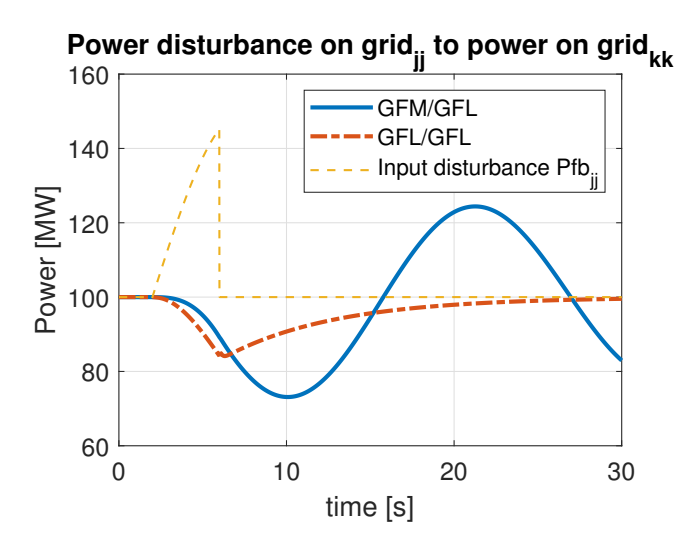


Figure 7.15: Response of GFM/GFL and GFL/GFL systems to an input power oscillation of 0.05 Hz at 0.1 per unit. Damping = 2000 pu, Droop = 0.02, H = 1 s,  $SCR_{ij} = SCR_{kk} = 5$ .

signal model.

The bode plots highlighted that the GFM/GFL has peaks in magnitude response at typically 0.01 Hz - 1 Hz, and at 100 Hz. The heat-maps act as a screening tool to highlight the parameters that cause large magnitude responses. The findings from the heat-maps are verified using the time domain models. The response in Figure 7.15 exhibits the firewall capability when subject to a low frequency input disturbance, corresponding to the 0.01 Hz to 1 Hz resonant peak. A 0.1 pu power oscillation at 0.05 Hz is input on  $grid_{ij}$ , and the power on  $grid_{kk}$  measured. The system parameters were selected from the heat-map screenings of Figure 7.13b, showing a larger oscillation can occur at damping = 2000 pu, DC voltage droop = 0.02, H = 1 s, and  $SCR_{jj}$  =  $SCR_{kk} = 5$ . The response of Figure 7.15 agrees with this screening, showing the GFM/GFL propagating a 0.05 Hz oscillation from  $grid_{jj}$  to  $grid_{kk}$  more than the GFL/GFL system. For the next tests, for both systems, harmonic injections at 100 Hz, of 0.2 pu and 0.15 pu were injected at the AC  $grid_{jj}$  grid voltage on phase a and phase b respectively. 100 Hz was selected as several of the frequency responses saw a magnitude peak at this frequency, as well as at 0.1 Hz - 1 Hz in the GFM/GFL system. Both grids are set at SCR = 4, GFM damping set at 1000 pu, H = 6 s, and DC voltage

droop is 0.2. Figure 7.16a shows the frequency spectrum of the a-phase voltage across the MMC upper arm sub-module at  $grid_{jj}$ , and Figure 7.16b shows the spectrum at  $grid_{kk}$ . The expected upper arm sub-module voltage is an oscillating DC voltage at half the DC link voltage. This is shown in Figure 7.16a by the amplitude peaks at 0 Hz and 50 Hz. Another amplitude peak is shown at 100 Hz in both systems at  $grid_{jj}$ , and it is significantly larger in the GFL/GFL system. Looking then at the converter at  $grid_{kk}$ , shown in Figure 7.16b, the 100 Hz oscillation is 3 times larger in the GFM/GFL system compared to the GFL/GFL, as well as a 200 Hz oscillation. However, considering the input disturbances (0.2 pu, and 0.15 pu harmonics injections on a and b phase), the propagation from  $grid_{jj}$  to  $grid_{kk}$  in the GFM/GFL system is still significantly more damped than the input disturbance. The GFM/GFL system, in almost all cases, has a larger propagation response from one grid to the next, but in very few situations, is the response significant enough to cause sustained oscillation issues in the connected AC grid. Furthermore, in these tuning and parameter conditions, the system tends towards instability, therefore they are not the optimal or suggested tunings.

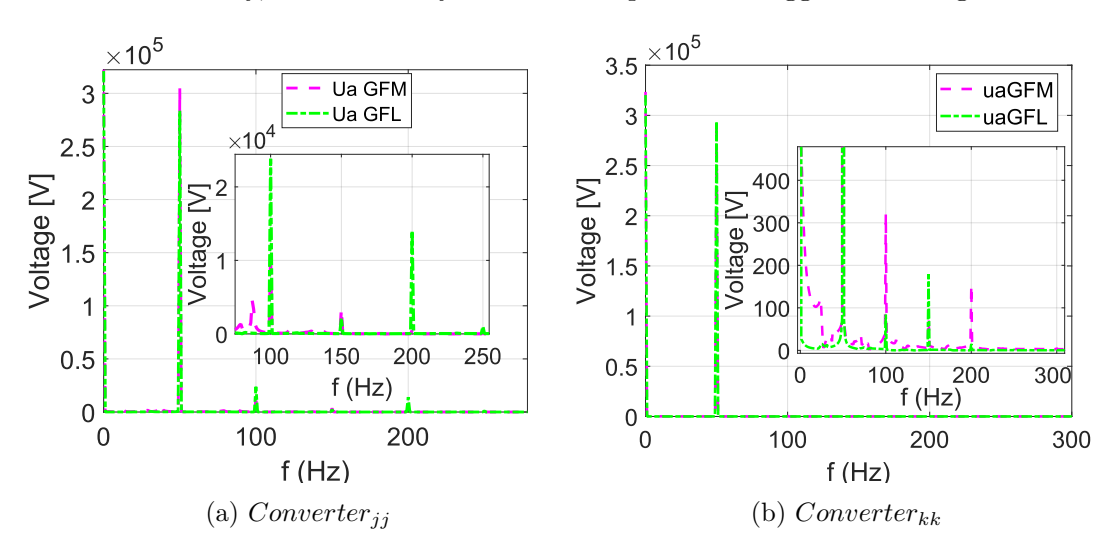


Figure 7.16: Frequency spectrum of voltage across phase a in sub-modules in MMC at (a)  $grid_{jj}$ . (b)  $grid_{kk}$ .

Considering now the measured PCC voltages, Fig. 7.17 presents the time domain response for both systems at  $grid_{jj}$  and  $grid_{kk}$ . Under the same harmonic 100 Hz injection of 0.2 pu, in the a-phase grid voltage, the GFM/GFL system manages to

Chapter 7. Effect of Grid Forming and Grid Following control on Firewall Capability of MMC-HVDC Systems

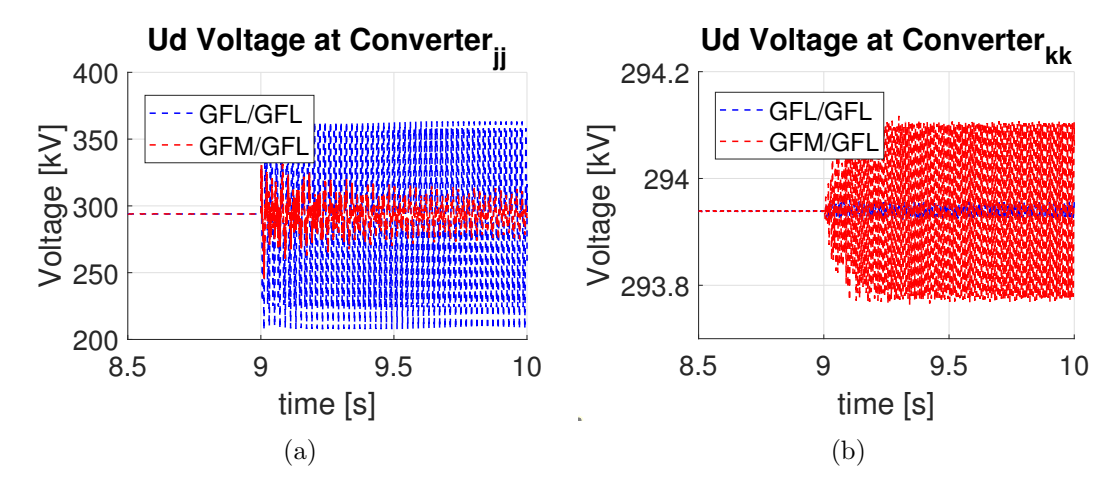


Figure 7.17: Time domain response of PCC voltage at when subject to a 100 Hz 0.2 pu voltage disturbance in AC  $grid_{jj}$  voltage  $ed_{jj}$ . (a) PCC voltage  $grid_{jj}$  (b) PCC voltage  $grid_{kk}$ .

dampen the PCC voltage more than the system controlled with the GFL/GFL on the  $grid_{jj}$ . However, this system sees larger oscillations on  $grid_{kk}$  PCC voltage, compared to the GFL/GFL system. The injected oscillation at  $grid_{jj}$  has an amplitude of 0.2 pu, and this is reflected in the GFL/GFL system in Figure 7.17a, whilst the GFM/GFL system has damped this oscillation to below 0.1 pu. However, on  $grid_{kk}$ , the oscillation in the GFL/GFL is 10 times smaller than the GFM/GFL system. The amplification of oscillations from  $grid_{jj}$  to  $grid_{kk}$  are greater in the GFM/GFL system compared to the GFL/GFL, although neither are significant.

### 7.7 Conclusion

The effect of a grid forming virtual synchronous machine converter on the inherent "firewall" capability of a monopole point-to-point MMC-HVDC system was investigated across a series of system parameters and tunings. The grid forming inertia, damping, grid following DC voltage droop and grid SCRs were varied to observe the effect on oscillation propagation. A small signal model of the full system was developed, including the MMC internal dynamics. Extensive parametric sweeps were performed for encompassing values of the aforementioned variables, to identify conditions in which firewall capability may be affected.

Across most responses, the propagation from input disturbance on  $grid_{jj}$  to output on  $grid_{kk}$  differed between the grid forming and following controls, with the former typically having a greater magnitude response across all parameters and responses. The GFM/GFL amplifies oscillations more than the GFL/GFL, but maintains better stability across the sweeps. The GFM/GFL typically amplifies low inertial frequencies (0.01 Hz - 1 Hz), and the second fundamental frequency, 100 Hz. For most of these parameter conditions, even though the GFM magnitude response on  $grid_{kk}$  was larger, it was not significant enough to cause a serious oscillation propagation. This was quantified using the proposed "firewall" metric to easily understand the impact of oscillation propagation irregardless of variable type. The results can be concluded as such:

- The  $SCR_{jj}$  can have a significant impact causing the GFM to draw "too much" of a response from AC  $grid_{kk}$ . The worst conditions are generally with a DC voltage droop above 0.02, damping above 1200 pu, and  $SCR_{jj}$ =4.
- $SCR_{kk}$  has limited impact on the *peak* magnitude propagated, however, it does still affect the whole response across the full frequency spectrum.
- A sufficient droop coefficient of < 0.02 is required for ensuring DC voltage maintenance, and reduce the oscillation propagation from one grid to the other.

  Anything over 0.02 results in an oscillation transfer between the grids).
- GFM Damping significantly affects the oscillation propagation and should be limited to below 1400 pu for droop above 0.02. For lower droop values, damping above 1400 pu can cause increased oscillations, especially above 2000 pu.
- Increasing GFM inertia does show a slight unwanted increase in magnitude response, but it only causes a variation in response at lower damping values (< 100pu), especially with an inertial constant above 3 s.
- The GFM/GFL system has a larger magnitude response from a disturbance on  $grid_{jj}$  to  $grid_{kk}$ , compared to the GFL/GFL system, in most parameter conditions. However, at typical values, the response is not significant enough

across most of the frequencies, and does not reach the threshold values (above 1 per unit response).

### Chapter 8

# Thesis Conclusion

The work presented in this thesis is summarised in the following chapter, giving general conclusions and goals for future work.

As detailed in Chapter 1, the motivation for this thesis is driven by the urgent need to decarbonise all energy sectors to combat the urgent threat of the climate emergency. Renewable converter interfaced generation will help contribute to this goal, but there are several developments to converter and transmission technology required to enable this. Many sites of renewable generation are located far from traditional synchronous generation sites (such as fossil fuel power stations), and far from demand locations. Therefore Medium and High Voltage Direct Current transmission has been increasingly utilised to enable low power loss power delivery across large scale distances.

One of the goals of this thesis is to present an overview of the possible capabilities of MVDC/HVDC systems in enabling the development of power grids, and to assess the benefits and issues of the controllers that can be implemented to support the grid in this transition. The difficulties experienced by the modern grid, from voltage instability, low SCR, varying X/R ratios and wide controller bandwidths, need to be understood by describing the technologies involved in MVDC/HVDC and converter systems. This is presented in Chapter 2, and the background modelling derivations used throughout this thesis are detailed in Chapter 3.

#### Chapter 8. Thesis Conclusion

In Chapter 4, the stability limits and support capability of a classical grid following current controller with grid supporting control is assessed to show the extent of inertia provision the controller can provide whilst maintaining system stability. GFL converters have typically been stated to be more suited to operation in a "stiff" or strong grid, and grid forming in a weaker grid [316]. However there are variations to this, dependent on the additional grid supporting features added in the GFL structure, the other system parameters and control tunings. Reference [13] highlights the comparability between inertia response provided by grid following and grid forming converters, showing across varying parameters, GFL control can have a very similar response to GFM control. Therefore, the study in Chapter 4 is important guidance to highlight the effect of control parameters on the maximum inertia that can be emulated in grid following control. The inner current loop controllers, the time constant of the phase locked loop, and the filter of the measured frequency all affect the maximum inertia that can be implemented. Some notable recommendations indicate that the typical inner current loop frequency range has reduced stability at higher inertia gains. The inner current loop should be 5 to 10 times slower than the converter switches (which have a frequency of 1-2 kHz, up to about 10 kHz [254]), therefore the inner current loop should be no faster than 10 ms. From the case study completed, higher inertia constants can be implemented whilst maintaining stability with very fast inner current tunings of below 1 ms, however this contradicts with the limit set by the converter switching (it should be noted that the switching of the converter was not included in the model, hence why the results show a larger inertia capability at very fast time constants). Therefore, in order to maintain system stability, the inner current loop must be tuned with a slower time constant to be able to set a larger inertia constant. Typically inertia is a slow response (however, beginning instantly, or within 5 ms defined by the UK grid code [226]), but if the current response is too slow it will lag the desired reference that has been generated to provide the inertial power required.

To ensure systems and converter controllers perform as expected, accurate modelling is essential especially for transmission system operators TSO and the Energy System Operator (ESO). As described in Chapters 5-6 there needs to be a balance between

#### Chapter 8. Thesis Conclusion

accurate modelling and computational burden, and therefore there are many different variations of models proposed in the literature, ranging from highly detailed models, to simplified low detail models. More specifically, there are several small signal models of varying dynamic detail, with simplifications that include the type of control utilised. Therefore, the accuracy of various small signal models has been analysed and presented in this thesis. In Chapter 5, three small signal models of grid-tied converters, with grid forming control, of increasing complexity are compared for their accuracy in matching the EMT time domain response of the system. These models are the full detail EMT SSM, a Jacobian representation [205], and the classical representation of a grid forming source to grid connection [21]. Across a series of changing system parameters, each small signal model was compared to the EMT model and the root mean square error was calculated across a set time window of the response. These tests are necessary to find the system conditions where lower detail models can, and cannot be used, as the study cases show that model accuracy is dependent on system parameters, even when linearised around the exact operating points. Specifically, for varying grid SCR, and X/R ratio, and GFM damping. A high X/R ratio results in a good decoupling between active and reactive power, however, conversely this also means poor decoupling in lower X/R ratio grids, such as in distribution grids. The Jacobian model does represent the relation between active power and voltage (therefore reactive power), however there are simplifications in the modelling assumptions to be able to represent the system as this simplified MIMO model. Chapter 5 shows the limitations with lower detail models exhibiting poor transient response accuracy at low X/R ratios, especially combined with low SCR values. The worst transient response for the lower detail models occurs at SCR < 2, X/R < 3, and a GFM damping ratio of  $\zeta$  < 0.2. The Jacobian model can adequately represent the transient response above these low values, however, it has the worst response when below this range. The transient response figures in Chapter 5 show some selected responses, highlighting the largest inaccuracy of lower detail models. The EMT non-linear and full detail SSM show oscillations of approximately 0.8 s (1.25) Hz), which is not a super-synchronous or fast oscillation that would not be expected of a low detail model to represent. Therefore, the aforementioned low value regions of X/R, SCR and damping result in the lower detail models having inaccurate transient responses, when they would be expected to be precise.

Continuing from the comparison of grid forming small signal models, the accuracy of three grid following small signal models of varying detail are compared in Chapter 6. A methodology is presented for screening the models to identify conditions where they do not identify poorly damped sub-synchronous oscillations, and instability. As with the studies in Chapter 5, it is anticipated that the lower detail models won't include fast dynamics, however there are parameter conditions where they cannot identify sub-synchronous modes or instability. CIGRE recommends [273] that TSOs, system operators, project owners and vendors must assess the capabilities of the models they are using and in what conditions they sufficiently represent instability and SSOs. Therefore, a full detail GFL SSM, a reduced order model, and simplified phasor model were assessed across a range of system SCR, X/R ratio and outer active power loop time constant. The case studies showed that the MOR method can represent when the system has poorly damped modes that could cause unwanted interactions, much more effectively that the simplified phasor model. However, with low SCR, the MOR fails to identify poorly damped SSOs even with larger tuning time constants (0.2 s - 0.3 s), that is would be expected to [224]. The simplified phasor can be slightly more suitable for identifying areas of instability at the lower SCR ranges, however this model is more inclined to producing false positives highlighting instability. Ultimately, the full detail SSM is advised for anything below SCR = 2, especially at lower  $\tau$  and X/R = 15 to 20.

Having highlighted the importance of accurate modelling in the previous sections, Chapter 7 presents a detailed small signal model of a point-to-point MMC-HVDC system. The MMC internal dynamics are included in the model, the grid and converter equations, and the DC link dynamics. The full description of the system small signal model derivation is explained in the chapter, and the effect of different controllers on the system is investigated. The ability of the MMC-HVDC system to control power flow and limit oscillation propagation from one side to the other is assessed across

a series of parameters. Two systems where tested, one with a GFM on the first AC grid and GFL on the second AC grid (referred to as the GFM/GFL), and then a system with a GFL controlling both grids (GFL/GFL). The goal of this research was to assess what conditions limit the controllers' abilities to prevent oscillation propagation. It was found that the GFM/GFL system limited this capability more than the GFL/GFL, however, across most conditions, it was not significant enough to be a "cause for concern". A comprehensive methodology was presented to identify parameter conditions where the GFM/GFL has a larger oscillation propagation from one grid to the next compared to the GFL/GFL system. The concept of "firewall" was quantified for ease of interpretation, as an input oscillation on  $grid_{jj}$ , resulting in an equivalent per unit response on  $grid_{kk}$ . Explanation of this is detailed in Chapter 7. It was concluded that the  $SCR_{jj}$  can have a significant impact causing the GFM to draw "too much" of a response from AC  $grid_{kk}$ . The worst conditions are generally with a DC voltage droop above 0.02, damping above 1200 pu, and  $SCR_{jj}=4$ . GFM Damping significantly affects the oscillation propagation and should be limited to below 1400 pu for droop above 0.02. For lower droop values, damping above 1400 pu can cause increased oscillations, especially above 2000 pu. Increasing GFM inertia does show a slight unwanted increase in magnitude response, but it only causes a variation in response at lower damping values (< 100pu), especially with an inertial constant above 3 s. Ultimately the GFM/GFL system has a larger magnitude response from a disturbance on  $grid_{jj}$  to  $grid_{kk}$ , compared to the GFL/GFL system, in most parameter conditions. However, at typical values, the response is not significant enough across most of the frequencies, and does not reach the threshold values (1 per unit disturbance).

Throughout this thesis, the importance of model accuracy has been brought to the spotlight, especially as the grid sees more IBRs connected and ever changing parameters at points of connection. CIGRE, TSOs, and system operators are requiring an even deeper understanding of the power system and the models they use. There is a serious need of models with low computational burden and high speed, however this thesis has shown there are system conditions where low detail models lack the precision they would

#### Chapter 8. Thesis Conclusion

be expected to offer. Repeatable and straightforward methodologies have been proposed to show when model simplifications are not adequate. The importance of detailed dynamic representation is further emphasised in Chapter 7, where the inclusion of the MMC dynamics is essential as they frequently participate in oscillation propagation between grids.

### 8.1 Future Work

Further work to extend the research completed in this thesis is described in this section.

Chapter 4 highlighted the capabilities of enhanced GFL controllers to provide an inertial response, also highlighting the limitations GFL inertia support can have on system stability when interacting with inner loop controls. Therefore, future work would be conducted to compare the stability between GFL control with inertia and GFM converters with inertia. The benefit of the fast response of GFLs needs to be assessed, as the results of Chapter 4 showed fast current loop and PLL time constants restricted the maximum inertial gain the converter could have whilst maintaining stability. However, the GFL could still provide inertia up to a set power limit (maintaining a suitably fast control response), therefore, the required power could be restricted, and assess the benefits of GFL in fault ride through compared to a GFM VSM topology which typically switches to GFL control during faults [317], or require significant inner current limiting control during faults.

Considering that the importance of model accuracy has been highlighted throughout this thesis, it would be beneficial to develop a model simplification method that simplifies grid tied converters with GFL and GFM control whilst accurately representing sub-synchronous oscillations. The fast frequency dynamics might not necessarily be required, but the SSOs that grid TSOs have not been able to predict would be desirable in a lower detail model. Incorporating dynamic phasors into simplified models to investigate if they can improve the sub-synchronous oscillation detail that is missed in the simplified models would be the first step, to create a model that can represent low order harmonics and inter-harmonics of the system.

#### Chapter 8. Thesis Conclusion

An extension to the studies completed on the MMC-HVDC point-to-point system in Chapter 7 is desired, specifically:

- Performing parametric sweep case study tests on an HVDC link interconnecting a *synchronous* AC grid.
- Following from this, a more detailed AC grid representation would need to be developed, compared to the previous infinite bus AC Grid. For example, a system similar to the IEEE 9-bus system [318], with modified HVDC link interconnecting two areas. This would offer a more in depth study into the propagation of oscillations, highlighting any inhibited firewall capabilities in future synchronous grids, with multiple HVDC links.
- A further goal is develop a metric that represents the "full" firewall capability for the system instead of each input-output pair, i.e., an interpretable value that weights the significance of individual large propagation oscillations between AC grids, and/or multiple smaller propagations, cumulating to make a significant effect overall.
- The effect of alternate GFM structures will also be investigated. The current GFM control uses VSM synchronisation, with AC voltage magnitude control and circulating current suppression. The effect of cascaded inner current and voltage control loops will be investigated. In particular, determining whether this inner additional control gives beneficial controllability or further damages the firewall capability. Additionally, energy based control has been recommended in the literature for control of MMC sub-module voltages [319], which should be implemented. Tuning of the control to suppress the unwanted harmonics in the MMC could be recommended from repeated case studies of this system, by varying the gains of these suppression loops, and ultimately, suggested improvements to the control.

# Appendix A

# Full Derivation of Small Signal Synchronous Reference Frame Phase Locked Loop

A detailed description of the steps and assumptions taken to produce the transfer function of the linearised phase locked loop was described in Section 3.5.2. In this section, the expanded substitutions are given, step by step, for improved reader clarity.

The relation between the estimation of the PLL angle and voltage was defined by, (3.66)

$$\hat{\theta}_{PLL} = \int \left( \omega_n + K_P * \hat{U}_{PCCq} + K_i \int (\hat{U}_{PCCq}) \right) dt$$
 (A.1)

$$\tilde{\theta} = \hat{\theta}_{PLL} - \theta_g \tag{A.2}$$

If  $\frac{d}{dt}\hat{\theta}_{PLL} = \frac{d}{dt}\tilde{\theta}_{PLL} + \frac{d}{dt}\theta_g$ , and it is assumed the feed-forward reference,  $\omega_n$  is equivalent to the grid frequency,  $\theta_g$ , then the following equations can be expanded.

$$\frac{d}{dt}\hat{\theta}_{PLL} = \frac{d}{dt}\tilde{\theta}_{PLL} + \frac{d}{dt}\theta_g = \frac{d}{dt}\tilde{\theta}_{PLL} + \omega_g \tag{A.3}$$

Appendix A. Full Derivation of Small Signal Synchronous Reference Frame Phase Locked Loop

$$\hat{\mathbf{U}}_{\mathbf{PLL}} = e^{-j\tilde{\theta}} \mathbf{U}_{\mathbf{PLL}} \tag{A.4}$$

$$\frac{d}{dt}\tilde{\theta}_{PLL} = K_P * \hat{U}_{PCCq} + K_i \int (\hat{U}_{PCCq}) dt$$
(A.5)

if (A.4) is linearised, then the substitution is as follows, where the PLL sub-suffix has been dropped for clarity.

$$\Delta \hat{\mathbf{U}}_{\mathbf{PLL}} = |e^{-j\tilde{\theta}} U_{PLL}|_{lin} = -je^{-j\tilde{\theta}_0} U_{PLL0} \Delta \tilde{\theta} + e^{-j\tilde{\theta}_0} \Delta \mathbf{U}_{\mathbf{PLL}}$$
(A.6)

$$\Delta \hat{U}_{d} + j\Delta \hat{U}_{q} = -j \left( \cos(\tilde{\theta}_{0}) - j\sin(\tilde{\theta}_{0}) \right) * (U_{d0} + jU_{q0}) \Delta \tilde{\theta} + \left( \cos(\tilde{\theta}_{0}) - j\sin(\tilde{\theta}_{0}) \right) (\Delta U_{d} + j\Delta U_{q}) \quad (A.7)$$

$$\Delta \hat{U}_d + j\Delta \hat{U}_q = \left(-jU_{d0}cos(\tilde{\theta}_0) + U_{d0}sin(\tilde{\theta}_0) + jU_{q0}sin(\tilde{\theta}_0) + U_{q0}cos(\tilde{\theta}_0)\right)\Delta \tilde{\theta} + \Delta V_d cos\tilde{\theta}_0 + \Delta V_q sin\tilde{\theta}_0 + j\Delta V_q cos\tilde{\theta}_0 - j\Delta V_d sin\tilde{\theta}_0 \quad (A.8)$$

Collecting real and imaginary terms and comparing them, the imaginary component  $\Delta \hat{U}_q$  can be expressed as

$$\Delta \hat{U}_{q} = \left(-U_{d0}cos(\tilde{\theta}_{0}) + jU_{q0}sin(\tilde{\theta}_{0})\right)\Delta \tilde{\theta} + \Delta U_{q}cos(\tilde{\theta}_{0}) - \Delta U_{d}sin(\tilde{\theta}_{0}) \quad (A.9)$$

The input of the  $\Delta U_q$  term is neglected and then A.9 is substituted into the linearised (A.5).

$$\frac{d}{dt}\Delta\tilde{\theta} = \left(Kp + \frac{Ki}{s}\right) \left(\left(-U_{d0}cos(\tilde{\theta}_0) + jU_{q0}sin(\tilde{\theta}_0)\right)\Delta\tilde{\theta} + \Delta U_qcos(\tilde{\theta}_0) - \Delta U_dsin(\tilde{\theta}_0)\right)$$
(A.10)

If this is transformed into the LaPlace domain

Appendix A. Full Derivation of Small Signal Synchronous Reference Frame Phase Locked Loop

$$s^{2}\Delta\tilde{\theta} + \left(Kp_{PLL}U_{d0}cos(\tilde{\theta}_{0}) - Kp_{PLL}U_{q0}sin(\tilde{\theta}_{0})\right)s + Ki_{PLL}U_{d0}cos(\tilde{\theta}_{0})$$
$$- Ki_{PLL}U_{q0}sin(\tilde{\theta}_{0}) = s\left(\Delta U_{q}Kp_{PLL}cos(\tilde{\theta}_{0}) + \Delta U_{q}Ki_{PLL}cos(\tilde{\theta}_{0})\right) \quad (A.11)$$

$$\frac{\Delta \tilde{\theta}}{\Delta U_q} = \frac{Kp_{PLL}cos(\tilde{\theta}_0)s + Ki_{PLL}cos((\tilde{\theta}_0))}{s^2 + a_0s + b_0} \tag{A.12}$$

where

$$a_0 = Kp_{PLL}cos(\theta_0)U_{d0} + Kp_{PLL}sin(\theta_0)U_{q0}$$
(A.13)

$$b_0 = Ki_{PLL}cos(\theta_0)U_{d0} + Ki_{PLL}sin(\theta_0)U_{q0}$$
(A.14)

If the initial angle difference is assumed to be zero,  $((\tilde{\theta}_0) = 0)$ , then this expression can be simplified to

$$\frac{\Delta \tilde{\theta}}{\Delta U_q} = \frac{Kp_{PLL}s + Ki_{PLL}}{s^2 + U_{d0}s + U_{d0}} \tag{A.15}$$

### Appendix B

# Jacobian Matrix Detail

The derivation of the Jacobian Matrix is extensively detailed in [205], however an overview of the equation derivations is shown here.

Firstly, the grid system equation,  $L\frac{d\mathbf{i}}{dt} = \mathbf{v} - \mathbf{E} - R\mathbf{i} - j\omega L\mathbf{i}$ , has some of the dq components represented in terms of magnitude and trigonometric functions.

$$V_d + jV_q = V\cos(\theta_v) + V\sin(\theta_v)$$
(B.1)

The following assumptions and function simplifications are assumed when linearised, shown in (B.2) to (B.2).

$$\theta_v = \theta_{v0} + \Delta\theta_v, i_d = i_{d0} + \Delta i_d, i_q = i_{q0} + \Delta i_q$$
(B.2)

$$sin(\theta_{v0} + \Delta\theta_V) \approx sin(\theta_{v0}) + cos(\theta_{v0})\Delta\theta_v$$
 (B.3)

$$cos(\theta_{v0} + \Delta\theta_V) \approx cos(\theta_{v0}) - sin(\theta_{v0})\Delta\theta_v$$
 (B.4)

Further explanation of the system substitutions that are applied to the grid equations are explained in [205], and the transfer functions for the Jacobian matrix are derived. The expanded form is given here.

Appendix B. Jacobian Matrix Detail

$$J_{P\theta}(s) = \frac{a_0 s^2 + a_1 s + a_2(\omega)}{(sL + R)^2 + (\omega L)^2}$$
(B.5)

where

$$a_0 = (Lpu/\omega_1) * (k_3 - k_1)$$

$$a_1 = (R_{pu}/\omega_1) * (k_3 - k_1) - L_{pu} * k_2$$

$$a_2 = (\omega_1 * L_{pu} * k_3 - R_{pu} * k_4)$$

$$J_{U_f\theta}(s) = \frac{a_0 s^2 + a_1 s + (\omega)}{(sL + R)^2 + (\omega L)^2}$$
(B.6)

where

$$a_0 = -L_{pu} * L_{gpu} * k_2 * U_{pu}$$
 
$$a_1 = -R_{pu} * L_{gpu} * k_2 * U_{pu}$$
 
$$a_2 = -\omega_1)^2 * L_{pu} * L_{gpu} * k_2 * U_{pu} - \omega_1 * R_{pu} * L_{gpu} * k_1 * U_{pu}$$

$$J_{PV}(s) = \frac{a_0 s^2 + a_1 s + (\omega)}{(sL + R)^2 + (\omega L)^2}$$
(B.7)

where

$$a_0 = (L_{pu}/\omega_1) * (k4 - k2)$$

$$a_1 = (Rpu/\omega_1) * (k4 - k2) + L_{pu} * k_1$$

$$a_2 = \omega_1 * L_{pu} * k_1 + Rpu * k_2$$

$$J_{U_f V}(s) = \frac{a_0 s^2 + a_1 s + (\omega)}{(sL + R)^2 + (\omega L)^2}$$
(B.8)

where

$$a_0 = L_{pu} * L_{gpu} * k_1/Upu$$
 
$$a_1 = Rpu * L_{gpu} * k_1/UTDpu$$
 
$$a_2 = (\omega_1^2) * L_{pu} * L_{gpu} * k_1/Upu - (\omega_1) * Rpu * L_{gpu} * k_2/Upu$$

The variables  $K_i$  are comprised of the per unit voltage magnitudes and angles.

### Appendix B. Jacobian Matrix Detail

```
\begin{split} K1 &= VTDpu * UTDpu * cos((ThetaTDV0 - (ThetaTDU0))) \\ K2 &= VTDpu * UTDpu * sin((ThetaTDV0 - (ThetaTDU0))) \\ K3 &= ETDpu * VTDpu * cos((ThetaTDV0)) \\ K4 &= ETDpu * VTDpu * sin((ThetaTDV0)) \end{split}
```

## Appendix C

# Model Order Reduction Detailed Expansion

A detailed expansion of the substitution steps to obtain the reduced order model from [282] are shown in this appendix. The variables have been defined in Chapter 6 in Section 6.3.3.

If the equation for the current control voltage references in the converter frame are considered as

$$\Delta v_{cd}^{c*} = \Delta u_d^c + G_{cl}(s) \left(\Delta i_{cd}^{c*} - \Delta i_{cd}^c - \omega L_c \Delta i_{ca}^c\right) \tag{C.1}$$

$$\Delta v_{cq}^{c*} = \Delta u_q^c + G_{cl}(s) \left(\Delta i_{cq}^{c*} - \Delta i_{cq}^c + \omega L_c \Delta i_{cd}^c\right)$$
 (C.2)

then the representation in the global reference frame is transformed using the relation shown in Chapter 6 in equations (6.33) and (6.34). This results in the converter reference voltages expressed in terms of the global reference frame.

$$\Delta v_{cd}^* = \Delta v_{cd}^{c*} - v_{cq0}^c \Delta \theta_{PLL}, \quad v_{cq}^* = \Delta v_{cq}^{c*} + v_{cd0}^c \Delta \theta_{PLL}$$
 (C.3)

$$\Delta v_{cd}^{c*} = \Delta v_{cd}^* + v_{cq0} \Delta \theta_{PLL}, \quad v_{cq}^{c*} = \Delta v_{cq}^* - v_{cd0} \Delta \theta_{PLL}$$
 (C.4)

Appendix C. Model Order Reduction Detailed Expansion

$$\Delta v_d^* = \Delta u_d + u_{q0} \Delta \theta_{PLL} + G_{CL}(s) \left( \Delta i_{cd}^* + i_{cq0}^* \Delta \theta_{PLL} - \Delta i_{cd} - i_{cq0} \Delta \theta_{PLL} \right)$$
$$- \omega L_{eq} \left( \Delta i_{cq} - i_{cd0} \Delta \theta_{PLL} \right) - v_{cq0}^c \Delta \theta_{PLL} \quad (C.5)$$

$$\Delta v_q^* = \Delta u_q - u_{d0} \Delta \theta_{PLL} + G_{CL}(s) \left( \Delta i_{cq}^* - i_{cd0}^* \Delta \theta_{PLL} - \Delta i_{cq} + i_{cd0} \Delta \theta_{PLL} \right)$$
$$+ \omega L_{eq} \left( \Delta i_{cd} + i_{cq0} \Delta \theta_{PLL} \right) + v_{cd0}^c \Delta \theta_{PLL} \quad (C.6)$$

The equations relating the converter side voltage to the PCC are shown again below in (C.7) and (C.8).

$$\Delta v_d - \Delta u_d = (sL_{eq} + R_{eq})\Delta i_{cd} - \omega L_{eq}\Delta i_{cq}$$
 (C.7)

$$\Delta v_q - \Delta u_q = (sL_{eq} + R_{eq})\Delta i_{cq} + \omega L_{eq}\Delta i_{cd}$$
 (C.8)

If the converter voltage in the global reference frame of (C.5) and (C.6) are substituted into (C.7) and (C.8), and assuming the  $v_{dq}^* = v_{dq}$ , then the following equations are produced:

$$(sL_{eq} + R_{eq} + G_{CL})\Delta i_{cd} = \omega L_{eq}\Delta i_{cq} - \Delta u_d + \Delta u_d + u_{q0}\Delta \theta_{PLL} + G_{CL}(s)(\Delta i_{cd}^{c*} - i_{cq0}\Delta \theta_{PLL}) - \omega L_{eq}(\Delta i_{cq} - i_{cd0}\Delta \theta_{PLL}) - v_{cq0}^c\Delta \theta_{PLL}$$
 (C.9)

$$(sL_{eq} + R_{eq} + G_{CL})\Delta i_{cq} = -\omega L_{eq}\Delta i_{cd} - \Delta u_q + \Delta u_q - u_{d0}\Delta \theta_{PLL} + G_{CL}(s)(\Delta i_{cq}^{c*} + i_{cd0}\Delta \theta_{PLL}) + \omega L_{eq}(\Delta i_{cd} + i_{cq0}\Delta \theta_{PLL}) + v_{cd0}^c\Delta \theta_{PLL}$$
 (C.10)

Furthermore, the PLL angle,  $\theta_{PLL}$ , was shown in Chapter 6 that it can be represented in terms of the converter currents

$$\Delta\theta_{PLL} = G_{PLL}((sL_g + R_g)\Delta i_{cq} + \omega L_g \Delta i_{cd})$$
 (C.11)

where  $G_{PLL}$  is the PLL transfer function, also described in Chapter 6. If the  $\Delta\theta_{PLL}$  in equations (C.9) and (C.10) is replaced with the expression in (C.11), then the grid

#### Appendix C. Model Order Reduction Detailed Expansion

current equations are simplified to (C.12) and (C.13) (note: the *reference* current only is considered in the converter reference frame for going forward).

$$\Delta i_{cd} = \frac{G_{CL}}{Z_{ic}} \Delta i_{cd}^{c*} - \frac{(G_{CL} + R_{eq})i_{cq0}}{Z_{ic}} G_{PLL} \omega L_g \Delta i_{cd} - \frac{(G_{CL} + R_{eq})i_{cq0}}{Z_{ic}} G_{PLL} (sL_g + R_g) \Delta i_{cq} \quad (C.12)$$

$$\Delta i_{cq} = \frac{G_{CL}}{Z_{ic}} \Delta i_{cq}^{c*} + \frac{(G_{CL} + R_{eq})i_{cd0}}{Z_{ic}} G_{PLL} \omega L_g \Delta i_{cd} + \frac{(G_{CL} + R_{eq})i_{cd0}}{Z_{ic}} G_{PLL} (sL_g + R_g) \Delta i_{cq} \quad (C.13)$$

where the variable  $Z_{ic}$  is introduced for simplification of the equations and is equivalent to  $Z_{ic} = sL_{eq} + R_{eq} + G_{CL}$ . Considering the current loop PI controller,  $G_{CL}$  is expressed

$$G_{CL} = K_{pCC}(1 + \frac{1}{T_{cc}s})$$
 (C.14)

then the following simplification can be derived

$$\frac{G_{CL}}{Z_{ic}} = \frac{\omega_{CL}(L_{eq} + \frac{R_{eq}}{s})}{sL_{eq} + R_{eq} + \omega_{CL}(L_{eq} + \frac{R_{eq}}{s})} = \frac{1}{\frac{s}{\omega_{CL}} + 1}$$
(C.15)

If the inner current loop is considered fast enough that the converter current directly follows the reference, and the grid dynamics are simplified as in [284], then the equations in (C.12) and (C.13) can be simplified to

$$\begin{bmatrix} \Delta i_{cd} \\ \Delta i_{cq} \end{bmatrix} = \begin{bmatrix} A & B \\ C & D \end{bmatrix} \begin{bmatrix} \Delta i_{cd}^* \\ \Delta i_{cq}^* \end{bmatrix}$$
 (C.16)

where A, B, C and D are transfer functions defined as

$$A = \frac{1}{1 + G_{PLL} X_q I_{cq0}} \tag{C.17}$$

$$B = 0 (C.18)$$

Appendix C. Model Order Reduction Detailed Expansion

$$C = \frac{G_{PLL}X_gI_{cd0}}{1 + G_{PLL}X_gI_{cq0}} \tag{C.19}$$

$$D = 1 \tag{C.20}$$

Further to this, the derivation to obtain the state space representation of input power and PCC voltage are the inputs, is described in Chapter 6, resulting in the final form of

$$\begin{bmatrix} \Delta P \\ \Delta u \end{bmatrix} = \begin{bmatrix} \frac{GPC0}{1+GPC0} & \frac{Y}{1+X} \\ \frac{M}{1+N} & \frac{GAC0}{1+GAC0} \end{bmatrix} \begin{bmatrix} \Delta P^* \\ \Delta u^* \end{bmatrix}$$
(C.21)

where the intermediate variables X, Y, M, N, GPC0 and GPC0 are defined by

$$X = K_p(s)(mA + nC), Y = K_U(s)(mB + nD)$$
 (C.22)

$$M = K_p(s)(pA + qC), N = K_U(s)(pB + qD)$$
 (C.23)

$$GPC0 = X - \frac{YM}{(1+N)} \tag{C.24}$$

$$GAC0 = N - \frac{YM}{(1+X)} \tag{C.25}$$

# Appendix D

# **Participation Factors**

The participation factor of a mode is derived to help identify how a dynamic variables affects the mode. For the state space model, referring to equation (6.1), the state component, x, of the system,

$$\frac{dx}{dt} = Ax \tag{D.1}$$

the vector of eigenvalues of the A matrix is defined by  $\lambda$  and  $\mathbf{v}$  is the eigenvector. The relation is denoted by

$$Av = \lambda v \tag{D.2}$$

The measure of the sensitivity of each eigenvalue to each diagonal entry of the A matrix  $(a_{kk})$  is the participation factor [311].

$$p_{ki} = \frac{\delta \lambda_i}{\delta a_{kk}} \tag{D.3}$$

The  $p_{ki}$  participation factor for each  $i^{th}$  eigenvalue and  $kk^{th}$  diagonal entry in A matrix relates the  $k^{th}$  state to the  $i^{th}$  eigenvalue.

From the participation factor equation defined in (7.5), the kth entries in the left and right eigenvectors,  $w_i$  and  $v_i$ , satisfy:

$$Av_i = \lambda_i v_i w_i^t A = w_i^t \lambda_i \tag{D.4}$$

# Appendix E

# MMC Equation Derivation Detail

The expansion of two oscillating signals, X(t) and Y(t), multiplied together in the dq reference frame can be represented by

$$\begin{split} Z(t) &= X(t)Y(t) \\ Z(t) &= (X_0Y_0 + \frac{X_DY_D}{2} + \frac{X_QY_Q}{2} + \frac{X_{D2}Y_{D2}}{2} + \frac{X_{Q2}Y_{Q2}}{2}) + \\ (X_DY_0 + X_0Y_D + \frac{X_{D2}Y_D}{2} + \frac{X_{Q2}Y_Q}{2} + \frac{X_DY_{D2}}{2} + \frac{X_QY_{Q2}}{2})cos(\omega t) \\ &+ (X_QY_0 + X_0Y_Q - \frac{X_{D2}Y_Q}{2} + \frac{X_{Q2}Y_D}{2} - \frac{X_QY_{D2}}{2} + \frac{X_DY_{Q2}}{2})sin(\omega t) \\ &+ (\frac{X_DY_D}{2} - \frac{X_QY_Q}{2} + X_{D2}Y_0 + X_{X_0}Y_{D2})cos(2\omega t) \\ &+ (\frac{X_QY_D}{2} + \frac{X_DY_Q}{2} + X_{Q2}Y_0 + X_{X_0}Y_{Q2})sin(2\omega t) \end{split} \tag{E.1}$$

# Appendix E. MMC Equation Derivation Detail

The expanded linearised equations for the converter side AC voltages in the dq frame can be defined by:

$$\begin{split} \Delta V_d &= \frac{\Delta M_d (2v_{UC00}^{\sum} + v_{UCD20}^{\sum})}{4} + \frac{\Delta M_q (v_{UCQ20}^{\sum})}{4} + \\ &\frac{\Delta M_{D2} (v_{UCD0}^{\sum})}{4} + \frac{\Delta M_{Q2} (v_{UCQ0}^{\sum})}{4} + \frac{\Delta v_{UCD2}^{\sum} M_{D0}}{4} + \\ &\frac{\Delta v_{UCQ2}^{\sum} M_{Q0}}{4} + \frac{\Delta v_{UCD}^{\sum} (-2 + M_{D20})}{4} + \\ &\frac{\Delta v_{UCQ}^{\sum} (M_{Q20})}{4} + \frac{\Delta v_{UCQ}^{\sum} (2M_{D0})}{4} \end{split}$$

$$\begin{split} \Delta V_q &= \frac{\Delta M_d(v_{UCQ20}^{\sum})}{4} + \frac{\Delta M_q(2v_{UC00}^{\sum} - v_{UCD20}^{\sum})}{4} - \\ &\frac{\Delta M_{D2}(v_{UCQ0}^{\sum})}{4} + \frac{\Delta M_{Q2}(v_{UCD0}^{\sum})}{4} - \frac{\Delta v_{UCD2}^{\sum} M_{Q0}}{4} + \\ &\frac{\Delta v_{UCQ2}^{\sum} M_{D0}}{4} + \frac{\Delta v_{UCD}^{\sum} (M_{Q20})}{4} - \\ &\frac{\Delta v_{UCQ}^{\sum} (2 + M_{D20})}{4} + \frac{\Delta v_{UC0}^{\sum} (2M_{Q0})}{4} \end{split}$$

- [1] G. D. Carne, M. Langwasser, M. Ndreko, R. Bachmann, R. W. D. Doncker, R. Dimitrovski, B. J. Mortimer, A. Neufeld, F. Rojas, and M. Liserre, "Which deepness class is suited for modeling power electronics?: A guide for choosing the right model for grid-integration studies," *IEEE Industrial Electronics Magazine*, vol. 13, no. 2, pp. 41–55, 6 2019, doi: 10.1109/MIE.2019.2909799.
- [2] NASA's earth observatory library. Accessed 22/10/2024. [Online]. Available: https://earthobservatory.nasa.gov/glossary
- [3] H. Lee and J. Romero, "IPCC, 2023: Climate Change 2023: Synthesis Report. Contribution of Working Groups I, II and III to the Sixth Assessment Report of the Intergovernmental Panel on Climate Change [Core Writing Team, H. Lee and J. Romero (eds.)]. IPCC, Geneva, Switzerland." pp. 35–115, July 2023, doi: 10.59327/IPCC/AR6-9789291691647.
- [4] Solar Power Europe, "2023: A milestone year for renewable energy in Europe Unveiling Ember's Electricity Review," Tech. Rep., 8/2/2024. [Online]. Available: https://www.solarpowereurope.org/news/2023-a-milestone-year-for-renewable-energy-in-europe-unveiling-ember-s-electricity-review
- [5] European Environment Agency, "Share of energy consumption from renewable sources in Europe," 27/3/2024. [Online]. Available: https://www.eea.europa.eu/en/analysis/indicators/share-of-energy-consumption-from
- [6] R. Aljarrah, B. B. Fawaz, Q. Salem, M. Karimi, H. Marzooghi, and R. Azizipanah-Abarghooee, "Issues and challenges of grid-following converters interfacing

- renewable energy sources in low inertia systems: A review," *IEEE Access*, vol. 12, pp. 5534–5561, 2024, doi: 10.1109/ACCESS.2024.3349630.
- [7] S. Xu, Y. Xue, and L. Chang, "Review of Power System Support Functions for Inverter-Based Distributed Energy Resources- Standards, Control Algorithms, and Trends," *IEEE Open Journal of Power Electronics*, vol. 2, pp. 88–105, 2021, doi: 10.1109/OJPEL.2021.3056627.
- [8] J. C. Hernández, P. G. Bueno, and F. Sanchez-Sutil, "Enhanced utility-scale photovoltaic units with frequency support functions and dynamic grid support for transmission systems," *IET Renewable Power Generation*, vol. 11, no. 3, pp. 361–372, 2017, doi: /10.1049/iet-rpg.2016.0714. [Online]. Available: https://ietresearch.onlinelibrary.wiley.com/doi/abs/10.1049/iet-rpg.2016.0714
- [9] J. Morren, S. W. de Haan, W. L. Kling, and J. A. Ferreira, "Wind turbines emulating inertia and supporting primary frequency control," *IEEE Transactions* on *Power Systems*, vol. 21, pp. 433–434, 2006, doi: 10.1109/TPWRS.2005.861956.
- [10] H.-P. Beck and R. Hesse, "Virtual synchronous machine," in 2007 9th International Conference on Electrical Power Quality and Utilisation, 2007, pp. 1–6, doi: 10.1109/EPQU.2007.4424220.
- [11] S. D'Arco and J. A. Suul, "Equivalence of Virtual Synchronous Machines and Frequency-Droops for Converter-Based MicroGrids," *IEEE Transactions on Smart Grid*, vol. 5, no. 1, pp. 394–395, 2014, doi: 10.1109/TSG.2013.2288000.
- [12] R. Musca, A. Vasile, and G. Zizzo, "Grid-forming converters. A critical review of pilot projects and demonstrators," *Renewable and Sustainable Energy Reviews*, vol. 165, p. 112551, 9 2022, doi: 10.1016/j.rser.2022.112551.
- [13] S. Harrison, C. Henderson, P. N. Papadopoulos, and A. Egea-Alvarez, "Demystifying inertial specifications; supporting the inclusion of grid-followers," *IET Renewable Power Generation*, vol. 17, no. 7, pp. 1768–1782, 2023, doi: 10.1049/rpg2.12711.

- [14] National Grid, "Operability Strategy Report December 2023," Tech. Rep., 2023.
  [Online]. Available: https://www.nationalgrideso.com
- [15] National Grid ESO, "Sub-synchronous oscillations in GB: Current state and plans for future management," May 2024.
- [16] U. Perera, A. M. T. Oo, and R. Zamora, "Sub Synchronous Oscillations under High Penetration of Renewables; A Review of Existing Monitoring and Damping Methods, Challenges, and Research Prospects," *Energies*, vol. 15, no. 22, 2022, doi: 10.3390/en15228477.
- Ρ. [17] E. Solutions. Understanding EMT RMS Simulations VS. inElectrical Power Systems. Accessed [10/03/2025].[Online]. Available: https://www.engineeringpowersolutions.co.uk/ emt-vs-rms-simulations-in-electrical-power-systems/#:~:text=Root%20Mean% 20Square%20(RMS)%20simulations%20use%20phasor%20representations% 20of%20voltages, and%20under%20steady%2Dstate%20conditions.
- [18] S. Zhao, R. Li, B. Gao, N. Wang, and S. Song, "Sub and Super Synchronous Oscillations between Type 4 Wind Turbines and Series Compensated AC Transmission Systems," in 2018 IEEE Power & Energy Society General Meeting (PESGM), 2018, pp. 1–5, doi: 10.1109/PESGM.2018.8586539.
- [19] J. Ma, L. Wang, and P. Cheng, "Research on the Mechanism of Simultaneous Instability of dq Frame Sub - and Super-Synchronous Oscillations in Grid-Tied Converter," *IEEE Transactions on Power Systems*, vol. 38, no. 3, pp. 2895–2913, 2023, doi: 10.1109/TPWRS.2022.3185787.
- [20] L. Carlsson, "HVDC: a "Firewall" against disturbances in high-voltage grids." ABB, Tech. Rep., March 2005.
- [21] P. Kundur, Power System Stability And Control, M. G. Balu, Neal J; Lauby, Ed. McGraw-Hill Professional, 1994, 10: 007035958X.

- [22] D. Kumar, F. Zare, and A. Ghosh, "DC Microgrid Technology: System Architectures, AC Grid Interfaces, Grounding Schemes, Power Quality, Communication Networks, Applications, and Standardizations Aspects," *IEEE Access*, vol. 5, pp. 12230–12256, 2017, doi: 10.1109/ACCESS.2017.2705914.
- [23] X. Kong, Z. Yan, R. Guo, X. Xu, and C. Fang, "Three-Stage Distributed State Estimation for AC-DC Hybrid Distribution Network under Mixed Measurement Environment," *IEEE Access*, vol. 6, pp. 39 027–39 036, 2018, doi: 10.1109/ACCESS.2018.2853664.
- [24] R. Ryndzionek and Łukasz Sienkiewicz, "Evolution of the HVDC link connecting offshore wind farms to onshore power systems," *Energies*, vol. 13, no. 8, 2020, doi: 10.3390/en13081914.
- [25] J. Yu, K. Smith, M. Urizarbarrena, M. Bebbington, N. Macleod, and A. Moon, "INITIAL DESIGNS FOR ANGLE-DC PROJECT: CHALLENGES CONVERTING EXISTING AC CABLE AND OVERHEAD LINE TO DC OPERATION," Circl 2017, vol. 2017, no. 0974, pp. 12–15, 2017.
- [26] L. Qu, Z. Yu, Q. Song, Z. Yuan, B. Zhao, D. Yao, J. Chen, Y. Liu, and R. Zeng, "Planning and analysis of the demonstration project of the MVDC distribution network in Zhuhai," Frontiers in Energy, vol. 13, no. 1, pp. 120–130, 2019, doi: 10.1007/s11708-018-0599-2.
- [27] M. Brenna, F. Foiadelli, and D. Zaninelli, Electrical Railway Transportation Systems. Wiley-IEEE Press, 2018, ch. DC Railway Electrification Systems, pp. 99–175.
- [28] A. Verdicchio, P. Ladoux, H. Caron, and S. Sanchez, "Future DC Railway Electrification System - Go for 9 kV," in 2018 IEEE International Conference on Electrical Systems for Aircraft, Railway, Ship Propulsion and Road Vehicles and International Transportation Electrification Conference, ESARS-ITEC 2018. IEEE, 2019, doi: 10.1109/ESARS-ITEC.2018.8607304.

- [29] A. Verdicchio, P. Ladoux, H. Caron, and C. Courtois, "New Medium-Voltage DC Railway Electrification System," *IEEE Transactions on Transportation Electrification*, vol. 4, pp. 591–604, 2018, doi: 10.1109/TTE.2018.2826780.
- [30] S. G. Jayasinghe, L. Meegahapola, N. Fernando, Z. Jin, and J. M. Guerrero, "Review of ship microgrids: System architectures, storage technologies and power quality aspects," *Inventions*, vol. 2, no. 1, pp. 1–19, 2017, doi: 10.3390/inventions2010004.
- [31] R. Soman, M. M. Steurer, T. A. Toshon, M. O. Faruque, and R. M. Cuzner, "Size and Weight Computation of MVDC Power Equipment in Architectures Developed Using the Smart Ship Systems Design Environment," *IEEE Journal of Emerging and Selected Topics in Power Electronics*, vol. 5, no. 1, pp. 40–50, 2017, doi: 10.1109/JESTPE.2016.2625030.
- [32] SP Energy Networks and Ofgem, "ANGLE-DC 2015 Electricity Network Innovation Competition," pp. 1–101, 2015, ISSN: 0360-5442.
- [33] L. Zhang, W. Tang, J. Liang, G. Li, Y. Cai, and T. Yan, "A Medium Voltage Hybrid Ac/Dc Distribution Network and its Economic Evaluation," in 12th IET International Conference on AC and DC Power Transmission (ACDC 2016), 2016, doi: 10.1049/cp.2016.0446.
- [34] S. Faddel, A. A. Saad, and O. Mohammed, "Decentralized energy management of hybrid energy storage on MVDC shipboard power system," 2018 IEEE Industry Applications Society Annual Meeting, IAS 2018, pp. 1–7, 2018, doi: 10.1109/IAS.2018.8544604.
- [35] H. Li, W. Li, M. Luo, A. Monti, and F. Ponci, "Design of smart MVDC power grid protection," *IEEE Transactions on Instrumentation and Measurement*, vol. 60, no. 9, pp. 3035–3046, 2011, doi: 10.1109/TIM.2011.2158152.
- [36] L. Wang, G. Zhang, M. Shen, H. Quan, and Z. Liu, "A Novel Traction Supply System for Urban Rail Transportation with Bidirectional Power Flow

- and Based on PWM Rectifier," in 2009 International Conference on Energy and Environment Technology, vol. 2, 2009, pp. 40–43, doi: 10.1109/ICEET.2009.246.
- [37] I. Ferencz, D. Petreus, and P. Tricoli, "Converter Topologies for MVDC Traction Transformers," in 2020 IEEE 26th International Symposium for Design and Technology in Electronic Packaging, SIITME 2020, 2020, pp. 362–367, doi: 10.1109/SIITME50350.2020.9292214.
- [38] J. M. Maza-Ortega, E. Acha, S. García, and A. Gómez-Expósito, "Overview of power electronics technology and applications in power generation transmission and distribution," *Journal of Modern Power Systems and Clean Energy*, vol. 5, no. 4, pp. 499–514, 2017, doi: 10.1007/s40565-017-0308-x.
- [39] S. Gao, S. Liu, Y. Liu, X. Zhao, and T. E. Song, "Flexible and Economic Dispatching of AC/DC Distribution Networks Considering Uncertainty of Wind Power," *IEEE Access*, vol. 7, pp. 100051–100065, 2019, doi: 10.1109/access.2019.2930248.
- [40] D. Kong, C. Liu, H. Ying, Z. Pei, J. Li, and H. Zhang, "Operating Modes Analysis and Control Strategy of Single-Stage Isolated Modular Multilevel Converter (I-MMC) for Medium Voltage AC/DC Grid," *IECON Proceedings* (Industrial Electronics Conference), vol. 2019-Octob, pp. 5674–5679, 2019, doi: 10.1109/IECON.2019.8927196.
- [41] G. Bathurst, G. Hwang, and L. Tejwani, "MVDC-the new technology for distribution networks," *IET Seminar Digest*, no. CP654, pp. 1–5, 2015, doi: 10.1049/cp.2015.0037.
- [42] V. Salehi, B. Mirafzal, and O. Mohammed, "Pulse-load effects on ship power system stability," in *IECON 2010 - 36th Annual Conference on IEEE Industrial Electronics Society*. IEEE, 2010, pp. 3353–3358, doi: 10.1109/IECON.2010.5675297.
- [43] C. Qi, K. Wang, Y. Fu, G. Li, B. Han, R. Huang, and T. Pu, "A decentralized optimal operation of AC/DC hybrid distribution grids," *IEEE Transactions on*

- Smart Grid, vol. 9, no. 6, pp. 6095–6105, 2018, doi: 10.1109/TSG.2017.2703582.
- [44] Q. Zhou and D. Yuan, "Prediction on future DC power system," 2009 IEEE 6th International Power Electronics and Motion Control Conference, IPEMC '09, vol. 3, pp. 1192–1195, 2009, doi: 10.1109/IPEMC.2009.5157564.
- [45] W. Cao, J. Wu, N. Jenkins, C. Wang, and T. Green, "Operating principle of Soft Open Points for electrical distribution network operation," *Applied Energy*, vol. 164, pp. 245–257, 2016, doi: 10.1016/j.apenergy.2015.12.005.
- [46] M. Bloemink, "Distribution-level power electronics: Soft open-points," Ph.D. dissertation, Imperial College London, 2013, doi: 10.25560/17991.
- [47] P. Simiyu, A. Xin, K. Wang, G. Adwek, and S. Salman, "Multiterminal medium voltage DC distribution network hierarchical control," *Electronics (Switzerland)*, vol. 9, no. 3, 2020, doi: 10.3390/electronics9030506.
- [48] A. Parastar, H. Hasanvand, M. Eshagi, and M. R. Zamani, "Multilevel Step-Up DC / DC Converter for MVDC Applications," in 30th Power System Conference, Tehran. IEEE, 2015, pp. 23–25, ISBN: 9781509027057.
- [49] D. Cahyagi, "Study of Shipboard Power Distribution System: Review on an Application of AC Zonal Distribution," *IPTEK Journal of Engineering*, vol. 4, 2018, doi: 10.12962/joe.v4i1.3734.
- [50] H. Rickover and P. Ross, "Fault Protection on Shipboard A-C Power-Distribution Systems," Transactions of the American Institute of Electrical Engineers, vol. 63, no. 12, p. 1109–1120, 1944, doi: 10.1109/T-AIEE.1944.5058854.
- [51] S. Dale, "Ship power system testing and simulation," in *IEEE Electric Ship Technologies Symposium*, 2005, doi: 10.1109/ESTS.2005.1524675.
- [52] D. Kumar and F. Zare, "A Comprehensive Review of Maritime Microgrids: System Architectures, Energy Efficiency, Power Quality, and Regulations," *IEEE Access*, vol. 7, pp. 67249–67277, 2019, doi:10.1109/ACCESS.2019.2917082.

- [53] J. D. Schuddebeurs, P. J. Norman, C. D. Booth, G. M. Burt, and J. R. Mcdonald, "Emerging research issues regarding integrated-full-electric-propulsion," in Proceedings of the 41st International Universities Power Engineering Conference, 2006, pp. 669–673.
- [54] M. Cupelli, F. Ponci, G. Sulligoi, A. Vicenzutti, C. S. Edrington, T. El-Mezyani, and A. Monti, "Power Flow Control and Network Stability in an All-Electric Ship," *Proceedings of the IEEE*, vol. 103, no. 12, pp. 2355–2380, 2015.
- [55] B. Z. Jin, G. Sulligoi, R. Cuzner, L. Meng, J. C. Vasquez, and J. M. Guerrero, "Next-Generation Shipboard DC Power System," *IEEE Electrification Magazine*, vol. 4, pp. 45–57, 2016.
- [56] F. Balsamo, D. Lauria, and F. Mottola, "Design and Control of Coupled Inductor DC – DC Converters for MVDC Ship Power Systems," *Energies*, vol. 12, no. 751, 2019, doi: 10.3390/en12040751.
- [57] A. Mariscotti, "Power quality phenomena, standards, and proposed metrics for DC grids," *Energies*, vol. 14, no. 20, 2021, doi: 10.3390/en14206453.
- [58] S. Castellan, R. Menis, A. Tessarolo, F. Luise, and T. Mazzuca, "A review of power electronics equipment for all-electric ship MVDC power systems," *Electrical Power and Energy Systems*, vol. 96, no. September 2017, pp. 306–323, 2018, doi:10.1016/j.ijepes.2017.09.040.
- [59] S. (GE). (2012)Queen Elizabeth Class (QEC) Aircraft Carrier. Rugby, Warwickshire. July 2021. [Online]. Accessed Available: https://www.gepowerconversion.com/sites/default/files/MARINE\_ GEA20337-QueenElizabeth-CaseStudy.pdf
- [60] M. Andrus, H. Ravindra, J. Hauer, M. Steurer, M. Bosworth, and R. Soman, "PHIL implementation of a MVDC fault management test bed for ship power systems based on megawatt-scale modular multilevel converters," 2015 IEEE Electric Ship Technologies Symposium, ESTS 2015, pp. 337–342, 2015, doi: 10.1109/ESTS.2015.7157915.

- [61] E. Skjong, E. Rødskar, M. Molinas, T. A. Johansen, and J. Cunningham, "The Marine Vessel's Electrical Power System: From its Birth to Present Day," *Proceedings of the IEEE*, vol. 103, no. 12, pp. 2410–2424, 2015, doi: 10.1109/JPROC.2015.2496722.
- [62] Kongsberg, "Autonomous Ship Project, Key Facts About Yara Birkeland," Accessed June 2021. [Online]. Available: https://www.kongsberg.com/maritime/support/themes/autonomous-ship-project-key-facts-about-yara-birkeland/
- [63] A. Kortsari, L. Mitropoulos, T. Heinemann, and H. H. Mikkelsen, "Evaluation report of the E-Ferry," Tech. Rep., 2020, issue 636027. E-Ferry. [Online]. Available: http://www.conf.eferry.eu/InfoPackage/eFerry\_Information\_Package. pdf
- [64] H. Helgesen, S. Henningsgård, and A. A. Langli, "Electrical Energy Storage for Ships," DNV GL Distribution, Norway, Tech. Rep., May 2020. [Online]. Available: http://www.emsa.europa.eu/news-a-press-centre/external-news/item/3906-electrical-energy-storage-for-ships.html
- [65] K. Sharifabadi, L. Harnefors, H. P. Nee, S. Norrga, and R. Teodorescu, Design, Control and Application of Modular Multilevel Converters for HVDC Transmission Systems. Wiley, 2016, doi: 10.1002/9781118851555.
- [66] Energy Corvus, "CASE STUDY: Norled AS, MF Ampere, Ferry," 2015. [Online]. Available: http://files7.webydo.com/42/421998/UploadedFiles/ a4465574-14ff-4689-a033-08ac32adada1.pdf
- [67] A. Gómez-Expósito, J. M. Mauricio, and J. M. Maza-Ortega, "VSC-Based MVDC Railway Electrification System," *IEEE Transactions on Power Delivery*, vol. 29, no. 1, pp. 422–431, 2014, doi: 10.1109/TPWRD.2013.2268692.
- [68] R. Nunno, "Electrification of U.S. Railways: Pie in the Sky, or Realistic Goal?" Environmental and Energy Study Institute, Tech. Rep., 2018, Accessed May 2021. [Online]. Available: https://www.eesi.org/articles/view/electrification-of-u.s.-railways-pie-in-the-sky-or-realistic-goal

- [69] Z. Fei, T. Konefal, and R. Armstrong, "AC railway electrification systems-An EMC perspective," *IEEE Electromagnetic Compatibility Magazine*, vol. 8, no. 4, pp. 62–69, 2019, doi: 10.1109/MEMC.2019.8985603.
- [70] J. J. Mwambeleko and T. Kulworawanichpong, "Battery and accelerating-catenary hybrid system for light rail vehicles and trams," 2017 International Electrical Engineering Congress, IEECON 2017, vol. 150, pp. 8–10, 2017, doi: 10.1109/IEECON.2017.8075778. ISBN: 9781509046669.
- [71] T. Ratniyomchai, S. Hillmansen, and P. Tricoli, "Recent developments and applications of energy storage devices in electrified railways," *IET Electrical* Systems in Transportation, vol. 4, no. 1, pp. 9–20, 2014, doi: 10.1049/ietest.2013.0031.
- [72] J. Hu, W. Liu, and J. Yang, "Application of power electronic devices in rail transportation traction system," *Proceedings of the International Symposium on Power Semiconductor Devices and ICs*, pp. 7–12, June 2015, doi: 10.1109/ISPSD.2015.7123376.
- [73] L. Abrahamsson, T. Schütte, and S. Östlund, "Use of converters for feeding of AC railways for all frequencies," *Energy for Sustainable Development*, vol. 16, no. 3, pp. 368–378, 2012, doi: 10.1016/j.esd.2012.05.003.
- [74] I. A. Barinov and O. V. Melnichenko, "Power IGBTs application in AC-wire DC-motor locomotive thyristor-based power circuit for regenerative brake energy efficiency increase," 2019 International Conference on Industrial Engineering, Applications and Manufacturing, ICIEAM 2019, 2019, doi: 10.1109/ICIEAM.2019.8742933.
- [75] H. Caron and C. C. S. Réseau, "New Medium Voltage DC railway Electrification System - Work Shop," *IEEE transaction on transportation electrification*, vol. 4, no. 2, pp. 591–604, 2018.
- [76] T. L. Tobing, T. D. Rachmilda, H. Hindersah, A. Rizqiawan, and Y. Haroen, "Rectifier substation optimum position on DC traction systems," in *Proceeding*

- 4th International Conference on Electric Vehicular Technology, ICEVT 2017, January 2018, pp. 134–138, doi: 10.1109/ICEVT.2017.8323548.
- [77] F. H. Pereira, C. L. Pires, and S. I. Nabeta, "Optimal placement of rectifier substations on DC traction systems," *IET Electrical Systems in Transportation*, vol. 4, no. 3, pp. 62–69, 2014, doi: 10.1049/iet-est.2010.0063.
- [78] K. Ogura, K. Nishimura, and Y. Oku, "A Bidirectional DC-DC Converter for Battery Electric Light Rail Vehicle and Its Test Run Results," Proceedings of the International Conference on Power Electronics and Drive Systems, July 2019, doi: 10.1109/PEDS44367.2019.8998957.
- [79] G. Crotti, A. D. Femine, D. Gallo, D. Giordano, C. Landi, M. Luiso, A. Mariscotti, and P. E. Roccato, "Pantograph-To-OHL Arc: Conducted Effects in DC Railway Supply System," *IEEE Transactions on Instrumentation and Measurement*, vol. 68, no. 10, pp. 3861–3870, 2019, doi: 10.1109/TIM.2019.2902805.
- [80] S. Midya, D. Bormann, T. Schütte, and R. Thottappillil, "Pantograph arcing in electrified railways - Mechanism and influence of various parameters - Part I: With DC traction power supply," *IEEE Transactions on Power Delivery*, vol. 24, no. 4, pp. 1931–1939, 2009, doi: 10.1109/TPWRD.2009.2021035.
- [81] Y. Seferi, S. M. Blair, C. Mester, and B. G. Stewart, "A Novel Arc Detection Method for DC Railway Systems," *Energies*, vol. 14, no. 2, pp. 1–21, 2021, doi: 10.3390/en14020444.
- [82] O. Boler, A. Ibrahem, A. A. Ali, M. G. Granger, H. Abdelgabir, Y. Sozer, and J. A. D. Abreu-Garcia, "A Novel High Frequency Impedance Analysis Method to Protect DC Electrical Railway Systems," *IEEE Transactions on Industry Applications*, vol. 56, no. 1, pp. 669–677, 2020, doi: 10.1109/TIA.2019.2955415.
- [83] H. Zhang, L. Harnefors, X. Wang, H. Gong, and J. P. Hasler, "Stability Analysis of Grid-Connected Voltage-Source Converters Using SISO Modeling," IEEE

- Transactions on Power Electronics, vol. 34, no. 8, pp. 8104–8117, 2019, doi: 10.1109/TPEL.2018.2878930.
- [84] L. Zhang, J. Liang, W. Tang, G. Li, Y. Cai, and W. Sheng, "Converting AC distribution lines to DC to increase transfer capacities and DG penetration," IEEE Transactions on Smart Grid, vol. 10, no. 2, pp. 1477–1487, 2019, doi: 10.1109/TSG.2017.2768392.
- [85] Working Group C6.31, "CIGRE Medium Voltage Direct Current (MVDC) Grid Feasibility Study," *ELECTRA CIGRE's Digital Magazine*, April 2020. [Online]. Available: https://electra.cigre.org/309-april-2020/technical-brochures/medium-voltage-direct-current-mvdc-grid-feasibility-study.html
- [86] A. Giannakis and D. Peftitsis, "MVDC Distribution Grids and Potential Applications: Future Trends and Protection Challenges," in 2018 20th European Conference on Power Electronics and Applications (EPE'18 ECCE Europe), 2018, pp. P.1–P.9.
- [87] V. M. Hrishikesan, D. Das, C. Kumar, H. Gooi, S. Mekhilef, and X. Guo, "Increasing Voltage Support Using Smart Power," vol. 46, 2020, doi: 10.1109/TIE.2020.3042165.
- [88] SIEMENS AG, "Whitepaper-MVDC Plus Managing the future grid," pp. 5–7, 2017.
- [89] M. Stieneker and R. W. D. Doncker, "Medium-voltage dc distribution grids in urban areas," in 2016 IEEE 7th International Symposium on Power Electronics for Distributed Generation Systems (PEDG), 2016, pp. 1–7, doi: 10.1109/PEDG.2016.7527045.
- [90] S. Wang, W. Ming, and J. Liang, "Interlinked Solid-state MVDC Circuit Breaker with Current Regulation Capability," *IECON Proceedings (Industrial Electronics Conference)*, pp. 5668–5673, October 2019, doi: 10.1109/IECON.2019.8927420.

- [91] N. Bayati, A. Hajizadeh, and M. Soltani, "Protection in DC microgrids: A comparative review," *IET Smart Grid*, vol. 1, no. 3, pp. 66–75, 2018, doi: 10.1049/iet-stg.2018.0035.
- [92] J. D. Park, "Ground fault detection and location for ungrounded DC traction power systems," *IEEE Transactions on Vehicular Technology*, vol. 64, no. 12, pp. 5667–5676, 2015, doi: 10.1109/TVT.2015.2388785.
- [93] G. F. Reed, B. M. Grainger, A. R. Sparacino, and Z. H. Mao, "Ship to grid: Medium-voltage DC concepts in theory and practice," *IEEE Power and Energy Magazine*, vol. 10, no. 6, pp. 70–79, 2012, doi: 10.1109/MPE.2012.2212613.
- [94] T. Joseph, J. Liang, G. Li, A. Moon, K. Smith, and J. Yu, "Dynamic Control of MVDC Link Embedded in Distribution Network:- Case Study on ANGLE-DC," Proceedings - IEEE Conference on Energy Internet and Energy System Integration, pp. 1–6, 2017.
- [95] J. Yu and I. Cameron, "Active response to Distribution Network contraints," UKPN, Tech. Rep., 2018.
- [96] G. LIU, Y. ZHAO, and Z. YUAN, "Study on Demonstration Project Technical Scheme of VSC-DC Distribution System in Shenzhen," Southern Power System Technology, vol. 10, no. 4, pp. 1–7, 2016.
- [97] L. Su, P. Zhu, A. Yan, Y. Ma, M. He, J. Mei, B. Wang, and G. Fan, "Design Scheme and Simulation Verification of Suzhou Medium Voltage DC Distribution Project," *Electric Power*, vol. 54, no. 1, pp. 78–88, 2021.
- [98] L. Hunter, C. Booth, A. J. Ferre, and S. Finney, "MVDC for enhanced utility scale distribution power delivery and control," 2017 52nd International Universities Power Engineering Conference, UPEC 2017, pp. 1–6, January 2017, doi: 10.1109/UPEC.2017.8232000.
- [99] D. Hardman, "FPL Development and Improvement Report," Western Power Distribution, Tech. Rep., 2019.

- [100] G. Abeynayake, G. Li, T. Joseph, and J. Liang, "Reliability and Cost-oriented Analysis, Comparison and Selection of Multi-level MVDC Converters," *IEEE Transactions on Power Delivery*, 2021, doi: 10.1109/TPWRD.2021.3051531.
- [101] J. Wenlin, "GE Strengthens Power Supply in Anglesey," 2017.
  [Online]. Available: https://www.gepowerconversion.com/press-releases/ge-supports-power-grids-future-europes-first-mvdc-link
- [102] S. Liu, Y. Zhao, L. Chen, and Z. Si, "Research on Control and Protection Strategy and Design Scheme of VSC-DC Distribution Network Control and Protection System," *Distribution & Utilization*, vol. 35, no. 1, pp. 34–39, 2018.
- [103] S. Rivera, F. Lizana, S. Kouro, T. Dragicevic, and B. Wu, "Bipolar DC Power Conversion: State-of-the-Art and Emerging Technologies," *IEEE Journal of Emerging and Selected Topics in Power Electronics*, vol. 9, 2021.
- [104] G. Jambrich, J. Stöckl, and M. Makoschitz, "MVDC ring-cable approach for new DC distribution and restructured AC grids," in 2019 IEEE Third International Conference on DC Microgrids (ICDCM), 2019, pp. 1–5, doi: 10.1109/ICDCM45535.2019.9232731.
- [105] G. Abeynayake, G. Li, T. Joseph, W. Ming, A. Moon, K. Smith, and J. Yu, "Reliability Evaluation of Voltage Source Converters for MVDC Applications," IEEE PESS Innovative Smart Grid Technologies Asia, pp. 2566–2570, 2019, ISBN: 9781728135205.
- [106] G. Abeynayake, G. Li, J. Liang, and N. Cutululis, "A Review on MVdc Collection Systems for High-Power Offshore Wind Farms," in 2019 14th Conference on Industrial and Information Systems (ICIIS), Kandy, Sri Lanka, 18–20 December 2019, pp. 407–412.
- [107] A. Cui, J. Hu, and R. D. Doncker, "Control and Experiment of a TLC-MMC Hybrid DC-DC Converter for the Interconnection of MVDC and HVDC Grids," IEEE Transactions Power Electronics, vol. 35, 2020.

- [108] D. Bosich, R. A. Mastromauro, and G. Sulligoi, "AC-DC interface converters for MW-scale MVDC distribution systems: A survey," 2017 IEEE Electric Ship Technologies Symposium, ESTS 2017, pp. 44–49, 2017, doi: 10.1109/ESTS.2017.8069258.
- [109] L. Shi, G. Adam, R. Li, and L. Xu, "Enhanced Control of Offshore Wind Farms Connected to MTDC Network Using Partially Selective DC Fault Protection," IEEE Journal of Emerging and Selected Topics in Power Electronics, vol. 9, 2020.
- [110] S. Lundberg, "Performance Comparison of Wind Park Configurations," Ph.D. dissertation, Chalmers University of Technology, Gothenburg, Sweden, 2003.
- [111] N. Holtsmark, H. Bahirat, M. Molinas, B. Mork, and H. Høidalen, "An All-DC offshore wind farm with series-connected turbines: An alternative to the classical parallel AC model?" *IEEE Transactions on Industrial Electronics*, vol. 60, p. 2420–2428, 2013.
- [112] ABB ForSea (Formerly HH Ferries Group) Completes Conversion of the World's Largest Batter Ferries, Powered by ABB. ABB. Accessed 01/11/20214. [Online]. Available: https://new.abb.com/news/detail/10434/ forsea-formerly-hh-ferries-group-completes-conversion-of-the-worlds-largest-battery-ferries-pow
- [113] Kongsberg Energy Products. Accessed April 2021.
  [Online]. Available: https://www.kongsberg.com/maritime/products/
  electrical-power-system/energy-products/
- [114] T. U. Okeke and R. G. Zaher, "Flexible AC Transmission Systems (FACTS)," 2013 International Conference on New Concepts in Smart Cities: Fostering Public and Private Alliances (SmartMILE), Gijon, pp. 1–4, 2013, ISBN: 9781479929115.
- [115] R. Bernacchi, "MVDC and Grid Interties: enabling new features in distribution, sub-transmission and industrial networks," *ABB Review*, pp. 1–10, 2019.

- [116] UK Power Networks, "High-level design specification of advanced automation solution: Active response project deliverable 1," 2019, Accessed October 2021.
  [Online]. Available: https://innovation.ukpowernetworks.co.uk/wp-content/uploads/2019/05/Active-Response-Project-Deliverable-1-Report.pdf
- [117] B. Li, Y. Liang, G. Wang, H. Li, and J. Ding, "A control strategy for soft open points based on adaptive voltage droop outer-loop control and sliding mode inner-loop control with feedback linearization," *International Journal of Electrical Power and Energy Systems*, vol. 122, p. 106205, 2020, doi: 10.1016/j.ijepes.2020.106205.
- [118] J. Yu, N. Macleod, K. Smith, and A. Moon, "NIC Project Medium Voltage Direct Current Link Technical Specification NIC Project Medium Voltage Direct Current Link Technical Specification," SPEN, Glasgow, Tech. Rep., 2017.
- [119] M. Fotopoulou, D. Rakopoulos, D. Trigkas, F. Stergiopoulos, O. Blanas, and S. Voutetakis, "State of the art of low and medium voltage direct current (Dc) microgrids," *Energies*, vol. 14, no. 18, 2021, doi: 10.3390/en14185595.
- [120] M. Yang, D. Xie, H. Zhu, and Y. Lou, "Architectures and control for multiterminal DC (MTDC) distribution network-A review," *IET Seminar Digest*, 2015, doi: 10.1049/cp.2015.0100.
- [121] D. Jovcic, M. Taherbaneh, J. P. Taisne, and S. Nguefeu, "Offshore DC grids as an interconnection of radial systems: Protection and control aspects," *IEEE Transactions on Smart Grid*, vol. 6, no. 2, pp. 903–910, 2015, doi: 10.1109/TSG.2014.2365542.
- [122] K. Prakash, A. Lallu, F. R. Islam, and K. A. Mamun, "Review of Power System Distribution Network Architecture," Proceedings Asia-Pacific World Congress on Computer Science and Engineering 2016 and Asia-Pacific World Congress on Engineering 2016, APWC on CSE/APWCE 2016, pp. 124–130, 2017, doi: 10.1109/APWC-on-CSE.2016.030.

- [123] S. Augustine, J. E. Quiroz, M. J. Reno, and S. Brahma, "DC Microgrid Protection: Review and Challenges Sandia National Laboratories," Sandia National Laboraties, Tech. Rep., 2018, doi: 10.2172/1465634.
- [124] R. T. Pinto, S. Rodrigues, P. Bauer, and J. Pierik, "Operation and control of a multi-terminal DC network," 2013 IEEE ECCE Asia Downunder - 5th IEEE Annual International Energy Conversion Congress and Exhibition, IEEE ECCE Asia 2013, pp. 474–480, 2013, doi: 10.1109/ECCE-Asia.2013.6579139.
- [125] A. Korompili, A. Sadu, F. Ponci, and A. Monti, "Flexible electric networks of the future: Project on control and automation in MVDC grids," *International* ETG Congress 2015; Die Energiewende - Blueprints for the New Energy Age, pp. 556–563, 2015.
- [126] Z. Zhuo, N. Zhang, C. Kang, R. Dong, and Y. Liu, "Optimal Operation of Hybrid AC/DC Distribution Network with High Penetrated Renewable Energy," IEEE Power and Energy Society General Meeting, pp. 0–4, August 2018, doi: 10.1109/PESGM.2018.8585802.
- [127] A. Musa, S. Rehan, L. Sabug, F. Ponci, and A. Monti, "Modeling and design of hybrid distribution network: Operational and technical features," 2017 IEEE PES Innovative Smart Grid Technologies Conference Europe, ISGT-Europe 2017 - Proceedings, pp. 1–6, January 2017, doi: 10.1109/ISGTEurope.2017.8260207.
- [128] M. Rouhani and G. J. Kish, "Multiport DC DC AC Modular Multilevel Converters For Hybrid AC/DC Power Systems," *IEEE Transactions on Power Delivery*, vol. 35, no. 1, pp. 408–419, 2020.
- [129] S. Jafarishiadeh, V. Dargahi, A. K. Sadigh, and M. Farasat, "Novel multi-terminal mmc-based dc/dc converter for mvdc grid interconnection," *IET Power Electronics*, vol. 11, no. 7, pp. 1266–1276, 2018, doi: 10.1049/iet-pel.2017.0164.
- [130] B. Zhao, R. Zeng, Q. Song, Z. Yu, and L. Qu, "The energy internet," W. Su and A. Q. Huang, Eds. Woodhead Publishing, 2019, ch. 6 Medium-voltage

- DC power distribution technology, pp. 123–152, doi: 10.1016/B978-0-08-102207-8.00006-0.
- [131] S. Thielemans, T. J. Vyncke, and J. A. Melkebeek, "Voltage Quality Analysis of a Three-Level Flying Capacitor Inverter with Model Based Predictive Control," 8th International Conference on Power Electronics - ECCE Asia: "Green World with Power Electronics", ICPE 2011-ECCE Asia, pp. 124–131, 2011, doi: 10.1109/ICPE.2011.5944560.
- [132] J. Wang, S. Yang, and W. Yang, "Harmonic reduction for 12-pulse four star thyristor rectifier with active auxiliary circuit," *Proceedings of the International* Conference on Power Electronics and Drive Systems, pp. 301–306, August 2015, doi: 10.1109/PEDS.2015.7203484.
- [133] C. Guo, C. Li, C. Zhao, X. Ni, K. Zha, and W. Xu, "An Evolutional Line-Commutated Converter Integrated with Thyristor-Based Full-Bridge Module to Mitigate the Commutation Failure," *IEEE Transactions on Power Electronics*, vol. 32, no. 2, pp. 967–976, 2017, doi: 10.1109/TPEL.2016.2544107.
- [134] F. Wang, L. Bertling, T. Le, A. Mannikoff, and A. Bergman, "An overview introduction of VSC-HVDC: State-of-art and potential applications in electric power systems," CIGRE 2011 Bologna Symposium The Electric Power System of the Future: Integrating Supergrids and Microgrids, 2011, ISBN: 9782858731657.
- [135] X. Huang, L. Qi, and J. Pan, "A New Protection Scheme for MMC-Based MVdc," IEEE Transactions on Industry Applications, vol. 55, no. 5, pp. 4515–4523.
- [136] B. Li, Y. Li, and J. He, "A DC fault handling method of the MMC-based DC system," International Journal of Electrical Power & Energy Systems, vol. 93, pp. 39–50, 2017, doi: 10.1016/j.ijepes.2017.05.011.
- [137] Siemens, "M2C it's short for "innovation"." [Online].

  Available: https://new.siemens.com/global/en/products/drives/
  sinamics/medium-voltage-converters/m2c-technology.html#:~:text=

- Modularmultilevelconverters display their strengths in combination, energy % 2 Coffshore and the metal industry % 2 C for example.
- [138] G. P. Adam, O. Anaya-lara, G. Burt, and J. Mcdonald, "Comparison between Two VSC-HVDC Transmission Systems Technologies: Modular and Neutral Point Clamped Multilevel Converter," Event IECON 2009, the 35th Annual Conference of the IEEE Industrial Electronics Society and ICELIE 2009, the 3rd IEEE International Conference on E-Learning in Industrial Electronics, Porto, 2009.
- [139] J. Sun and H. Liu, "Impedance modeling and analysis of modular multilevel converters," 2016 IEEE 17th Workshop on Control and Modeling for Power Electronics, COMPEL 2016, 2016, doi: 10.1109/COMPEL.2016.7556781.
- [140] G. Konstantinou, J. Pou, S. Ceballos, and V. G. Agelidis, "Active redundant submodule configuration in modular multilevel converters," *IEEE Transactions on Power Delivery*, vol. 28, no. 4, pp. 2333–2341, 2013, doi: 10.1109/TPWRD.2013.2264950.
- [141] D. Vozikis, G. P. Adam, P. Rault, D. Tzelepis, D. Holliday, and S. Finney, "Steady-state performance of state-of-the-art modular multilevel and alternate arm converters with DC fault-blocking capability," *International Journal* of Electrical Power and Energy Systems, vol. 99, pp. 618–629, 2018, doi: 10.1016/j.ijepes.2018.01.054.
- [142] M. Hagiwara and H. Akagi, "Control and Experiment of Pulsewidth-Modulated Modular Multilevel Converters," *IEEE Transactions on Power Electronics*, vol. 24, no. 7, pp. 1737–1746, 2009, doi: 10.1109/TPEL.2009.2014236.
- [143] J. A. Ansari, C. Liu, and S. A. Khan, "MMC Based MTDC Grids: A Detailed Review on Issues and Challenges for Operation, Control and Protection Schemes," *IEEE Access*, vol. 8, pp. 168 154–168 165, 2020, doi: 10.1109/access.2020.3023544.
- [144] J. Qin, M. Saeedifard, A. Rockhill, and R. Zhou, "Hybrid design of modular multilevel converters for HVDC systems based on various submodule circuits,"

- *IEEE Transactions on Power Delivery*, vol. 30, no. 1, pp. 385–394, 2015, doi: 10.1109/TPWRD.2014.2351794.
- [145] F. Deng, Y. Lü, C. Liu, Q. Heng, Q. Yu, and J. Zhao, "Overview on submodule topologies, modeling, modulation, control schemes, fault diagnosis, and tolerant control strategies of modular multilevel converters," *Chinese Journal of Electrical Engineering*, vol. 6, no. 1, pp. 1–21, 2020, doi: 10.23919/CJEE.2020.000001.
- [146] B. Zhao, R. Zeng, J. Li, T. Wei, Z. Chen, Q. Song, and Z. Yu, "Practical Analytical Model and Comprehensive Comparison of Power Loss Performance for Various MMCs Based on IGCT in HVDC Application," *IEEE Journal of Emerging and Selected Topics in Power Electronics*, vol. 7, no. 2, pp. 1071–1083, 2019, doi: 10.1109/JESTPE.2018.2871191.
- [147] T. Yin, C. Xu, L. Lin, and K. Jing, "A SiC MOSFET and Si IGBT Hybrid Modular Multilevel Converter with Specialized Modulation Scheme," *IEEE Transactions on Power Electronics*, vol. 35, no. 12, pp. 12623–12628, 2020, doi: 10.1109/TPEL.2020.2993366.
- [148] GE Siemens, "MV7000 Flat Pack (FP)," GE Siemens, Tech. Rep., 2019.
- [149] T. Jonsson, B. Jacobson, P. Karlsson, G. Asplund, and L. Harnefors, "VSC-HVDC Transmission with Cascaded Two-Level Converter Converter Topology and Main Circuit," CIGRE, Tech. Rep., 2010.
- [150] I. Alhurayyis, S. Member, A. Elkhateb, S. Member, and D. J. Morrow, "Isolated and Non-Isolated DC-to-DC Converters for Medium Voltage DC Networks: A Review," *IEEE Journal of Emerging and Selected Topics in Power Electronics*, 2020.
- [151] R. W. Erickson and D. Maksimović, Fundamentals of Power Electronics, 2nd ed. Springer Science and Business Media, doi: 10.1007/978-1-4471-5104-3'2 ISBN: 9781447151036.

- [152] M. A. Chewale, R. A. Wanjari, V. B. Savakhande, and P. R. Sonawane, "A Review on Isolated and Non-isolated DC-DC Converter for PV Application," 2018 International Conference on Control, Power, Communication and Computing Technologies, ICCPCCT 2018, pp. 399–404, 2018, doi: 10.1109/ICCPCCT.2018.8574312.
- [153] N. Hou, W. Song, Y. Zhu, X. Sun, and W. Li, "Dynamic and static performance optimization of dual active bridge DC-DC converters," *Journal of Modern Power Systems and Clean Energy*, vol. 6, no. 3, pp. 607–618, 2018, doi: 10.1007/s40565-017-0343-7.
- [154] I. Alhurayyis, A. Elkhateb, and D. J. Morrow, "Bidirectional DC-DC Resonant Converter Design for Electric Vehicle Charging Stations Integration to MVDC Grids," in 9th International Conference on Renewable Energy Research and Applications, Glasgow, 2020, pp. 236–241.
- [155] M. STOJADINOVIĆ, "Bidirectional DC-DC Converters for MVDC Applications," Ph.D. dissertation, ETH Zurich, 2020.
- [156] L. Wang, Q. Zhu, W. Yu, and A. Q. Huang, "A Medium-Voltage Medium-Frequency Isolated DC-DC Converter Based on 15-kV SiC MOSFETs," IEEE Journal of Emerging and Selected Topics in Power Electronics, vol. 5, no. 1, pp. 100–109, 2017, doi: 10.1109/JESTPE.2016.2639381.
- [157] G. J. Kish, "On the emerging class of non-isolated modular multilevel DC-DC converters for DC and hybrid AC-DC systems," *IEEE Transactions on Smart Grid*, vol. 10, no. 2, pp. 1762–1771, 2019, doi: 10.1109/TSG.2017.2777473.
- [158] M. Ashraf, Y. Nazih, F. Alsokhiry, K. H. Ahmed, A. S. Abdel-khalik, and Y. Al-Turki, "A New Hybrid Dual Active Bridge Modular Multilevel Based DC-DC Converter for HVDC Networks," *IEEE Access*, 2021, doi: 10.1109/ACCESS.2021.3074543.
- [159] J. A. Ferreira, "The multilevel modular DC converter," *IEEE Transactions* on *Power Electronics*, vol. 28, no. 10, pp. 4460–4465, 2013, doi:

- 10.1109/TPEL.2012.2237413.
- [160] X. Xiang, "The Modular Multilevel DC Converters for MVDC and HVDC Applications," Ph.D. dissertation, Imperial College London, 2019.
- [161] B. Zahedi, "Shipboard DCHybrid Power Systems: Modeling, efficiency analysis and stability control," Ph.D. dissertation, Norwegian and Technology, University of Science 2014, ISBN: 9788232605149. [Online]. Available: https://brage.bibsys.no/xmlui/bitstream/handle/11250/ 258034/759213\_FULLTEXT01.pdf?sequence=1
- [162] C. Sun, X. Cai, J. Zhang, and G. Shi, "A Modular Multilevel DC-DC Converter with Self Voltage Balancing and Soft Switching," Proceedings - 2018 IEEE International Power Electronics and Application Conference and Exposition, PEAC 2018, pp. 12–17, 2018, doi: 10.1109/PEAC.2018.8590357.
- [163] S. P. Engel, M. Stieneker, N. Soltau, S. Rabiee, H. Stagge, and R. W. D. Doncker, "Comparison of the Modular Multilevel DC Converter and the Dual-Active Bridge Converter for Power Conversion in HVDC and MVDC Grids," *IEEE Transactions on Power Electronics*, vol. 30, no. 1, pp. 124–137, 2015.
- [164] "Scottish Power Energy Networks. LV Engine—Project Overview," Glasgow, UK, Tech. Rep.
- [165] R. Wang, B. Zhang, S. Zhao, L. Liang, and Y. Chen, "Design of an IGBT-series-based Solid-State Circuit Breaker for Battery Energy Storage System Terminal in Solid-State Transformer," IECON 2019—45th Annual Conference of the IEEE Industrial Electronics Society, Lisbon, Portugal, 14–17 October 2019.
- [166] M. Liserre, G. Buticchi, M. Andresen, G. D. Carne, L. F. Costa, and Z. X. Zou, "The Smart Transformer: Impact on the Electric Grid and Technology Challenges," *IEEE Industrial Electronics Magazine*, vol. 10, no. 2, pp. 46–58, 2016, doi: 10.1109/MIE.2016.2551418.

- [167] V. M. Hrishikesan and C. Kumar, "Smart Transformer Based Meshed Hybrid Microgrid with MVDC Interconnection," IECON Proceedings (Industrial Electronics Conference), pp. 4961–4966, October 2020, doi: 10.1109/IECON43393.2020.9255284.
- [168] A. Aithal and J. Wu, "OPERATION AND PERFORMANCE OF A MEDIUM VOLTAGE DC LINK," 24th International Conference on Electricity Distribution, Glasgow, vol. 05, no. 1, pp. 12–15, 2017, doi: 10.1049/oap-cired.2017.0946.
- [169] M. Andersen and G. D. Carne, "LV Engine Smart Transformer Hardware, Power Converter Control and Reliability," SP Energy Networks and University of Strathclyde, Glasgow, Tech. Rep., 2018.
- [170] A. Allca-Pekarovic, P. J. Kollmeyer, P. Mahvelatishamsabadi, T. Mirfakhrai, P. Naghshtabrizi, and A. Emadi, "Comparison of IGBT and SiC Inverter Loss for 400V and 800V DC Bus Electric Vehicle Drivetrains," ECCE 2020 -IEEE Energy Conversion Congress and Exposition, pp. 6338–6344, 2020, doi: 10.1109/ECCE44975.2020.9236202.
- [171] S. Palanisamy, T. Basler, J. Lutz, C. Kunzel, L. Wehrhahn-Kilian, and R. Elpelt, "Investigation of the bipolar degradation of SiC MOSFET body diodes and the influence of current density," *IEEE International Reliability Physics Symposium* Proceedings, pp. 1–6, March 2021, doi: 10.1109/IRPS46558.2021.9405183.
- [172] A. Ong, J. Carr, J. Balda, and A. Mantooth, "A comparison of silicon and silicon carbide MOSFET switching characteristics," 2007 IEEE Region 5 Technical Conference, TPS, pp. 273–277, 2007, 10.1109/TPSD.2007.4380318.
- [173] Y. C. Liang, G. S. Samudra, and C.-F. Huang, "Insulated-Gate Bipolar Transistor," *Power Microelectronics*, pp. 191–248, 2017, doi: 10.1142/9789813200258'0005.
- [174] C.-H. Noh, C.-H. Kim, G.-H. Gwon, M. O. Khan, and S. Z. Jamali, "Development of protective schemes for hybrid AC/DC low-voltage distribution system,"

- International Journal of Electrical Power & Energy Systems, vol. 105, pp. 521–528, 2019.
- [175] S. Wang, W. Ming, and J. Liang, "Interlinked solid-state mvdc circuit breaker with current regulation capability," in *IECON 2019 - 45th Annual Conference* of the *IEEE Industrial Electronics Society*, vol. 1, 2019, pp. 5668–5673, doi: 10.1109/IECON.2019.8927420.
- [176] N. Bayati, A. Hajizadeh, and M. Soltani, "Protection in DC microgrids: a comparative review," *IET Smart Grid*, vol. 1, no. 3, pp. 66–75, 2018.
- [177] A. Giannakis and D. Peftitsis, "MVDC distribution grids and potential applications: Future trends and protection challenges," in 2018 20th european conference on power electronics and applications (EPE'18 ECCE Europe). IEEE, 2018, pp. P–1.
- [178] J. A. Ansari, C. Liu, and S. A. Khan, "MMC based MTDC grids: A detailed review on issues and challenges for operation, control and protection schemes," *IEEE Access*, vol. 8, pp. 168 154–168 165, 2020.
- [179] T. Guillod, F. Krismer, and J. W. Kolar, "Protection of MV converters in the grid: The case of MV/LV solid-state transformers," *IEEE Journal of Emerging* and Selected Topics in Power Electronics, vol. 5, no. 1, pp. 393–408, 2016.
- [180] G. Li, J. Liang, S. Balasubramaniam, T. Joseph, C. E. Ugalde-Loo, and K. F. Jose, "Frontiers of DC circuit breakers in HVDC and MVDC systems," in 2017 IEEE conference on energy internet and energy system integration (EI2). IEEE, 2017, pp. 1–6.
- [181] C. Ding, T. Nie, X. Tian, T. Chen, and Z. Yuan, "Analysis of the influence of RC buffer on DC solid-state circuit breaker," *Energy Reports*, vol. 6, pp. 1483–1489, 2020.
- [182] A.-D. Nguyen, T.-T. Nguyen, and H.-M. Kim, "A comparison of different hybrid direct current circuit breakers for application in HVDC system," *International*

- Journal of Control and Automation, vol. 9, no. 4, pp. 381–394, 2016.
- [183] T. Zheng, W. Lv, Q. Wu, R. Li, X. Liu, C. Zhang, and L. Xu, "An integrated control and protection scheme based on FBSM-MMC active current limiting strategy for DC distribution network," *IEEE Journal of Emerging and Selected Topics in Power Electronics*, vol. 9, no. 3, pp. 2632–2642, 2020.
- [184] B. Li, J. He, Y. Li, and B. Li, "A review of the protection for the multi-terminal VSC-HVDC grid," Protection and Control of Modern Power Systems, vol. 4, no. 1, p. 21, 2019.
- [185] R. Rosso, X. Wang, M. Liserre, X. Lu, and S. Engelken, "Grid-Forming Converters: Control Approaches, Grid-Synchronization, and Future Trends—A Review," *IEEE Open Journal of Industry Applications*, vol. 2, pp. 93–109, 2021, doi: 10.1109/OJIA.2021.3074028.
- [186] T. Liu and X. Wang, "Physical Insight Into Hybrid-Synchronization-Controlled Grid-Forming Inverters Under Large Disturbances," *IEEE Transactions* on Power Electronics, vol. 37, no. 10, pp. 11475–11480, 2022, doi: 10.1109/TPEL.2022.3168902.
- [187] G. Denis and T. Prevost, "MIGRATE D3.6: Requirement guidelines for operating a grid with 100% power electronic devices." Tech. Rep., December 2019, doi: 10.13140/RG.2.2.36586.67528.
- [188] T. Castelo-De-Oliveira, F. V. Overbeeke, V. Cuk, and E. D. Jong, "MVDC Application: Switching Processes AC-to-DC, DC -to- AC and Imbalance Mitigation through DC Mode," 2019 IEEE PES Innovative Smart Grid Technologies Europe (ISGT-Europe), Bucharest, Romania, 29 September-2 October 2019.
- [189] R. Chai, B. Zhang, and J. Dou, "Improved DC voltage margin control method for DC grid based on VSCs," 2015 IEEE 15th International Conference on Environment and Electrical Engineering (EEEIC), Rome, Italy, p. 1683–1687, 10–13 June 2015.

- [190] A. Korompili and A. Monti, "Analysis of the dynamics of dc voltage droop controller of DC-DC converters in multi-terminal DC grids," 2017 IEEE Second International Conference on DC Microgrids (ICDCM), Nuremburg, Germany, 27–29 June 2017.
- [191] P. Simiyu, A. Xin, G. Bitew, M. Shahzad, K. Wang, and L. Tuan, "Review of the DC voltage coordinated control strategies for multi-terminal VSC-MVDC distribution network," *Energies*, pp. 1492 – 1468, 2019.
- [192] Y. Wang, W. Wen, C. Wang, H. Liu, X. Zhan, and X. Xiao, "Adaptive Voltage Droop Method of Multiterminal VSC-HVDC Systems for DC Voltage Deviation and Power Sharing," *IEEE Transaction on Power Delivery*, vol. 34, p. 169–176, 2019.
- [193] F. Torres, S. Martinez, C. Roa, and E. Lopez, "Comparison between voltage droop and voltage margin controllers for MTDC systems," IEEE ICA-ACCA 2018—IEEE International Conference on Automation/23rd Congress of the Chilean Association of Automatic Control: Towards an Industry 4.0, Concepcion, Chile, 17–19 October 2018.
- [194] A. Egea-Alvarez, J. Beerten, D. V. Hertem, and O. Gomis-Bellmunt, "Hierarchical power control of multiterminal HVDC grids." *Electrical Power Systems Research*, vol. 121, 2015.
- [195] J. D. Taft, "Roles and Responsibilities for Distribution Grids: DER Sensing and Communication Networks," Pacific Northwest National Lab.(PNNL), Richland, WA (United States), Tech. Rep., 2017.
- [196] M. Abedrabbo, M. Wang, P. Tielens, F. Z. Dejene, W. Leterme, J. Beerten, and D. Van Hertem, "Impact of DC grid contingencies on AC system stability," in 13th IET international conference on AC and DC power transmission (ACDC 2017). IET, 2017, p. 25.
- [197] Y. Ji, Z. Yuan, J. Zhao, C. Lu, Y. Wang, Y. Zhao, Y. Li, and Y. Han, "Hierarchical control strategy for MVDC distribution network under large

- disturbance," IET Generation, Transmission & Distribution, vol. 12, no. 11, pp. 2557-2565, 2018.
- [198] E. Glende, P. Trojan, I. Hauer, A. Naumann, C. Brosinsky, M. Wolter, and D. Westermann, "Communication infrastructure for dynamic grid control center with a hardware-in-the-loop model," in 2018 IEEE PES Innovative Smart Grid Technologies Conference Europe (ISGT-Europe). IEEE, 2018, pp. 1–6.
- [199] J. Pan, S. Bala, M. Callavik, and P. Sandeberg, "Platformless DC Collection and Transmission for Offshore Wind," in 11th IET International Conference on AC and DC Power Transmission, 2015, pp. 1–6, doi: 10.1049/cp.2015.0075.
- [200] M. Basu, V. R. Mahindara, J. Kim, R. M. Nelms, and E. Muljadi, "Comparison of Active and Reactive Power Oscillation Damping With PV Plants," *IEEE Transactions on Industry Applications*, vol. 57, no. 3, pp. 2178–2186, 2021, doi: 10.1109/TIA.2021.3059810.
- [201] L. C. Hunter, C. D. Booth, A. Egea-Alvarez, A. Dyśko, S. J. Finney, and A. Junyent-Ferré, "A New Fast-Acting Backup Protection Strategy for Embedded MVDC Links in Future Distribution Networks," *IEEE Transactions on Power Delivery*, vol. 36, no. 2, pp. 861–869, 2021, doi: 10.1109/TPWRD.2020.2995479.
- [202] M. Hadjikypris, O. Marjanovic, and V. Terzija, "Damping of inter-area power oscillations in hybrid AC-DC power systems based on supervisory control scheme utilizing FACTS and HVDC," in 2016 Power Systems Computation Conference (PSCC), 2016, pp. 1–7, doi: 10.1109/PSCC.2016.7540886.
- [203] C. J. O'Rourke, M. M. Qasim, M. R. Overlin, and J. L. Kirtley, "A Geometric Interpretation of Reference Frames and Transformations: dq0, Clarke, and Park," *IEEE Transactions on Energy Conversion*, vol. 34, no. 4, pp. 2070–2083, 2019, doi: 10.1109/TEC.2019.2941175.
- [204] A. Egea-Alvarez, S. Fekriasl, F. Hassan, and O. Gomis-Bellmunt, "Advanced Vector Control for Voltage Source Converters Connected to Weak Grids," IEEE

- Transactions on Power Systems, vol. 30, no. 6, pp. 3072–3081, 2015, doi: 10.1109/TPWRS.2014.2384596.
- [205] L. Zhang, L. Harnefors, S. Member, and H.-P. Nee, "Modeling and Control of VSC-HVDC Links Connected to Island Systems," PhD Thesis, Royal Institute of Technology, Stockholm, 2010, ISBN: 9789174156409.
- [206] A. Yazdani and R. Iravani, Voltage-Sourced Converters in Power Systems: Modeling, Control, and Applications, 2010, ch. Space Phasors and Two-Dimensional Frames, pp. 69–114, doi: 10.1002/9780470551578.ch4.
- [207] S.-H. Kim, Ed., Electric Motor Control. Elsevier, 2017, ch. 4 Modeling of alternating current motors and reference frame theory, pp. 153–202, doi: 10.1016/B978-0-12-812138-2.00004-0 ISBN: 978-0-12-812138-2.
- [208] L. Harnefors, M. Bongiorno, and S. Lundberg, "Input-Admittance Calculation and Shaping for Controlled Voltage-Source Converters," *IEEE Transactions* on *Industrial Electronics*, vol. 54, no. 6, pp. 3323–3334, 2007, doi: 10.1109/TIE.2007.904022.
- [209] B. Wen, D. Boroyevich, R. Burgos, P. Mattavelli, and Z. Shen, "Analysis of D-Q Small-Signal Impedance of Grid-Tied Inverters," *IEEE Transactions on Power Electronics*, vol. 31, 01 2015, 10.1109/TPEL.2015.2398192.
- [210] A. Egea-Alvarez, A. Junyent-Ferré, and O. Gomis-Bellmunt, Active and Reactive Power Control of Grid Connected Distributed Generation Systems. Berlin, Heidelberg: Springer Berlin Heidelberg, 2012, pp. 47–81, doi: 10.1007/978-3-642-22904-6'3 ISBN: 978-3-642-22904-6.
- [211] "Park Transform." [Online]. Available: https://uk.mathworks.com/help/sps/ref/parktransform.html
- [212] K.-H. Kim, S. Cui, and J.-J. Jung, "Current-Oriented Phase-Locked Loop Method for Robust Control of Grid-Connected Converter in Extremely Weak Grid," IEEE

- Transactions on Power Electronics, vol. 39, no. 10, pp. 11963–11968, 2024, doi: 10.1109/TPEL.2024.3419445.
- [213] Özgür Can Sakinci and J. Beerten, "Impact of PLL dynamics on the small-signal stability of the MMC using dynamic phasor modeling in the ABC frame," *Electric Power Systems Research*, vol. 189, p. 106729, 2020, doi: 10.1016/j.epsr.2020.106729.
- [214] F. Hans, W. Schumacher, and L. Harnefors, "Small-Signal Modeling of Three-Phase Synchronous Reference Frame Phase-Locked Loops," *IEEE Transactions on Power Electronics*, vol. 33, no. 7, pp. 5556–5560, 2018, doi: 10.1109/TPEL.2017.2783189.
- [215] S.-K. Chung, "A phase tracking system for three phase utility interface inverters," IEEE Transactions on Power Electronics, vol. 15, no. 3, pp. 431–438, 2000, doi: 10.1109/63.844502.
- [216] A. Kulkarni and V. John, "Analysis of Bandwidth-Unit-Vector-Distortion Tradeoff in PLL During Abnormal Grid Conditions," *IEEE Transactions* on *Industrial Electronics*, vol. 60, no. 12, pp. 5820–5829, 2013, doi: 10.1109/TIE.2012.2236998.
- [217] V. Kaura and V. Blasko, "Operation of a phase locked loop system under distorted utility conditions," *IEEE Transactions on Industry Applications*, vol. 33, no. 1, pp. 58–63, 1997, doi: 10.1109/28.567077.
- [218] A. Ghoshal and V. John, "Performance evaluation of three phase SRF-PLL and MAF-SRF-PLL," Turkish Journal of Electrical Engineering and Computer Sciences, vol. 23, no. 6, 2015, doi: 10.3906/elk-1404-488.
- [219] Z. Dai, G. Li, M. Fan, J. Huang, Y. Yang, and W. Hang, "Global Stability Analysis for Synchronous Reference Frame Phase-Locked Loops," *IEEE Transactions on Industrial Electronics*, vol. 69, pp. 10182 10191, 2021, doi: 10.1109/TIE.2021.3125655.

- [220] J.-W. Choi and S.-K. Sul, "Fast current controller in three-phase ac/dc boost converter using d-q axis crosscoupling," *IEEE Transactions on Power Electronics*, vol. 13, no. 1, pp. 179–185, 1998.
- [221] J. Schönberger, "Space Vector Control of a Three-Phase Rectifier using PLECS," 2015. [Online]. Available: https://www.plexim.com/sites/default/files/plecs\_sym.pdf
- [222] T. Qoria, F. Gruson, F. Colas, X. Guillaud, M.-S. Debry, and T. Prevost, "Tuning of Cascaded Controllers for Robust Grid-Forming Voltage Source Converter," in 2018 Power Systems Computation Conference (PSCC), 2018, pp. 1–7, doi: 10.23919/PSCC.2018.8443018.
- [223] L. Harnefors and H.-P. Nee, "Model-based current control of AC machines using the internal model control method," *IEEE Transactions on Industry Applications*, vol. 34, no. 1, pp. 133–141, 1998, doi: 10.1109/28.658735.
- [224] C. Bajracharya, M. Molinas, J. Suul, and T. Undeland, "Understanding of Tuning Techniques of Converter Controllers for VSC-HVDC," Nordic Workshop on Power and Industrial Electronics, June 2008.
- [225] N. Hatziargyriou, J. Milanovic, C. Rahmann, V. Ajjarapu, C. Canizares, I. Erlich, D. Hill, I. Hiskens, I. Kamwa, B. Pal, P. Pourbeik, J. Sanchez-Gasca, A. Stankovic, T. Van Cutsem, V. Vittal, and C. Vournas, "Definition and Classification of Power System Stability Revisited & Extended," *IEEE Transactions on Power Systems*, vol. 36, no. 4, pp. 3271–3281, 2021, doi: 10.1109/TPWRS.2020.3041774.
- [226] National Grid, "Draft Grid Code Grid Forming Converter Specification 21st December 2020," Tech. Rep., 2020. [Online]. Available: https://www.nationalgrideso.com
- [227] M. Maharjan, A. Ekic, M. Beedle, J. Tan, and D. Wu, "Evaluating grid strength under uncertain renewable generation," *International Journal of Electrical Power & Energy Systems*, vol. 146, p. 108737, 2023, doi: 10.1016/j.ijepes.2022.108737.

- [228] AEMO, "Renewable integration study stage 1. enabling secure operation of the nem with very high penetrations of renewable energy," AEMO, Australia, Tech. Rep., 2020.
- [229] N. Mararakanye and B. Bekker, "Renewable energy integration impacts within the context of generator type, penetration level and grid characteristics," *Renewable and Sustainable Energy Reviews*, vol. 108, pp. 441–451, 2019, doi: 10.1016/j.rser.2019.03.045.
- [230] M. Eremia and M. Shahidehpour, Handbook of Electrical Power System Dynamics: Modeling, Stability, and Control, Voltage and Reactive Power Control, 2013, doi:10.1002/9781118516072.ch7.
- [231] E. Rokrok, T. Qoria, A. Bruyere, B. Francois, H. Zhang, M. Belhaouane, and X. Guillaud, "Impact of grid-forming control on the internal energy of a modular multilevel converter," in 2020 22nd European Conference on Power Electronics and Applications (EPE'20 ECCE Europe), 2020, pp. 1–10, doi: 10.23919/EPE20ECCEEurope43536.2020.9215646.
- [232] S. D'Arco and J. A. Suul, "Virtual synchronous machines Classification of implementations and analysis of equivalence to droop controllers for microgrids," in 2013 IEEE Grenoble Conference, 2013, pp. 1–7, doi: 10.1109/PTC.2013.6652456.
- [233] L. Zhang, L. Harnefors, and H.-P. Nee, "Power-Synchronization Control of Grid-Connected Voltage-Source Converters," *IEEE Transactions on Power Systems*, vol. 25, no. 2, pp. 809–820, 2010, doi: 10.1109/TPWRS.2009.2032231.
- [234] C. Arghir, T. Jouini, and F. Dörfler, "Grid-forming control for power converters based on matching of synchronous machines," *Automatica*, vol. 95, pp. 273–282, 2018, doi: 10.1016/j.automatica.2018.05.037.
- [235] R. Ghosh, N. R. Tummuru, and B. S. Rajpurohit, "A New Virtual Oscillator-Based Grid-Forming Controller with Decoupled Control Over Individual

- Phases and Improved Performance of Unbalanced Fault Ride-Through," *IEEE Transactions on Industrial Electronics*, vol. 70, no. 12, pp. 12465–12474, 2023.
- [236] J. F. Morris, K. H. Ahmed, and A. Egea-Àlvarez, "Power-Synchronization Control for Ultra-Weak AC Networks: Comprehensive Stability and Dynamic Performance Assessment," *IEEE Open Journal of the Industrial Electronics* Society, vol. 2, pp. 441–450, 2021, doi: 10.1109/OJIES.2021.3103278.
- [237] A. Tayyebi, F. Kupzog, F. Dörfler, and W. Hribernik, "Grid-Forming Converters
   Inevitability, Control Strategies and Challenges in Future Grid Applications," in CIRED Workshop 2018, Ljubljana, June 2018.
- [238] M. Sinha, F. Dörfler, B. B. Johnson, and S. V. Dhople, "Uncovering Droop Control Laws Embedded Within the Nonlinear Dynamics of Van der Pol Oscillators," *IEEE Transactions on Control of Network Systems*, vol. 4, no. 2, pp. 347–358, 2017, doi: 10.1109/TCNS.2015.2503558.
- [239] C.-K. Nguyen, T.-T. Nguyen, H.-J. Yoo, and H.-M. Kim, "Improving Transient Response of Power Converter in a Stand-Alone Microgrid Using Virtual Synchronous Generator," *Energies*, vol. 11, no. 1, 2018, doi: 10.3390/en11010027.
- [240] A. A. Abdelrahim, M. Smailes, K. Ahmed, P. Mckeever, and A. Egea-alvarez, "Modified grid forming converter controller with fault ride through capability without PLL or current loop," in 18th Wind Integration Workshop, Dublin, October 2019, pp. 1–8.
- [241] H. Beltran, S. Harrison, A. Egea-Àlvarez, and L. Xu, "Techno-economic assessment of energy storage technologies for inertia response and frequency support from wind farms," *Energies*, vol. 13, no. 13, 2020, doi: 10.3390/en13133421.
- [242] V. Mallemaci, F. Mandrile, S. Rubino, A. Mazza, E. Carpaneto, and R. Bojoi, "A comprehensive comparison of Virtual Synchronous Generators with focus on virtual inertia and frequency regulation," *Electric Power Systems Research*, vol. 201, p. 107516, 2021, doi: 10.1016/j.epsr.2021.107516.

- [243] Y. Lamrani, F. Colas, T. V. Cutsem, C. Cardozo, T. Prevost, and X. Guillaud, "On the stabilizing contribution of different grid-forming controls to power systems," *IET Generation, Transmission & Distribution*, November 2024, doi: 10.1049/gtd2.13269.
- [244] P. Kundur, J. Paserba, V. Ajjarapu, G. Andersson, A. Bose, C. Canizares, N. Hatziargyriou, D. Hill, A. Stankovic, C. Taylor, T. Van Cutsem, and V. Vittal, "Definition and classification of power system stability IEEE/CIGRE joint task force on stability terms and definitions," *IEEE Transactions on Power Systems*, vol. 19, no. 3, pp. 1387–1401, 2004, doi: 10.1109/TPWRS.2004.825981.
- [245] O. P. Mahela and A. G. Shaik, "A review of distribution static compensator," Renewable and Sustainable Energy Reviews, vol. 50, pp. 531–546, 2015.
- [246] H. Emanuel, J. Brombach, R. Rosso, and K. Pierros, "Requirements for control strategies of grid-connected converters in the future power system," *IET Renewable Power Generation*, vol. 14, no. 8, pp. 1288–1295, 2020, doi: 10.1049/iet-rpg.2020.0156.
- [247] L. H. Kocewiak, J. Hjerrild, and C. L. Bak, "Wind turbine converter control interaction with complex wind farm systems," *IET Renewable Power Generation*, vol. 7, no. 4, pp. 380–389, 2013, doi: 10.1049/iet-rpg.2012.0209.
- [248] R. Teodorescu and F. Blaabjerg, "Flexible control of small wind turbines with grid failure detection operating in stand-alone and grid-connected mode," *IEEE Transactions on Power Electronics*, vol. 19, no. 5, pp. 1323–1332, 2004, doi: 10.1109/TPEL.2004.833452.
- [249] H. Bevrani, T. Ise, and Y. Miura, "Virtual synchronous generators: A survey and new perspectives," *International Journal of Electrical Power and Energy Systems*, vol. 54, pp. 244–254, 2014, doi: 10.1016/j.ijepes.2013.07.009.
- [250] IEEE. (2018) IEEE vTools Events. Practical power flow controller brings benefits of power electronics to the Grid. [Online]. Available: https://events.vtools.ieee.org/m/169041

- [251] J.-W. Choi and S.-K. Sul, "Fast current controller in three-phase AC/DC boost converter using d-q axis crosscoupling," *IEEE Transactions on Power Electronics*, vol. 13, no. 1, pp. 179–185, 1998, doi: 10.1109/63.654973.
- [252] D. Cashman and W. Uijlings, "Final Report Phase 1 RoCoF Alternative Solutions Technology Assessment," DNV GL Energy Advisory, London, Tech. Rep., 17th August 2015, version 5.
- [253] M. Bahrman, J. Johansson, and B. Nilsson, "Voltage source converter transmission technologies: the right fit for the application," in 2003 IEEE Power Engineering Society General Meeting (IEEE Cat. No.03CH37491), vol. 3, 2003, pp. 1840–1847 Vol. 3, doi: 10.1109/PES.2003.1267441.
- [254] O. Kukrer, S. Bayhan, and H. Komurcugil, "Model-Based Current Control Strategy with Virtual Time Constant for Improved Dynamic Response of Three-Phase Grid-Connected VSI," *IEEE Transactions on Industrial Electronics*, vol. 66, no. 6, pp. 4156–4165, doi: 10.1109/TIE.2018.2863195.
- [255] B. Hartmann, I. Vokony, and I. Táczi, "Effects of decreasing synchronous inertia on power system dynamics—overview of recent experiences and marketisation of services," *International Transactions on Electrical Energy Systems*, vol. 29, no. 12, pp. 1–14, 2019, doi: 10.1002/2050-7038.12128.
- [256] E. Lidström and D. Wall, "Frequency support by synthetic inertia from variable speed wind turbines," in CIRED Workshop 2016, 2016, pp. 1–4, doi: 10.1049/cp.2016.0676.
- [257] S. C. Johnson, D. J. Papageorgiou, D. S. Mallapragada, T. A. Deetjen, J. D. Rhodes, and M. E. Webber, "Evaluating rotational inertia as a component of grid reliability with high penetrations of variable renewable energy," *Energy*, vol. 180, pp. 258–271, 2019, doi: 10.1016/j.energy.2019.04.216.
- [258] ENTSO-E, "High Penetration of Power Electronic Interfaced Power Sources and the Potential Contribution of Grid Forming Converters," 2019. [Online]. Available: https://www.entsoe.eu/Documents/Publications/

- SOC/High\_Penetration\_of\_Power\_Electronic\_Interfaced\_Power\_Sources\_and\_the\_ Potential\_Contribution\_of\_Grid\_Forming\_Converters.pdf
- [259] R. N. Damas, Y. Son, M. Yoon, S.-Y. Kim, and S. Choi, "Subsynchronous Oscillation and Advanced Analysis: A Review," *IEEE Access*, vol. 8, pp. 224 020–224 032, 2020, doi: 10.1109/ACCESS.2020.3044634.
- [260] B. Shao, Q. Xiao, L. Xiong, L. Wang, Y. Yang, Z. Chen, F. Blaabjerg, and J. M. Guerrero, "Power coupling analysis and improved decoupling control for the VSC connected to a weak AC grid," *International Journal of Electrical Power* & Energy Systems, vol. 145, p. 108645, 2023, doi: 10.1016/j.ijepes.2022.108645.
- [261] G. Misyris, T. Van Cutsem, J. Møller, M. Dijokas, O. R. Estragués, B. Bastin, S. Chatzivasileiadis, A. Nielsen, T. Weckesser, J. Østergaard et al., "North sea wind power hub: System configurations, grid implementation and technoeconomic assessment," arXiv preprint arXiv:2006.05829, 2020.
- [262] G. S. Misyris, S. Chatzivasileiadis, and T. Weckesser, "Grid-forming converters: Sufficient conditions for RMS modeling," *Electric Power Systems Research*, vol. 197, p. 107324, 2021, doi: 10.1016/j.epsr.2021.107324.
- [263] VDE, "FNN Guideline: Grid forming behaviour of HVDC systems and DC-connected PPMs," 2020. [Online]. Available: https://shop.vde.com/en/fnn-guideline-hvdc-systems-2
- [264] "Technical Report on the events of 9 August 2019," National Grid ESO, Tech. Rep., 9 September 2019.
- [265] X. Wang and F. Yang, "Equivalent simplification of torsional dynamics in the closely coupled identical turbine-generators," 2006 IEEE Power Engineering Society General Meeting, PES, pp. 13–16, 2006, doi: 10.1109/pes.2006.1708851.
- [266] Y. Fan, W. Xitian, X. Yingxin, and C. Chen, "Dynamic equivalence of torsional interaction in multi-identical-machine power system," *Electric*

- Power Components and Systems, vol. 35, no. 5, pp. 525-537, 2007, doi: 10.1080/15325000601078161.
- [267] Y. Gu and T. C. Green, "Power System Stability With a High Penetration of Inverter-Based Resources," *Proceedings of the IEEE*, pp. 1–22, 2022, doi: 10.1109/JPROC.2022.3179826.
- [268] National Grid, "Provision of short circuit level data a system operability framework document," Tech. Rep., 2022. [Online]. Available: https://www.nationalgrideso.com/document/162271/download
- [269] IEEE Standards Board, "IEEE Guide for planning DC links terminating at AC locations having low short-circuit capacities," Tech. Rep., 1997, ISBN: 1-55937-936-7.
- [270] A. Hammoudeh, M. I. A. Saaideh, E. A. Feilat, and H. Mubarak, "Estimation of Synchronizing and Damping Torque Coefficients Using Deep Learning," in 2019 IEEE Jordan International Joint Conference on Electrical Engineering and Information Technology (JEEIT), 2019, pp. 488–493, doi: 10.1109/JEEIT.2019.8717432.
- [271] J. Ritonja, M. Petrun, J. Cernelic, R. Brezovnik, and B. Polajžer, "Analysis and Applicability of Heffron-Phillips Model," *Elektronika ir Elektrotechnika*, vol. 22, 12 December 2016, doi: 10.5755/j01.eie.22.4.15905.
- [272] J. Matevosyan, B. Badrzadeh, T. Prevost, E. Quitmann, D. Ramasubramanian, H. Urdal, S. Achilles, J. Macdowell, S. H. Huang, V. Vital, J. Osullivan, and R. Quint, "Grid-forming inverters: Are they the key for high renewable penetration?" *IEEE Power and Energy Magazine*, vol. 17, no. 6, pp. 89–98, 11 November 2019, doi: 10.1109/MPE.2019.2933072.
- [273] C. Karawita and U. Annakkage, "Guidelines for Subsynchronous Oscillation Studies in Power Electronics Dominated Power Systems," CIGRE, JWG C4/B4.52, Tech. Rep., 2023.

- [274] V. A. Lacerda, E. P. Araujo, M. Cheah-Mañe, and O. Gomis-Bellmunt, "Phasor Modeling Approaches and Simulation Guidelines of Voltage-Source Converters in Grid-Integration Studies," *IEEE Access*, vol. 10, pp. 51826–51838, 2022, doi: 10.1109/ACCESS.2022.3174958.
- [275] J. Vega, C. Rahmann, F. Valencia, and K. Strunz, "Analysis and Application of Quasi-Static and Dynamic Phasor Calculus for Stability Assessment of Integrated Power Electric and Electronic Systems," *IEEE Transactions on Power Systems*, vol. 36, no. 3, pp. 1750–1760, 11 2020, doi: 10.1109/TPWRS.2020.3030225.
- [276] J. D. Lara, R. Henriquez-Auba, D. Ramasubramanian, S. Dhople, D. S. Callaway, and S. Sanders, "Revisiting Power Systems Time-Domain Simulation Methods and Models," *IEEE Transactions on Power Systems*, vol. 39, no. 2, pp. 2421–2437, 2024, doi: 10.1109/TPWRS.2023.3303291.
- [277] M. Cheah-Mane, A. Egea-Alvarez, E. Prieto-Araujo, H. Mehrjerdi, O. Gomis-Bellmunt, and L. Xu, "Modeling and analysis approaches for small-signal stability assessment of power-electronic-dominated systems," WIREs Energy and Environment, vol. 12, no. 1, p. e453, 2023, doi: 10.1002/wene.453.
- [278] L. Huang, C. Wu, D. Zhou, F. Blaabjerg, and S. He, "Large-Signal Modeling of Grid-Following Inverter: from Sixth-Order Model to Second-Order Model," in 2024 IEEE 10th International Power Electronics and Motion Control Conference (IPEMC2024-ECCE Asia), 2024, pp. 3413–3420, doi: 10.1109/IPEMC-ECCEAsia60879.2024.10567659.
- [279] I. Abuishmais, Q. Salem, R. Aljarrah, and A. Al-Quraan, "A Comparative Study between Reduced-Order and Switching Models of Grid-Following Inverter Interfacing Renewable Energy Sources," *International Journal of Energy Research*, vol. 2023, no. 1, p. 8849576, 2023, doi: 10.1155/2023/8849576.
- [280] M. John, A. Mertens, M. Popp, and W. Mathis, "Model order reduction for a full scale grid converter for grid simulations," in 2017 19th European Conference on

- Power Electronics and Applications (EPE'17 ECCE Europe), 2017, pp. P.1–P.9, doi: 10.23919/EPE17ECCEEurope.2017.8099410.
- [281] Q. Chen, S. Bu, and C. Y. Chung, "Small-Signal Stability Criteria in Power Electronics-Dominated Power Systems: A Comparative Review," *Journal of Modern Power Systems and Clean Energy*, vol. 12, no. 4, pp. 1003–1018, 2024, doi: 10.35833/MPCE.2023.000526.
- [282] G. Wu, H. Sun, X. Zhang, A. Egea-Alvarez, B. Zhao, S. Xu, S. Wang, and X. Zhou, "Parameter Design Oriented Analysis of the Current Control Stability of the Weak-Grid-Tied VSC," *IEEE Transactions on Power Delivery*, vol. 36, no. 3, pp. 1458–1470, 2021, doi: 10.1109/TPWRD.2020.3009517.
- [283] R. D. Zimmerman, C. E. Murillo-Sánchez, and R. J. Thomas, "MATPOWER: Steady-State Operations, Planning, and Analysis Tools for Power Systems Research and Education," *IEEE Transactions on Power Systems*, vol. 26, no. 1, pp. 12–19, 2011, doi: 10.1109/TPWRS.2010.2051168.
- [284] G. Wu, B. Zhao, X. Zhang, S. Wang, A. Egea-Àlvarez, Y. Sun, Y. Li, D. Guo, and X. Zhou, "Impact of Non-Minimum-Phase Zeros on the Weak-Grid-Tied VSC," *IEEE Transactions on Sustainable Energy*, vol. 12, no. 2, pp. 1115–1126, 2021, doi: 10.1109/TSTE.2020.3034791.
- [285] K. Jiang, D. Liu, K. Cao, P. Xiong, and X. Ji, "Small-Signal Modeling and Configuration Analysis of Grid-Forming Converter under 100% Renewable Electricity Systems," *Electronics*, vol. 12, no. 19, 2023, doi: 10.3390/electronics12194078.
- [286] J. Sheng, C. Li, X. Xiang, W. Li, and D. Dujic, "Dc-Link Ripple Suppression of Cascaded H-Bridge Based MV Grid Emulator Apparatus for Analysis and Testing of Grid-Tied Converters in Distribution System," *IEEE Transactions on Power Delivery*, vol. 39, no. 1, pp. 622–634, 2024, doi: 10.1109/TPWRD.2023.3335842.
- [287] Z. Duan, Y. Meng, T. Wang, H. Zhang, X. Wang, and X. Wang, "Large-Signal Stability Analysis Using Takagi-Sugeno Fuzzy Model Theory

- for Fractional Frequency Transmission System Under Grid Faults," *IEEE Transactions on Power Systems*, vol. 39, no. 1, pp. 2227–2238, 2024, doi: 10.1109/TPWRS.2023.3268650.
- [288] S. Jeong and G. Jang, "Stability analysis of a weak-grid-connected voltage-sourced rectifier considering the phase-locked loop dynamics," *IEEE Transactions on Power Systems*, vol. 38, no. 1, pp. 436–446, 2023, doi: 10.1109/TPWRS.2022.3169176.
- [289] M. Schweizer, S. Almér, S. Pettersson, A. Merkert, V. Bergemann, and L. Harnefors, "Grid-forming vector current control," *IEEE Transactions* on Power Electronics, vol. 37, no. 11, pp. 13091–13106, 2022, doi: 10.1109/TPEL.2022.3177938.
- [290] M. Yousaf, M. A. Shahid, D. Khan, and S. Khalid, "Improved Coordinated Control of AVM based Multi-Terminal HVdc System using Steady-State Analysis," *International Journal on Electrical Engineering and Informatics*, vol. 12, pp. 296–321, June 2020, doi: 10.15676/ijeei.2020.12.2.8.
- [291] S. M. Alizadeh, C. Ozansoy, and T. Alpcan, "The impact of X/R ratio on voltage stability in a distribution network penetrated by wind farms," in 2016 Australasian Universities Power Engineering Conference (AUPEC), 2016, pp. 1–6, doi: 10.1109/AUPEC.2016.7749289.
- [292] X. Liang and M. Abbasipour, "HVDC Transmission and its Potential Application in Remote Communities: Current Practice and Future Trend," *IEEE Transactions on Industry Applications*, vol. 58, no. 2, pp. 1706–1719, 2022, doi: 10.1109/TIA.2022.3146117.
- [293] R. H. Chandio, F. A. Chachar, J. B. Soomro, J. A. Ansari, H. M. Munir, H. M. Zawbaa, and S. Kamel, "Control and protection of MMC-based HVDC systems: A review," *Energy Reports*, vol. 9, pp. 1571–1588, 2023.
- [294] L. Carlsson, "TRANSMISSION HVDC A firewall against disturbances in HV grids," pp. 34–37, May 2006.

- [295] N. S. Hasan, N. Rosmin, D. A. A. Osman, and A. H. M. Jamal, "Reviews on multilevel converter and modulation techniques," *Renewable and Sustainable Energy Reviews*, vol. 80, pp. 163–174, 2017, doi: 10.1016/j.rser.2017.05.163.
- [296] M. A. Perez, S. Ceballos, G. Konstantinou, J. Pou, and R. P. Aguilera, "Modular Multilevel Converters: Recent Achievements and Challenges," *IEEE Open Journal of the Industrial Electronics Society*, vol. 2, pp. 224–239, 2021, doi: 10.1109/OJIES.2021.3060791.
- [297] A. U. Lawan, H. A. F. Almurib, J. G. Khor, and S. Babani, "Circulating Current control of a Modular Multilevel Converter (MMC) with State Feedback Controller and Harmonic Current Suppression," in 2018 IEEE International Conference on Electrical Systems for Aircraft, Railway, Ship Propulsion and Road Vehicles & International Transportation Electrification Conference (ESARS-ITEC), 2018, pp. 1–8, doi: 10.1109/ESARS-ITEC.2018.8607268.
- [298] D. B. RATHNAYAKE, M. AKRAMI, C. PHURAILATPAM, S. P. ME, S. HADAVI, G. JAYASINGHE, S. ZABIHI, and B. BAHRANI, "Grid Forming Inverter Modeling, Control, and Applications," *IEEE POWER & ENERGY SOCIETY SECTION*, vol. 9, pp. 114781–114807, 2021, doi: 10.1109/ACCESS.2021.3104617.
- [299] X. Lu, W. Xiang, W. Lin, and J. Wen, "Small-signal modeling of MMC based DC grid and analysis of the impact of DC reactors on the small-signal stability," *International Journal of Electrical Power & Energy Systems*, vol. 101, pp. 25–37, 2018, doi: 10.1016/j.ijepes.2018.01.046.
- [300] W. Liu, R. Wang, T. Kerekes, T. Dragicevic, and R. Teodorescu, "Small Signal Model of Modular Multilevel Converter with Power Synchronization Control," in 2023 IEEE Applied Power Electronics Conference and Exposition (APEC), 2023, pp. 2815–2820, doi: 10.1109/APEC43580.2023.10131442.
- [301] C. Jiang, A. D. Sinkar, and A. M. Gole, "Small signal analysis of a gridforming modular multilevel converter with a novel virtual synchronous generator

- control," *Electric Power Systems Research*, vol. 223, p. 109621, 2023, doi: 10.1016/j.epsr.2023.109621.
- [302] L. F. N. Lourenço, F. Perez, A. Iovine, G. Damm, R. M. Monaro, and M. B. C. Salles, "Stability Analysis of Grid-Forming MMC-HVDC Transmission Connected to Legacy Power Systems," *Energies*, vol. 14, no. 23, 2021. [Online]. Available: https://www.mdpi.com/1996-1073/14/23/8017
- [303] F. Puricelli and J. Beerten, "Small-signal stability analysis of an MMC-based bipolar HVDC link in grid-forming control mode," in 19th International Conference on AC and DC Power Transmission (ACDC 2023), vol. 2023, 2023, pp. 215–219, doi: 10.1049/icp.2023.1331.
- [304] F. Palombi, L. Piegari, S. D'Arco, A. G. Endegnanew, and J. A. Suul, "Impact on Power System Frequency Dynamics from an HVDC Transmission System With Converter Stations Controlled as Virtual Synchronous Machines," in 2019 IEEE Milan PowerTech, 2019, pp. 1–6, doi: 10.1109/PTC.2019.8810855.
- [305] F. Giacomo Puricelli, S. D'Arco, J. Are Suul, and L. Piegari, "Evaluation of Inertia Emulation Strategies for DC- Voltage-Controlled and Power-Controlled Converter Stations in HVDC Interconnections," in 2020 International Symposium on Power Electronics, Electrical Drives, Automation and Motion (SPEEDAM), 2020, pp. 832–838, doi: 10.1109/SPEEDAM48782.2020.9161845.
- [306] M. Ramirez-Gonzalez, F. R. S. Sevilla, and P. Korba, "Tuning of grid-forming converters with a settings-free optimization algorithm to improve frequency response of low-inertia systems," in 2023 IEEE International Conference on Environment and Electrical Engineering and 2023 IEEE Industrial and Commercial Power Systems Europe (EEEIC / I&CPS Europe), 2023, pp. 1–6, doi: 10.1109/EEEIC/ICPSEurope57605.2023.10194694.
- [307] L. Sun, P. Wang, J. Han, Y. Wang, C. Yu, and M. Chen, "Adaptive Inertia Control of Virtual Synchronous Generator Based on Power Feedback," in 2021

- IEEE 4th International Electrical and Energy Conference (CIEEC), 2021, pp. 1–5, doi: 10.1109/CIEEC50170.2021.9510442.
- [308] W. Wang, L. Jiang, Y. Cao, and Y. Li, "A Parameter Alternating VSG Controller of VSC-MTDC Systems for Low Frequency Oscillation Damping," IEEE Transactions on Power Systems, vol. 35, no. 6, pp. 4609–4621, 2020, doi: 10.1109/TPWRS.2020.2997859.
- [309] L. Huang, H. Xin, and Z. Wang, "Damping Low-Frequency Oscillations Through VSC-HVdc Stations Operated as Virtual Synchronous Machines," *IEEE Transactions on Power Electronics*, vol. 34, no. 6, pp. 5803–5818, 2019, doi: 10.1109/TPEL.2018.2866523.
- [310] S. D'Arco, J. A. Suul, and O. B. Fosso, "Automatic Tuning of Cascaded Controllers for Power Converters Using Eigenvalue Parametric Sensitivities," *IEEE Transactions on Industry Applications*, vol. 51, no. 2, pp. 1743–1753, 2015, doi: 10.1109/TIA.2014.2354732.
- [311] P. Sauer and M. Pai, Power System Dynamics and Stability, 1st ed. Prentice Hall, 1998, ISBN 9780136788300.
- [312] X. Lu, W. Lin, J. Wen, W. Yao, T. An, and Y. Li, "Dynamic phasor modelling and operating characteristic analysis of half-bridge mmc," 05 2016, pp. 2615– 2621, doi: 10.1109/IPEMC.2016.7512710.
- [313] Y. Chen, L. Xu, A. Egea-Àlvarez, B. Marshall, M. H. Rahman, and A. D. Oluwole, "MMC Impedance Modeling and Interaction of Converters in Close Proximity," IEEE Journal of Emerging and Selected Topics in Power Electronics, vol. 9, no. 6, pp. 7223–7236, 2021, doi: 10.1109/JESTPE.2020.3031489.
- [314] W. Wang, M. Barnes, and O. Marjanovic, "Stability limitation and analytical evaluation of voltage droop controllers for VSC MTDC," *CSEE Journal of Power and Energy Systems*, vol. 4, no. 2, pp. 238–249, 2018, doi: 10.17775/CSEEJPES.2016.00670.

- [315] Y. Liu, W. Deng, P. Yang, Y. Teng, X. Zhang, Y. Yang, and W. Pei, "Dispatchable Droop Control Strategy for DC Microgrid," vol. 9, pp. 98–102, 2023, doi: 10.1016/j.egyr.2023.09.158.
- [316] X. Gao, D. Zhou, A. Anvari-Moghaddam, and F. Blaabjerg, "Stability Analysis of Grid-Following and Grid-Forming Converters Based on State-Space Modelling," *IEEE Transactions on Industry Applications*, vol. 60, no. 3, pp. 4910–4920, 2024, doi: 10.1109/TIA.2024.3353158.
- [317] D. Ríos-Castro, D. Pérez-Estévez, and J. Doval-Gandoy, "Grid-Connected Converter With Grid-Forming and Grid-Following Modes Presenting Symmetrical and Asymmetrical Fault Ride-Through Capability," *IEEE Journal of Emerging* and Selected Topics in Power Electronics, vol. 12, no. 2, pp. 2082–2096, 2024, doi: 10.1109/JESTPE.2024.3355297.
- [318] P. M. Anderson and A. A. Fouad, Power System Stability, 2003, pp. 2–12, doi: 10.1109/9780470545577.ch1.
- [319] K. E. Cheikh Ali, P. Briff, A. Adamczyk, and O. Jasim, "Median valve submodule voltage control of MMC VSC for energy management application," in 19th International Conference on AC and DC Power Transmission (ACDC 2023), vol. 2023, 2023, pp. 148–153.